frontiers | Research Topics

Global excellence in oncology: Asia and australia 2021

Edited by
Zheng Huachuan, Xiongbing Zu, Young Hyeh Ko and Kun Zhang

Published in
Frontiers in Oncology
Frontiers in Pharmacology

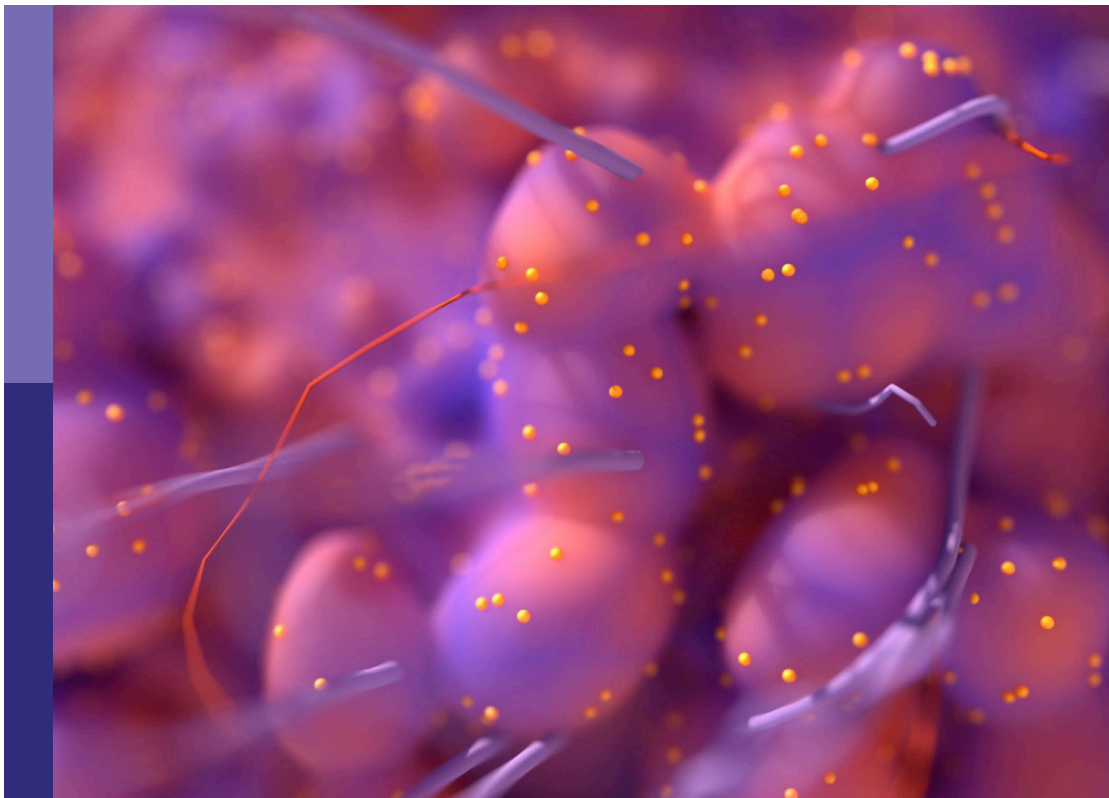

ISSN 1664-8714
ISBN 978-2-8325-0018-7
DOI 10.3389/978-2-8325-0018-7

About Frontiers

Frontiers is more than just an open access publisher of scholarly articles: it is a pioneering approach to the world of academia, radically improving the way scholarly research is managed. The grand vision of Frontiers is a world where all people have an equal opportunity to seek, share and generate knowledge. Frontiers provides immediate and permanent online open access to all its publications, but this alone is not enough to realize our grand goals.

Frontiers journal series

The Frontiers journal series is a multi-tier and interdisciplinary set of open-access, online journals, promising a paradigm shift from the current review, selection and dissemination processes in academic publishing. All Frontiers journals are driven by researchers for researchers; therefore, they constitute a service to the scholarly community. At the same time, the *Frontiers journal series* operates on a revolutionary invention, the tiered publishing system, initially addressing specific communities of scholars, and gradually climbing up to broader public understanding, thus serving the interests of the lay society, too.

Dedication to quality

Each Frontiers article is a landmark of the highest quality, thanks to genuinely collaborative interactions between authors and review editors, who include some of the world's best academicians. Research must be certified by peers before entering a stream of knowledge that may eventually reach the public - and shape society; therefore, Frontiers only applies the most rigorous and unbiased reviews. Frontiers revolutionizes research publishing by freely delivering the most outstanding research, evaluated with no bias from both the academic and social point of view. By applying the most advanced information technologies, Frontiers is catapulting scholarly publishing into a new generation.

What are Frontiers Research Topics?

Frontiers Research Topics are very popular trademarks of the *Frontiers journals series*: they are collections of at least ten articles, all centered on a particular subject. With their unique mix of varied contributions from Original Research to Review Articles, Frontiers Research Topics unify the most influential researchers, the latest key findings and historical advances in a hot research area.

Find out more on how to host your own Frontiers Research Topic or contribute to one as an author by contacting the Frontiers editorial office: frontiersin.org/about/contact

Global excellence in oncology: Asia and australia 2021

Topic editors

Zheng Huachuan — Chengde Medical University, China
Xiongbing Zu — Central South University, China
Young Hyeh Ko — Sungkyunkwan University, Republic of Korea
Kun Zhang — Tongji University, China

Citation

Huachuan, Z., Zu, X., Ko, Y. H., Zhang, K., eds. (2023). *Global excellence in oncology: Asia and australia 2021*. Lausanne: Frontiers Media SA.
doi: 10.3389/978-2-8325-0018-7

Table of contents

frontiers | Frontiers in Oncology

TYPE Editorial
PUBLISHED 10 August 2022
DOI 10.3389/fonc.2022.980419

OPEN ACCESS

EDITED AND REVIEWED BY
Alessandro Isidori,
AORMN Hospital, Italy

*CORRESPONDENCE
Kun Zhang
zhang1986kun@126.com

SPECIALTY SECTION
This article was submitted to Hematologic Malignancies, a section of the journal Frontiers in Oncology

RECEIVED 28 June 2022
ACCEPTED 07 July 2022
PUBLISHED 10 August 2022

CITATION
Zhang K (2022) Editorial: Global excellence in oncology: Asia and Australia 2021.
Front. Oncol. 12:980419.
doi: 10.3389/fonc.2022.980419

Editorial: Global excellence in oncology: Asia and Australia 2021

Kun Zhang*

Central Laboratory, Shanghai Tenth People's Hospital, Tongji University School of Medicine, Shanghai, China

KEYWORDS

oncology, Australia, Asia, diagnosis, therapy

Editorial on the Research Topic
Global excellence in oncology: Asia and Australia 2021

Cancer is one of the most challenging healthcare issues worldwide. In 2021 we called for submissions on the topic of cancer prevalence in Asia and Australia. We received 13 submissions, contributed by 89 authors, which have already had 6,583 views at the time of writing.

Park et al., in their analysis of antitumor medicine consumption in South Korea in recent decades, reported that, among breast, colorectal, liver, lung, gastric, and prostate cancer patients, breast cancer patients were the greatest consumers of antitumor medicine. This analysis provides data-based evidence for policymakers seeking to make cost efficiency improvements. Park et al. reported on postpartum breast cancer, analyzing the incidence rate, related factors, and prognosis according to the timing of breast cancer. Wang et al. analyzed the 5-year relative survival (RS) rate among liver cancer patients in a small city located southeast China, which was reported as 32.4% during the period 2014–2018. To investigate the association between bone cancer (BC) mortality and sex, age, and premature death, Ma et al. conducted population-based epidemiological research for BC mortality in Pudong, Shanghai, China. It was observed that a decrease in BC mortality accompanied the urbanization of the city, and there were clear disparities according to sex and age. Zheng et al. used The Cancer Proteome Atlas and bioinformatics technology to build a predictive model for the prognosis of stomach adenocarcinoma (STAD). The result was a prognostic model consisting of three proteins [collagen VI, cluster of differentiation 20 (CD20), and TP53-inducible glycolysis and apoptosis regulator (TIGAR)] that can predict 3-year overall survival rates. The study may set the tone for further research on STAD. As for colorectal cancer, Li et al. have developed a machine learning-based CT radiomics model to predict metachronous liver metastasis (MLM) in patients with colorectal cancer. A fusion model combining radiomics and clinical features seems to be a valuable model for predicting MLM. Seeking to improve pelvic radiotherapy, O'Connor et al. compared several methods of synthetic computed tomography (sCT) for MRI-only planning in radiation therapy,

demonstrating that bulk density assignment, tissue class segmentation, hybrid atlas, and deep learning sCT generation methods can greatly expand the accessibility of MRI-only planning in radiation therapy.

In research on tumors, Wang et al. found that phospholipase D2 (PLD2) plays a critical role in cancer cell motility and migration and other pathophysiological processes, suggesting that it could be a new therapeutic target for cancer treatment. Xi et al. have reported that microbubbles ultrasonic cavitation can lower the interstitial fluid pressure (IFP) in tumor tissues, leading to an accumulation of sonosensitizers, increasing the therapeutic effects of sonodynamic therapy (SDT). In non-small cell lung cancer (NSCLC), Wang et al. found that profilin 1 (PFN1) oversecretion increased microvesicle (MV) secretion through the rho kinase (ROCK)/phosphorylated myosin light chain (p-MLC) pathway, promoting NSCLC metastasis. By that means, PFN1 is a potential therapeutic target for NSCLC metastasis. Moreover, by reducing the secretion of MVs, it may be possible to partially reverse PFN1 overexpression-induced NSCLC cell migration. This study suggests a potential new approach in NSCLC metastasis treatment.

Regarding diagnostic imaging of the abdomen, Zhang et al. have discussed several intravenous contrast media (CM) for liver imaging according to biobehavioral features, such as an internal distribution and metabolization pathway, and acknowledge the potential value of a 'summarized navigating map' of CMs for common use in the clinic. Beyond the wash-in and wash-out data provided by common blood pool contrast agents, additional Kupffer phase data could be provided by Sonazoid®, GE Healthcare, Chicago USA, a micrometer-scaled microbubble with inert gas enveloped inside as an ultrasound contrast agent (UCA). Reticuloendothelial system-specific and hepatocyte-selective contrast agents can result in images that are more informative in diagnostic MRI. Moreover, certain molecular imaging agents, including immune molecular probes, stimulus-responsive/microenvironment-dependent contrast agents, and scale-dependent particles, constitute a blueprint for future liver imaging. Hu et al. discuss the clinical characterizations of pancreatic cystic neoplasms (PCNs), including intraductal papillary mucinous neoplasms (IPMNs), mucinous cystic neoplasms (MCNs), solid pseudopapillary neoplasms (SPNs), and serous cystic neoplasms (SCNs), associated diagnostic imaging and precision imaging for radiomics, and emerging techniques such as endoscopic ultrasound (EUS) with fine-needle aspiration (FNA) and molecular markers that compensate for the limitations posed by cytology and tumor markers.

Readers will certainly benefit from the above research.

Author contributions

The author confirms being the sole contributor of this work and has approved it for publication.

Conflict of interest

The author declares that the research was conducted in the absence of any commercial or financial relationships that could be construed as a potential conflict of interest.

Publisher's note

frontiers in Oncology

ORIGINAL RESEARCH
published: 08 February 2022
doi: 10.3389/fonc.2022.822687

Comparison of Synthetic Computed Tomography Generation Methods, Incorporating Male and Female Anatomical Differences, for Magnetic Resonance Imaging-Only Definitive Pelvic Radiotherapy

Laura M. O'Connor[1,2*], *Jae H. Choi*[1,3], *Jason A. Dowling*[4], *Helen Warren-Forward*[2], *Jarad Martin*[1,5] *and Peter B. Greer*[1,3]

[1] Department of Radiation Oncology, Calvary Mater Hospital, Newcastle, NSW, Australia, [2] School of Health Sciences, University of Newcastle, Callaghan, NSW, Australia, [3] School of Mathematical and Physical Sciences, University of Newcastle, Callaghan, NSW, Australia, [4] Commonwealth Scientific and Industrial Research Organisation (CSIRO), Australian E-Health Research Centre, Herston, QLD, Australia, [5] School of Medicine and Public Health, University of Newcastle, Callaghan, NSW, Australia

OPEN ACCESS

Edited by:
Tonghe Wang,
Emory University, United States

Reviewed by:
Bin Tang,
Sichuan Cancer Hospital, China
Joshua Pohyun Kim,
Henry Ford Health System,
United States

***Correspondence:**
Laura M. O'Connor
Laura.OConnor@calvarymater.org.au

Specialty section:
This article was submitted to Radiation Oncology, a section of the journal Frontiers in Oncology

Received: 26 November 2021
Accepted: 11 January 2022
Published: 08 February 2022

Citation:
O'Connor LM, Choi JH, Dowling JA, Warren-Forward H, Martin J and Greer PB (2022) Comparison of Synthetic Computed Tomography Generation Methods, Incorporating Male and Female Anatomical Differences, for Magnetic Resonance Imaging-Only Definitive Pelvic Radiotherapy. Front. Oncol. 12:822687. doi: 10.3389/fonc.2022.822687

Purpose: There are several means of synthetic computed tomography (sCT) generation for magnetic resonance imaging (MRI)-only planning; however, much of the research omits large pelvic treatment regions and female anatomical specific methods. This research aimed to apply four of the most popular methods of sCT creation to facilitate MRI-only radiotherapy treatment planning for male and female anorectal and gynecological neoplasms. sCT methods were validated against conventional computed tomography (CT), with regard to Hounsfield unit (HU) estimation and plan dosimetry.

Methods and Materials: Paired MRI and CT scans of 40 patients were used for sCT generation and validation. Bulk density assignment, tissue class density assignment, hybrid atlas, and deep learning sCT generation methods were applied to all 40 patients. Dosimetric accuracy was assessed by dose difference at reference point, dose volume histogram (DVH) parameters, and 3D gamma dose comparison. HU estimation was assessed by mean error and mean absolute error in HU value between each sCT and CT.

Results: The median percentage dose difference between the CT and sCT was <1.0% for all sCT methods. The deep learning method resulted in the lowest median percentage dose difference to CT at –0.03% (IQR 0.13, –0.31) and bulk density assignment resulted in the greatest difference at –0.73% (IQR –0.10, –1.01). The mean 3D gamma dose agreement at 3%/2 mm among all sCT methods was 99.8%. The highest agreement at 1%/1 mm was 97.3% for the deep learning method and the lowest was 93.6% for the bulk density method. Deep learning and hybrid atlas techniques gave the lowest difference to CT in mean error and mean absolute error in HU estimation.

Conclusions: All methods of sCT generation used in this study resulted in similarly high dosimetric agreement for MRI-only planning of male and female cancer pelvic regions. The choice of the sCT generation technique can be guided by department resources available and image guidance considerations, with minimal impact on dosimetric accuracy.

Keywords: MRI radiotherapy planning, image-guided radiotherapy, synthetic CT, computer-assisted radiotherapy planning, rectum neoplasms, cervix neoplasms, endometrium neoplasms, anal canal neoplasms

1 INTRODUCTION

Magnetic resonance imaging (MRI)-based radiotherapy treatment planning is an increasingly popular concept in radiation oncology. MRI affords greater soft tissue contrast for tumor and organ at risk (OAR) definition than computed tomography (CT), and MRI-based planning reduces the registration errors associated with supplementary image registration (1–3). To move away from the conventional use of CT in treatment planning, a synthetic CT (sCT) is created from the MRI, to facilitate MRI-based treatment planning. The sCT is an estimation of the electron densities of the tissues in the body, which allows for dose calculation in the radiation therapy treatment planning systems.

Larger pelvic treatment sites have received less attention in this area of work than prostate treatment sites, with previous larger pelvis sCT generation methods utilizing small groups of patient numbers and without consideration of the differences in male and female pelvic anatomy (4–7). This is also significant as the treatment volumes for colorectal and gynecological cancers traverse a more variable body contour and bony anatomy than prostate treatments. Rectum, anal canal, and gynecological treatments involve the treatment of larger and more variable body contour and bony anatomy than prostate treatments with differing prescription doses to the gross tumor volume, surrounding tissue deemed to be at high risk of tumor spread; the disease-positive nodes; and the surrounding local nodal volumes.

Several methods of sCT creation have been reported in the literature, which can be summarized into essentially four popular methods: bulk density assignment, tissue class density assignment, atlas-based, and computer learning (8). However, more commonly, the hybrid approaches of these methods are being utilized for greater accuracy (9, 10). The choice of the sCT generation technique can be guided by the need for extra resources, the ease of application, dosimetric accuracy, and image guidance considerations.

Bulk density assignment involves applying a single Hounsfield unit (HU) value to an entire volume, usually assuming water equivalency. This method may also differentiate between bone and tissue regions and apply a separate HU value to bone for greater accuracy. It is a relatively easy method to implement, usually manually performed, meaning that it requires minimal resources such as additional software or complex scanning protocols. The limitations of this method are that it does not take tissue inhomogeneity into account and it also may not generate realistic digitally reconstructed radiographs (DRRs) for treatment image guidance structures (1, 8). This method is currently utilized in brachytherapy treatment planning, in which image guidance is not a consideration and tissue inhomogeneity is not of great concern, given the relatively sharp dose fall off around the applicator (11). Bulk density assignment has also been investigated for prostate and brain treatments and has been utilized for sCT quality assurance measures (1, 12–14).

Tissue class density assignment is an extension of bulk density assignment, in which tissue inhomogeneity is addressed to some extent. This method involves using particular MRI sequences, such as a DIXON sequence, to classify body tissues into subtypes, i.e., muscle, fat, bone, and air. Each of these tissue subtypes is assigned an appropriate HU value (15). Tissue class density assignment has been a popular method of sCT creation, commonly combined with other atlas-based methods to improve bone region estimations, and has been utilized in commercial software (9, 10, 16). Previous applications of this method have focused mostly on the pelvic region (12, 17, 18).

An atlas-based approach involves comparing an MRI to a library atlas of co-registered CT and MRI pairs. The MRI scans in the atlas are non-rigidly registered to the acquired MRI scan, and the deformation matrix is applied to the corresponding CT pairs, to create the sCT. This approach can be performed using a single atlas pair, but has seen greater success for pelvis sites when multiple atlases are registered and combined with local weighted voting of atlas patch values, termed a hybrid multi-atlas approach (19–21). This method takes tissue inhomogeneity into account and can be used with image guidance. This method has successfully been translated to the clinic and has also been used for bone definition in commercial hybrid sCT generation products (9, 21–23).

Deep learning is an increasingly popular machine learning method for sCT generation, utilizing deep convolutional neural networks to convert an MRI into an sCT scan. Deep learning methods have been used successfully in the literature for pelvic and brain sCT creation, with the model outperforming other sCT generation methods (4, 24, 25). Models can be trained using CT/MRI pairs or can utilize unpaired MRI and CT data, thereby reducing the errors introduced in the registration process between the two images (4, 26, 27). Deep learning methods commonly utilize generative adversarial networks (GAN) composed of a generator and discriminator trained with paired CT/MRI data, such that the generator creates the sCT from the MRI, while the discriminator differentiates whether the image is real or fake, providing feedback to the generator. This continues

until the discriminator can no longer determine that the image is synthetic (27). Unpaired generative methods utilize a cycle GAN model in which a single GAN network creates the sCT as described above, while a second GAN network converts the sCT image back to an MRI, and the difference between the images is fed back to the training loop (27). Similar to atlas-based methods, deep learning can be used for image guidance.

Each of these methods has its advantages and trade-offs in its accuracy, time, and ease of conversion. sCT methods have been predominantly developed to date for prostate and brain treatment sites, and previous comparisons of sCT generation methods have been performed for prostate treatments (28–30). More recently, a deep-learning method was developed using a multicenter anorectal cancer patient cohort (31).

This work provides a comparison of four major methods for the generation of synthetic CT: bulk density assignment, tissue class density assignment, hybrid multi-atlas, and deep learning sCT generation for a large dataset of male and female rectum, anal canal, cervix, and endometrium treatments. The sCT methods were compared with the conventional CT scan in terms of dosimetric impact on the treatment plan and mean error and mean absolute error in Hounsfield unit values.

2 MATERIALS AND METHODS

2.1 Patient Data Collection

Ethics approval for the study was obtained through the local health district human research ethics committee (ref:17/06/21/3.02), and all patients gave informed consent to participate in the trial. MRI and CT datasets and treatment plans of 40 patients (20 male, 20 female) who received radiation treatment for histologically confirmed malignancy of either the rectum, anal canal, cervix, or endometrium were used for the study.

Patients were positioned with their legs flat using a CIVCO Vac-Lok bag (CIVCO Medical Instruments, IA, USA) for immobilization. CT scans were acquired on a SOMATOM Confidence CT scanner (Siemens Healthineers, Erlangen, Germany) at 120 kV with 2.0 mm slice thickness. Oral or intravenous contrast was administered at the request of the radiation oncologist. MRI scans were performed immediately following the planning CT scan, on a MAGNETOM Skyra 3T MRI scanner (Siemens Healthineers, Erlangen, Germany), equipped with a Qfix flat couch (Qfix, PA, USA) and DORADOnova MR 3T external laser bridge (LAP, Luneburg, Germany). A 32-channel spine coil was utilized under the flat couch top and two 18-channel body coils were used over the pelvic region. To avoid compression of the external body contour, body coils were positioned in a Qfix INSIGHT MR Body coil holder. A stitched T1 VIBE Dixon MRI sequence (**Table 1**) was acquired to facilitate sCT generation. The Dixon imaging technique provides an in-phase, out-of-phase, fat-weighted, and water-weighted image from a single acquisition. The MRI and CT scan range included the entire lumbar spine to mid femur, and patients were scanned with a full bladder and empty bowels.

Treatment planning was performed on the CT scan using the Eclipse TPS (version 15.6; Varian Medical Systems, Palo Alto, USA). Three patients in the male cohort were planned as intensity-modulated radiation therapy (IMRT), while all the other patients were planned as 6-MV, 2–3 arc volumetric-modulated arc therapy (VMAT). The three patients planned as IMRT were re-planned as VMAT retrospectively, to standardize the planning technique analyzed for the study.

TABLE 1 | MRI acquisition parameters.

Parameter	T1 VIBE Dixon
Scan type	VIBE Dixon
TE (ms)	1.23/2.46
TR (ms)	4.19
Flip angle (°)	9
FOV (mm)	256 * 499
Slice thickness (mm)	1.6
Base resolution	160
Acquisition plane	Coronal
Phase direction	R>L
Bandwidth (Hz/px)	1,200
Fat-water shift (px)	0.3
Distortion correction	3D
Acquisition stages	2
Overlap (mm)	48
Composing	Inline

2.2 sCT Creation

2.2.1 Bulk Density Assignment

The bulk density assignment included two tissue classes—bone and soft tissue. The bone regions were outlined manually on the T1 in-phase Dixon MRI sequence, while the whole body region was defined by image thresholding. Choi et al. had previously derived the optimal bulk density values for bone and tissue to patients treated for prostate cancer, which equated to a relative electron density of 1.20 and mass density of 1.25 g/cm^3 for bone regions and a relative electron density of 0.97 and mass density of 0.99 g/cm^3 for tissue (12).

2.2.2 Tissue Class Density Assignment

For the tissue class density assignment method, the tissue was separated into three tissue classes: fat, muscle/visceral, and bone. The entire body region was defined using image thresholding and the bone regions were outlined manually on the T1 in-phase Dixon MRI sequence. The fat tissue was segmented from the fat-weighted Dixon MRI image using image thresholding. The muscle and visceral tissue was defined by a Boolean subtraction of the fat and bone regions from the body contour. The optimal electron densities of each tissue class in this study were also determined by Choi et al. for prostate treatments, which equated to a relative electron density of 1.16 and mass density of 1.20 g/cm^3 for bone regions, a relative electron density of 1.02 and mass density of 1.03 g/cm^3 for muscle, and a relative electron density of 0.91 and mass density of 0.92 g/cm^3 for fat (12).

2.2.3 Hybrid Multi-Atlas Based

Participants were separated into male (n = 20) and female (n = 20) cohorts for the creation of gender-specific atlases. A bias field

correction was applied to the MRI image to homogenize the image intensity across the field, and the hybrid atlas-based sCT generation method of Dowling et al. was utilized, with a leave-one-out cross-validation approach applied for both groups (i.e., 19 CT/MRI pairs were used to generate an sCT for each target patient MRI) (21). This approach was modified from the original method to account for the larger field of view, by utilizing a custom structure-guided rigid (6 degrees of freedom) and non-rigid registration (using binary labels based on the bone and bladder contours) between each CT and MRI pair in the atlas set. Each MRI in the atlas set was registered to the acquired MRI initially by using the body mask, and then deformably registered to the target MRI. A local weighted voting was then applied with a 3D radius and a gain parameter to increase the sensitivity of patch value similarities. These weightings were applied to the corresponding patches in each of the co-registered CT scans in the atlas to create the sCT.

2.2.4 Deep Learning

The deep learning model was created using a conditional generative adversarial network (cGAN), consisting of a single generator and a discriminator, trained using the paired MRI-CT data (32). The network is set with a condition, meaning that both the generator and the discriminator of the network are conditioned on the CT (target) image for a direct MRI to sCT conversion (32). The CT and MRI scans were preprocessed using a binary mask to remove the background and the scans were resampled to a matrix of 320 × 320 voxels. A bias field correction was applied to the MRI image to homogenize the image intensity across the field, and then standardization of the image intensity peaks was applied to standardize tissue weightings across the whole cohort. Image registration between the CT and MRI was performed using structure-guided (bone) non-rigid registration. The patient cohort was separated into four groups of 10 and then used for training and testing four individual cGAN models using four-fold cross-validation, that is, each model was trained with the CT/MRI pairs of 30 patients and generated sCT scans of 10 patients for testing.

The generator was a modified U-net with a similar architecture to the model proposed by Han et al. and Largent et al. (**Figure 1**) (26, 30). The network was an encoding–decoding network that extracted features from the input MRI and reconstructed an sCT using these features. At the encoding part, features were extracted through the convolutional blocks with a filter size of 3 × 3 and stride 1. The features were then down-sampled through the down-sampling convolutional blocks

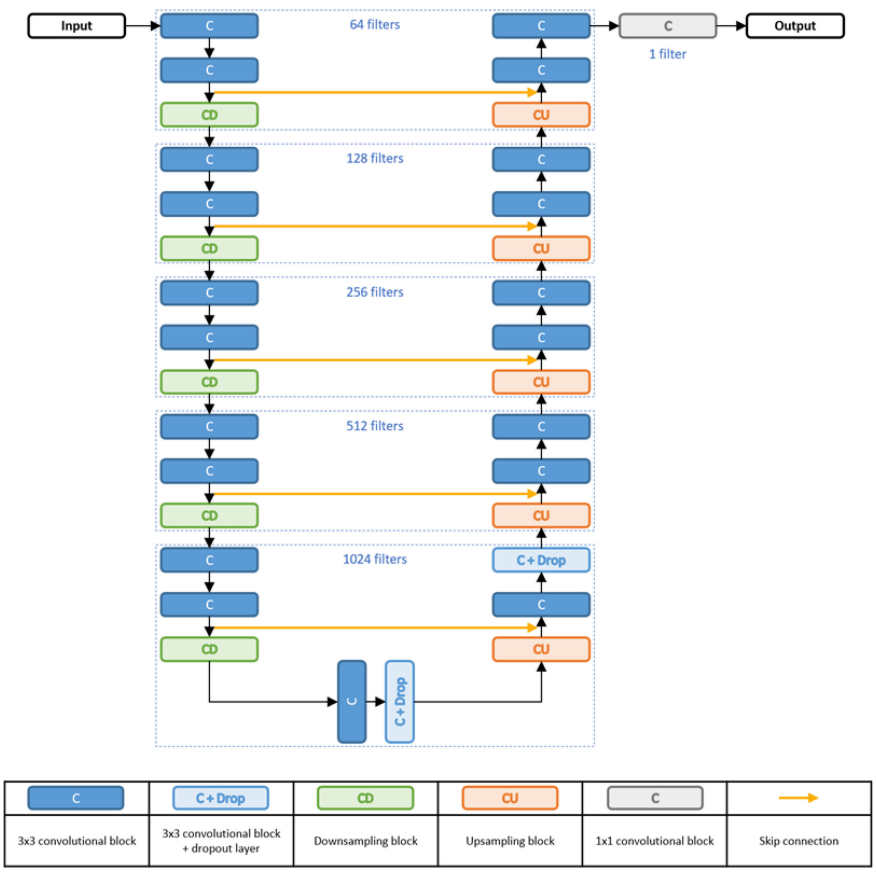

FIGURE 1 | Generator architecture. Note that the number of filters (i.e., 64 filters) indicates the number of filters in each convolutional layer.

with a filter size of 3 × 3 and stride 2, as suggested by Largent et al. (30). The features from the encoding part were then used in the decoding part to construct the sCT. At the decoding part, the feature maps were up-sampled *via* a 3 × 3 transpose convolution with stride 2, also suggested by Largent et al. (30). The last convolution block of the decoder part consisted of a 1 × 1 convolution with stride 1, followed by a hyperbolic tangent activation to output the sCT. In all except the last block, each convolutional block in the generator used batch normalization and a rectified linear unit (ReLU) activation function. Skip connections were added between the encoder and the decoder for concatenating the channels of the feature map. Furthermore, two dropout layers with a drop rate of 0.5 were applied, one after the bottleneck and the other after the CU1024 block to prevent overfitting.

The discriminator was a small CNN-based image classifier, and its architecture was similar to the model proposed by Largent et al. (30). It can be defined as:

Discriminator:CD8-CD16-CD32-CD64-CD128-C128-F where CD was the down-sampling block and F was the fully connected layer with sigmoid activation. The numbers on each block indicate the number of filters. All the CD blocks of the discriminator used the leaky ReLU, with the slope coefficient 0.2, as the activation function for allowing a small gradient for the input that is less than zero (33). The last convolutional block (C128) operated a 1 × 1 convolution with stride = 1. The output was then fully connected for 1D output. The discriminator was a binary classification model using binary cross entropy so that it predicts an output in the range of 0 (fake) and 1 (real).

The weights of both models were initialized with a normal distribution with mean = 0 and standard deviation = 1e-4. For updating the generator, a loss was calculated by adding the adversarial loss, calculated *via* the discriminator, and the L1 (mean absolute error) loss between the generated output (sCT) and the target image (CT). Weights on both the adversarial and the L1 losses were set to 1. Adam optimization algorithm was used for stochastic gradient descent optimization and the learning rate was set to 1e-4. Batch size and training epochs were set to 10 and 20, respectively.

2.3 sCT Validation

The CT scan, T1 VIBE Dixon MRI, and sCT datasets were imported into the treatment planning system. For each subject, the atlas-based and deep learning sCT datasets were co-registered to the MRI and the MRI registered to the CT using rigid registration, with a registration boundary of the top of the second lumbar vertebrae to the greater trochanter. The bulk density and tissue class segmentation methods were performed on the MRI scan. To reduce disparity introduced by bowel gas, the bowel gas on the datasets was overridden to average surrounding tissue HU value for 10 patients. Two patients with a large discrepancy in body contour of >4 cm in the lateral posterior region, between the CT and MRI, due to tensing of the gluteal muscles in CT, had this region removed from the sCT calculation volume, so as to not affect the results.

The treatment plan, structure set, and International Commission of Radiation Units and Measurements (ICRU) reference point were copied from the original CT to each sCT, and the plan was recalculated with identical monitor unit values. Dosimetry was compared using the dose difference at the plan ICRU point, relevant dose volume histogram (DVH) dose parameters for planning target volume (PTV) and organ at risk (OAR) structures per standard guidelines for each treatment site, and a 3D dose gamma comparison (34, 35). The plan on the CT scan was used as the gold standard. As several DVH parameters were evaluated for PTV and OAR structures, the average dose difference is a combined average of each of these parameters for all structures. The percentage dose difference was calculated by the formula (DsCT – DCT)/DCT * 100%. Due to the non-parametric nature of the data, statistical significance was determined using a Mann–Whitney ***U***-test with a significance level of 0.05. Three-dimensional gamma analysis was performed using an in-house MATLAB code (MATLAB; MathWorks, Massachusetts, USA), using dose difference (%) and distance to agreement (mm) criteria of 3%/2 mm, 2%/2 mm, and 1%/1 mm. An erosion of 15 mm of the body perimeter was applied to exclude failures which occurred at the skin edge due to small unavoidable differences in body contour between datasets, and a 10% low-dose threshold was applied.

Hounsfield unit estimation accuracy was assessed using mean error (ME) and mean absolute error (MAE) in HU value for the entire body and bone region. To account for regions of image degradation in some sCT datasets, the superior and inferior 30 mm of the datasets was not included in these calculations.

3 RESULTS

Detailed patient demographics are outlined in **Table 2**. Of the 40 patient datasets used in the trial, 4 patients in the male cohort and 11 patients in the female cohort received iodine-based oral contrast, while 1 patient in the female cohort received iodine-based IV contrast for the planning CT scan.

All sCT generation methods were successfully applied to the MRI scan of each patient. An example of the conventional CT scan, T1-weighted MRI, and each sCT generation method for a single patient is shown in **Figure 2**. The closest agreement in ME and MAE in HU estimation was for the deep learning and hybrid atlas techniques for the whole body, bone, and soft tissue estimations (**Table 3**). The dosimetric results correlated well with the ME and MAE results, with the greatest difference in ME and MAE resulting in the greatest dosimetric error for the bulk density method.

There was no statistically significant dose difference to CT at the ICRU reference point for any of the sCT methods (**Table 3**). The median DVH dose difference for all structures and parameters combined was less than 0.5% for all sCT methods, with the greatest agreement for the deep learning method and the least agreement in the bulk density method (**Table 3** and **Figure 3**). There was a statistically significant difference (p = 0.002) for the bulk density sCT, with a median percentage dose difference at the ICRU reference point between the male and female cohort of −0.89% [interquartile range (IQR) of −0.72, −1.15) and −0.09% (IQR of 0.09, −0.83), respectively.

TABLE 2 | Patient demographics.

	Cohort size	Age range	BMI range (kg/m^2)	Relevant surgical history	Primary treatment site	Staging range
Male cohort	20	49–88 (mean = 65)	20.5–33.6 (mean = 25.5)	Hernia repairs (*n* = 3) Rectal resections (*n* = 2) Appendectomy (*n* = 1)	Rectum (*n* = 20)	T1N0–T4N1
Female cohort	20	41–85 (mean = 61)	18.0–36.9 (mean = 26.2)	Hysterectomy (*n* = 6) Common iliac stent (*n* = 1) Caesarean (*n* = 1) Hernia repair (*n* = 2) Appendectomy (*n* = 3)	Rectum (*n* = 4) Anal canal (*n* = 4) Cervix (*n* = 8) Endometrium (*n* = 4)	T3N0–T3N2 T1N0–T3N1 IIA–IIB IIIA–IIIC

There was no statistically significant difference in the median percentage dose difference at the ICRU reference point between the male and female cohort for the other sCT methods.

The 3D gamma results with criteria of 3%/2 mm for all sCT methods were within the American Association of Physics in Medicine (AAPM) TG218 report guidelines of >95% (**Table 4**) (36). The closest agreement at 1%/1 mm was seen for the deep learning sCT, while the greatest difference between the male and female cohort was in the hybrid atlas-based and bulk density methods.

4 DISCUSSION

The results presented in this article compare favorably to previous studies of sCT generation for MRI-only planning. The methods chosen for sCT generation in this article were based on previous literature, which returned similarly high dosimetric agreement in separate studies on MRI-only planning for pelvic treatments. The bulk density assignment was based on the bone–tissue maps of Choi et al., which was applied to 54 prostate treatment plans (12). Choi et al. presented a dose agreement at ICRU point of −0.15% ± 0.90% (IQR = 0.31, −0.65) and a mean 3D gamma agreement of 90.7% ± 0.2% with a criteria of 1%/1 mm (12). The bone and body contours in this study were assigned the same densities to the study of Choi et al., to determine if those values are also applicable to male and female patients with anal canal, rectal, endometrial, or cervical cancer (12). Compared with the study of Choi et al., the dose agreement at ICRU point in this study was lower at −0.73% ± 0.59%, while the mean 3D gamma agreement at 1%/1 mm was higher at 93.6% ± 3.8%. The difference in the results may be due to the study of Choi et al. being optimized for prostate treatments, while this study applied the method to male and female cohorts with treatment regions in the pelvis and lower abdominal region (12). The bulk density values of the tissue could have been affected by a difference in fat to water ratio in this region and body mass index between the different cohorts of patients (37).

The fact that the density values were not re-optimized for the cohort of this study would also explain the difference in the results for the tissue class density assignment results. The tissue

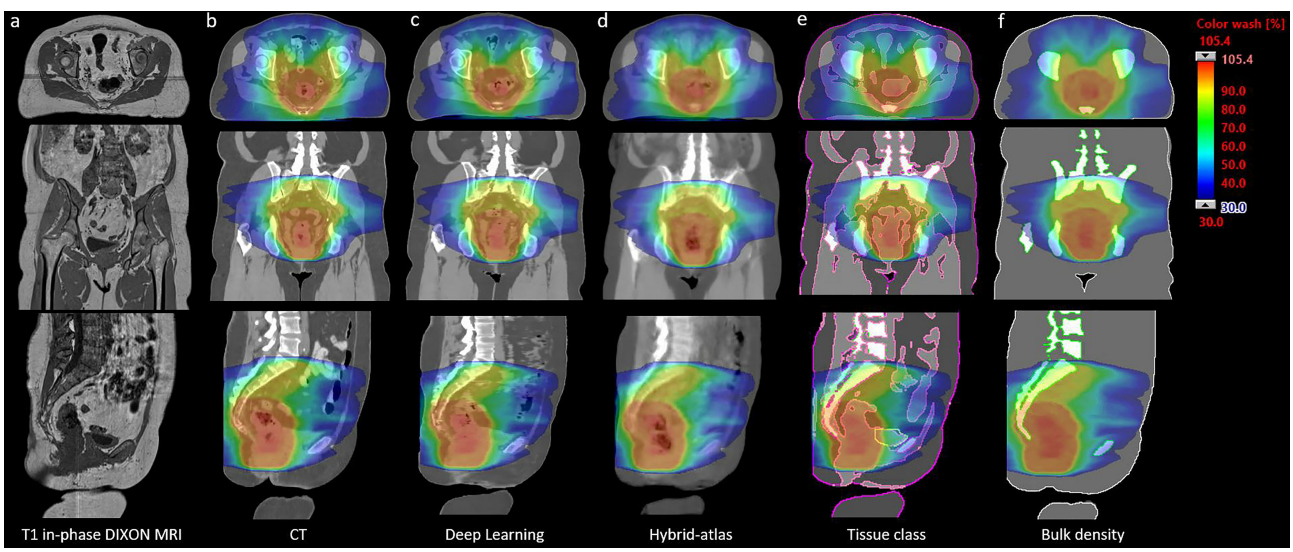

FIGURE 2 | CT and sCT scans (with corresponding MRI) with treatment plan calculated and dose color wash displayed. Column **(A)** T1 in-phase-stitched T1 VIBE Dixon; column **(B)** original CT scan column; column **(C)** deep learning-generated sCT; column **(D)** hybrid atlas-generated sCT; column **(E)** tissue class density assignment sCT (three tissue classes); and column **(F)** bulk density overrides sCT.

TABLE 3 | ICRU median percentage dose difference and median DVH dose difference by the sCT method.

	ICRU %DD		DVH %DD		Mean absolute error (HU)			Mean error (HU)		
	Median (IQR)	*p*-value	Median (IQR)	*p*-value	Whole body	Bone	Soft tissue	Whole body	Bone	Soft tissue
Deep learning	−0.03 (0.13, −0.31)	1.00	0.18 (0.40, −0.05)	0.93	34.7 ± 5.1	109.4 ± 12.3	25.2 ± 3.4	−2.5 ± 5.8	−46.0 ± 19.6	−0.7 ± 6.3
Hybrid atlas	−0.30 (−0.02, −0.57)	0.82	−0.27 (0.12, −0.77)	0.76	57.4 ± 8.0	186.9 ± 17.9	47.3 ± 7.8	−2.0 ± 9.0	−78.0 ± 35.3	4.1 ± 8.5
Tissue class	−0.48 (−0.28, −0.85)	0.68	−0.48 (0.11, −0.66)	0.71	58.8 ± 10.4	228.2 ± 11.2	44.6 ± 8.5	−9.8 ± 7.3	−25.8 ± 39.7	−8.6 ± 7.5
Bulk density	−0.73 (−0.10, −1.01)	0.64	−0.33 (0.19, −0.67)	0.70	89.1 ± 7.7	244.1 ± 10.0	76.1 ± 6.7	8.0 ± 13.7	5.7 ± 39.3	7.8 ± 14.7

Mean absolute error and mean error in whole body and bone HU ± 1 SD by the sCT method.

class density assignment method was based on the bone–muscle–fat (BMF) maps of Choi et al. which were once again applied to 54 prostate treatment plans (12). Compared with the cohort in this study, the dose agreement at the ICRU point was higher for Choi et al. −0.16% ± 0.65% (IQR 0.22, −0.60), compared with −0.48% ± 0.44% (IQR −0.28, −0.85), while the mean 3D gamma agreement at 1%/1 mm was lower at 93.8% ± 8.6% than in this study at 95.3% ± 3.3%.

The atlas-based method was based on the hybrid atlas sCT generation method of Dowling et al., which had previously shown to outperform the atlas-based method of the group (20, 21). Dowling et al. applied the hybrid atlas approach to 39 prostate cancer treatment plans. The hybrid atlas approach was modified in our study, for a larger anatomical region by incorporating structure-guided rigid and non-rigid registration (bone and bladder) in the atlas set. The results of the study of Dowling et al. correlate strongly with the results of this study, with similarly low percentage difference of the dose calculated at the ICRU reference point of −0.3% ± 0.8% and −0.3% ± 0.5%, respectively, and a mean 3D gamma agreement at 1%/1 mm of >95% and 94.8%, respectively (21).

The deep learning approach to sCT generation in this study is similar to that of Largent et al. and Maspero et al. (4, 30). The cGAN approach was favored for our study over a cycle GAN due

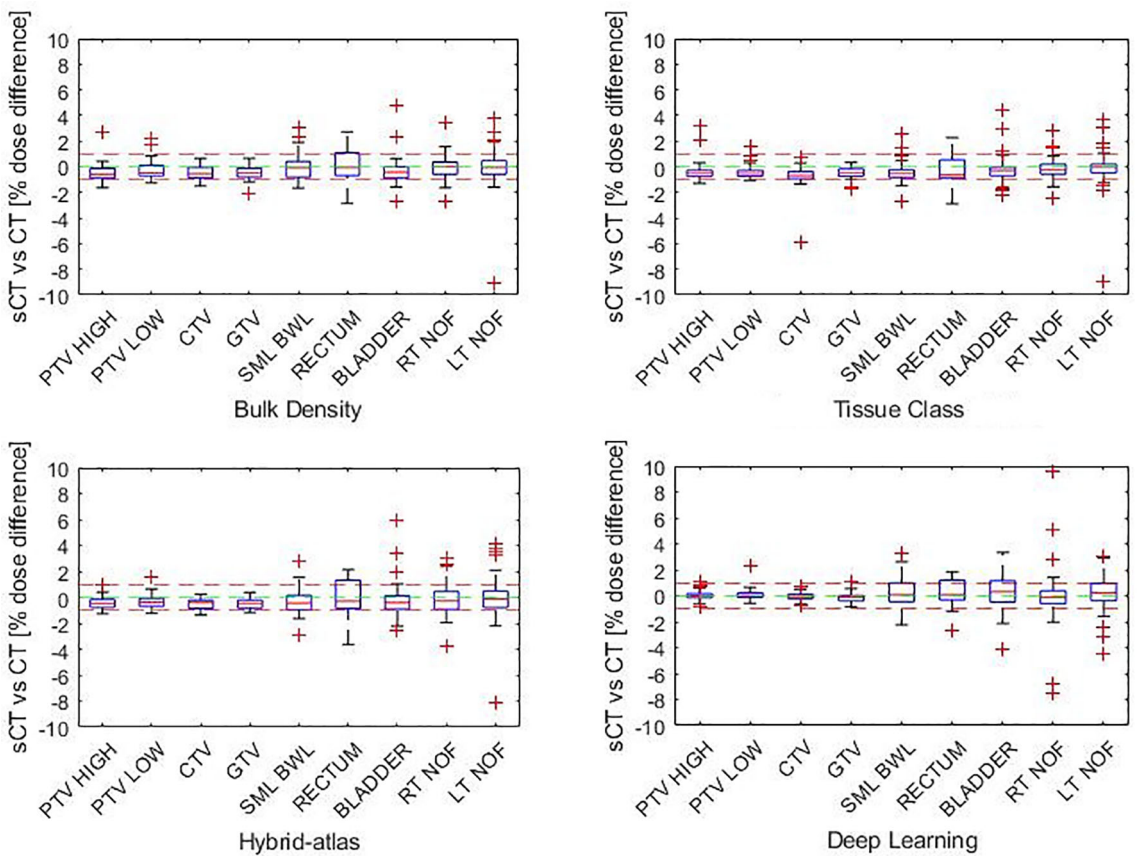

FIGURE 3 | Percentage DVH dose difference by structure (each structure parameter combined) for each synthetic CT method.

TABLE 4 | 3D gamma dose comparison for each sCT technique (mean ± 1 SD).

		3%/2 mm		2%/2 mm		1%/1 mm	
		Pass rate (%)	Average gamma	Pass rate (%)	Average gamma	Pass rate (%)	Average gamma
Deep learning	All	99.8 ± 0.3	0.09 ± 0.02	99.7 ± 0.4	0.14 ± 0.03	97.3 ± 2.0	0.28 ± 0.07
	Female	99.8 ± 0.3	0.10 ± 0.02	99.6 ± 0.4	0.14 ± 0.03	97.4 ± 1.2	0.28 ± 0.06
	Male	99.9 ± 0.3	0.09 ± 0.03	99.7 ± 0.4	0.14 ± 0.03	97.1 ± 2.5	0.27 ± 0.08
Hybrid atlas	All	99.8 ± 0.3	0.12 ± 0.04	99.7 ± 0.3	0.17 ± 0.05	94.8 ± 4.5	0.35 ± 0.11
	Female	99.8 ± 0.3	0.13 ± 0.04	99.7 ± 0.4	0.19 ± 0.06	93.4 ± 5.2	0.38 ± 0.12
	Male	99.8 ± 0.2	0.10 ± 0.03	99.7 ± 0.3	0.15 ± 0.04	96.3 ± 3.2	0.31 ± 0.09
Tissue class	All	99.8 ± 0.3	0.12 ± 0.03	99.7 ± 0.4	0.18 ± 0.04	95.3 ± 3.3	0.35 ± 0.08
	Female	99.8 ± 0.3	0.12 ± 0.02	99.7 ± 0.4	0.18 ± 0.03	95.2 ± 3.1	0.36 ± 0.07
	Male	99.9 ± 0.2	0.12 ± 0.03	99.7 ± 0.4	0.17 ± 0.04	95.4 ± 3.2	0.34 ± 0.09
Bulk density	All	99.8 ± 0.3	0.14 ± 0.03	99.7 ± 0.4	0.19 ± 0.05	93.6 ± 3.8	0.38 ± 0.09
	Female	99.8 ± 0.4	0.12 ± 0.03	99.6 ± 0.4	0.17 ± 0.05	95.1 ± 3.3	0.34 ± 0.09
	Male	99.9 ± 0.2	0.13 ± 0.03	99.7 ± 0.4	0.21 ± 0.05	92.1 ± 3.6	0.42 ± 0.09

to the high GPU memory requirements and long training times of the cycle GAN method. Maspero et al. applied the cGAN approach to sCT generation for pelvic radiotherapy, performing dose analysis on 30 patients (10 prostate, 10 rectum, and 10 cervix) (4). Maspero et al. reported a similar dose difference of 0.1%–0.3% to this study of −0.03% ± 0.42% and a gamma agreement at 2%/2 mm of 94.8% compared with this study of 99.7% ± 0.4%.

All sCT generation methods assessed in this study returned similarly high dosimetry agreement when compared with CT and were all within clinically acceptable ranges. However, image guidance and the amount of resources required are other drivers in the choice of an sCT generation method. Accurate bony anatomy is required for image guidance on treatment. Although bulk density and tissue class density assignment methods do not necessarily require additional software to perform, the manual contouring of the bone regions on MRI can be time-consuming. As such, these methods have successfully been combined with an atlas-based approach for the bone mask and are the basis of commercial sCT generation products (9, 10). Atlas-based and deep learning methods both provide reliable bone definition and are increasingly favored for MRI-only planning due to image guidance considerations. Deep learning methods have the advantage over atlas-based methods in the time it takes to generate an sCT. The deep learning method presented in this study took 3.5 s for a single sCT generation, while the atlas-based method took approximately 50 min. Therefore, for the methods presented in this study, there are advantages and drawbacks of each method, and centers are able to use this knowledge to identify the most suitable method for MRI-only planning.

This study has shown that a bulk density assignment, tissue class segmentation, hybrid atlas, and deep learning methods of sCT generation can be utilized for MRI-only planning of male and female cancers of the rectum, anal canal, cervix, and endometrium. The implications of this study indicate that selection of an sCT generation technique can be driven by department resources, with minimal impact to plan dosimetry, therefore greatly expanding the accessibility of MRI-only planning in radiation therapy.

DATA AVAILABILITY STATEMENT

The datasets presented in this article are not readily available because ethics approval for this study does not allow for sharing of individual patient scans. Other study data, which do not include patient datasets, are available from the corresponding author on reasonable request. Requests to access the datasets should be directed to Laura.OConnor@calvarymater.org.au

ETHICS STATEMENT

The studies involving human participants were reviewed and approved by Hunter New England Human Research Ethics Committee. The patients/participants provided their written informed consent to participate in this study. Written informed consent was obtained from the individual(s) for the publication of any potentially identifiable images or data included in this article.

AUTHOR CONTRIBUTIONS

LO'C was involved in the study design, patient recruitment, data collection, data analysis and wrote the manuscript. JC developed the deep learning-based synthetic CT creation method used in this study. The tissue class density assignment and bulk density synthetic CT methods were based on previous work by JC. JD developed the atlas-based synthetic CT creation method used in this study. JD, JC, PG, HW-F, and JM contributed to the study design data analysis and revised the manuscript critically for important intellectual content. JM contributed to the formal analysis. All authors read and approved the final manuscript.

FUNDING

LMO, PG, JD and JM received research grant funding through the Calvary Mater Newcastle Hospital (Margaret Mitchell Research grant 16-12) for the development of atlas-based algorithms. JHC and PG received research grant funding through the Australian National Health and Medical Research Fund (The Australian MRI-Linac Program) for the development of deep learning algorithms.

REFERENCES

1. Tyagi N. "Challenges and Requirements". In: G Liney, U van der Heide, editors. *MRI for Radiotherapy. 1st Ed*. Manhattan, New York: Springer International Publishing (2019). p. 119–29. doi: 10.1007/978-3-030-14442-5_8
2. Dean CJ, Sykes JR, Cooper RA, Hatfield P, Carey B, Swift S, et al. An Evaluation of Four CT–MRI Co-Registration Techniques for Radiotherapy Treatment Planning of Prone Rectal Cancer Patients. *Br J Radiol* (2012) 85 (1009):61–8. doi: 10.1259/bjr/11855927
3. Krempien RC, Daeuber S, Hensley FW, Wannenmacher M, Harms W. Image Fusion of CT and MRI Data Enables Improved Target Volume Definition in 3D-Brachytherapy Treatment Planning. *Brachytherapy* (2003) 2(3):164–71. doi: 10.1016/s1538-4721(03)00133-8
4. Maspero M, Savenije MHF, Dinkla AM, Seevinck PR, Intven MPW, Jurgenliemk-Schulz IM, et al. Dose Evaluation of Fast Synthetic-CT Generation Using a Generative Adversarial Network for General Pelvis MR-Only Radiotherapy. *Phys Med Biol* (2018) 63(18):185001. doi: 10.1088/1361-6560/aada6d
5. Kemppainen R, Suilamo S, Ranta I, Pesola M, Halkola A, Eufemio A, et al. Assessment of Dosimetric and Positioning Accuracy of a Magnetic Resonance Imaging-Only Solution for External Beam Radiotherapy of Pelvic Anatomy. *Phys Imaging Radiat Oncol* (2019) 11:1–8. doi: 10.1016/j.phro.2019.06.001
6. Maspero M, Tyyger MD, Tijssen RHN, Seevinck PR, Intven MPW, van den Berg CAT. Feasibility of Magnetic Resonance Imaging-Only Rectum Radiotherapy With a Commercial Synthetic Computed Tomography Generation Solution. *Phys Imaging Radiat Oncol* (2018) 7:58–64. doi: 10.1016/j.phro.2018.09.002
7. Wang H, Du K, Qu J, Chandarana H, Das IJ. Dosimetric Evaluation of Magnetic Resonance-Generated Synthetic CT for Radiation Treatment of Rectal Cancer. *PLoS One* (2018) 13(1):e0190883. doi: 10.1371/journal.pone.0190883
8. Johnstone E, Wyatt JJ, Henry AM, Short SC, Sebag-Montefiore D, Murray L, et al. Systematic Review of Synthetic Computed Tomography Generation Methodologies for Use in Magnetic Resonance Imaging–Only Radiation Therapy. *Int J Radiat Oncol Biol Phys* (2018) 100(1):199–217. doi: 10.1016/j.ijrobp.2017.08.043
9. Siemens Healthineers. *White Paper: MR-Only RT Planning for Brain and Pelvis With Synthetic Ct*. Erlangen, Germany: Siemens Healthcare GmbH (2019).
10. Köhler M, Vaara T, Grootel MV, Hoogeveen R, Kemppainen R, Renisch S. *MR-Only Simulation for Radiotherapy Planning. White Paper: Philips MRCAT for Prostate Dose Calculations Using Only MRI Data*. Amsterdam, Netherlands: Koninklijke Philips N.V (2015).
11. Tanderup K, Viswanathan A, Kirisits C, Frank SJ. Mri-Guided Brachytherapy. *Semin Radiat Oncol* (2014) 24(3):181–91. doi: 10.1016/j.semradonc.2014.02.007
12. Choi JH, Lee D, O'Connor L, Chalup S, Welsh JS, Dowling J, et al. Bulk Anatomical Density Based Dose Calculation for Patient-Specific Quality Assurance of MRI-Only Prostate Radiotherapy. *Front Oncol* (2019) 9:997. doi: 10.3389/fonc.2019.00997
13. Lee Y, Bollet M, Charles-Edwards G, Flower MA, Leach MO, McNair H, et al. Radiotherapy Treatment Planning of Prostate Cancer Using Magnetic Resonance Imaging Alone. *Radiother Oncol* (2003) 66(2):203–16. doi: 10.1016/s0167-8140(02)00440-1
14. Kim SW, Shin HJ, Hwang JH, Shin JS, Park SK, Kim JY, et al. Image Similarity Evaluation of the Bulk-Density-Assigned Synthetic CT Derived From MRI of Intracranial Regions for Radiation Treatment. *PLoS One* (2017) 12(9): e0185082. doi: 10.1371/journal.pone.0185082
15. Karotki A, Mah K, Meijer G, Meltsner M. Comparison of Bulk Electron Density and Voxel-Based Electron Density Treatment Planning. *J Appl Clin Med Phys* (2011) 12(4):3522. doi: 10.1120/jacmp.v12i4.3522
16. Winkel D, Bol GH, Kroon PS, van Asselen B, Hackett SS, Werensteijn-Honingh AM, et al. Adaptive Radiotherapy: The Elekta Unity Mr-Linac Concept. *Clin Transl Radiat Oncol* (2019) 18:54–9. doi: 10.1016/j.ctro.2019.04.001
17. Kemppainen R, Suilamo S, Tuokkola T, Lindholm P, Deppe MH, Keyrilainen J. Magnetic Resonance-Only Simulation and Dose Calculation in External Beam Radiation Therapy: A Feasibility Study for Pelvic Cancers. *Acta Oncol* (2017) 56(6):792–8. doi: 10.1080/0284186X.2017.1293290
18. Tyagi N, Fontenla S, Zhang J, Cloutier M, Kadbi M, Mechalakos J, et al. Dosimetric and Workflow Evaluation of First Commercial Synthetic CT Software for Clinical Use in Pelvis. *Phys Med Biol* (2017) 62(8):2961–75. doi: 10.1088/1361-6560/aa5452
19. Arabi H, Koutsouvelis N, Rouzaud M, Miralbell R, Zaidi H. Atlas-Guided Generation of Pseudo-CT Images for MRI-Only and Hybrid PET-MRI-Guided Radiotherapy Treatment Planning. *Phys Med Biol* (2016) 61 (17):6531–52. doi: 10.1088/0031-9155/61/17/6531
20. Dowling JA, Lambert J, Parker J, Salvado O, Fripp J, Capp A, et al. An Atlas-Based Electron Density Mapping Method for Magnetic Resonance Imaging (MRI)-Alone Treatment Planning and Adaptive MRI-Based Prostate Radiation Therapy. *Int J Radiat Oncol Biol Phys* (2012) 83(1):e5–11. doi: 10.1016/j.ijrobp.2011.11.056
21. Dowling JA, Sun J, Pichler P, Rivest-Henault D, Ghose S, Richardson H, et al. Automatic Substitute Computed Tomography Generation and Contouring for Magnetic Resonance Imaging (MRI)-Alone External Beam Radiation Therapy From Standard MRI Sequences. *Int J Radiat Oncol Biol Phys* (2015) 93(5):1144–53. doi: 10.1016/j.ijrobp.2015.08.045
22. Siversson C, Nordström F, Nilsson T, Nyholm T, Jonsson J, Gunnlaugsson A, et al. MRI-Only Radiotherapy Planning Using the Statistical Decomposition Algorithm. *Med Phys* (2015) 42(10):6090–7. doi: 10.1118/1.4931417
23. Persson E, Gustafsson C, Nordstrom F, Sohlin M, Gunnlaugsson A, Petruson K, et al. MR-OPERA: A Multicenter/Multivendor Validation of Magnetic Resonance Imagingeonly Prostate Treatment Planning Using Synthetic Computed Tomography Images. *Int J Radiat Oncol Biol Phys* (2017) 99 (3):692–700. doi: 10.1016/j.ijrobp.2017.06.006
24. Maspero M, Bentvelzen LG, Savenije MHF, Guerreiro F, Seravalli E, Janssens GO, et al. Deep Learning-Based Synthetic CT Generation for Paediatric Brain Mronly Photon and Proton Radiotherapy. *Radiother Oncol* (2020) 153:197–204. doi: 10.1016/j.radonc.2020.09.029
25. Nie D, Cao X, Gao Y, Wang L, Shen D. "Estimating CT Image From MRI Data Using 3d Fully Convolutional Networks". In: G Carneiro, D Mateus, L Peter, A Bradley, JMRS Tavares, V Belagiannis, et al, editors. *Deep Learning and Data Labeling for Medical Applications. DLMIA 2016, LABELS 2016. Lecture Notes in Computer Science*, vol. 10008 . Cham: Springer (2016). p. 170–8. doi: 10.1007/978-3-319-46976-8_18
26. Han X. MR-Based Synthetic CT Generation Using a Deep Convolutional Neural Network Method. *Med Phys* (2017) 44(4):1408–19. doi: 10.1002/mp.12155
27. Wolterink JM, Dinkla AM, Savenije MHF, Seevinck PR, va den Berg CAT, Isgum I. "Deep MR to CT Synthesis Using Unpaired Data Simulation and Synthesis in Medical Imaging". In: S Tsaftaris, A Gooya, A Frangi, editors. *Simulation and Synthesis in Medical Imaging SASHIMI 2017 Lecture Notes in Computer Science*, vol. 10557 . Cham: Springer (2017). p. 14–23. doi: 10.1007/978-3-319-68127-6_2
28. 1Kim J, Garbarino K, Schultz L, Levin K, Movsas B, Siddiqui MS, et al. Dosimetric Evaluation of Synthetic CT Relative to Bulk Density Assignment-Based Magnetic Resonance-Only Approaches for Prostate Radiotherapy. *Radiat Oncol* (2015) 10:239. doi: 10.1186/s13014-015-0549-7
29. Arabi H, Dowling JA, Burgos N, Han X, Greer PB, Koutsouvelis N, et al. Comparative Study of Algorithms for Synthetic CT Generation From MRI: Consequences for MRI-Guided Radiation Planning in the Pelvic Region. *Med Phys* (2018) 45(11):5218–33. doi: 10.1002/mp.13187
30. Largent A, Barateau A, Nunes J-C, Mylona E, Castelli J, Lafond C, et al. Comparison of Deep Learning-Based and Patch-Based Methods for Pseudo-CT Generation in MRI-Based Prostate Dose Planning. *Int J Radiat Oncol Biol Phys* (2019) 105(5):1137e50. doi: 10.1016/j.ijrobp.2019.08.049
31. Bird D, Nix MG, McCallum H, Teo M, Gilbert A, Casanova N, et al. Multicentre, Deep Learning, Synthetic-CT Generation for Ano-Rectal MR-Only Radiotherapy Treatment Planning. *Radiother Oncol* (2021) 156:23–8. doi: 10.1016/j.radonc.2020.11.027
32. Goodfellow I, Pouget-Abadie J, Mirza M, Xu B, Warde-Farley D, Ozair S, et al. Generative Adversarial Nets. *Adv Neural Inf Process Syst* (2014) 27:2672–80. doi: 10.1145/3422622
33. AL Maas, AY Hannun, AY Ng eds. *Rectifier Nonlinearities Improve Neural Network Acoustic Models*. San Diego, California: ICML (2013).
34. Cancer Institute NSW. *Clinical Resource: Gynaecological Endometrium Adjuvant Ebrt V.6* (2019). Available at: https://www.eviq.org.au/radiation-oncology/gynaecological/233-gynaecological-endometrium-adjuvant-ebrt (Accessed 23 July 2021).
35. Cancer Institute NSW. *Clinical Resource: Colorectal Rectum Neoadjuvant Ebrt Chemoradiation Pre-Operative Long-Course V.6* (2021). Available at: https://

www.eviq.org.au/radiation-oncology/colorectal/1863-rectal-neoadjuvant-ebrt-chemoradiation-pre-op (Accessed 23 July 2021).
36. Miften M, Olch A, Mihailidis D, Moran J, Pawlicki T, Molineu A, et al. Tolerance Limits and Methodologies for IMRT Measurement-Based Verification QA: Recommendations of AAPM Task Group No. 218. *Med Phys* (2018) 45(4):e53–83. doi: 10.1002/mp.12810
37. Karastergiou K, Smith SR, Greenberg AS, Fried SK. Sex Differences in Human Adipose Tissues - the Biology of Pear Shape. *Biol Sex Differ* (2012) 3(1):13. doi: 10.1186/2042-6410-3-1

Conflict of Interest: The authors declare that the research was conducted in the absence of any commercial or financial relationships that could be construed as a potential conflict of interest.

Publisher's Note: All claims expressed in this article are solely those of the authors and do not necessarily represent those of their affiliated organizations, or those of the publisher, the editors and the reviewers. Any product that may be evaluated in this article, or claim that may be made by its manufacturer, is not guaranteed or endorsed by the publisher.

frontiers in Oncology

ORIGINAL RESEARCH
published: 28 February 2022
doi: 10.3389/fonc.2022.861892

Assessment of Primary Colorectal Cancer CT Radiomics to Predict Metachronous Liver Metastasis

Yue Li[1,2†], Jing Gong[1,2†], Xigang Shen[1,2†], Menglei Li[1,2], Huan Zhang[1,2], Feng Feng[3] and Tong Tong[1,2*]*

[1] Department of Radiology, Fudan University Shanghai Cancer Center, Shanghai, China, [2] Department of Oncology, Shanghai Medical College, Fudan University, Shanghai, China, [3] Department of Radiology, Affiliated Tumor Hospital of Nantong University, Nantong, China

OPEN ACCESS

Edited by:
Kun Zhang,
Tongji University, China

Reviewed by:
Yanfen Cui,
Shanxi Provincial Cancer Hospital, China
Fang Zhang,
Fudan University, China
Qiufeng Zhao,
Shanghai University of Traditional Chinese Medicine, China
Marc Gollub,
Memorial Sloan Kettering Cancer Center, United States

***Correspondence:**
Feng Feng
drfengfeng@163.com
Tong Tong
t983352@126.com

[†]These authors have contributed equally to this work and share first authorship

Specialty section:
This article was submitted to Radiation Oncology, a section of the journal Frontiers in Oncology

Received: *25 January 2022*
Accepted: *07 February 2022*
Published: *28 February 2022*

Citation:
Li Y, Gong J, Shen X, Li M, Zhang H, Feng F and Tong T (2022) Assessment of Primary Colorectal Cancer CT Radiomics to Predict Metachronous Liver Metastasis. Front. Oncol. 12:861892. doi: 10.3389/fonc.2022.861892

Objectives: To establish and validate a machine learning-based CT radiomics model to predict metachronous liver metastasis (MLM) in patients with colorectal cancer.

Methods: In total, 323 patients were retrospectively recruited from two independent institutions to develop and evaluate the CT radiomics model. Then, 1288 radiomics features were extracted to decode the imaging phenotypes of colorectal cancer on CT images. The optimal radiomics features were selected using a recursive feature elimination selector configured by a support vector machine. To reduce the bias caused by an unbalanced dataset, the synthetic minority oversampling technique was applied to resample the minority samples in the datasets. Then, both radiomics and clinical features were used to train the multilayer perceptron classifier to develop two classification models. Finally, a score-level fusion model was developed to further improve the model performance.

Results: The area under the curve (AUC) was 0.78 ± 0.07 for the tumour feature model and 0.79 ± 0.08 for the clinical feature model. The fusion model achieved the best performance, with AUCs of 0.79 ± 0.08 and 0.72 ± 0.07 in the internal and external validation cohorts.

Conclusions: Radiomics models based on baseline colorectal contrast-enhanced CT have high potential for MLM prediction. The fusion model combining radiomics and clinical features can provide valuable biomarkers to identify patients with a high risk of colorectal liver metastases.

Keywords: tomography, x-ray computed, colorectal neoplasms, neoplasm metastasis, liver neoplasms, machine learning

INTRODUCTION

Colorectal cancer (CRC) is the third leading type of cancer and the second most common cause of cancer death worldwide (1). Liver metastasis (LM) is the leading cause of death in patients with CRC (2). Approximately 50% of patients with CRC will develop LM over the course of their life, and surgical resection is the only treatment modality with curative intent and has 5-year and 10-year

survival rates of 40% and 25% (3, 4). LM is a known prognostic predictor, and as a long-standing challenge in the treatment of CRC, the early identification of high-risk LM patients is crucial to improve clinical outcomes.

To the best of our knowledge, clinical parameters, including age, carcinoembryonic antigen (CEA) level, genetic mutations, and invasion of adjacent tissues [lymphovascular invasion (LVI) and perineural invasion (PNI)], are potential biomarkers to identify patients with a higher risk of distant metastasis (5–8). However, some predictors can only be obtained after radical resection and cannot be used as a guide for developing preoperative treatment strategies. The radiomics analysis method has the potential to noninvasively evaluate tumour heterogeneity objectively and quantitatively by analysing high-throughput information extracted from images (9). Evidence has gradually accumulated that computed tomography (CT) texture features are related to parameters such as tumour grade, tumour cellular processes and genetic mutations (10). In recent studies, some CT texture features have been linked to prognosis and clinical outcomes. Most of these features are based on the analysis of metastatic lesions, and few studies have focused on primary colorectal lesions. Effective and robust baseline biomarkers for the prediction of colorectal LMs are still lacking. The combination of radiomics and machine learning algorithms might unearth valuable features that can reflect the tumour heterogeneity of primary CRC and contribute to the prediction of the risk of metastasis.

The early identification of patients with a distinct likelihood of metachronous liver metastasis (MLM) may allow the consideration of different treatment strategies (e.g., neoadjuvant chemoradiotherapy) and a more intensive follow-up programme to improve the prognosis of patients. The purpose of this study was to determine whether the radiomics features of baseline colorectal contrast-enhanced CT can predict MLM in CRC patients.

MATERIALS AND METHODS

Patients

This retrospective study was approved by the institutional review boards of all the participating institutions, and the requirement for informed consent was waived. We enrolled 323 CRC patients who underwent contrast-enhanced CT between October 2010 and January 2020. Dataset 1 (for model training, tuning, and internal validation) included patients enrolled from Fudan University Shanghai Cancer Centre, and dataset 2 (for independent external validation, n=75) included patients enrolled from Nantong Tumor Hospital. Dataset 1 was composed of a training cohort (n=171) and an internal validation cohort (n=77). The inclusion criteria were as follows: (1) histopathologically confirmed CRC; (2) performance of standard contrast-enhanced CT of the abdomen and pelvis before any treatment; (3) availability of clinical characteristics; and (4) availability of complete CT datasets. The exclusion criteria were as follows: (1) treatment (including radiotherapy or systemic chemotherapy) prior to initial CT examination; (2) LM before colorectal radical surgery; (3) presence of other tumour diseases during the same period; and (4) unavailable clinicopathologic or follow-up data.

CT Scanning Protocol

All selected patients at both institutions underwent contrast-enhanced abdominal or pelvic CT with 64-row spiral CT scanners (Philips Healthcare, Siemens Healthcare) using a current of 200 mA and a tube voltage of 120 kV. All CT images were reconstructed with the standard reconstruction kernel, including 5.0 mm slice thickness, 5.0 mm increment, 1.4 or 0.9 pitch, 512×512 matrix and 4.11 cm field of view. The CT digital imaging and communications in medicine (DICOM) images were retrieved from the picture archiving and communication system (PACS).

CT Radiomics Feature Model Development

Figure 1 illustrate the flowchart of our proposed prediction model. To evaluate the intra-class and inter-class agreement between different radiologists in segmentation process, we computed the Dice coefficient based on the segmentation results delineated by different radiologists. We initially chose 50 random colorectal contrast-enhanced CT images for ROI segmentation and feature extraction. The ROI segmentation was performed by two experienced radiologists independently. The Dice coefficients of inter-/intra-reader were higher than 0.85. To select the robustness of radiomics features, we calculated the inter-class/intra-class correlation coefficient (ICC) of each feature. As the ICC greater than 0.75 was considered good agreement, we just selected the radiomics features with inter- and inra-reader ICC

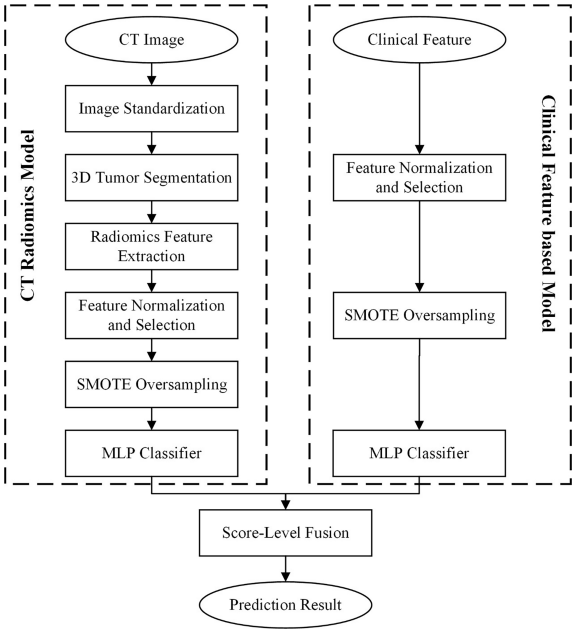

FIGURE 1 | The flowchart of our proposed prediction model.

values higher than 0.75. The boundaries of each tumour were delineated on CT images in a slice-by-slice fashion. ITK-SNAP software (version: 3.8.0, http://itksnap.org/) was used to segment the 3D tumour. **Figure S1** showed the diagram of our segmentation and workflow.

After segmenting the 3D tumour on the CT image, a cubic B-spline interpolation algorithm was applied to resample the CT scan with a new spacing of [1 mm, 1 mm, 5 mm]. Then, we computed the radiomics features by using Python programming software with the Pyradiomics package. A total of 1288 radiomics features were computed and extracted to decode the imaging phenotypes of 3D colorectal tumours. The original CT image and two types of transformed images, including wavelet images and Laplacian of Gaussian (LoG) images, were used to calculate image features. The LoG image filter was configured with δ values of 1, 2, 3, 4, and 5. Thus, the initial radiomics features consisted of 105 original image features, 728 wavelet image features and 455 LoG image features. The radiomics feature calculation progress following the IBSI (https://theibsi.github.io/) guidelines.

An L2-based normalization method was used to rescale each type of radiomics feature. Then, the recursive feature elimination (RFE) method was applied to reduce the dimensionality of feature spacing and remove the redundant image features. The linear support vector machine (SVM) classifier was selected as the estimator to configure the RFE feature selector. After selecting optimal radiomics features, an optimal imaging feature pool was selected from the initial radiomics features to build the classification model. Since our dataset was unbalanced, synthetic minority oversampling technique (SMOTE) was used to increase the number of minority samples in the dataset. In the CT radiomics development process, the SMOTE method was used to oversample only the training dataset. Finally, the multilayer perceptron (MLP) classifier was applied to build the classification model.

Clinical Feature-Based Model Development

Clinical and pathological features were used to develop a clinical feature-based model to predict MLM in CRC patients. A min-max normalization scaler was first used to normalize the feature to a scale of [0,1]. Then, the optimal clinical features were selected according to the scores measured by using ANOVA F-value analysis. The minority samples were also resampled by using the SMOTE method. The MLP classifier was applied to build the classification model.

CT Radiomics and Clinical Feature Fusion Model Development

To improve the model performance, a fusion model was developed by combining CT radiomics features and clinical features. A score-level fusion method was used to combine the prediction scores generated by the CT radiomics model and the clinical feature-based model. Three score fusion strategies, namely, the minimum score fusion strategy, maximum score fusion strategy, and weighted score fusion strategy, were used to build the CT radiomics and clinical feature fusion model. The prediction score of the minimum or maximum score fusion strategy was generated by comparing the prediction scores of each case yielded by the CT radiomics model and the clinical feature-based model to select the minimum or maximum score. The prediction score of the weighted score fusion strategy was generated by systematically increasing the weighting factor from 0.1 to 0.9 applied to the prediction scores generated by the CT radiomics model (or 0.9 to 0.1 applied to the prediction scores generated by the clinical feature-based model). A similar score-level fusion method was used in our previously reported study (11).

Statistical Analysis

All data analyses were performed using Python 3.7.6. A P value of less than 0.05 was considered significant. A L2 based normalization method was used to rescale each type of the radiomics feature. The recursive feature elimination (RFE) method and linear support vector machine (SVM) classifier were implemented to select the optimal image features. And the optimal clinical features were selected according to the scores measured by using the ANOVA F-value analysis. Then, multi-layer perceptron (MLP) classifier was applied to build the classification model. The diagnostic performance of the models was evaluated by receiver operating characteristic (ROC) curves. The AUC of different models were compared using Delong test.

RESULTS

Patient Characteristics

Based on the inclusion and exclusion criteria, a total of 323 patients were included, and 58.5% were male. The median age of the patients was 61 years (interquartile range, 53-69 years). Patients with MLM were defined as liver metastases that occurred after radical excision of the primary colorectal cancer (12). In dataset 1, 176 patients (71.0%) developed MLM. To avoid selection bias and reflect the natural distribution of morbidity, the patients in dataset 1 were divided into a training cohort (n=171) and a validation cohort (n=77) according to the date of the first visit. In dataset 2, 23 patients (30.7%) developed MLM. The baseline characteristics of the three cohorts are summarized in **Table 1**.

Intra-Observer and Inter-Observer Reproducibility of Radiomics Feature Extraction

The intra-observer ICC calculated based on two measurements of reader A was 0.983. The inter-observer ICC was 0.776. An ICC greater than 0.75 was considered good agreement. The results indicated stable intra and inter-observer feature extraction reproducibility.

Selected Features for the Clinical Model

After normalization and ANOVA F-value analysis, clinical factors including age, mismatch repair (MMR) status, preoperative TNM stage, tumour markers (CEA and CA19-9),

TABLE 1 | Patient characteristics.

characteristic		Training cohort (n = 171)	Validation cohort 1 (n = 77)	Validation cohort 2 (n = 75)
Age SD [years]		57.7 ± 12.4	60.9 ± 12.6	64.9 ± 10.7
Gender (%)	Male	95 (55.6%)	46 (59.7%)	48 (64.0%)
	Female	76 (44.4%)	31 (40.3%)	27 (36.0%)
Location (%)	Right	71 (41.5%)	29 (37.7%)	25 (33.3%)
	Left	100 (58.5%)	48 (62.3%)	50 (66.7%)
MMR (%)	pMMR	122 (71.3%)	66 (85.7%)	68 (90.7%)
	dMMR	49 (28.7%)	11 (14.3%)	7 (9.3%)
KRAS (%)	WT	13 (7.6%)	5 (6.5%)	33 (44.0%)
	M	3 (1.8%)	4 (5.2%)	18 (24.0%)
	NA	155 (90.6%)	68 (88.3%)	24 (32.0%)
NRAS (%)	WT	16 (9.4%)	8 (10.4%)	0
	NA	155 (90.6%)	69 (89.6%)	75 (100.0%)
BRAF (%)	WT	16 (9.4%)	9 (11.7%)	17 (22.7%)
	M	0	0	31 (41.3%)
	NA	155 (90.6%)	68 (88.3%)	27 (36.0%)
Tumor stage (%)	T1	7 (4.1%)	2 (2.6%)	0
	T2	17 (9.9%)	11(14.3%)	5 (6.7%)
	T3	47 (27.5%)	24 (31.2%)	24 (32.0%)
	T4	100 (58.5%)	40 (51.9%)	46 (61.3%)
New tumour stage(%)	T1-2	24(14%)	13(13.9%)	5(6.7%)
	T3	47 (27.5%)	24 (31.2%)	24 (32.0%)
	T4	100 (58.5%)	40 (51.9%)	46 (61.3%)
Nodal stage (%)	N0	96 (56.1%)	40 (51.9%)	39 (52.0%)
	N1	53 (31.0%)	22 (28.6%)	27 (36.0%)
	N2	22 (12.9%)	15 (19.5%)	9 (12.0%)
Metastasis stage(%)	M0	161 (94.2%)	76 (98.7%)	75 (100%)
	M1	10 (5.8%)	1 ((1.3%)	0
Pre CA-19-9 (%)	Normal	150 (87.7%)	62 (80.5%)	68 (90.7%)
	Elevated	21 (12.3%)	15 (19.5%)	7 (9.3%)
Pre CEA (%)	Normal	98 (57.3%)	52 (67.5%)	43 (57.3%)
	Elevated	73 (42.7%)	25 (32.5%)	32 (42.7%)
LVI (%)	Positive	40 (23.4%)	62 (80.5%)	25 (33.3%)
	Negative	131 (76.6%)	15 (19.5%)	50 (66.7%)
PNI (%)	Positive	40 (23.4%%)	57 (74.0%)	15 (20.0%)
	Negative	131 (76.0%)	20 (26.0%)	60 (80.0%)

pMMR, proficient mismatch repair gene expressing; dMMR, deficient mismatch repair gene expressing; WT, wild type; M, mutant type; NA, not available; pre CA 19-9, the level of carbohydrate antigen 19-9 before any treatment; pre CEA, the level of carcinoembryonic antigen before any treatment; LVI, lymphatic vascular infiltration; PNI, peripheral nerve invasion.

genetic mutations (KRAS, NRAS, and BRAF) and invasion of adjacent tissues (LVI and PNI) were significantly different between the CRC LM (CRLM) group and the non-CRLM group (P <0.05). The distributions of these features in the CRLM and non-CRLM groups are shown in **Figure 2**.

Selected Features for the CT Radiomics Model

In total, 1288 image features were selected by the SVM-RFE method. Six features passed the suggestive significance level (P <0.05), including three original image features, two wavelet image features and one LoG image feature. The distributions of radiomics features in the CRLM and non-CRLM groups are shown in **Figure 3**.

Model Validation and Comparison

The radiomics feature-based model and clinical feature-based model had approximate performance in the validation sets [validation set 1, area under the curve (AUC): 0.70 ± 0.07 and 0.69 ± 0.08; validation set 2, AUC: 0.64 ± 0.07 and 0.68 ± 0.07]. Using score-level methods, combinations of various features of the radiomics and clinical models were adopted to validate which combination of features was more conducive to improving the prediction performance. No significant improvement in the prediction performance was found with the different weighted score fusion strategies (P<0.05). The minimum score fusion strategy did not contribute to the improvement of prediction performance. Ultimately, the fusion model using the maximum score fusion strategy achieved the best performance in validation set 1 (AUC: 0.79 ± 0.06, 95% CI 0.68-0.87, P<0.05) and validation set 2 (AUC: 0.72 ± 0.06, 95% CI 0.60-0.82, P<0.05). The detailed performance of different combinations of radiomics and clinical features from the respective models is provided in **Table 2**.

The accuracy, sensitivity, specificity, positive predictive value, and negative predictive value of the internal and external validation sets for each model are reported in **Table 3**, which shows that the fusion model is the best among all models (P<0.05).

Overall, the tumour feature model (mean AUC: 0.78) performed similarly to the clinical feature model (mean AUC: 0.79), and the fusion model outperformed these models (mean AUC: 0.85). The receiver operating characteristic (ROC) curves

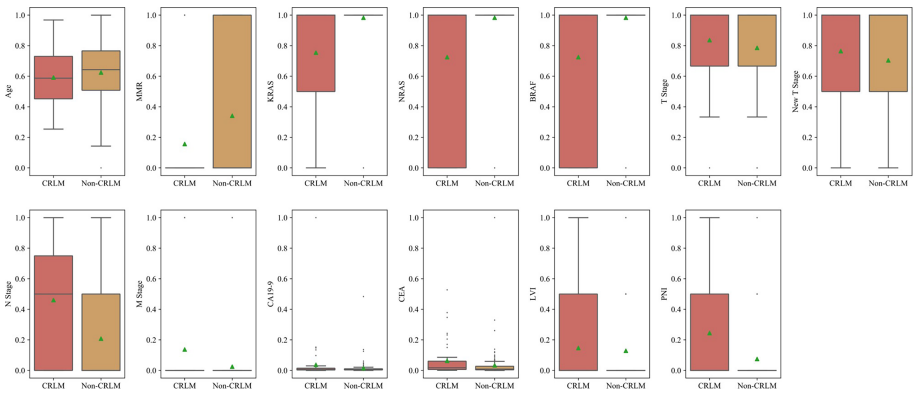

FIGURE 2 | Box plot of clinical features of CRLM and Non-CRLM sets.

of the three models are presented in **Figure 4**. The ROC curves of the three models in training set are presented in **Figure S2**.

DISCUSSION

This study aimed to develop and validate a machine learning-based CT radiomics model by using primary colorectal lesions to predict MLM. In this study, the fusion model that integrated radiomics features and clinical features significantly outperformed the radiomics and clinical models. It achieved good performance in both internal and external validations (AUC: 0.79, 95% CI 0.68-0.87; AUC: 0.72, 95% CI 0.60-0.82; P<0.05). Our results indicate that radiomics features have the potential to predict LMs and that the fusion model can provide valuable biomarkers to identify patients with a high risk of colorectal LMs.

The median survival of untreated patients with colorectal liver metastases is only 6.9 months, while median survival of patients undergoing radical resection of liver metastases is 35 months, with 5-year survival rates at around 40% (3, 13). Main clinical questions concern the ability of tools to accurately discern liver metastases and select patients for radical surgery. Our model could alert clinicians to patients with a higher risk of MLM. By implementing a more intensive follow-up programme or undergo neoadjuvant treatment for the high-risk MLM group, opportunities for radical resection of liver metastases can be offered and result in longer survival (14, 15).

Some clinical factors, including age, TNM stage, tumour markers (CEA and CA19-9), and genetic mutations (KRAS, NRAS, and BRAF), have been reported as risk factors for colorectal metastasis in previous studies (16–21). Although these factors have good predictive performance, they are only available after invasive operations. All of the above clinical features were also incorporated into our model. It should be noted that the new T stage mentioned in our clinical model combined stages T1 and T2 as one stage and compared it with stage T3 and stage T4. It showed predictive value for MLM in the study. The underlying mechanism has yet to be explored, and future validation in larger and more diverse samples is needed. In addition, this study included other factors, including MMR status and invasion of adjacent tissues (LVI and PNI). However, the AUC of clinical model were 0.69 ± 0.08 and 0.68 ± 0.07 in internal and external validation set, respectively. And the performance was not satisfactory.

By combining radiomics features including GrayLevel NonUniformity at GLRLM, GLDM, HLH, LoG filtration with sigma =2.0 and LALGLE at GLSZM, the predictive performance was improved to 0.79 and 0.72 in internal and external validation set, respectively.

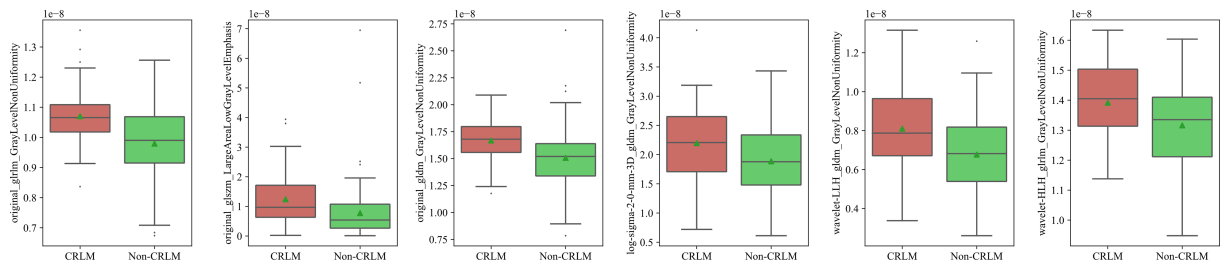

FIGURE 3 | Box plot of radiomics features of CRLM and Non-CRLM sets.

TABLE 2 | The diagnostic performance of different combination of radiomics and clinical features.

Model	Validation Dataset 1		Validation Dataset 2	
	AUC	95% CI	AUC	95% CI
Rad	0.70 ± 0.07	[0.58, 0.80]	0.64 ± 0.07	[0.53, 0.74]
Cli	0.69 ± 0.08	[0.57, 0.82]	0.68 ± 0.07	[0.55, 0.80]
Minimum	0.68 ± 0.07	[0.56, 0.81]	0.70 ± 0.07	[0.58, 0.82]
Maximum	**0.79 ± 0.06**	**[0.68, 0.87]**	**0.72 ± 0.06**	**[0.60, 0.82]**
0.1*Rad+0.9*Cli	0.69 ± 0.08	[0.57, 0.82]	0.68 ± 0.07	[0.55, 0.80]
0.2*Rad+0.8*Cli	0.69 ± 0.08	[0.57, 0.82]	0.68 ± 0.07	[0.55, 0.80]
0.3*Rad+0.7*Cli	0.69 ± 0.08	[0.57, 0.82]	0.68 ± 0.07	[0.55, 0.80]
0.4*Rad+0.6*Cli	0.69 ± 0.08	[0.57, 0.82]	0.68 ± 0.07	[0.55, 0.80]
0.5*Rad+0.5*Cli	0.69 ± 0.08	[0.57, 0.82]	0.68 ± 0.07	[0.55, 0.80]
0.6*Rad+0.4*Cli	0.69 ± 0.08	[0.57, 0.82]	0.68 ± 0.07	[0.55, 0.80]
0.7*Rad+0.3*Cli	0.69 ± 0.08	[0.57, 0.82]	0.68 ± 0.07	[0.55, 0.80]
0.8*Rad+0.2*Cli	0.69 ± 0.08	[0.57, 0.82]	0.68 ± 0.07	[0.55, 0.80]
0.9*Rad+0.1*Cli	0.69 ± 0.08	[0.57, 0.82]	0.68 ± 0.07	[0.55, 0.80]

All data was rounded up to percentile. The prediction performance with the different weighted score fusion strategies differed in four decimal places and was found no significant improvement. The bold values refer to the diagnostic performance of our final fusion model.
Rad, Radiomics Feature based Model; Cli, Clinical Feature based Model.

TABLE 3 | The accuracy, sensitivity, specificity, positive predictive value, and negative predictive value of the internal and external validation sets for each model.

Model	Validation Dataset 1			Validation Dataset 2		
	Radiomics model	Clinical model	Fusion models	Radiomics model	Clinical model	Fusion models
Accuracy (%)	58.4	72.7	74.0	65.3	66.7	72.0
Sensitivity (%)	85.7	52.4	38.1	65.2	69.6	78.3
Specificity (%)	48.2	80.4	87.5	65.4	65.4	61.5
PPV (%)	38.3	50.0	53.3	45.5	47.1	47.4
NPV (%)	90.0	81.8	79.0	81.0	82.9	86.5
P Value		Validation Dataset 1			Validation Dataset 2	
Rad *vs* Fusion		4.8×10^{-6}			3.6×10^{-8}	
Cli *vs* Fusion		1.3×10^{-7}			7×10^{-5}	
Rad *vs* Cli		3.80			0.123	

PPV, positive predictive value; NPV, negative predictive value.

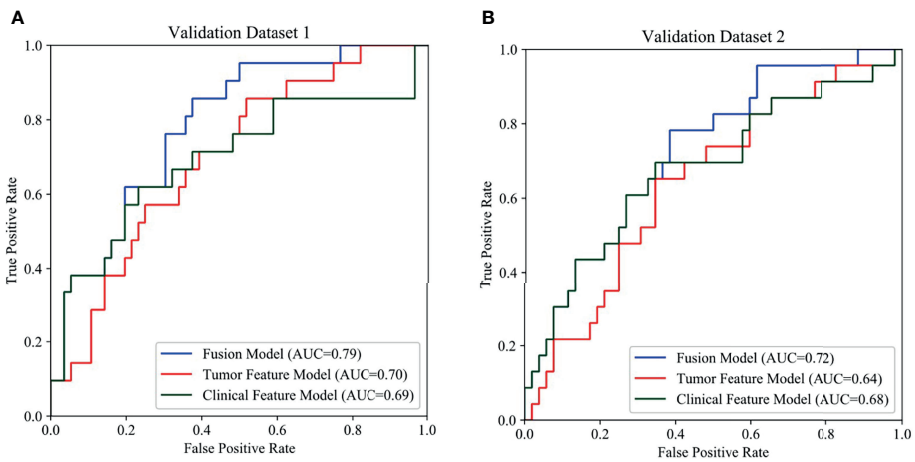

FIGURE 4 | Comparison of prediction performance among the three models using different features. In the ROCs, the blue, red, green curves show the models based on fusion features, tumor features and clinical features, respectively. **(A)** ROCs of internal validation set, **(B)** ROCs of external validation set.

There are no studies evaluating the performance of CT radiomics model based on the primary colorectal cancer to predict MLM. But several studies have investigated texture analysis of liver or rectal cancer to predict liver metastases. Beckers et al. reported texture analysis (uniformity at LoG filtration with sigma = 0.5) of liver could predict patients at risk of developing early LMs in ≤6 months but was not robust enough to identify patients at risk of developing metastases at later stages (22). In contrast, Lee et al. and Taghavi et al. showed that a CT radiomics nomogram based on the whole liver can provide a valuable assessment of the risk of MLM (23, 24). These findings suggest that radiomics and clinical features are complementary and mutually authenticated; thus, the comprehensive evaluation achieved a better prediction performance. Our study applied primary CRC features rather than liver features and found an increase in the predictive performance of the fusion model, which achieved good performance in the independent external validation. Some studies have shown that the heterogeneity of primary CRC tumours is linked to the aggressiveness of CRLMs and can predict the potential for LM (25–27). Based on similar inferences, Liu and Shu applied radiomics features of primary magnetic resonance imaging (MRI) rectal tumour images to predict synchronous LM (28, 29). Li et al. applied a single slice that included the largest tumour to predict MLM (30), and Liang et al. showed that radiomics models based on baseline rectal MRI had high potential for MLM prediction (31). Our study applied the assessment of whole primary lesions with CT scans rather than single slices to predict MLM and improved the model performance by using a machine learning algorithm.

Compared with previous studies, one strength of this study is the availability of an external test cohort. Independent external test cohorts contribute to evaluating the generalizability of predictive models (32). Another strength is the segmentation based on the entire 3D volume of the tumour and radiomics feature extraction using a machine learning algorithm, which can maximize the potential information underlying the images and thus identify the features with the highest predictive value. Moreover, this study focused on the primary lesions. Assessing the risk of LM using CT scans of primary CRC tends to be more routine, quick and economical, thus supporting its future application.

There are some limitations to our study. First, as a retrospective study with a limited dataset, selection bias and the presence of unknown confounders were possible. Although the patients were divided into a training cohort and a validation cohort according to the date of the first visit to avoid selection bias as much as possible, the small dataset may limit the generalization performance of the proposed model. Second, gene sequencing was not routinely applied, and thus, the genetic profiles were inadequate and formed a small sample. Third, the use of MLP classifier and maximum score strategy may be overoptimistic for the task. Further analysis will be made when additional cases are included in the advanced study. Finally, pre-treated patients were intentionally excluded to control for confounders and patients with other distant metastases were included. This may reduce the prediction efficiency of our model in general clinical practice. Prospective investigation using larger datasets and richer clinical profiles is needed to further validate the robustness and reproducibility of our conclusions. Despite these limitations, we hope that these findings will contribute to the prediction of MLM in patients with CRC.

In conclusion, combining CT radiomics and clinicopathologic features to develop a machine learning-based prediction model was feasible to predict MLM in patients with CRC. Before the proposed model is widely implemented in the clinic, more validation experiments need to be conducted by using diverse multicentre datasets, detailed genetic profiles and prospective studies.

DATA AVAILABILITY STATEMENT

The raw data supporting the conclusions of this article will be made available by the authors, without undue reservation.

AUTHOR CONTRIBUTIONS

YL and JG performed the statistical analysis. XS contributed to the image acquisition. ML and HZ performed the image segmentation. YL and JG wrote the draft of the manuscript. FF contributed to the external validation dataset. TT contributed to conception and design of the study. All authors contributed to manuscript revision, read, and approved the submitted version.

FUNDING

This study has received funding from the National Natural Science Foundation of China (grant number: 81971687) and Natural Science Foundation of Shanghai (grant number: 20ZR1412700).

SUPPLEMENTARY MATERIAL

The Supplementary Material for this article can be found online at: https://www.frontiersin.org/articles/10.3389/fonc.2022.861892/full#supplementary-material

Supplementary Figure S1 | The diagram of study workflow.

Supplementary Figure S2 | The diagnostic performances of three models on the training set.

REFERENCES

1. Sung H, Ferlay J, Siegel RL, Laversanne M, Soerjomataram I, Jemal A, et al. Global Cancer Statistics 2020: GLOBOCAN Estimates of Incidence and Mortality Worldwide for 36 Cancers in 185 Countries. *CA: Cancer J Clin* (2021) 71(3):209–49. doi: 10.3322/caac.21660
2. van der Pool AE, Damhuis RA, Ijzermans JN, de Wilt JH, Eggermont AM, Kranse R, et al. Trends in Incidence, Treatment and Survival of Patients With

Stage IV Colorectal Cancer: A Population-Based Series. *Colorectal Dis Off J Assoc Coloproctology Great Britain Ireland* (2012) 14(1):56–61. doi: 10.1111/j.1463-1318.2010.02539.x
3. House MG, Kemeny NE, Gönen M, Fong Y, Allen PJ, Paty PB, et al. Comparison of Adjuvant Systemic Chemotherapy With or Without Hepatic Arterial Infusional Chemotherapy After Hepatic Resection for Metastatic Colorectal Cancer. *Ann Surg* (2011) 254(6):851–6. doi: 10.3390/cancers13225631
4. Kanas GP, Taylor A, Primrose JN, Langeberg WJ, Kelsh MA, Mowat FS, et al. Survival After Liver Resection in Metastatic Colorectal Cancer: Review and Meta-Analysis of Prognostic Factors. *Clin Epidemiol* (2012) 4:283–301. doi: 10.2147/CLEP.S34285
5. Margonis GA, Kim Y, Sasaki K, Samaha M, Amini N, Pawlik TM. Codon 13 KRAS Mutation Predicts Patterns of Recurrence in Patients Undergoing Hepatectomy for Colorectal Liver Metastases. *Cancer* (2016) 122(17):2698–707. doi: 10.1002/cncr.30085
6. Beppu T, Sakamoto Y, Hasegawa K, Honda G, Tanaka K, Kotera Y, et al. A Nomogram Predicting Disease-Free Survival in Patients With Colorectal Liver Metastases Treated With Hepatic Resection: Multicenter Data Collection as a Project Study for Hepatic Surgery of the Japanese Society of Hepato-Biliary-Pancreatic Surgery. *J Hepato-Biliary-Pancreatic Sci* (2012) 19 (1):72–84. doi: 10.1002/cncr.30085
7. Vauthey JN, Zimmitti G, Kopetz SE, Shindoh J, Chen SS, Andreou A, et al. RAS Mutation Status Predicts Survival and Patterns of Recurrence in Patients Undergoing Hepatectomy for Colorectal Liver Metastases. *Ann Surg* (2013) 258(4):619–27. doi: 10.1097/SLA.0b013e3182a5025a
8. Shindoh J, Nishioka Y, Yoshioka R, Sugawara T, Sakamoto Y, Hasegawa K, et al. KRAS Mutation Status Predicts Site-Specific Recurrence and Survival After Resection of Colorectal Liver Metastases Irrespective of Location of the Primary Lesion. *Ann Surg Oncol* (2016) 23(6):1890–6. doi: 10.1245/s10434-016-5087-5
9. Aerts HJ, Velazquez ER, Leijenaar RT, Parmar C, Grossmann P, Carvalho S, et al. Decoding Tumour Phenotype by Noninvasive Imaging Using a Quantitative Radiomics Approach. *Nat Commun* (2014) 5:4006. doi: 10.1038/ncomms5006
10. Lubner MG, Smith AD, Sandrasegaran K, Sahani DV, Pickhardt PJ. CT Texture Analysis: Definitions, Applications, Biologic Correlates, and Challenges. *Radiographics Rev Publ Radiological Soc North Am Inc* (2017) 37(5):1483–503. doi: 10.1148/rg.2017170056
11. Gong J, Liu JY, Jiang YJ, Sun XW, Zheng B, Nie SD. Fusion of Quantitative Imaging Features and Serum Biomarkers to Improve Performance of Computer-Aided Diagnosis Scheme for Lung Cancer: A Preliminary Study. *Med Phys* (2018) 45(12):5472–81. doi: 10.1002/mp.13237
12. Adam R, de Gramont A, Figueras J, Kokudo N, Kunstlinger F, Loyer E, et al. Managing Synchronous Liver Metastases From Colorectal Cancer: A Multidisciplinary International Consensus. *Cancer Treat Rev* (2015) 41 (9):729–41. doi: 10.1016/j.ctrv.2015.06.006
13. de Jong MC, Pulitano C, Ribero D, Strub J, Mentha G, Schulick RD, et al. Rates and Patterns of Recurrence Following Curative Intent Surgery for Colorectal Liver Metastasis: An International Multi-Institutional Analysis of 1669 Patients. *Ann Surg* (2009) 250(3):440–8. doi: 10.1097/SLA.0b013e3181b4539b
14. Chow FC, Chok KS. Colorectal Liver Metastases: An Update on Multidisciplinary Approach. *World J Hepatol* (2019) 11(2):150–72. doi: 10.4254/wjh.v11.i2.150
15. Carlomagno C, De Stefano A, Rosanova M, De Falco S, Attademo L, Fiore G, et al. Multiple Treatment Lines and Prognosis in Metastatic Colorectal Cancer Patients. *Cancer metastasis Rev* (2019) 38(1-2):307–13. doi: 10.1007/s10555-018-9748-7
16. Landreau P, Drouillard A, Launoy G, Ortega-Deballon P, Jooste V, Lepage C, et al. Incidence and Survival in Late Liver Metastases of Colorectal Cancer. *J Gastroenterol Hepatol* (2015) 30(1):82–5. doi: 10.1111/jgh.12685
17. Stojkovic Lalosevic M, Stankovic S, Stojkovic M, Markovic V, Dimitrijevic I, Lalosevic J, et al. Can Preoperative CEA and CA19-9 Serum Concentrations Suggest Metastatic Disease in Colorectal Cancer Patients? *Hellenic J Nucl Med* (2017) 20(1):41–5. doi: 10.1967/s002449910505
18. Manfredi S, Lepage C, Hatem C, Coatmeur O, Faivre J, Bouvier AM. Epidemiology and Management of Liver Metastases From Colorectal Cancer. *Ann Surg* (2006) 244(2):254–9. doi: 10.1097/01.sla.0000217629.94941.cf
19. Finkelstein SD, Sayegh R, Christensen S, Swalsky PA. Genotypic Classification of Colorectal Adenocarcinoma. Biologic Behavior Correlates With K-Ras-2 Mutation Type. *Cancer* (1993) 71(12):3827–38. doi: 10.1002/1097-0142(19930615)71:12<3827::aid-cncr2820711207>3.0.co;2-n
20. Lipsyc M, Yaeger R. Impact of Somatic Mutations on Patterns of Metastasis in Colorectal Cancer. *J Gastrointestinal Oncol* (2015) 6(6):645–9. doi: 10.3978/j.issn.2078-6891.2015.045
21. Liu X, Jakubowski M, Hun JL. KRAS Gene Mutation in Colorectal Cancer Is Correlated With Increased Proliferation and Spontaneous Apoptosis. *Am J Clin Pathol* (2011) 135(2):245–52. doi: 10.1309/AJCP7FO2VAXIVSTP
22. Beckers R, Lambregts D, Schnerr RS, Maas M, Rao SX, Kessels A, et al. Whole Liver CT Texture Analysis to Predict the Development of Colorectal Liver Metastases-A Multicentre Study. *Eur J Radiol* (2017) 92:64–71. doi: 10.1016/j.ejrad.2017.04.019
23. Lee S, Choe EK, Kim SY, Kim HS, Park KJ, Kim D. Liver Imaging Features by Convolutional Neural Network to Predict the Metachronous Liver Metastasis in Stage I-III Colorectal Cancer Patients Based on Preoperative Abdominal CT Scan. *BMC Bioinf* (2020) 21(Suppl 13):382. doi: 10.1186/s12859-020-03686-0
24. Taghavi M, Trebeschi S, Simões R, Meek DB, Beckers R, Lambregts D, et al. Machine Learning-Based Analysis of CT Radiomics Model for Prediction of Colorectal Metachronous Liver Metastases. *Abdominal Radiol (New York)* (2021) 46(1):249–56. doi: 10.1007/s00261-020-02624-1
25. Li M, Li X, Guo Y, Miao Z, Liu X, Guo S, et al. Development and Assessment of an Individualized Nomogram to Predict Colorectal Cancer Liver Metastases. *Quantitative Imaging Med Surg* (2020) 10(2):397–414. doi: 10.21037/qims.2019.12.16
26. Liang M, Cai Z, Zhang H, Huang C, Meng Y, Zhao L, et al. Machine Learning-Based Analysis of Rectal Cancer MRI Radiomics for Prediction of Metachronous Liver Metastasis. *Acad Radiol* (2019) 26(11):1495–504. doi: 10.1016/j.acra.2018.12.019
27. Cucchetti A, Russolillo N, Johnson P, Tarchi P, Ferrero A, Cucchi M, et al. Impact of Primary Cancer Features on Behaviour of Colorectal Liver Metastases and Survival After Hepatectomy. *BJS Open* (2018) 3(2):186–94. doi: 10.1002/bjs5.100
28. Sottoriva A, Kang H, Ma Z, Graham TA, Salomon MP, Zhao J, et al. A Big Bang Model of Human Colorectal Tumor Growth. *Nat Genet* (2015) 47 (3):209–16. doi: 10.1038/ng.3214
29. Joung JG, Oh BY, Hong HK, Al-Khalidi H, Al-Alem F, Lee HO, et al. Tumor Heterogeneity Predicts Metastatic Potential in Colorectal Cancer. *Clin Cancer Res* (2017) 23(23):7209–16. doi: 10.1158/1078-0432.CCR-17-0306
30. Liu M, Ma X, Shen F, Xia Y, Lu J. MRI-Based Radiomics Nomogram to Predict Synchronous Liver Metastasis in Primary Rectal Cancer Patients. *Cancer Med* (2020) 9(14):5155–63. doi: 10.1002/cam4.3185
31. Shu Z, Fang S, Ding Z, Mao D, Cai R, Chen Y, et al. MRI-Based Radiomics Nomogram to Detect Primary Rectal Cancer With Synchronous Liver Metastases. *Sci Rep* (2019) 9(1):3374. doi: 10.1038/s41598-019-39651-y
32. Lambin P, Leijenaar R, Deist TM, Peerlings J, de Jong E, van Timmeren J, et al. Radiomics: The Bridge Between Medical Imaging and Personalized Medicine. *Nat Rev Clin Oncol* (2017) 14(12):749–62. doi: 10.1038/nrclinonc.2017.141

Conflict of Interest: The authors declare that the research was conducted in the absence of any commercial or financial relationships that could be construed as a potential conflict of interest.

The reviewer FZ declared a shared affiliation, with no collaboration, with the authors to the handling editor at the time of the review.

frontiers in Oncology

REVIEW
published: 01 March 2022
doi: 10.3389/fonc.2022.860740

Cystic Neoplasms of the Pancreas: Differential Diagnosis and Radiology Correlation

Feixiang Hu[1], Yue Hu[2], Dan Wang[3], Xiaowen Ma[1], Yali Yue[4], Wei Tang[1], Wei Liu[1], Puye Wu[5], Weijun Peng[1] and Tong Tong[1]**

[1] Department of Radiology, Fudan University Shanghai Cancer Center, Department of Oncology, Shanghai Medical College, Fudan University, Shanghai, China, [2] Hefei Cancer Hospital, Chinese Academy of Sciences (CAS), Hefei, China, [3] Shanghai Municipal Hospital of Traditional Chinese Medicine, Shanghai, China, [4] Children's Hospital, Fudan University, Shanghai, China, [5] General Electric (GE) Healthcare, Shanghai, China

OPEN ACCESS

Edited by:
Kun Zhang,
Tongji University, China

Reviewed by:
Yanfen Cui,
Shanxi Provincial Cancer Hospital, China
Qiufeng Zhao,
Shanghai University of Traditional Chinese Medicine, China
Xiao-Yan Zhang,
Beijing Cancer Hospital, China

***Correspondence:**
Weijun Peng
cjr.pengweijun@vip.163.com
Tong Tong
t983352@126.com

Specialty section:
This article was submitted to Radiation Oncology, a section of the journal Frontiers in Oncology

Received: *23 January 2022*
Accepted: *04 February 2022*
Published: *01 March 2022*

Citation:
Hu F, Hu Y, Wang D, Ma X, Yue Y, Tang W, Liu W, Wu P, Peng W and Tong T (2022) Cystic Neoplasms of the Pancreas: Differential Diagnosis and Radiology Correlation. Front. Oncol. 12:860740. doi: 10.3389/fonc.2022.860740

Although the probability of pancreatic cystic neoplasms (PCNs) being detected is raising year by year, their differential diagnosis and individualized treatment are still a challenge in clinical work. PCNs are tumors containing cystic components with different biological behaviors, and their clinical manifestations, epidemiology, imaging features, and malignant risks are different. Some are benign [e.g., serous cystic neoplasms (SCNs)], with a barely possible that turning into malignant, while others display a low or higher malignant risk [e.g., solid pseudopapillary neoplasms (SPNs), intraductal papillary mucinous neoplasms (IPMNs), and mucinous cystic neoplasms (MCNs)]. PCN management should concentrate on preventing the progression of malignant tumors while preventing complications caused by unnecessary surgical intervention. Clinically, various advanced imaging equipment are usually combined to obtain a more reliable preoperative diagnosis. The challenge for clinicians and radiologists is how to accurately diagnose PCNs before surgery so that corresponding surgical methods and follow-up strategies can be developed or not, as appropriate. The objective of this review is to sum up the clinical features, imaging findings and management of the most common PCNs according to the classic literature and latest guidelines.

Keywords: pancreatic cystic neoplasms (PCNs), radiology, intraductal papillary mucinous neoplasms (IPMNs), mucinous cystic neoplasms (MCNs), solid pseudopapillary neoplasms (SPN), serous cystic neoplasms (SCN)

INTRODUCTION

In recent years, the diagnostic rate of PCNs has risen and still keeps an increasing trend. Most patients have no clinical symptoms, and many are found incidentally. Because the etiology and malignant potential of PCNs are often not very clear, diagnosis and management of these neoplasms are challenging. Except for the tail, most of the pancreas is located outside the peritoneum on the posterior wall of the abdominal cavity. Early detection of PCNs is difficult in the absence of clinical symptoms, due to its deep position; most of them are detected incidentally on cross-sectional imaging, and these patients do not have typical pancreatic symptoms (i.e., pancreatitis, jaundice, and new-onset diabetes) (1). It is estimated that approximately 2% to 49% of routine imaging

examinations such as computed tomography (CT) or magnetic resonance imaging (MRI) incidentally detect pancreatic cystic lesions, and this proportion increases with age (2).

The most common PCNs are IPMN, MCN, SCN and SPN. Based on epidemiological data, the incidence of MCN, SCN, and SPN in women is significantly higher than that in men, accounting for approximately 95%, 70%, and 80%, respectively, while IPMN is similar or slightly higher than that in men, approximately 55% (3). In recent years, people's consciousness of these neoplasms has increased, partly due to the application of high-resolution CT/MR imaging. Although the awareness environment of the natural history and most appropriate treatment of various types of cystic lesions is gradually ameliorating, the diagnosis and treatment of PCNs are still challenging. They are usually composed of different solid components, and each solid component exhibits divergent biological behavior, occurring from benign to borderline or even malignant (4). Due to the partial overlap of benign and malignant imaging features, the differential diagnosis of benign versus malignant PCNs is relatively difficult. Moreover, in view of the potential malignant transformation of some benign tumors, the "silent epidemic" of symptomless PCNs has created a real predicament in the treatment and management strategies of such patients.

Different PCNs have relatively specific imaging manifestations, so we can not only identify these tumors by morphological features but also objectively and quantitatively analyze the tumor phenotype by radiomics. Radiomics features have broad application prospects in differential diagnosis, prognosis and efficacy evaluation of PCNs (5). Combined with clinical manifestations and imaging features, radiomics provides an opportunity for the preoperative accurate diagnosis of pancreatic cystic tumors. This review will focus on the clinical features and typical imaging manifestations of different types of PCNs and discusses the latest radiomics research. Thus, it provides an important reference for the precise preoperative diagnosis and individualized management of PCNs. A comprehensive discussion of nonneoplastic pancreatic cystic lesions (PCLs) are not included in this review.

THE MAJOR PANCREATIC CYSTIC NEOPLASMS

The most common types of PCNs (**Figure 1**) are mucin-producing intraductal papillary mucinous neoplasms (IPMNs, encompassing branch-duct IPMNs, main-duct IPMNs and mixed-type IPMNs) and mucinous cystic neoplasms (MCNs). Less common subtypes include nonmucinous tumors such as solid pseudopapillary neoplasms (SPNs) and serous cystic neoplasms (SCNs) (6). The incidence of PCNs varies with the population distribution. For example, IPMNs approximately 21% to 33%, MCNs account for 10% to 45%, SPNs account for less than 10%, and SCNs account for 32% to 39% of all PCNs in the Western Hemisphere. There was a national survey report from Korea shows that IPMNs approximately 41%, MCNs approximately 25.2%, SPNs approximately 18.3%, SCNs approximately 15.2%, and others account for 0.3% of PCNs (7, 8). However, the actual incidence of various types of PCN is unknown. The estimated relative frequencies of PCNs removal from one center of 14,424 patients that treated with surgery over a 15-year period were as detailed below: MD-IPMN, BD-IPMN, MCN, SCA, and SPN account for 25%, 26%,11-18%,13-23% and 4-7%, respectively (9). PCNs often do not have typical clinical symptoms. An Italian multicenter prospective study of pancreatic cystic tumors showed that 338 of 1370 cases (24.7%) had one or more clinical symptoms: abdominal pain (214, 15.6%), acute pancreatitis (106, 7.7%), diarrhea (12, 0.9%), gallstones (39, 2.8%), weight loss (21, 1.5%), fatigue (9, 0.7%), loss of appetite (2, 0.1%), diabetes (40, 2.9%) and jaundice (14,10%). However, most patients were asymptomatic (1036, 75.6%) (10). The specific characteristics of the four most common PCNs are exhibition in **Table 1**.

Intraductal Papillary Mucinous Neoplasm

IPMN is a benign, borderline, low-grade dysplasia or invasive cancer derived from pancreatic ductal epithelium. Tumor cells are tall columnar mucous-rich epithelial cells, with or without papillary protrusions, extensively invading the main pancreatic duct (MPD) and/or branch pancreatic duct (BPD), causing cystic dilation. With the continuous development of diagnostic standardization and imaging techniques, IPMNs are becoming increasingly routinely diagnosed in clinical practice. According to the communication with the pancreatic duct, they are morphologically divided into MD-IPMN, BD-IPMN and MT-IPMN. Approximately 40% to 65% of IPMNs occur in the branch pancreatic ducts, while they are found in the MPD accounting for about 15% to 35% cases. The probability of simultaneous occurrence in the both pancreatic ducts is only 15%-20% (28).

According to the different histology and mucin expression of IPMN, it can be divided into four epithelial subtypes as below: gastric-type, intestinal-type, pancreatobiliary-type and oncocytic-type, each of which has various kinds of risks of malignant progression. Oncocytic- and gastric-type IPMNs are often low-grade neoplasms, while intestinal- and pancreatobiliary-type IPMNs have a disposition to high-grade neoplasms and are usually related to invasive cancer (IC) (11). The prognosis of IPMNs is superior to pancreatic ductal adenocarcinoma (PDAC) after surgical resection (29). It has been reported that the incidence of cancers derived from IPMN is between 6% and 46% (30–33), including IPMN with high-grade dysplasia (HGD) and IC, and its prognosis is as poor as that of PDAC (34). Assessing the rate of malignancy in IPMN has become a clinical challenge. The risk factors for malignant tumors include weight loss, patient age, relationship with mural nodules, increased jaundice/bilirubin levels, and elevated CEA levels. However, there is no established standard that can safely and accurately distinguish malignant and nonmalignant lesions (35). Therefore, the key to the treatment of IPMN is to accurately predict the risk of malignancy. At the same time, it is also important to evaluate the probability of surgical resection

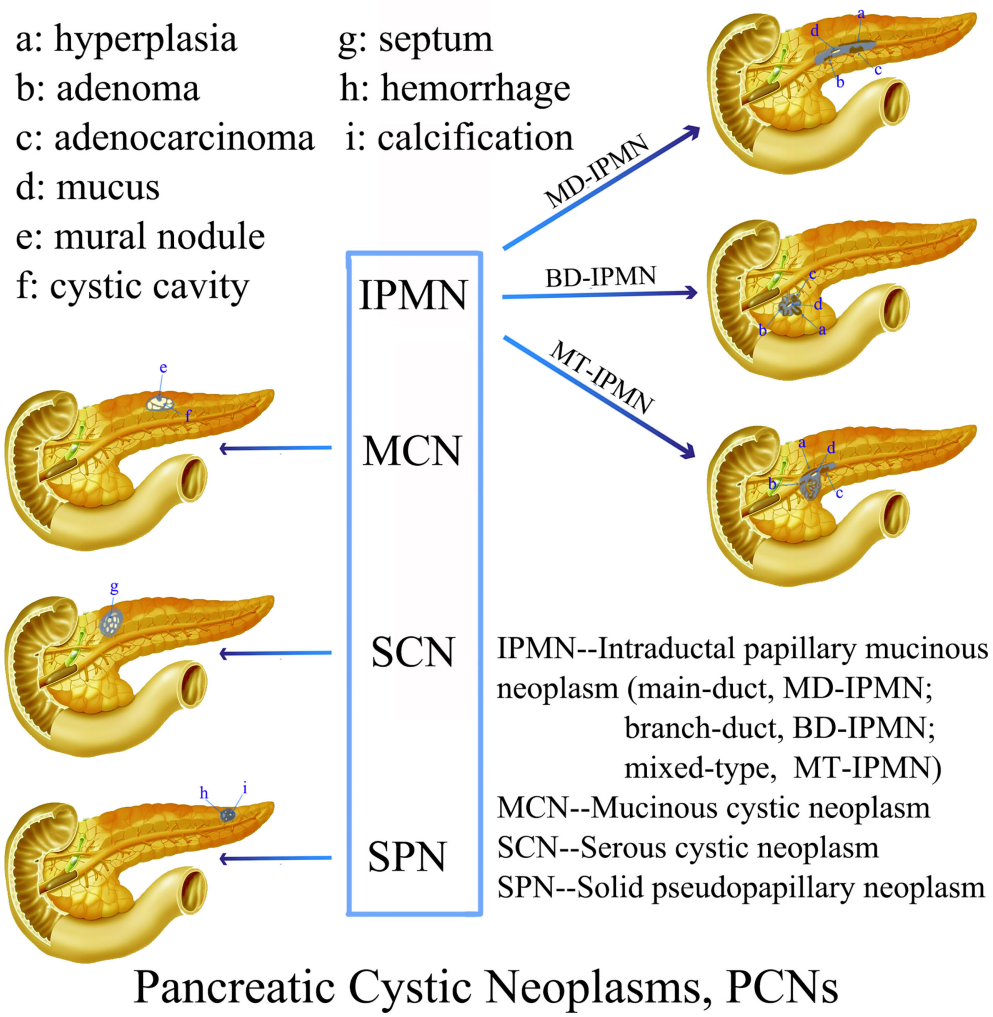

FIGURE 1 | Schematic representation of the characteristic morphological and imaging features of various PCNs.

benefit. Imaging takes a significant role in the evaluation and detection of IPMNs (36).

The aims of imaging examination of IPMN are as follows: first, to detect IPMN and exclude other PCLs; second, to distinguish the relationship between lesions and the pancreatic duct, which is conducive to typing; and third, to determine the key risk factor of malignancy and estimate the resectability of clinical surgery. Various imaging methods are used to achieve these goals.

Mucinous Cystic Neoplasm

MCNs are cystic tumors derived from the pancreatic epithelium that have the potential for malignancy. They are relatively rare pancreatic cystic tumors in the clinic, accounting for 29% of all PCNs (37). Compared with IPMNs, MCNs do neither communication with the MPD nor BPD system. They are often solitary and are covered by a thin fibrous cyst wall. The cyst is lined with tall columnar mucous cells that secrete mucin and often form papillae, and the subepithelial stroma is often ovarian-like stroma with abundant cells (38). There is no significant difference in incidence between sexes in their 60s and 70s, and the probability of occurrence in the body/tail of the pancreas is greater than that in the pancreatic head (67.3%–99.4%) (39), with 89.5% in the present series.

The malignant probability of MCNs varies between 6% and 36%, which is still significant (12). The features predictive of malignancy include irregular or focal thickening of the cyst wall, a large volume, and solid content inside or outside the cyst (40, 41). The size (> 8.5 cm) and volume of the MCNs on CT/MR imaging are the only features associated with HGD/IC, and the average growth rate is very slow, about 4 millimeters (0.16 in) every year (42). The mucinous transitional epithelium is the origin of almost whole malignancies arising from MCNs. MCNs can be divided into three major categories according to the grade of dysplasia as well as IPMNs: low- or intermediate-GD, HGD and IC (13, 43). Resection is advocated for whole types of MCNs

TABLE 1 | The clinical and image features of common pancreatic cystic neoplasms (4, 10–27).

Characteristics	IPMN	MCN	SCN	SPN
Age (decade)	5th-7th	4th-5th	5th-6th	2-3th
Gender distribution	Equal	90-95% female	70% female	90% female
Location	Common in pancreatic head	Body and tail	Entire pancreas	Throughout, common in body and tail
Imaging features	Multiple mural nodules, pancreatic duct dilatation, ductal communication, cyst or cluster of cysts	Large cysts with thick septae, peripheral calcification, mural nodules	Star-shaped central scar with calcification, microcystic multiple small cyst, sometimes oligocytic	Local capsule interruption, cystic degeneration, calcification and hemorrhage, floating cloud sign
Cyst fluid	Viscous, mucin-rich	Viscous, mucin-rich	Thin	Bloody
Classification	MD-IPMN, BD-IPMN, MT-IPMN	Low- or intermediate-grade dysplasia, high-grade dysplasia, an associated invasive carcinoma	SMA, SOA, SSCA	Low malignant neoplasm
Clinical symptoms	Incidental finding, jaundice, pancreatitis, malignancy-related	Incidental finding, abdominal pain, malignancy-related	Incidental finding, abdominal pain, mass effect	Incidental finding, abdominal pain, mass effect
Connection with MPD	Yes	No	No	No
Solitary or multifocal	Solitary/multifocal	Solitary	Solitary	Solitary
CEA	≥192~200ng/ml (80%)	≥192~200ng/ml (80%)	<5ng/ml	Unknown
Amylase	High	Low	Low	Low
Molecular markers	KRAS mutation(+) (80%), GNAS mutation(+) (41-66%)	KRAS mutation(+) (50%-75%), GNAS mutation(-), CTNNB1 mutation(-)	VHL, VEGF-A>8500pg/mL, VEGF-C>200pg/mL, MUC1, MUC6	CTNNB1, B-catenin, LEF1, TFE3S, SOX11
Cytology	Columnar cells, +mucin, variable atypia	Columnar cells, +mucin, variable atypia	Often acellular or cuboidal cells stain, +glycogen	Branching papillae with myxoid stroma
Malignant probability	Medium or high	Medium	Negligible	Low or medium

IPMN, intraductal papillary mucinous neoplasms; MCN, Mucinous Cystic Neoplasm; SCN, Serous Cystic Neoplasm; SPN, solid pseudopapillary neoplasms; MPD, main pancreatic duct; MD-IPMN, main-duct IPMN; BD-IPMN, branch-duct IPMN; MT-IPMN, mixed-type IPMN; SMA, serous microcystic adenoma; SOA, serous oligocystic adenoma; SSCA, solid serous cystadenomas.

according to current the guidelines and clinical consensus unless there are contraindications to surgery (44). For MCNs with IC, the prognosis is closely related to the extent of lesions invasion, tumor stage and R0 resection rate. The two- and five-years survival rates of resectable MCNs with IC are 67% and 50%, respectively (7). Therefore, early detection and identification of MCNs with invasive cancer by imaging methods are of great significance.

Solid Pseudopapillary Neoplasm

SPNs are an rare pancreatic tumor and, as their name implies, have a solid pseudopapillary structure formed by epithelial cells of a single shape in a loose arrangement. They are prone to hemorrhage and cystic transformation. These tumors account for only 0.2~2.7% of all exocrine pancreatic neoplasms (45). According to the morphological and structural characteristics of the lesion, different reports use the nomenclature solid-cystic neoplasm, papillary-cystic neoplasm, solid-cystic acinar neoplasm, solid-papillary neoplasm, but the actual use of "solid pseudopapillary neoplasm" (SPN) is similarly only a descriptive name that represents morphological features yet retains the openness of histogenesis. Regardless of the presence or absence of metastatic disease, SPNs are generally considered to be low-grade tumors with an indolent growth pattern. The origin of these tumor cells in the pancreas is uncertain. There are two classical theories about the origin of SPN: the one suggests that it origins from pluripotent pancreatic cell, then the other proposes a female genital bud origin (46).

Due to the wide application of high-quality and -resolution imaging examinations, mainly US, CT, and MRI, it has been reported high frequency in the past few decades. In a recent review of all SPN description that published in the English journal up to 2014, Law et al. (47) confirmed a total of 2744 cases of this neoplasm. Yao et al. systematically reviewed 2,450 SPN cases in a Chinese population before January 2020, which was published in both the Chinese and English literature (48). They concluded that SPN is an indolent neoplasm and seldom seen that mainly occurs in young females. The clinical manifestations are abdominal masses and abdominal pain, most of them present as pancreatic head and tail space occupying, and the prognosis is excellent after complete resection. Generally, they are indolent, but a few have malignant potential. Regrettably, the prognostic factors that predict malignant potential have been hard to identify (49). Most patients present with local lesions, and only 9-15% have metastases or local infiltration.

At present, the main treatment is still surgical resection, and its prognosis is different from that of pancreatic cancer. According to reports, the five-year survival rate can be as high as 94-97% (45, 50). Rare SPNs can occur at any age and in both genders, especially young females. Although the survival rate is typically high, histological images cannot accurately predict its biological behavior. Lesions without obvious malignant signs but only suspicious morphological signs can also cause late

recurrence, metastasis and even death. The exact histogenesis is still unclear, and it may originate from primordial cells. More research on SPT is needs for further clarification.

Serous Cystic Neoplasms

SCNs are benign tumors of the pancreatic exocrine glands that account for 16%~33.3% of whole cystic neoplasms of the pancreas. It is a slow-growing benign lesion with an extremely low probability of malignant transformation (14, 15, 51). The concept of SCNs as benign disease entities without the risk of malignant transformation was revised after George et al. revealed the first case of a malignant pancreatic SCN in 1989 (52). The malignancy of SCNs, serous cystadenocarcinomas, are limited to 25~30 cases report in the global literature, representing <1% of all SCNs (15), including the largest sample size, which found three patients with serous cystadenocarcinomas among 2622 cases (53). Therefore, SCNs of the pancreas have extremely low malignant potential but are not totally benign.

Patients are often discovered with SCN in their late 50th or early 60th. SCN usually develops in the body/tail of the pancreas. Despite these neoplasms are mostly benign, they often grow slowly and may have large diameters (13). SCNs are representatively honeycombed microcystic tumors consisting of uniform, cuboidal, glycogen-rich epithelial cells. Thus far, there are four known variants of serous cystadenoma, namely, macrocystic serous cystadenoma, solid serous adenoma, VHL-related SCN, and mixed serous neuroendocrine neoplasm, in which the serous epithelial components of these variants are identical to those of serous cystadenoma.

Pancreatic serous cystadenomas are benign lesions and could be regulated by surveillance, which does not commonly mandate surgical resection unless they exhibit aggressiveness or unspecific characteristics that hinder accurate diagnosis. CT is the preferred first-line examination modality for characterizing SCNs and differentiating them from their mimickers (54).

IMAGING DIAGNOSIS AND PRECISION IMAGING

Multiple imaging modalities can help to further distinguish a PCN, facilitating the findings, characterization, and evaluation of the presence of aggressive behavior and the evaluation of resectability in patients with obviously malignancy. Imaging modalities have unique advantages and potential weaknesses in terms of PCN evaluation. Radiomics is an emerging field in quantitative imaging that uses techniques that advance imaging features to objectively and quantitatively investigate tumor phenotypes. Noninvasive medical imaging such as US, MRI, CT, and positron emission tomography (PET) can be used to assess tumor and anatomical tissue features for tumor management (55–57). Radiomics can obtain high-content information through identification, extraction, quantitation, and processing to identify imaging signatures or phenotypes.

Information from surrogate imaging biomarkers combined with multifarious demographic, biologic ("omic") and outcome-driven methods can be used to develop precision medicine strategies. Accurate imaging biomarkers have been described in a large number of neoplasms. Medical images store more information than trained physicians can see; thus, more details about the region of interest that are embedded in this hidden information can be extracted and analyzed by computational tools than has been previously observed (58, 59). Manual identification of cyst type has an accuracy of only 60~70%, even by well-trained radiologists (60). Therefore, the development of imaging markers using radiomics could increase the correct identification of the type and malignant rates of PCNs.

Regrettably, radiological research to assess the risk of PCN malignancies, especially IPMN, is very limited. In one of the earliest research, an algorithm that distinguishes between the four most common types of PCNs (IPMN, MCN, SCA, and SPN) was proposed by Dmitriev and his colleagues. They revealed an integrated model that combines patient demographic factors with intensity and shape characteristics extracted from cyst images. Segmentation of the cystic neoplasms was acquired by a semi-automated graph-based segmentation technique, at the same time, an random forest classifier and convolutional neural networks were applied for feature selection. This groundbreaking research acquired an accuracy of approximately 84% in distinguishing various types of cysts (61). A recent research revealed a computer-aided diagnosis (CAD) scheme based on radiomics and emphasized the role of radiomics analysis as a new noninvasive tool to improve the accuracy of the preoperative diagnosis of SCN (59). Another study showed that a comprehensive nomogram combining clinical characteristics and fusion radiomics features could identify SCNs from mucin-producing PCNs (58). With the in-depth study of radiomics methods in the field of tumors, it is believed that more research will focus on the differential diagnosis of PCNs in the future.

At present, advanced imaging techniques are increasingly utilized in clinical practice, and the detection rate of PCLs has started to increase gradually. For example, Laffan et al. reported that PCLs were detected in about 2.6% of items using multidetector computed tomography (MDCT) (62), suggesting that CT is the first available source of imaging data for diagnosis. One previous study revealed an accuracy of 67-70% for discriminating 130 pancreatic cysts on CT scans, which were performed by two readers with more than 10-years of experience in abdominal diagnosis (60). In addition, the accuracy of MDCT for characterizing PCN ranges from 56% to 85% (63), and the wide availability, high spatial resolution, and rapidity of acquisition make MDCT ideal for the initial PCN assessment (63). Furthermore, the presence of high-risk stigmata, including a solid component or mass within the cyst, or the presence of mural nodules can be identified by CT imaging. However, MDCT also has disadvantages. It is still difficult to characterize the histopathologic subtype of PCN, as their CT features overlap (64). Besides, the ionizing radiation inherent to CT might result in suboptimal use effects, especially for continued follow-up examinations.

The raising availability and use of dual-energy CT scanners may be advantageous to reduce the overall dose to the patient, thus decreasing the number of acquired phases by using virtual

unenhanced imaging. Although CT spectral imaging can provide additional information and multiparametric analysis can achieve greater results than single-parameter analysis in differentiating serous and mucinous content, it is difficult to combine multiparametric analysis and CT spectral imaging-derived quantitative parameters to improve the diagnostic performance (65).

Given the extensive use of high-quality and -resolution MDCT, recent studies have assessed advanced computer-based quantitative image analysis to obtain additional information for identifying characteristics that might be helpful to predict high-risk IPMN. Hanania et al. evaluated 53 cases with IPMN and distinguished 14 imaging characteristics (biomarkers) to differentiate between LGD and HGD in IPMN. Using the top 10 of the 14 biomarkers, an AUC of 0.96 was achieved, with a sensitivity of 97% and specificity of 88% (66). The results of this study indicated that HGD/IC IPMNs have distinct radiomics features that could be utilized to stratify patients *via* noninvasive imaging. Permuth et al. also distinguished malignant from benign IPMN by using radiomics with 14 radiologic features in 38 cases; however, they integrated 5-miRNA data and achieved an AUC of 0.92, with a sensitivity of 83% and specificity of 89% (67). Such high sensitivity and specificity are conducive to improving the clinical discrimination ability of benign and malignant IPMNs so that targeted and individualized treatment strategies can be adopted.

Yang et al. (68) identified 25 patients with MCN from 53 patients with SCN using a preliminary model based on texture features (GLCM, GLRLM, GLZLM, and NGLDM) extracted from contrast-enhanced CT images that were selected *via* LASSO regression and random forest classifiers. Fascinatingly, they also found a good correlation among the extracted texture features extracted from CT images of 2 mm and 5 mm thick slices, which had previously been neglected in many previous studies. Although the feature extraction was not affected by a difference in slice thickness, they suggested using CT images with similar slice thicknesses for radiomics analysis. They acquired an accuracy of 74% in the slice thickness of 2 mm group and 83% in the slice thickness of 5 mm group in the validation group.

The proposed radiomics-based CAD scheme could increase the accuracy of the preoperative diagnosis of pancreatic serous cystic neoplasms, showing an AUC of 0.767 in the cross-validation group and 0.837 in the independent validation group (59). It has also been suggested that using CT alone is of limited value in differentiating between serous and mucinous lesions (69). The study showed that PCNs displaying central scarring, central calcification or the circumvascular sign on CT could be diagnosed as SCAs. When either of the first two features is combined with the circumvascular sign, the diagnostic sensitivity could be improved (14). The malignant probability of SCN is significantly lower than that of MCN. Thus, a follow-up observation strategy can be used for some patients.

The reported incidence of detecting asymptomatic pancreatic cysts on MRI is about 15% (70). The prevalence on MRI is higher overall, ranging from 2.4% to 20%, and increases with age to approximately 40% in patients older than 70y (71, 72). T_2WI are exquisitely sensitive to fluid-filled structures. Thus, small parenchymal pancreatic cysts or the MPD/BPD system with MRCP can be visualized by T_2-weighted MRI, which is the primary MRI pulse sequence (73). Compared to MDCT, MRI is more sensitive overall for detecting small pancreatic cysts < 3 cm (74). Furthermore, MRI can detect more PCLs smaller than 20 mm than CT. For lesions larger than or equal to 20 mm, MRI can depict a greater level of internal details than CT, which could aid clinicians in making management decisions (75). Hoffman et al. (76) demonstrated that entropy could be prognostic for malignancy by extracting a few intensity histogram-based statistical features from MR images of 18 patients with BD-IPMN. In a concept-of-proof study involving 38 patients, there were 20 benign and 18 malignant IPMNs. MRI/MRCP has an additional advantage over MDCT for patients who require repeated imaging for follow-up because of the lack of radiation exposure. Disadvantages of MRI include its lower spatial resolution, low sensitivity to detect calcifications, and motion-related artifacts.

The CT and MR Manifestations of IPMN

Among the three types of IPMN, the branched type is the most common, followed by the mixed type, and the MPD type is relatively rare. The latter is further divided into two sub-types, the segmental type and the diffuse type. The communication between cystic lesions and the MPD is one of the diagnostic points of branch-type IPMN. Branch-type IPMN specific imaging findings are as follows: tubular or earthworm-like shadows in low-density cystic lesions, cystic walls and septate microenhancing nodules. The dilated MPD is not limited to the distal end of the lesion. The imaging signs that affect the diagnosis are as follows: the lesions are oval or dumbbell-shaped, the lesions' density is close to that of water, and there are non-separations or tiny nodules in the lesions. Thin-slice scanning combined with three-phase enhancement, coronal or sagittal image reconstruction, and careful observation of cyst wall and intralesional structures can help improve the diagnostic accuracy (**Figure 2**).

The MD-type IPMN-specific imaging manifestations are as below: moderate or greater dilatation of the MPD, continuous expansion of the pancreatic duct without bead-like changes, enhanced mural nodules on the cyst wall, slight atrophy of the pancreatic parenchyma, and markedly dilated MPD asymmetry with mildly atrophied pancreatic parenchyma (**Figure 3**). Imaging signs that affect the diagnosis are as follows: in the early stage of the disease, dilatation of the MPD is limited or mild. In the early stage of the disease, this is easily confused with the slight dilatation of the pancreatic duct caused by anatomical variations; diffuse IPMN is easily confused with chronic pancreatitis, and localized IPMN is easily confused with pancreatic fusiform pseudocysts.

Mixed-type IPMN often comprises both branched IPMN and MPD IPMN, but it is not a simple combination of the two. In MT-IPMN, the expansion of the MPD can be localized or diffuse, and localized expansion can manifest as multiple discrete segmental expansions, but no beaded changes occur. There is no strict boundary between the limited MPD dilatation and branched IPMN with mild MPD dilatation. Some studies believe

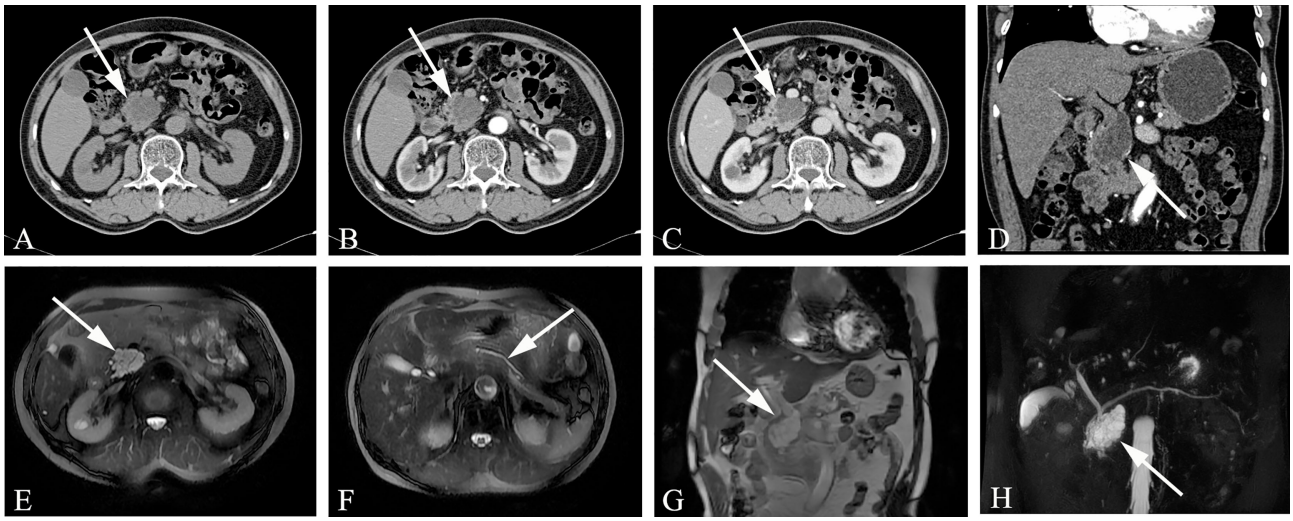

FIGURE 2 | Branch-type IPMN (Male, 66y, physical examination revealed a pancreatic mass for a week). **(A–C)** The CT plain scan, arterial phase and venous phase at the same level; **(D)** Coronal image in arterial phase. **(E)** T_2-weighted cross-sectional image; **(F)** T_2-weighted cross-sectional image at another level of the same patient; **(G)**. T_2-weighted coronal image; H. MRCP reconstruction map; **(A)** The CT plain scan showed multilocular cystic mass of pancreatic head with septation and clear boundary. The density is slightly higher than that of water. **(B–D)** Contrast enhanced scan showed moderate enhancement of mural nodules in the dilated branch pancreatic duct. **(E–H)** Septa can be seen in the lesion and the MPD was slightly dilated. The white arrows in the Figures only indicate the location of the neoplasm.

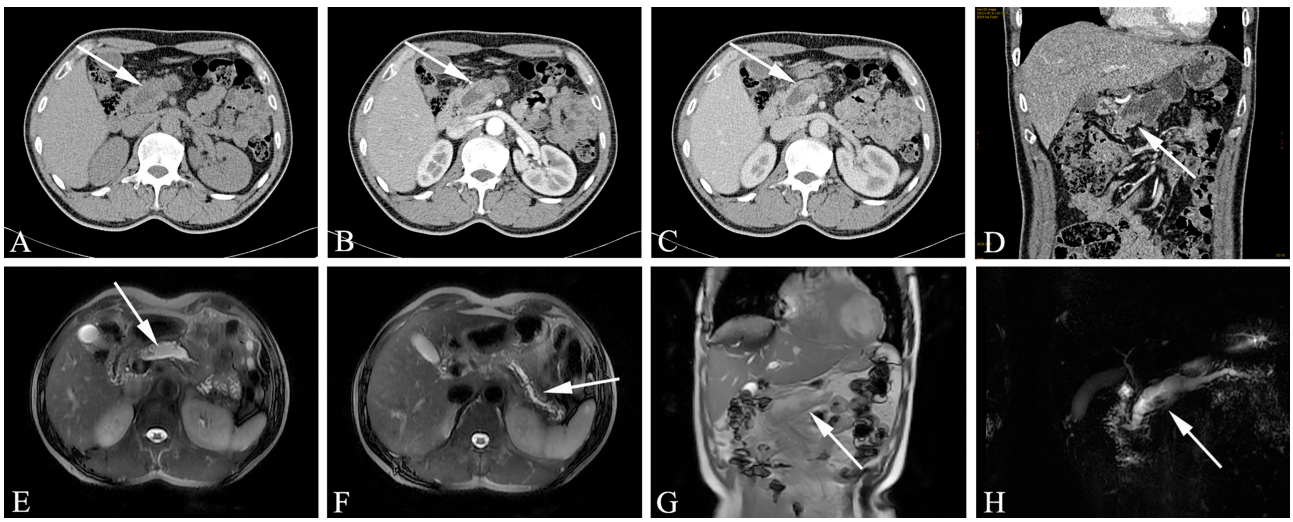

FIGURE 3 | Main-duct IPMN (Male, 57y, abdomen pain for one month). The sequence distribution of images is the same as that in **Figure 2**. **(A)** The CT plain scan showed nodule in the neck of the pancreas, with a CT value of about 31HU. The MPD is obviously dilated, the pancreatic parenchyma is slightly atrophied, the dilated pancreatic duct is low-density, and the density is similar to that of water. **(B, D)** In the arterial phase, the nodule of the pancreatic neck was moderate enhanced, with a CT value of about 65HU, and the dilated pancreatic duct showed more clearly. **(C)** In the venous phase, the nodule showed continuous enhancement, at this time, the CT value is 72HU; **(E–G)** The T_2-weighted imaging shows pancreatic duct dilatation with multiple mural nodules. **(H)** MRCP shows the MPD dilated significantly throughout the whole pancreas. The white arrows in the Figures only indicate the location of the neoplasm.

that mixed IPMN is caused by the further development of branched IPMN, which is the key to distinguishing between branched IPMN and the mixed type. It is unclear whether there are tiny nodules in the MPD that are adjacent to the expansion, and if there are tiny nodules in the expanded MPD, it is of a mixed-type (**Figure 4**). Mixed-type IPMN can be accompanied by one or more branch types. Therefore, the imaging manifestations of mixed-type IPMN are more complex and can differ, but simultaneous expansion of the BPT and MPD is also the easiest subtype to diagnose.

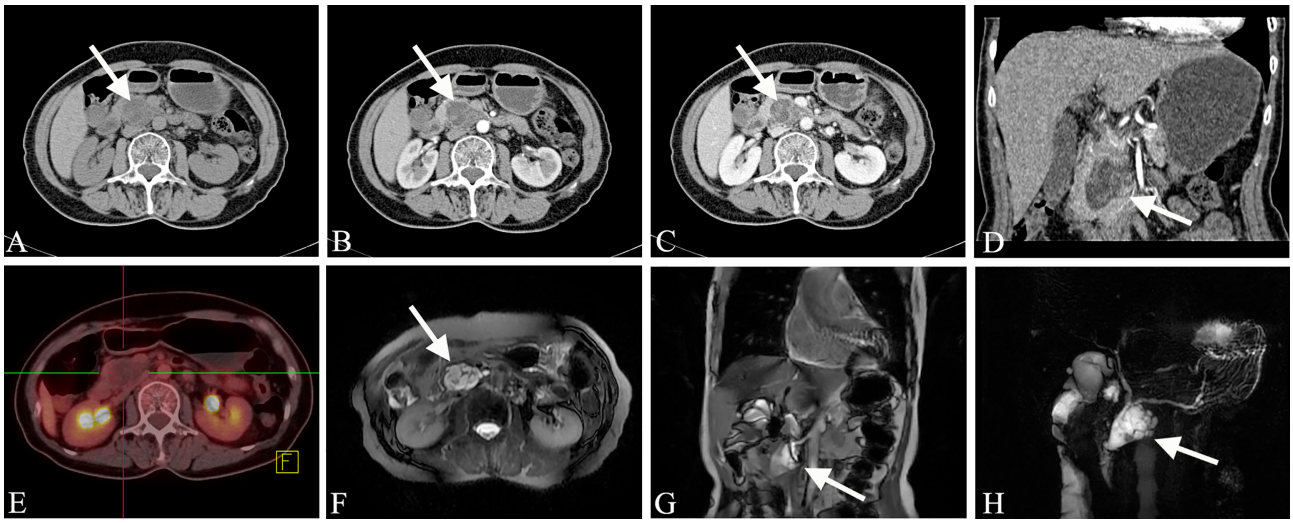

FIGURE 4 | Mixed-type IPMN (Female, 56y, abdomen pain for half year). **(A–C)** The CT plain scan, arterial phase and venous phase at the same level; **(D)** Coronal image in arterial phase. **(E)** PET cross-sectional image; **(F)** T_2-weighted cross-sectional image; **(G)** T_2-weighted coronal image; **(H)** MRCP reconstruction map; **(A)** The CT plain scan showed multilocular cystic mass of pancreatic head with septation and clear boundary. The density is slightly higher than that of water. **(B, C)** Contrast enhanced scan showed moderate enhancement of mural nodules in the dilated MPD and branch pancreatic duct. **(D)** Diffuse dilatation of the MPD with enhanced mural nodules, which is the key to the diagnosis of mixed-type IPMN. **(E)** No obvious FDG uptake was found in the lesions by PET-CT. **(F–H)** Magnetic resonance imaging showed a multilocular cystic mass in the pancreatic head with multiple mural nodules, which communicated with the pancreatic duct. The white arrows in the Figures only indicate the location of the neoplasm.

Magnetic resonance T_1WI showed that the liquid in the pancreatic duct of the IPMN dilated pancreatic duct had a low signal that was slightly higher than water; T_2WI showed a high signal that was slightly lower than water. Some lesions showed hyperintensity on T_1WI and hyperintensity on T_2WI. The spatial resolution of MRI is limited, and the ability to show small mural nodules is not as good as CT, but MR helps to show larger nodules. The nodules show a lower signal on T_1WI, which is between normal pancreatic tissue and dilated pancreatic duct fluid. T_2WI is helpful to show streak-like hypointense separation or dilated pancreatic duct wall within the hyperintensity of branched IPMN, showing isohypointense mural nodules in the dilated pancreatic duct. The DWI signal of pancreatic IPMN varies greatly. Some DWI is isointense, and some is hyperintense. DWI helps to detect metastatic lymph nodes. MRCP helps to determine the relationship between the lesion and the MPD and shows the MPD protruding into the duodenum. Thin-layer MRCP is more helpful to determine the relationship between the MPD and the duodenum. During dynamic enhancement, the enhancement of the pancreatic duct wall of IPMN is similar to that of CT, the enhancement of small nodules is not as good as that of CT, and the enhancement of large nodules is close to or better than CT.

The CT and MR Manifestations of MCN

Mucinous cystadenoma with invasive carcinoma often manifests as multilocular cystic lesions with uneven wall thickness, wall nodules and calcifications in the lesion. After enhancement, the intracapsular septum thickens, and the wall nodules are obviously strengthened. Sometimes it is not easy to distinguish between benign and malignant tumors by imaging. If the following signs appear in the cyst, mucinous cystadenoma with invasive carcinoma is often indicated: ①There are more solid components in the cyst. ②There are obviously enhanced mural nodules. ③ Irregular thickening of the cyst wall and the presence of multiple daughter cyst near the large cyst. ④Local pancreatic lymphadenopathy and intrahepatic metastasis are observed and adjacent large blood vessels have been invaded. ⑤The tumor is large, with a diameter >8 cm.

Mucinous cystadenoma usually manifests as a clear boundary with hypo-intensity on T_1WI and hyper-intensity on T_2WI, but sometimes it has different manifestations due to the composition of the cyst fluid. The advantage of MRI is that it can accurately reflect the composition of the cyst fluid of mucinous cystadenoma. Sometimes the signal on T_1WI is uneven and has a high signal, which is pathologically related to mucin in the cyst fluid or intracystic hemorrhage. In addition, MRI shows better separation between the wall and wall nodules in the lesion capsule than CT. The cyst cavity of mucinous cystadenoma is generally not connected to the pancreatic duct, which helps to distinguish it from intraductal papilloma (communicating with the pancreatic duct). MRCP examination is helpful for determining whether the mucinous cystadenoma is connected to the pancreatic duct. MR examination of mucinous cystadenoma with invasive carcinoma can not only show that the tumor is cystic but also clearly depicts the tumor cyst wall, septum and mural nodules (**Figure 5**).

Uneven thickening of the intratumoral septum and cyst wall or the appearance of mural nodules, invasion of the common bile duct (CBD) or pancreatic duct (PD) and surrounding blood vessels are all helpful for the diagnosis of mucinous cystadenoma with invasive carcinoma. MR examination is helpful for the differentiation of

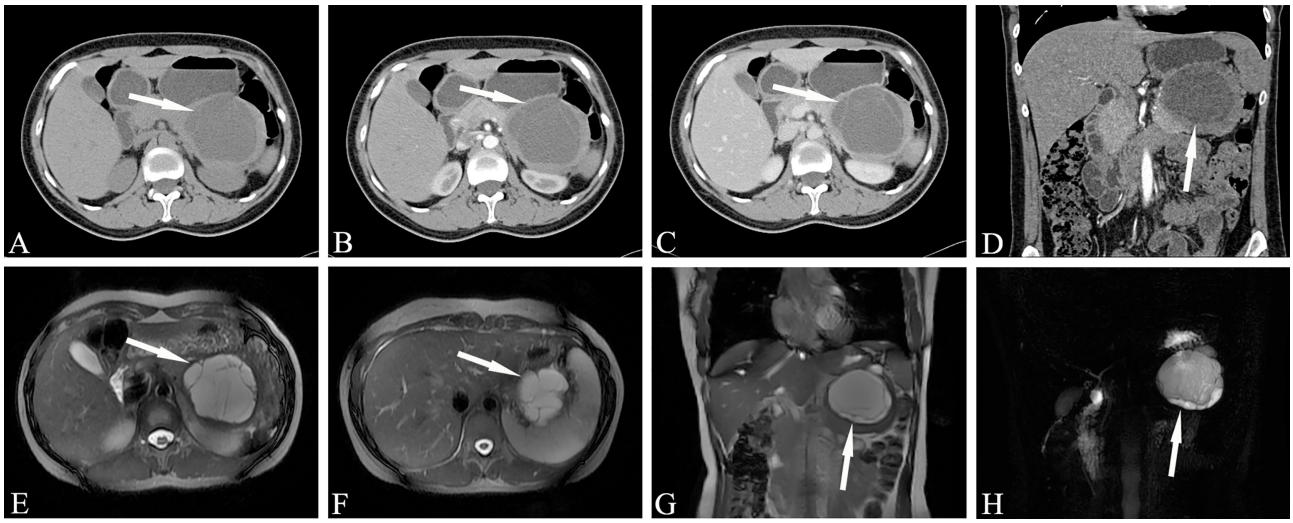

FIGURE 5 | Mucinous cystic neoplasms, MCN (Female, 33y, physical examination revealed a pancreatic mass for one month). The sequence distribution of images is the same as that in **Figure 2**. **(A–D)** Huge cystic mass in the body and tail of the pancreas, irregular in shape, high tension, watery low density, thin and uniform cyst wall, multiple thin septum and small walled cysts can be seen in the cyst, and the septation and mild cyst wall can be seen enhanced after contrast injection. **(E–H)** Magnetic resonance images showed clearer septum and small sacs. There were no signs of pancreatic duct dilatation. The white arrows in the Figures only indicate the location of the neoplasm.

benign and malignant pancreatic mucinous cystadenoma. Since the blood supply of the tumor is mainly concentrated in the cyst wall and septum, enhancement may appear after an enhanced scan.

The CT and MR Manifestations of SCN

CT scans of serous microcystic adenoma show a clear boundary, lobulation, and a mass formed by several small water-like cysts. The diameter of a single capsule is usually less than 2 cm. Star-shaped central scars can be seen in the lesions, and calcifications usually occur in the central scars. The enhanced scan shows progressive medium-strength enhancement of the central scars. It is often difficult to identify the tumor septum when it is thin, and enhancement can help with visualization when it is thicker. Star-shaped central scarring with or without calcification is considered to be a specific manifestation of serous microcystic adenoma. CT showing the intratumoral septum, central scar and size of the cyst is key to the imaging diagnosis of microserous microcystic adenoma. Sometimes serous microcystic adenomas are composed of numerous tiny vesicles, which show a honeycomb or spongy appearance, and most of the single cysts are one to several millimeters long (**Figure 6**). Clear edges and a cystic space with soft tissue structure can be seen on plain CT scan, and moderate enhancement is observed during the enhanced scan. At this time, it should be distinguished from SPN. When the lesion wall is thick, the internal components are complicated, and there is bleeding, calcification, liquefaction and necrosis, a solid pseudopapillary tumor is indicated.

MR shows serous cystadenoma basically similar to the CT appearance. However, the ability of MR to display calcification is weaker than that of CT, and MR can better display intracapsular hemorrhage, separation, and capsule wall. it can reveals more soft tissue information than CT scans. Soft tissue display can provide more information than CT. In addition, the display of the pancreatic duct and bile duct is more valuable for the differential diagnosis of diseases. Serous microcystic adenoma showed typical polycystic or honeycomb changes on MRI. The contents of the sac are a clear protein-containing liquid, generally showing a liquid signal shadow of long T_1 and long T_2. Sometimes the cyst cavity shows a slightly low signal shadow on T_2WI, which is caused by the local fluid concentration in the cyst cavity and the high protein content. Small cysts can only sometimes be a few millimeters. Intensified scanning of the cyst wall and separation are often mildly continuously enhanced. The lobulated contour, as if the collapsed wall dumped toward the center, is a feature of microcystic serous cystadenoma caused by the traction of the central star-shaped scar; the central scar sometimes has calcification, which appears to be sunlight-radiating on CT, with certain characteristics, but MRI has obvious shortcomings in showing scar tissue calcification.

MRI can almost show the cyst wall and the space within it, even for tumors with small diameters. The intratumoral septum can be seen more clearly on T_2WI. Serous tumor microcystic adenoma of the pancreas generally does not cause dilation of the CBD and PD. Although serous microcystic adenoma of the pancreatic head is adjacent to the CBD, there are few signs of abnormal compression or obstruction in the bile duct system. This may be due to the tumor's soft body and slow growth, which does not compress the bile duct, also proving that the tumor is not aggressive. However, a small number of cases of serous microcystic adenoma with mild dilation of the pancreatic duct or CBD have also been reported. Mild pancreatic duct widening may be caused by mild compression changes or mild inflammatory changes in the pancreas. The

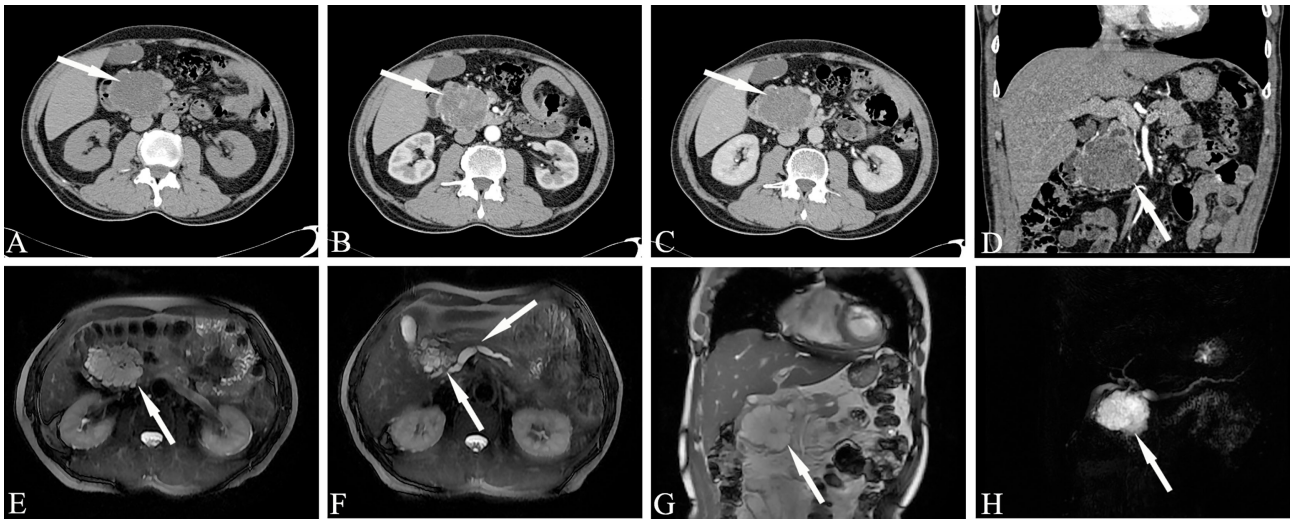

FIGURE 6 | Serous microcystic adenoma, SMA (Male, 65y, physical examination revealed a pancreatic mass for one month). The sequence distribution of images is the same as that in **Figure 2**. **(A–D)** Polycystic or honeycomb cystic foci in the head of the pancreas, with a lobulated outline, like a collapsed wall dumping to the center, and slightly continuous enhancement of the cyst wall and septum. Punctate calcification can be seen in the capsule wall. The enhanced scan shows progressive medium-strength enhancement of the central scars. **(E–H)** Magnetic resonance imaging reveals microcapsule-like structures more clearly and the MPD was slightly dilated. A stellate scar can be seen in the center of the lesion. The white arrows in the Figures only indicate the location of the neoplasm.

relationship between the cyst cavity and the pancreaticobiliary duct is of great significance to the diagnosis and differential diagnosis of this disease.

Serous microcystic adenomas caused by pancreatic tail duct dilatation should be differentiated from BD-IPMN. MRCP can easily determine the relationship between the neoplasm and the pancreatic duct. Microcystic cystadenoma with typical changes and other pancreatic cystic tumors are not difficult to distinguish. Serous oligocystic adenoma tumors show typical unicystic or multicystic changes on MRI. Cystic lesions are larger than serous microcystic adenomas. The lesions are clearly separated from the surrounding pancreas, and the edges are smooth. The characteristics of the signal of the cyst contents and the relationship with the pancreaticobiliary duct are roughly similar to those of serous microcystic adenoma. There is no sign of communication between the cyst cavity of the lesion and the pancreatic duct, and the adjacent CBD often shows no obvious compression or obstruction (**Figure 7**).

Solid serous cystadenoma contains a large number of fibrous interstitial blood vessels, and there is no cyst in the tumor according to general pathology. Only tiny cysts can be seen under the microscope, with abundant interstitial blood vessels (**Figure 8**). This type of cystadenoma is rare. Because the capsule is very small, it is difficult to display watery signals in the lesion on T_2WI, which often leads to the misdiagnosis of pancreatic neuroendocrine tumors.

CT and MR Manifestations of SPN

Regarding the typical CT appearance of a SPN, the solid part of the pancreas is slightly low-density, and cystic necrosis is shown as a lower-density area. The pathological basis that causes uneven density and mixed signals is tumor cystic transformation, hemorrhage, and the calcification of lesions(**Figure 9**). The distribution of cystic and solid components are also different; they can exist alternately, solid components can be located around the tumor, or multiple cysts of different sizes can be located at the edge of the tumor. Pathologically, the tumor cells in the pseudopapillary area form branched pseudopapillae with slender fibrous blood vessels as the axis. The cells are arranged in nests or lumps and in multiple layers. They are far away from the tumor cells around the blood vessels and are prone to degeneration. Necrosis, liquefaction and cystic changes can occur. Histologically, bleeding is prone to occur due to the large number of fragile, thin-walled blood vessels and the lack of a strong stent structure. Hemorrhage is one of the characteristics of this tumor.

Bleeding can occur in the cystic part or the solid part, showing gel-like or cystic tissue; the cystic and solid components of CT are scattered and patchy and show a high density. Calcification in the lesion is more common and can manifest in various ways: small spots, diffuse calcification, incomplete arc-shaped calcification of the envelope (**Figure 9**), and sometimes complete arc-shaped calcification. If the lesion is mainly cystic, most of the cyst is not strengthened, and a few solid parts inside are obviously strengthened, which are distributed in the low-density liquid tissue in the form of sheets, forming the so-called "floating cloud sign" (**Figure 10**). The surrounding envelope is obviously enhanced. In the case of a cystic solid structure, the solid part of the arterial phase is mostly papillary or wall nodular enhancement. For the solid structure, the solid part of the arterial phase is slightly enhanced, and the parenchymal and delayed phases are further strengthened, showing progressive filling, but both are lower than the degree of pancreatic parenchymal enhancement.

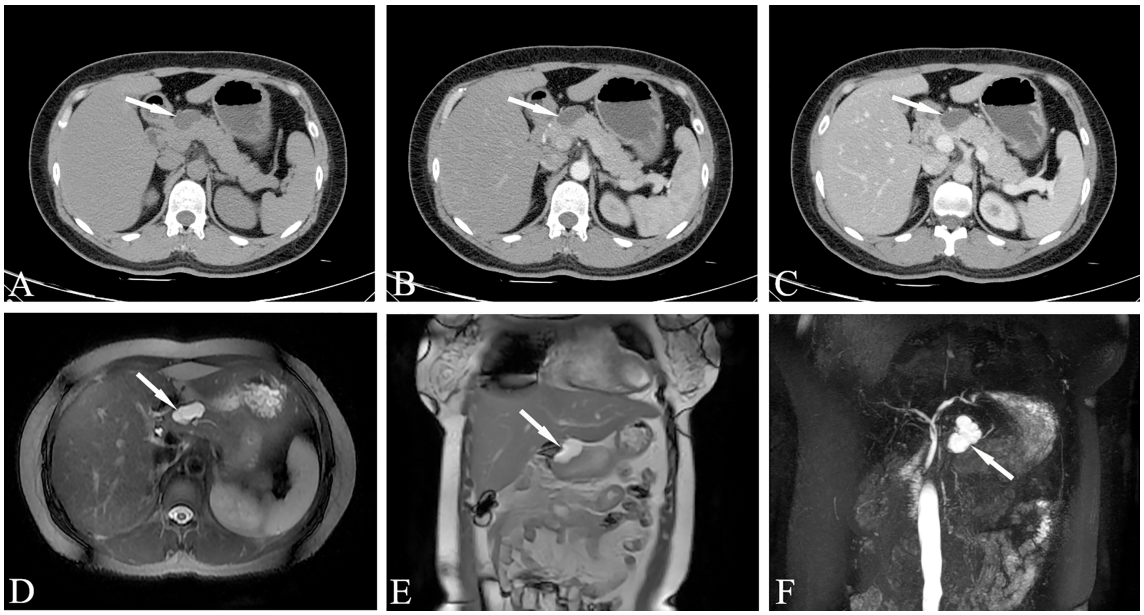

FIGURE 7 | Serous oligocystic adenoma, SOA (Female, 39y, physical examination revealed a pancreatic mass for two weeks). **(A–C)** The CT plain scan, arterial phase and venous phase at the same level; **(D)** T_2-weighted cross-sectional image; **(E)**. T_2-weighted coronal image; **(F)** MRCP reconstruction map; **(A–C)** Low-density cystic mass in the neck of the pancreas with clear boundary and uniform density, no enhancement on dynamic contrast enhancement phase. **(D–F)** Magnetic resonance fat suppression T_2WI showed a small cyst and a thin-walled separation next to the large cyst, and no signs of pancreatic duct dilatation. The white arrows in the Figures only indicate the location of the neoplasm.

For larger lesions, where cystic and solid lesions are often the main focus, the cystic component is not enhanced after enhancement, and the solid and cystic structures are clearly demarcated. Note that the pancreatic tissue has a "cup-mouth" boundary (**Figure 10**). Although the lesion is sometimes large, the MPD or CBD is generally not dilated. In a few cases, it may be slightly dilated, usually due to tumor compression of the adjacent duct. MRCP shows expansion of the MPD more intuitively than MDCT. A larger SPT can cause compression of adjacent blood vessels in the portal vein, splenic vein, inferior vena cava, and renal vein.

The MRI scan of SPN showed tumors with mixed signals on T_1WI and T_2WI and slightly hyper-intensity on DWI. The basis for the confounding of tumor signals is the tumor's cystic degeneration, necrosis, hemorrhage and calcification. MRI is more sensitive to the detection of tumor hemorrhage than CT. Usually, hemorrhage MRI shows a hyper-intensity on T_1WI and a hyper- or hypo-intensity on T_2WI. Due to the coexistence of blood and other liquid components, signs of stratification can be seen, showing liquid levels. MRCP helps to show dilatation of the pancreaticobiliary duct.

Endoscopic Ultrasound With Fine-Needle Aspiration

Recently, EUS has been recognized as an essential diagnostic tool for PCN management. When the results of the radiological diagnosis of malignant tumors are certain and/or when the PCNs are considered to have clinical or radiological characteristics, EUS is nominated as a second-line examination method after CT/MRI. Because the stomach and pancreas are adjacent to each other in the body, the EUS transducer can be placed close to the pancreas, and the gland can be clearly imaged. In this way, the pancreatic cyst wall and its contents can be evaluated in detail, and internal septae and solid areas within the cysts can be differentiated.

One study (77) showed that EUS is the best diagnostic method for differentiating nonneoplastic cysts and PCNs and to characterize PCNs, being superior to both CT and MRI. However, another large multicenter study reported the opposite result: the accuracy of applying EUS to diagnose mucinous versus nonmucinous cysts was only 51% (16). It is speculated that one of the limitations of EUS may be due to different interpretations among endoscopists. Another study revealed that the accuracy of detecting neoplasms with malignant potential ranged from 40% to 93% among 8 different endoscopists invited to interpret the same EUS procedure (78).

Making an accurate diagnosis with cross-sectional imaging and EUS alone is challenging, so EUS-FNA (fine needle aspiration) is frequently employed to obtain a cyst aspirate. Cyst fluid cytology suffers from poor sensitivity, which is specific. During EUS, various analyses (cytology, biochemistry and molecular) of pancreatic cyst fluid acquired from FNA can observably increase the accuracy of diagnosis (1, 16, 79). In terms of the rate of correct diagnosis, EUS-FNA increased the accuracy by 36% after CT and the accuracy by 54% after MRI (80). The risk of infection, hemorrhage, and pancreatitis of EUS-FNA

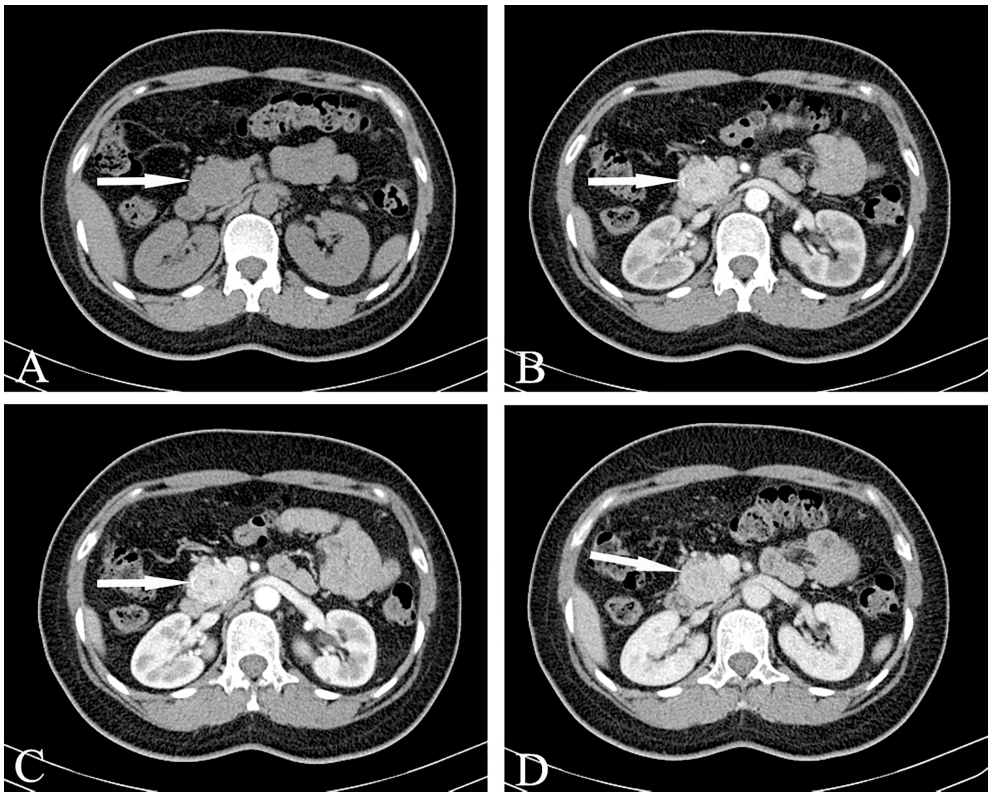

FIGURE 8 | Solid serous cystadenomas, SSCA (Female, 43y, physical examination revealed a pancreatic mass for three weeks). **(A–D)** The CT plain scan, arterial phase, portal and venous phase at the same level; **(A)** The CT plain scan showed a solid mass in the head of the pancreas, with a CT value of about 31HU. **(B)** In the arterial phase, the mass of the pancreatic head was obviously enhanced, with a CT value of about 123HU. The focal low enhancement area can be seen in the center. **(C)** In the portal phase, the neoplasm showed progressive significantly enhancement, at this time, the CT value was 163HU; **(D)** The contrast wash-out can be seen in the venous phase of the mass, with a CT value of about 120HU. The overall manifestation was solid tumor with rich blood supply of pancreas. The white arrows in the Figures only indicate the location of the neoplasm.

increases compared to noninvasive imaging, while most studies have shown that its benefits outweigh the risks (81, 82).

Cytology

EUS-FNA is a commonly used method of diagnosing IPMNs. However, the interpretation of cytological features relies on clinical and radiological findings. The presence of large amounts of thick mucin in the correct clinical setting can only suggest a diagnosis of IPMN. In contrast, it is difficult to distinguish the presence of limited mucin and low-grade mucinous epithelium from the presence of normal gastric epithelium (4). Compared with low-grade IPMN, the following features are more supportive of differentiating HGD IPMN: background of necrosis, aberrant chromatin patterns (hypochromasia or hyperchromasia), the presence of large vacuole single cells, significant nuclear irregularities, increased nuclear-plasmic ratio, and small cell sizes (≤12 μm duodenal cell) (83). Furthermore, The high-grade atypia of IPMNs tend to be larger (≥30 mm), have enhanced mural nodules (≥5 mm) (84) or have solid contents and dilated MPD (≥5 mm) (85).

Differentiating between IPMN and MCN is also difficult for cytopathologists. Due to involvement with the pancreatic duct observed with IPMN but not MCN, correlation with radiologic findings can significantly facilitate diagnosis compared to others. At the same time, mucinous cystic tumors develop almost entirely in females, and presence of an ovarian stroma is pathognomonic. Aspirates of low-grade MCNs (mucinous cystic adenomas) that account for more than 75% of MCNs will show honeycomb sheets of bland mucin-containing epithelium but often lack the presence of complex papillary architecture compared to high-grade MCNs (4). The mucin-containing nucleus has a smooth contour, fine chromatin, and inconspicuous nucleoli (86).

EUS with FNA for SCNs has both low specificity and sensitivity, SCNs usually contain hemosiderin-laden macrophages and paucicellular cells with clear or hemorrhagic backgrounds. The highly vascularized fibrous septa of the SCN leads to the hemorrhagic nature of these specimens. SCNs do not involvement with the PD system and have low CEA levels, with cysts are often filled of clear-yellow serous fluid with low viscosity, compared with IPMNs. The cells of SCNs are bland. The nucleus is round, and the contour is smooth. Chromatin is evenly distributed in the nucleus, and the nucleoli are inconspicuous. When the background contains mucin,

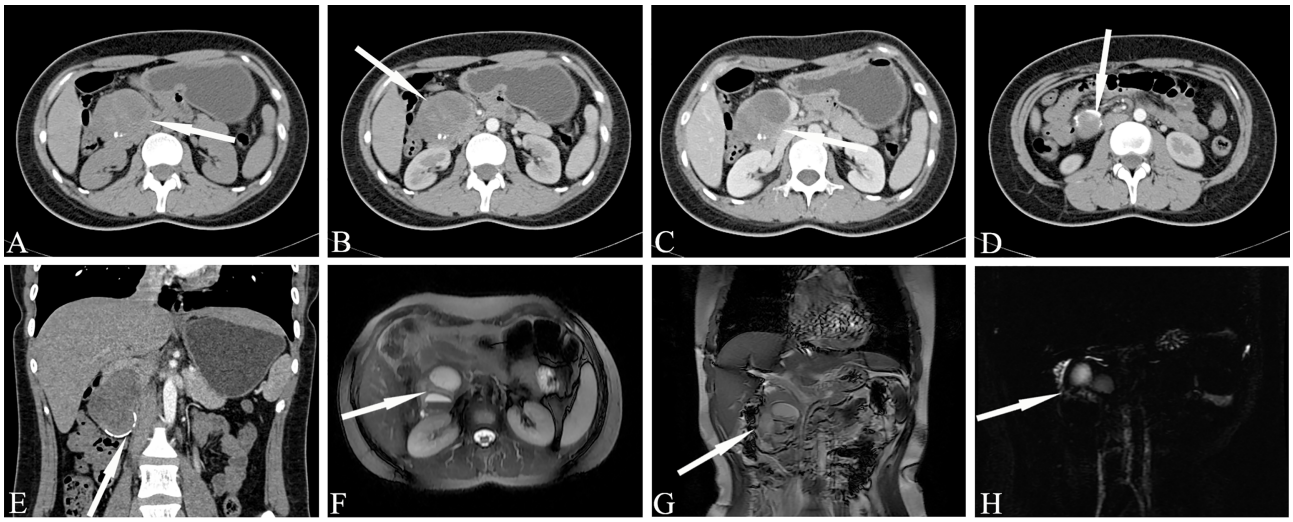

FIGURE 9 | Solid pseudopapillary neoplasm, SPN (Female, 28y, physical examination revealed a pancreatic mass for a week). **(A–C)** The CT plain scan, arterial phase and venous phase at the same level; **(D)** Coronal image in arterial phase. **(E)** Arterial phase cross-sectional image at another level of the same patient. **(F)**. T_2-weighted cross-sectional image; **(G)** T_2-weighted coronal image; **(H)**. MRCP reconstruction map; **(A)** The CT plain scan showed a low-density mass in the head of the pancreas with cystic degeneration. Calcification was visible in the mass. **(B–E)** The solid component reinforcement was not obvious. The incomplete arc-shaped calcification of the envelope can be seen. **(F–H)** MRI shows old hemorrhagic signal with fluid-fluid level. There were no signs of pancreatic duct dilatation. The white arrows in the Figures only indicate the location of the neoplasm.

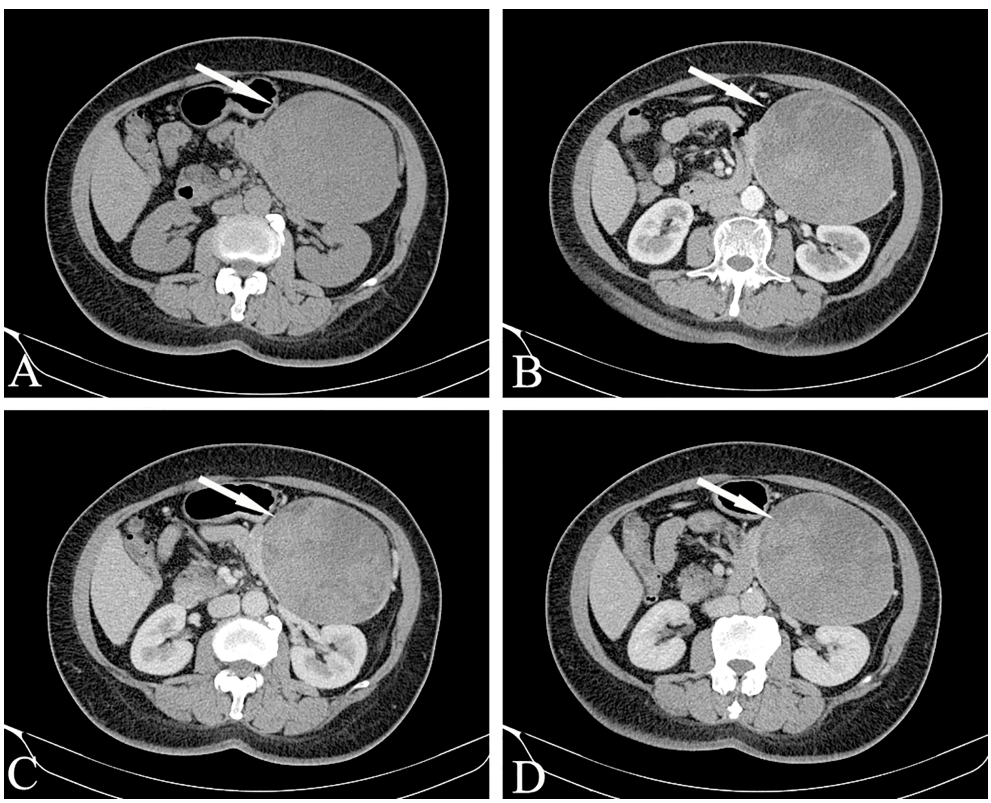

FIGURE 10 | Solid pseudopapillary neoplasm, SPN (Female, 58y, physical examination revealed a pancreatic mass for one month). **(A–D)** The CT plain scan, arterial phase, portal phase and venous phase at the same level. The lesions are large in size, with cystic and solid components visible inside. The cystic part is not enhanced, but the internal solid components are enhanced and distributed in patches in low-density liquid tissue, showing the "floating cloud sign". Besides, note that the pancreatic tissue had a "cup-mouth" boundary. The white arrows in the Figures only indicate the location of the neoplasm.

associate with CEA levels and radiologic imaging would be cautiously exclude MCN. Macroscopically, SCNs are usually arranged around star-shaped scars, which show cysts with a distinctive spongy or honeycomb appearance.

The contents of hypercellular smears shown by EUS-guided FNA of SPTs include slender papillary fragments with fibrous vascular stalks and perivascular myxoid matrix. They are arranged by monomorphic cubic cells into cohesive groups and isolated cells. The neoplastic cells are round to oval, and the cytoplasmic boundary was unclear. The nucleus is grooved or bean-shaped, while the chromatin is fine-grained, and occasionally invisible or small nucleoli can be seen. Macroscopically, SPNs are large, with round to oval shapes, clear margin and fibrous pseudocapsules. SPNs are complex neoplasms with varies components (e.g., solid, cystic, hemorrhagic, and necrotic). Cystic degeneration is a common phenomenon that occurs during progression. Moreover, the larger the neoplasm is, the more obvious the cystic component (45, 87).

Tumor Markers

Studies have shown that pancreatic cyst fluid analysis of tumor markers and molecular markers can help characterize PCNs. At present, perfect biomarker testing for detecting pancreatic tumor has not yet been developed. The most commonly used blood test to monitor and detect pancreatic cancer is the serum marker CA 19-9. However, its sensitivity is limited, especially for small malignancies (88). When CEA levels > 192 ng/mL, the sensitivity and specificity of the diagnosis of mucus lesions are 73% and 84%, respectively (16). Negative and positive predictive values for mucin etiology are both 94% when CEA levels <5 ng/mL or >800 ng/mL (17). The utilization of CEA using pancreatic cyst fluid to diagnose malignant cysts is less effective, as a previous meta-analysis suggested that both the diagnostic sensitivity and the specificity were 63% (89). Chemical analysis of liquid CEA and amylase levels may be helpful, but this approach cannot differentiate between MCNs and IPMNs. Elevated CEA can be used as a marker to distinguish between mucinous and non-mucinous cysts rather than benign or malignant cysts. When the critical value of CEA was ≥192~200 ng/mL, the accuracy increased to 80% for the diagnosis of mucinous cysts, showing high specificity but low sensitivity (16).

The current view is that serous cystic adenomas originate from centroacinar cells, where staining for cytokeratins and calretinin is positive but staining for CEA, mucin, estrogen receptors, and progesterone receptors is negative. SCN and ductal adenocarcinoma and neuroendocrine tumors can be distinguished by inhibin and calcarein, which were found to be helpful immunostaining markers in recent studies (90, 91).

Molecular Markers

To compensate for the limitations posed by cytology and tumor markers, specific molecular markers for diagnosing PCNs and predicting malignant tumors are currently being developed. A molecular DNA analysis method for pancreatic cyst fluid is currently on the market. However, a molecular analysis method for cyst fluid is still in development. KRAS mutations support the diagnosis of mucous cysts more accurately, but KRAS does not always indicate a malignant cyst. It may be helpful to use GNAS mutations to differentiate between obvious mucinous cysts and indolent cysts that can be managed conservatively (92). Genetic analysis showed that the dual mutations in KRAS and GNAS were highly specific for IPMN. Compared with MCNs and SCN (lack GNAS codon 201 mutations), several research found that mutations in GNAS codon 201 are present in some IPMNs (41%-66%) and can even reach 74% to 100% in enteric IPMN (18–20).

With the aim of distinguishing MCNs from other PCNs, such as IPMN and SPN, some research have revealed that MCN is a kind of cystic neoplasm without the GNAS mutation and generally without the CTNNB1 mutation (21). KRAS mutations have been reported in MCNs (50%-75%) (19, 21). In serous cystadenomas, the absence of CTNNB1 mutation can be used to distinguish them from SPNs. In addition, KRAS and GNAS mutations are often expressed in IPMNs and MCNs rather than SCNs. There are a few studies of protein expression in SCAs. VEGF is a protein inhibited by a kind of tumor suppressor that is usually encoded by the VHL gene. In cysts or pancreatic duct fluid, VEGF-A levels can aid in diagnosis. The sensitivity and specificity for diagnosing SCAs were 100% and 97%, respectively, when VEGF-A levels were > 8500 pg/mL and 100% and 90%, respectively, when VEGF-C levels were > 200 pg/mL (22). Combining both VEGF-A and VEGF-C provides 100% sensitivity and specificity for the diagnosis of SCA. In addition, VEGF-A (using a critical value of >5000 pg/mL) combined with CEA (<10 ng/mL) can detect SCAs with a sensitivity of 95.5% and a specificity of 100% (93).

Few research have focused on the glycoproteomics of SCAs. The research have shown that SCAs express MUC1 and MUC6 instead of MUC5AC, which provides proof that SCAs originate from pancreatic central cells and intralebar ducts (23, 24). An extracellular matrix protein implicated in pancreatic cancer called periostin was found to increase 8-fold in SCA cyst fluid compared to mucinous lesions (94). On the other side of the shield, serous cystadenomas are related to von Hippel Lindau (VHL) syndrome, while mutations in the VHL gene are present in all SCAs in patients with VHL syndrome. VHL loss-of-function mutations may also be reflected in the development of sporadic SCAs (95). The macrocyst (oligocyst) variant is a rare type of SCN with fewer but more numerous cysts and without a stellate central scar (96); solid variant, which is devoid of cysts; and mixed serous-neuroendocrine variant (91).

Studies have been performed to study several proteins related to the above genes in SPN tissue: B-catenin, androgen receptor, lymphoid enhancer-binding factor 1 (LEF1), and transcription factor for immunoglobulin heavy-chain enhancer 3 (TFE3) (25). Among them, B-catenin has a sensitivity of 98.9% and a specificity of 97% for the diagnosis of SPT, which is the most sensitive indicator of diagnosis. The combination of LEF1 and TFE3S increases the sensitivity to 100% but decreases the specificity to 91.9%. Another investigation explored the use of B-catenin to diagnose SPT, reporting a 100% sensitivity and 87% specificity (26). The combined application of B-catenin, TEF3, and SOX11 can be used to distinguish SPN, with a sensitivity and specificity of 97%. These tissue findings are also relevant for

EUS-FNA biopsy samples (27). The absence of KRAS, GNAS, or RNF43 can distinguish SPTs from other PCNs. Because of the good prognosis of SPNs, complete resection of these inert neoplasms can be cured.

THE MANAGEMENT OF PCNS

Because of the significant overlap in the morphology of benign and premalignant lesions, characterizing and managing PCN poses a substantial dilemma for the clinical arena. However, compared with clinical and radiological suspicion, the patients are the most important parameter leading to clinical decision-making in surgery treatment. Patients fitness for surgery are continuous variable that should be considered in terms of age, life expectancy, health status, degree of frailty, patient preference, motivation for surgery, and availability of benefit. This parameter is crucial because the overall malignancy rate of PCNs is low. Each patient should be carefully evaluated by clinicians according to the patient's own situation after adequate consultation. Another significant factor in the final decision is the surgery type, as pancreaticoduodenectomy and distal pancreatectomy have different responsibilities in terms of morbidity, mortality, and sequelae.

There are two aspects that should guide the management of IPMN (1): whether the IPMN is malignant and (2) whether the IPMN will become malignant during a patient's lifetime. Clinicians still face the problem of detecting the presence of a malignancy in IPMN and determining its future malignant potential (97). According to the 2012 international consensus guidelines (44), surveillance of BD-type IPMN without "high-risk stigmata" was recommended based on the size stratification. On the basis of American Gastroenterological Association Institute guidelines, patients with pancreatic cysts <3 cm without a solid component or a dilated pancreatic duct should undergo MRI at 1 year. If there is no change in size or characteristics, they should undergo MRI every 2 years afterward for a total of 5 years (70).

In the last 20 years, management recommendations for patients with IPMN have changed dramatically along with advances in our knowing of the natural history of this neoplasm. The reason for this evolution is that various studies have identified clinical, imaging and biologic predictors that may correctly distinguish IPMN with HGD and IC. Models with remarkable accuracy are being developed by combining clinical and imaging characteristics with promising cyst fluid markers. Given the relative rarity of this disease, enhancing constant international collaboration is necessary to successfully obtain a prevention strategy to reduce the incidence of pancreatic cancer arising from IPMN. Patients who have suspected findings but without absolute indications for surgery should undergo CE-EUS. For patients in whom it has been difficult to confirm malignancy under endoscopy, further development of the disease should be closely monitored by MRI/MRCP, tumor markers, and CE-EUS. Once an SCN is detected, then the focus should be excision and long-term monitoring based on questions surrounding symptoms of local growth and progression, not cancer development.

If patients are doubted of having IPMNS, MCNs, and SPTs, appropriate lymphadenectomy and negative resection margins based on intraoperative frozen section assessment should be considered during surgical resection to completely remove the tumor. Given that the disease is usually malignant, parenchyma-sparing pancreatectomy is not a safe procedure for whole PCN cases. Overall, it should be considered only for selected cases or for SCNs.

However, it has not been demonstrated that prolonged follow-up reduces cancer-related mortality, but all these studies revealed that cyst stability over 5y does not exclude the risk of future progression to pancreatic cancer, and thus, there is a lifelong risk of malignancy. Therefore, follow-up should be continued due to the importance of repeated observations for risk stratification. Currently, several follow-up schedules have been suggested in the current guidelines (92, 98); unfortunately, none of these schedules have been shown to be highly cost-effective. In general, the authors recommend that MRI/MRCP and oncological markers should be followed-up every 6 months for the 1st year in the absence of the suspicious features mentioned above. In the absence of progression, it is necessary to maintain follow-up with MRI/MRCP and serum markers for 12 or 18 months.

CONCLUSIONS

In recent years, the incidence of PCLs, especially PCNs, has increased daily. Due to the particularity of its anatomical location, the complexity of endocrine function, the diversity of pathological types, and the unsatisfactory prognosis, clinicians have become a great concern. The key issue is early diagnosis and early treatment, so the imaging diagnosis of pancreatic cystic tumors shows important value in diagnosis. The accuracy of preoperative imaging diagnosis is essential to improve clinicians' confidence in surgery and individualized management. In conclusion, we hope that in the future, imaging biomarkers can be used along with histopathology to provide greater theoretical support for the precise treatment of tumor patients.

AUTHOR CONTRIBUTIONS

FH and YH are the co-first authors of this paper and have contributed equally to this work. WP and TT are the co-corresponding authors. They are responsible for the quality of the review. All authors made substantial contributions to all of the following: (1) the conception and design of the study, or acquisition of data, or analysis and interpretation of data, (2) drafting the article or revising it critically for important intellectual content, (3) final approval of the version to be submitted. Publication is approved by all authors. There are no conflicts of interests associated with this work.

FUNDING

The research was supported by the National Natural Science Foundation of China (No. 81971687/No. 81801702)

REFERENCES

1. van Huijgevoort N, Del CM, Wolfgang CL, van Hooft JE, Besselink MG. Diagnosis and Management of Pancreatic Cystic Neoplasms: Current Evidence and Guidelines. *Nat Rev Gastroenterol Hepatol* (2019) 16:676–89. doi: 10.1038/s41575-019-0195-x
2. Mamone G, Barresi L, Tropea A, Di Piazza A, Miraglia R. MRI of Mucinous Pancreatic Cystic Lesions: A New Updated Morphological Approach for The Differential Diagnosis. *Updates Surg* (2020) 72:617–37. doi: 10.1007/s13304-020-00800-y
3. Perri G, Marchegiani G, Frigerio I, Dervenis CG, Conlon KC, Bassi C, et al. Management of Pancreatic Cystic Lesions. *Dig Surg* (2020) 37:1–9. doi: 10.1159/000496509
4. Abdelkader A, Hunt B, Hartley CP, Panarelli NC, Giorgadze T. Cystic Lesions of the Pancreas: Differential Diagnosis and Cytologic-Histologic Correlation. *Arch Pathol Lab Med* (2020) 144:47–61. doi: 10.5858/arpa.2019-0308-RA
5. Dalal V, Carmicheal J, Dhaliwal A, Jain M, Kaur S, Batra SK. Radiomics in Stratification of Pancreatic Cystic Lesions: Machine Learning in Action. *Cancer Lett* (2020) 469:228–37. doi: 10.1016/j.canlet.2019.10.023
6. Keegan MJ, Paranandi B. Diagnosis and Management of Pancreatic Cystic Neoplasms. *Frontline Gastroenterol* (2019) 10:300–8. doi: 10.1136/flgastro-2018-101122
7. Yoon WJ, Brugge WR. Pancreatic Cystic Neoplasms: Diagnosis and Management. *Gastroenterol Clin North Am* (2012) 41:103–18. doi: 10.1016/j.gtc.2011.12.016
8. Brugge WR, Lauwers GY, Sahani D, Fernandez-del CC, Warshaw AL. Cystic Neoplasms of the Pancreas. *N Engl J Med* (2004) 351:1218–26. doi: 10.1056/NEJMra031623
9. Kearns M, Ahmad NA. Diagnosis and Management of Pancreatic Cystic Neoplasms. *Curr Treat Options Gastroenterol* (2017) 15:587–602. doi: 10.1007/s11938-017-0162-y
10. Pezzilli R, Buscarini E, Pollini T, Bonamini D, Marchegiani G, Crippa S, et al. Epidemiology, Clinical Features and Diagnostic Work-Up of Cystic Neoplasms of the Pancreas: Interim Analysis of the Prospective PANCY Survey. *Dig Liver Dis* (2020) 52:547–54. doi: 10.1016/j.dld.2020.02.003
11. Distler M, Kersting S, Niedergethmann M, Aust DE, Franz M, Rückert F, et al. Pathohistological Subtype Predicts Survival in Patients With Intraductal Papillary Mucinous Neoplasm (IPMN) of the Pancreas. *Ann Surg* (2013) 258:324–30. doi: 10.1097/SLA.0b013e318287ab73
12. Testini M, Gurrado A, Lissidini G, Venezia P, Greco L, Piccinni G. Management of Mucinous Cystic Neoplasms of the Pancreas. *World J Gastroenterol* (2010) 16:5682–92. doi: 10.3748/wjg.v16.i45.5682
13. Sakorafas GH, Smyrniotis V, Reid-Lombardo KM, Sarr MG. Primary Pancreatic Cystic Neoplasms Revisited: Part II. Mucinous Cystic Neoplasms. *Surg Oncol* (2011) 20:e93–101. doi: 10.1016/j.suronc.2010.12.003
14. Wang GX, Wang ZP, Chen HL, Zhang D, Wen L. Discrimination of Serous Cystadenoma From Mucinous Cystic Neoplasm and Branch Duct Intraductal Papillary Mucinous Neoplasm in the Pancreas With CT. *Abdom Radiol (NY)* (2020) 45:2772–8. doi: 10.1007/s00261-020-02664-7
15. Chandwani R, Allen PJ. Cystic Neoplasms of the Pancreas. *Annu Rev Med* (2016) 67:45–57. doi: 10.1146/annurev-med-051914-022011
16. Brugge WR, Lewandrowski K, Lee-Lewandrowski E, Centeno BA, Szydlo T, Regan S, et al. Diagnosis of Pancreatic Cystic Neoplasms: A Report of the Cooperative Pancreatic Cyst Study. *Gastroenterology* (2004) 126:1330–6. doi: 10.1053/j.gastro.2004.02.013
17. van der Waaij LA, van Dullemen HM, Porte RJ. Cyst Fluid Analysis in the Differential Diagnosis of Pancreatic Cystic Lesions: A Pooled Analysis. *Gastrointest Endosc* (2005) 62:383–9. doi: 10.1016/s0016-5107(05)01581-6
18. Lee LS, Doyle LA, Houghton J, Sah S, Bellizzi AM, Szafranska-Schwarzbach AE, et al. Differential Expression of GNAS and KRAS Mutations in Pancreatic Cysts. *JOP* (2014) 15:581–6. doi: 10.6092/1590-8577/2432
19. Wu J, Matthaei H, Maitra A, Dal Molin M, Wood LD, Eshleman JR, et al. Recurrent GNAS Mutations Define an Unexpected Pathway for Pancreatic Cyst Development. *Sci Transl Med* (2011) 3:66r–92r. doi: 10.1126/scitranslmed.3002543
20. Furukawa T, Kuboki Y, Tanji E, Yoshida S, Hatori T, Yamamoto M, et al. Whole-Exome Sequencing Uncovers Frequent GNAS Mutations in Intraductal Papillary Mucinous Neoplasms of the Pancreas. *Sci Rep* (2011) 1:161. doi: 10.1038/srep00161
21. Springer S, Wang Y, Dal Molin M, Masica DL, Jiao Y, Kinde I, et al. A Combination of Molecular Markers and Clinical Features Improve the Classification of Pancreatic Cysts. *Gastroenterology* (2015) 149:1501–10. doi: 10.1053/j.gastro.2015.07.041
22. Yip-Schneider MT, Wu H, Dumas RP, Hancock BA, Agaram N, Radovich M, et al. Vascular Endothelial Growth Factor, a Novel and Highly Accurate Pancreatic Fluid Biomarker for Serous Pancreatic Cysts. *J Am Coll Surg* (2014) 218:608–17. doi: 10.1016/j.jamcollsurg.2013.12.019
23. Kosmahl M, Wagner J, Peters K, Sipos B, Klöppel G. Serous Cystic Neoplasms of the Pancreas: An Immunohistochemical Analysis Revealing Alpha-Inhibin, Neuron-Specific Enolase, and MUC6 as New Markers. *Am J Surg Pathol* (2004) 28:339–46. doi: 10.1097/00000478-200403000-00006
24. Reid MD, Choi H, Balci S, Akkas G, Adsay V. Serous Cystic Neoplasms of the Pancreas: Clinicopathologic and Molecular Characteristics. *Semin Diagn Pathol* (2014) 31:475–83. doi: 10.1053/j.semdp.2014.08.009
25. Kim EK, Jang M, Park M, Kim H. LEF1, TFE3, and AR are Putative Diagnostic Markers of Solid Pseudopapillary Neoplasms. *Oncotarget* (2017) 8:93404–13. doi: 10.18632/oncotarget.21854
26. Harrison G, Hemmerich A, Guy C, Perkinson K, Fleming D, McCall S, et al. Overexpression of SOX11 and TFE3 in Solid-Pseudopapillary Neoplasms of the Pancreas. *Am J Clin Pathol* (2017) 149:67–75. doi: 10.1093/ajcp/aqx142
27. Foo WC, Harrison G, Zhang X. Immunocytochemistry for SOX-11 and TFE3 as Diagnostic Markers for Solid Pseudopapillary Neoplasms of the Pancreas in FNA Biopsies. *Cancer Cytopathol* (2017) 125:831–7. doi: 10.1002/cncy.21931
28. Castellano-Megías VM, Andrés CI, López-Alonso G, Colina-Ruizdelgado F. Pathological Features and Diagnosis of Intraductal Papillary Mucinous Neoplasm of The Pancreas. *World J Gastrointest Oncol* (2014) 6:311–24. doi: 10.4251/wjgo.v6.i9.311
29. Mino-Kenudson M, Fernández-del CC, Baba Y, Valsangkar NP, Liss AS, Hsu M, et al. Prognosis of Invasive Intraductal Papillary Mucinous Neoplasm Depends on Histological and Precursor Epithelial Subtypes. *Gut* (2011) 60:1712–20. doi: 10.1136/gut.2010.232272
30. Salvia R, Crippa S, Falconi M, Bassi C, Guarise A, Scarpa A, et al. Branch-Duct Intraductal Papillary Mucinous Neoplasms of the Pancreas: To Operate or Not to Operate? *Gut* (2007) 56:1086–90. doi: 10.1136/gut.2006.100628
31. Maguchi H, Tanno S, Mizuno N, Hanada K, Kobayashi G, Hatori T, et al. Natural History of Branch Duct Intraductal Papillary Mucinous Neoplasms of the Pancreas: A Multicenter Study in Japan. *Pancreas* (2011) 40:364–70. doi: 10.1097/MPA.0b013e31820a5975
32. Rodriguez JR, Salvia R, Crippa S, Warshaw AL, Bassi C, Falconi M, et al. Branch-Duct Intraductal Papillary Mucinous Neoplasms: Observations in 145 Patients Who Underwent Resection. *Gastroenterology* (2007) 133:72–9, 309-10. doi: 10.1053/j.gastro.2007.05.010
33. Yamada S, Fujii T, Murotani K, Kanda M, Sugimoto H, Nakayama G, et al. Comparison of the International Consensus Guidelines for Predicting Malignancy in Intraductal Papillary Mucinous Neoplasms. *Surgery* (2016) 159:878–84. doi: 10.1016/j.surg.2015.08.042
34. Maire F, Hammel P, Terris B, Paye F, Scoazec JY, Cellier C, et al. Prognosis of Malignant Intraductal Papillary Mucinous Tumours of the Pancreas After Surgical Resection. Comparison With Pancreatic Ductal Adenocarcinoma. *Gut* (2002) 51:717–22. doi: 10.1136/gut.51.5.717
35. Heckler M, Brieger L, Heger U, Pausch T, Tjaden C, Kaiser J, et al. Predictive Performance of Factors Associated With Malignancy in Intraductal Papillary Mucinous Neoplasia of the Pancreas. *BJS Open* (2018) 2:13–24. doi: 10.1002/bjs5.38
36. Konstantinou F, Syrigos KN, Saif MW. Intraductal Papillary Mucinous Neoplasms of the Pancreas (IPMNs): Epidemiology, Diagnosis and Future Aspects. *JOP* (2013) 14:141–4. doi: 10.6092/1590-8577/1467
37. Bojanapu S, Kasi A. Pancreatic Mucinous Cystadenoma. (2022).
38. Yeh MM, Tang LH, Wang S, Robert ME, Zheng W, Jain D. Inhibin Expression in Ovarian-Type Stroma in Mucinous Cystic Neoplasms of the Pancreas. *Appl Immunohistochem Mol Morphol* (2004) 12:148–52. doi: 10.1097/00129039-200406000-00009
39. Lennon AM, Wolfgang C. Cystic Neoplasms of the Pancreas. *J Gastrointest Surg* (2013) 17:645–53. doi: 10.1007/s11605-012-2072-6

40. Levy MJ. Pancreatic Cysts. *Gastrointest Endosc* (2009) 69:S110–6. doi: 10.1016/j.gie.2008.12.011
41. Gress F, Gottlieb K, Cummings O, Sherman S, Lehman G. Endoscopic Ultrasound Characteristics of Mucinous Cystic Neoplasms of the Pancreas. *Am J Gastroenterol* (2000) 95:961–5. doi: 10.1111/j.1572-0241.2000.01976.x
42. Garces-Descovich A, Beker K, Castillo-Angeles M, Brook A, Resnick E, Shinagare S, et al. Mucinous Cystic Neoplasms of the Pancreas: High-Resolution Cross-Sectional Imaging Features With Clinico-Pathologic Correlation. *Abdom Radiol (NY)* (2018) 43:1413–22. doi: 10.1007/s00261-017-1326-x
43. Bai XL, Zhang Q, Masood N, Masood W, Zhang Y, Liang TB. Pancreatic Cystic Neoplasms: A Review of Preoperative Diagnosis and Management. *J Zhejiang Univ Sci B* (2013) 14:185–94. doi: 10.1631/jzus.B1200283
44. Tanaka M, Fernández-del CC, Adsay V, Chari S, Falconi M, Jang JY, et al. International Consensus Guidelines 2012 for the Management of IPMN and MCN of the Pancreas. *Pancreatology* (2012) 12:183–97. doi: 10.1016/j.pan.2012.04.004
45. Papavramidis T, Papavramidis S. Solid Pseudopapillary Tumors of the Pancreas: Review of 718 Patients Reported in English Literature. *J Am Coll Surg* (2005) 200:965–72. doi: 10.1016/j.jamcollsurg.2005.02.011
46. Ren Z, Zhang P, Zhang X, Liu B. Solid Pseudopapillary Neoplasms of the Pancreas: Clinicopathologic Features and Surgical Treatment of 19 Cases. *Int J Clin Exp Pathol* (2014) 7:6889–97.
47. Law JK, Ahmed A, Singh VK, Akshintala VS, Olson MT, Raman SP, et al. A Systematic Review of Solid-Pseudopapillary Neoplasms: Are These Rare Lesions? *Pancreas* (2014) 43:331–7. doi: 10.1097/MPA.0000000000000061
48. Yao J, Song H. A Review of Clinicopathological Characteristics and Treatment of Solid Pseudopapillary Tumor of the Pancreas With 2450 Cases in Chinese Population. *BioMed Res Int* (2020) 2020:2829647. doi: 10.1155/2020/2829647
49. Jutric Z, Rozenfeld Y, Grendar J, Hammill CW, Cassera MA, Newell PH, et al. Analysis of 340 Patients With Solid Pseudopapillary Tumors of the Pancreas: A Closer Look at Patients With Metastatic Disease. *Ann Surg Oncol* (2017) 24:2015–22. doi: 10.1245/s10434-017-5772-z
50. Reddy S, Cameron JL, Scudiere J, Hruban RH, Fishman EK, Ahuja N, et al. Surgical Management of Solid-Pseudopapillary Neoplasms of the Pancreas (Franz or Hamoudi Tumors): A Large Single-Institutional Series. *J Am Coll Surg* (2009) 208:950–7, 957-9. doi: 10.1016/j.jamcollsurg.2009.01.044
51. Dababneh Y, Mousa OY. Pancreatic Serous Cystadenoma. (2022).
52. George DH, Murphy F, Michalski R, Ulmer BG. Serous Cystadenocarcinoma of the Pancreas: A New Entity? *Am J Surg Pathol* (1989) 13:61–6. doi: 10.1097/00000478-198901000-00009
53. Jais B, Rebours V, Malleo G, Salvia R, Fontana M, Maggino L, et al. Serous Cystic Neoplasm of the Pancreas: A Multinational Study of 2622 Patients Under The Auspices of the International Association of Pancreatology and European Pancreatic Club (European Study Group on Cystic Tumors of the Pancreas). *Gut* (2016) 65:305–12. doi: 10.1136/gutjnl-2015-309638
54. Chu LC, Singhi AD, Haroun RR, Hruban RH, Fishman EK. The Many Faces of Pancreatic Serous Cystadenoma: Radiologic and Pathologic Correlation. *Diagn Interv Imaging* (2017) 98:191–202. doi: 10.1016/j.diii.2016.08.005
55. Jederán É. Importance of Conventional Pancreas Imaging: Ultrasound, CT, and MRI. Facts and Possibilities. *Magy Onkol* (2021) 65:237–49.
56. Harrington KA, Shukla-Dave A, Paudyal R, Do R. MRI of the Pancreas. *J Magn Reson Imaging* (2021) 53:347–59. doi: 10.1002/jmri.27148
57. Wang G, Dang H, Yu P, Liu H, Wu Y, Yao S, et al. Multiparameter Analysis Using (18)F-FDG PET/CT in the Differential Diagnosis of Pancreatic Cystic Neoplasms. *Contrast Media Mol Imaging* (2021) 2021:6658644. doi: 10.1155/2021/6658644
58. Chen S, Ren S, Guo K, Daniels MJ, Wang Z, Chen R. Preoperative Differentiation of Serous Cystic Neoplasms From Mucin-Producing Pancreatic Cystic Neoplasms Using a CT-Based Radiomics Nomogram. *Abdom Radiol (NY)* (2021) 46:2637–46. doi: 10.1007/s00261-021-02954-8
59. Wei R, Lin K, Yan W, Guo Y, Wang Y, Li J, et al. Computer-Aided Diagnosis of Pancreas Serous Cystic Neoplasms: A Radiomics Method on Preoperative MDCT Images. *Technol Cancer Res Treat* (2019) 18:1077091987. doi: 10.1177/1533033818824339
60. Sahani DV, Sainani NI, Blake MA, Crippa S, Mino-Kenudson M, Del-Castillo CF. Prospective Evaluation of Reader Performance on MDCT in Characterization of Cystic Pancreatic Lesions and Prediction of Cyst Biologic Aggressiveness. *AJR Am J Roentgenol* (2011) 197:W53–61. doi: 10.2214/AJR.10.5866
61. Dmitriev K, Kaufman AE, Javed AA, Hruban RH, Fishman EK, Lennon AM, et al. Classification of Pancreatic Cysts in Computed Tomography Images Using a Random Forest and Convolutional Neural Network Ensemble. *Med Image Comput Comput Assist Interv* (2017) 10435:150–8. doi: 10.1007/978-3-319-66179-7_18
62. Laffan TA, Horton KM, Klein AP, Berlanstein B, Siegelman SS, Kawamoto S, et al. Prevalence of Unsuspected Pancreatic Cysts on MDCT. *AJR Am J Roentgenol* (2008) 191:802–7. doi: 10.2214/AJR.07.3340
63. Sahani DV, Kambadakone A, Macari M, Takahashi N, Chari S, Fernandez-del CC. Diagnosis and Management of Cystic Pancreatic Lesions. *AJR Am J Roentgenol* (2013) 200:343–54. doi: 10.2214/AJR.12.8862
64. Sahani DV, Kadavigere R, Saokar A, Fernandez-del CC, Brugge WR, Hahn PF. Cystic Pancreatic Lesions: A Simple Imaging-Based Classification System for Guiding Management. *Radiographics* (2005) 25:1471–84. doi: 10.1148/rg.256045161
65. Lin XZ, Wu ZY, Li WX, Zhang J, Xu XQ, Chen KM, et al. Differential Diagnosis of Pancreatic Serous Oligocystic Adenoma and Mucinous Cystic Neoplasm With Spectral CT Imaging: Initial Results. *Clin Radiol* (2014) 69:1004–10. doi: 10.1016/j.crad.2014.05.003
66. Hanania AN, Bantis LE, Feng Z, Wang H, Tamm EP, Katz MH, et al. Quantitative Imaging to Evaluate Malignant Potential of IPMNs. *Oncotarget* (2016) 7:85776–84. doi: 10.18632/oncotarget.11769
67. Permuth JB, Choi J, Balarunathan Y, Kim J, Chen DT, Chen L, et al. Combining Radiomic Features With a miRNA Classifier may Improve Prediction of Malignant Pathology for Pancreatic Intraductal Papillary Mucinous Neoplasms. *Oncotarget* (2016) 7:85785–97. doi: 10.18632/oncotarget.11768
68. Yang J, Guo X, Ou X, Zhang W, Ma X. Discrimination of Pancreatic Serous Cystadenomas From Mucinous Cystadenomas With CT Textural Features: Based on Machine Learning. *Front Oncol* (2019) 9:494:494. doi: 10.3389/fonc.2019.00494
69. Curry CA, Eng J, Horton KM, Urban B, Siegelman S, Kuszyk BS, et al. CT of Primary Cystic Pancreatic Neoplasms: Can CT be Used for Patient Triage and Treatment? *AJR Am J Roentgenol* (2000) 175:99–103. doi: 10.2214/ajr.175.1.1750099
70. Vege SS, Ziring B, Jain R, Moayyedi P. American Gastroenterological Association Institute Guideline on the Diagnosis and Management of Asymptomatic Neoplastic Pancreatic Cysts. *Gastroenterology* (2015) 148:819–22, e12-3. doi: 10.1053/j.gastro.2015.01.015
71. Lee KS, Sekhar A, Rofsky NM, Pedrosa I. Prevalence of Incidental Pancreatic Cysts in the Adult Population on MR Imaging. *Am J Gastroenterol* (2010) 105:2079–84. doi: 10.1038/ajg.2010.122
72. de Jong K, Bruno MJ, Fockens P. Epidemiology, Diagnosis, and Management of Cystic Lesions of the Pancreas. *Gastroenterol Res Pract* (2012) 2012:147465. doi: 10.1155/2012/147465
73. Sandrasegaran K, Lin C, Akisik FM, Tann M. State-Of-the-Art Pancreatic MRI. *AJR Am J Roentgenol* (2010) 195:42–53. doi: 10.2214/ajr.10.4421
74. Lee HJ, Kim MJ, Choi JY, Hong HS, Kim KA. Relative Accuracy of CT and MRI in the Differentiation of Benign From Malignant Pancreatic Cystic Lesions. *Clin Radiol* (2011) 66:315–21. doi: 10.1016/j.crad.2010.06.019
75. Zhu S, Wang WT, Shang XS, Ni T, Wu WC, Lou WH, et al. Difference Analysis in Prevalence of Incidental Pancreatic Cystic Lesions Between Computed Tomography and Magnetic Resonance Imaging. *BMC Med Imaging* (2019) 19:43. doi: 10.1186/s12880-019-0341-5
76. Hoffman DH, Ream JM, Hajdu CH, Rosenkrantz AB. Utility of Whole-Lesion ADC Histogram Metrics for Assessing the Malignant Potential Of Pancreatic Intraductal Papillary Mucinous Neoplasms (IPMNs). *Abdom Radiol (NY)* (2017) 42:1222–8. doi: 10.1007/s00261-016-1001-7
77. Du C, Chai NL, Linghu EQ, Li HK, Sun LH, Jiang L, et al. Comparison of Endoscopic Ultrasound, Computed Tomography and Magnetic Resonance Imaging in Assessment of Detailed Structures of Pancreatic Cystic Neoplasms. *World J Gastroenterol* (2017) 23:3184–92. doi: 10.3748/wjg.v23.i17.3184
78. Ahmad NA, Kochman ML, Brensinger C, Brugge WR, Faigel DO, Gress FG, et al. Interobserver Agreement Among Endosonographers for the Diagnosis of Neoplastic Versus Non-Neoplastic Pancreatic Cystic Lesions. *Gastrointest Endosc* (2003) 58:59–64. doi: 10.1067/mge.2003.298

79. Khalid A, Brugge W. ACG Practice Guidelines for the Diagnosis and Management of Neoplastic Pancreatic Cysts. *Am J Gastroenterol* (2007) 102:2339–49. doi: 10.1111/j.1572-0241.2007.01516.x
80. Khashab MA, Kim K, Lennon AM, Shin EJ, Tignor AS, Amateau SK, et al. Should We do EUS/FNA on Patients With Pancreatic Cysts? The Incremental Diagnostic Yield of EUS Over CT/MRI for Prediction of Cystic Neoplasms. *Pancreas* (2013) 42:717–21. doi: 10.1097/MPA.0b013e3182883a91
81. Lim SJ, Alasadi R, Wayne JD, Rao S, Rademaker A, Bell R, et al. Preoperative Evaluation of Pancreatic Cystic Lesions: Cost-Benefit Analysis and Proposed Management Algorithm. *Surgery* (2005) 138:672–9, 679-80. doi: 10.1016/j.surg.2005.07.033
82. Wang KX, Ben QW, Jin ZD, Du YQ, Zou DW, Liao Z, et al. Assessment of Morbidity and Mortality Associated With EUS-Guided FNA: A Systematic Review. *Gastrointest Endosc* (2011) 73:283–90. doi: 10.1016/j.gie.2010.10.045
83. Pitman MB, Centeno BA, Daglilar ES, Brugge WR, Mino-Kenudson M. Cytological Criteria of High-Grade Epithelial Atypia in the Cyst Fluid of Pancreatic Intraductal Papillary Mucinous Neoplasms. *Cancer Cytopathol* (2014) 122:40–7. doi: 10.1002/cncy.21344
84. Anand N, Sampath K, Wu BU. Cyst Features and Risk of Malignancy in Intraductal Papillary Mucinous Neoplasms of The Pancreas: A Meta-Analysis. *Clin Gastroenterol Hepatol* (2013) 11:913–21.e59-60. doi: 10.1016/j.cgh.2013.02.010
85. Salvia R, Fernández-del CC, Bassi C, Thayer SP, Falconi M, Mantovani W, et al. Main-Duct Intraductal Papillary Mucinous Neoplasms of the Pancreas: Clinical Predictors of Malignancy and Long-Term Survival Following Resection. *Ann Surg* (2004) 239:678–85, 685-7. doi: 10.1097/01.sla.0000124386.54496.15
86. Recine M, Kaw M, Evans DB, Krishnamurthy S. Fine-Needle Aspiration Cytology of Mucinous Tumors of the Pancreas. *Cancer-Am Cancer Soc* (2004) 102:92–9. doi: 10.1002/cncr.20052
87. Santini D, Poli F, Lega S. Solid-Papillary Tumors of the Pancreas: Histopathology. *JOP* (2006) 7:131–6.
88. Goggins M. Molecular Markers of Early Pancreatic Cancer. *J Clin Oncol* (2005) 23:4524–31. doi: 10.1200/JCO.2005.19.711
89. Ngamruengphong S, Bartel MJ, Raimondo M. Cyst Carcinoembryonic Antigen in Differentiating Pancreatic Cysts: A Meta-Analysis. *Dig Liver Dis* (2013) 45:920–6. doi: 10.1016/j.dld.2013.05.002
90. Marsh WL, Colonna J, Yearsley M, Bloomston M, Frankel WL. Calponin is Expressed in Serous Cystadenomas of the Pancreas But Not in Adenocarcinomas or Endocrine Tumors. *Appl Immunohistochem Mol Morphol* (2009) 17:216–9. doi: 10.1097/pai.0b013e31818c1aa6
91. Charville GW, Kao CS. Serous Neoplasms of the Pancreas: A Comprehensive Review. *Arch Pathol Lab Med* (2018) 142:1134–40. doi: 10.5858/arpa.2017-0195-RS
92. Tanaka M, Fernández-Del CC, Kamisawa T, Jang JY, Levy P, Ohtsuka T, et al. Revisions of International Consensus Fukuoka Guidelines for the Management of IPMN of the Pancreas. *Pancreatology* (2017) 17:738–53. doi: 10.1016/j.pan.2017.07.007
93. Carr RA, Yip-Schneider MT, Dolejs S, Hancock BA, Wu H, Radovich M, et al. Pancreatic Cyst Fluid Vascular Endothelial Growth Factor a and Carcinoembryonic Antigen: A Highly Accurate Test for the Diagnosis of Serous Cystic Neoplasm. *J Am Coll Surg* (2017) S1072-7515(17):30452–0. doi: 10.1016/j.jamcollsurg.2017.05.003
94. Gbormittah FO, Haab BB, Partyka K, Garcia-Ott C, Hancapie M, Hancock WS. Characterization of Glycoproteins in Pancreatic Cyst Fluid Using a High-Performance Multiple Lectin Affinity Chromatography Platform. *J Proteome Res* (2014) 13:289–99. doi: 10.1021/pr400813u
95. Mohr VH, Vortmeyer AO, Zhuang Z, Libutti SK, Walther MM, Choyke PL, et al. Histopathology and Molecular Genetics of Multiple Cysts and Microcystic (Serous) Adenomas of the Pancreas in Von Hippel-Lindau Patients. *Am J Pathol* (2000) 157:1615–21. doi: 10.1016/S0002-9440(10)64799-2
96. Basturk O, Coban I, Adsay NV. Pancreatic Cysts: Pathologic Classification, Differential Diagnosis, and Clinical Implications. *Arch Pathol Lab Med* (2009) 133:423–38. doi: 10.5858/133.3.423
97. Baiocchi GL, Molfino S, Frittoli B, Pigozzi G, Gheza F, Gaverini G, et al. Increased Risk of Second Malignancy in Pancreatic Intraductal Papillary Mucinous Tumors: Review of the Literature. *World J Gastroenterol* (2015) 21:7313–9. doi: 10.3748/wjg.v21.i23.7313
98. Chiaro MD, Besselink MG, Scholten L, Bruno MJ, Cahen GL, Gress TM, et al. European Evidence-Based Guidelines on Pancreatic Cystic Neoplasms. *Gut* (2018) 67:789–804. doi: 10.1136/gutjnl-2018-316027

Conflict of Interest: Author PW was employed by GE Healthcare.

The remaining authors declare that the research was conducted in the absence of any commercial or financial relationships that could be construed as a potential conflict of interest.

frontiers | Frontiers in Oncology

ORIGINAL RESEARCH
published: 26 April 2022
doi: 10.3389/fonc.2022.852454

Microbubbles Ultrasonic Cavitation Regulates Tumor Interstitial Fluid Pressure and Enhances Sonodynamic Therapy

Fen Xi[1,2,3], *Yuyi Feng*[2,3], *Qiaoli Chen*[2,3], *Liping Chen*[2,3] *and Jianhua Liu*[1,2,3]*

[1] The First Affiliated Hospital, Jinan University, Guangzhou, China, [2] Department of Ultrasound Medical, Guangzhou First People's Hospital, Guangzhou Medical University, Guangzhou, China, [3] The Second Affiliated Hospital, School of Medicine, South China University of Technology, Guangzhou, China

Sonodynamic therapy (SDT) is a promising treatment method for solid tumors. However, the high interstitial fluid pressure (IFP) in tumor tissues limits the accumulation of sonosensitizers. In the present study, microbubbles ultrasonic cavitation was used to regulate the tumor's IFP and evaluate SDT effects. Rabbit VX2 tumor tissues were treated with microbubbles ultrasonic cavitation. The IFP of different tumor parts before and after cavitation was measured by the WIN method. The accumulation of the sonosensitizers hematoporphyrin monomethyl ether (HMME) in tumor tissues was observed using an ultramicro spectrophotometer and laser confocal microscope. Then, tumor-bearing rabbits were treated with SDT once a week for eight weeks and the therapeutic effect was evaluated. After microbubbles ultrasonic cavitation treatment, the tumor's IFP decreased and the HMME concentration increased. We concluded that microbubbles ultrasonic cavitation can increase HMME accumulation in rabbit VX2 tumors and increase SDT therapeutic effects.

Keywords: ultrasound, microbubbles, cavitation, tumor interstitial fluid pressure, SDT

OPEN ACCESS

Edited by:
Kun Zhang,
Tongji University, China

Reviewed by:
Francesco Prada,
Carlo Besta Neurological Institute Foundation (IRCCS), Italy
Tianqing Liu,
Western Sydney University, Australia

***Correspondence:**
Jianhua Liu
eyliujianhua@scut.edu.cn

Specialty section:
This article was submitted to Cancer Imaging and Image-directed Interventions, a section of the journal Frontiers in Oncology

Received: *11 January 2022*
Accepted: *30 March 2022*
Published: *26 April 2022*

Citation:
Xi F, Feng Y, Chen Q, Chen L and Liu J (2022) Microbubbles Ultrasonic Cavitation Regulates Tumor Interstitial Fluid Pressure and Enhances Sonodynamic Therapy. Front. Oncol. 12:852454. doi: 10.3389/fonc.2022.852454

INTRODUCTION

Tumors cause important diseases threatening to human health, and their treatment methods are still developing, including surgery, chemotherapy alone or in combination, radiotherapy, interventional therapy, microwave ablation, immunotherapy etc. Among them Sonodynamic therapy (SDT) (1) is a new tumor treatment strategy and have advantages such as safety, being non-invasive, and having good targeting and great clinical application prospects. SDT mainly refers to the irradiation of the tumor site with ultrasound of specific frequencies and intensities for a certain time to activate ultrasound-sensitive drugs enriched in tumor tissues. This can significantly enhance drugs' cytotoxicity in the targeted area and specifically kill tumor cells. Compared with photodynamic therapy (PDT), SDT has a deeper tissue penetration. Some studies (2) have shown that after A549 tumor-bearing mice were irradiated with pulsed focused ultrasound (5 W/cm2), the

dense and hard extracellular matrix became loose, collagen fibers were destroyed, and the targeting and penetration of nanoparticles were significantly enhanced.

Hematoporphyrin monomethyl ether (HMME) (3–5) is a second-generation porphyrin sonosensitizer and has advantages such as single composition, stable performance, high tumor selectivity, and low phototoxicity to normal tissues. Its concentration in tumor has an important effect on the therapeutic effect of SDT. In many cases, the delivery of sonosensitizers or specific targeted drugs to tumors uses the vascular system, but many solid tumors have abnormal vascular structures, lymphatic dysfunctions, and extracellular matrix components imbalances, increasing the interstitial fluid pressure (IFP) (6, 7) which is one of the important reasons for the low accumulation of acoustic sensitizers in tumor tissues. In normal tissues (8), the IFP is about -1~3 mmHg (7) but animal and human tumors present higher IFPs (9–11) about 30 mmHg in breast cancer, and even more in cervical cancer, metastatic melanoma, colon cancer liver metastases, head, and neck tumors. At the same time, studies (12) have shown that a high IFP is related to reduced radiotherapy sensitivity and insufficient uptake of chemotherapy drugs. Therefore, Reducing IFP to increase the permeability of HMME in tumor tissue and increase the effective concentration of HMME can be one of the breakthroughs to enhance SDT.

Microbubbles are spheres (diameter 1-10 μm) composed of polymers, proteins, or thin lipid shells filled with inert gas. They have cavitation effects under ultrasonic irradiation, producing shock waves and microjets, which can destroy tumor microvascular structures, damage endothelial cells, and even cause cell lysis (13, 14). Therefore, through ultrasonic cavitation, blood vessels can be destroyed and embolized, tumor cell apoptosis and necrosis induced, tumor cell density reduced, tissue space expanded, and the IFP reduced. In a previous study (15, 16) we established a VX2 transplanted tumor model in the superficial muscle layer of a rabbit left hind limb and selected low-frequency unfocused ultrasounds combined with microbubbles to irradiate the tumor (ultrasound parameters: center frequency 1 MHz; ultrasound pressure 1, 3, and 5 MPa; pulse repetition frequency 10 Hz; duty cycle 0.2%; pulse emission/gap time 9 s/3 s). Results showed that medium-high ultrasound pressure (3 and 5 MPa) and low-frequency unfocused ultrasound irradiation for 5 min decreased the IFP. Lower ultrasound pressure (1 MPa) prolonging the irradiation time for 10 min also led to tumor IFP decrease. Hence, in the present study, we used microbubbles ultrasonic cavitation biological effects to regulate tumors IFP and explore the best therapeutic ultrasound parameters to improve the permeability of sonosensitizers in tumors, and finally, increase SDT effects and analyze its possible mechanisms **(Figure 1)**.

MATERIALS AND METHODS

Reagents and Animal Models

The HMME was purchased from Shanghai Dibo Biotechnology Co., Ltd., China, and was stored in a refrigerator protected from light at 4°C. Microbubbles for injection (SonoVue) were purchased from Bracco Suisse SA Italy. The main components of SonoVue are sulfur hexafluoride gas and phospholipid. The average diameter is 2.5 μm and the diameter of 90% microbubbles is less than 6 μm with very low solubility in blood, and can be exhaled through microcirculation.

Healthy adult female New Zealand White rabbits (2.0-2.5 kg) were purchased from the experimental animal center of Guangdong Province. They were adapted in a suitable feeding environment for 7 d. After weighing, they were anesthetized by

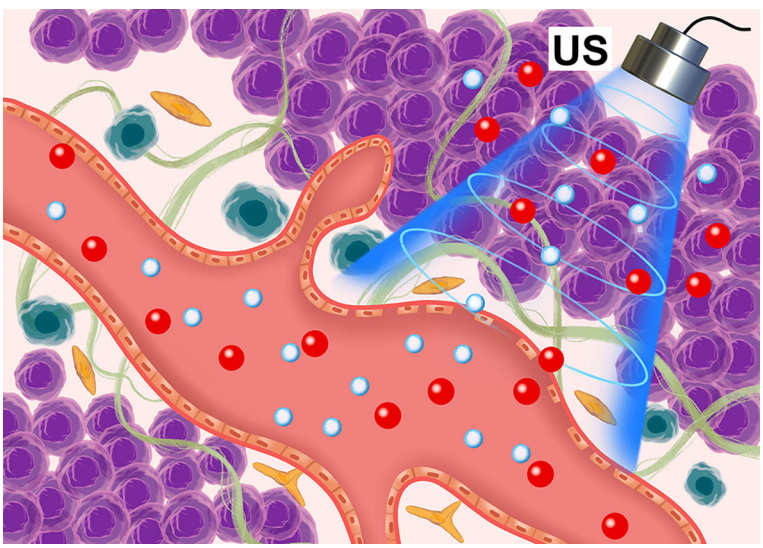

FIGURE 1 | Schematic diagram of the microbubble ultrasonic cavitation pretreatment with the ultrasound-sensitizer HMME.

compound anesthesia. The anesthesia was intramuscularly injected and consisted of 0.15 mL/kg Sumianxin II and 20 mg/kg 2% Pentobarbital sodium. After the corneal reflex disappeared, rabbits were fixed in the lateral position on the experimental table and the skin of the left hind limb was prepared. The rabbit's VX2 tumor tissue block was cut to 1 mm^3 and placed in normal saline to form a suspension. Then, a 1 mL syringe was used to connect the G needle, 1~2 tissue blocks were sucked and injected into the superficial muscle layer of the left hind limb of the rabbit (depth: 2.5 ± 0.5 mm from the body surface). The tumor size of rabbits was observed by ultrasonic diagnostic instrument (GE LOGIQ E9, probe: ML6-15) every day and grew to L 10 ± 0.7 mm and W 5 ± 0.8 mm in about 10 d. All animal experiments were carried out following the guidelines of the National Institute of Health. The care and use of experimental animals were approved by the animal ethics committee of the South China University of Technology.

Contrast-Enhanced Ultrasound Examination

All tumor-bearing rabbits received contrast-enhanced ultrasound before and after microbubbles ultrasonic cavitation treatment. The Color Doppler ultrasound diagnostic instrument (GE LOGIQ E9, probe: ML6-15) was used in the contrast-enhanced ultrasound mode. SonoVue microbubbles were diluted with 0.2 mL normal saline, then injected through rabbit ear marginal vein by mass injection. Next, the normal saline flushing tube was connected, and the angiography started. The dynamic image was recorded and stored for 1 min, and the angiography peak intensity (PI) was recorded and analyzed (**Figure 2B**).

Microbubbles Ultrasonic Cavitation Therapy

Twenty tumor-bearing rabbits without defects related to the above contrast medium were divided into four groups (five rabbits in each group): HMME + MBUS1, HMME + US1, HMME, and blank control. Each group was treated as follows: in the HMME + MBUS1 group, each rabbit was intravenously injected with 5.0 mg/kg HMME at the ear margin 1 h later, ultrasonic emission frequency of 2.5 MPa, pulse repetition frequency of 10 Hz, a duty cycle of 0.2%, pulse emission/gap time of 9 s/3 s (The choice of this parameter is based on prior research that we are currently publishing), and irradiation time of 5 min(Shenzhen Wilde Medical Electronics Co., Ltd., models dct-700 and kht-017; effective diameter 20 mm). The probe irradiated the tumor and the SonoVue microbubbles diluted (5 mL with sterile normal saline) were slowly injected (0.5 mL/kg); in the HMME + US1 group, after each tumor-bearing rabbit was injected with the same HMME dose for 1 h, the ultrasound treatment probe was irradiated and the same volume of normal saline was slowly injected; in the HMME group, after each tumor-bearing rabbit was injected with the same HMME dose for 1 h, the ultrasound was sham irradiated for 5 min; in the

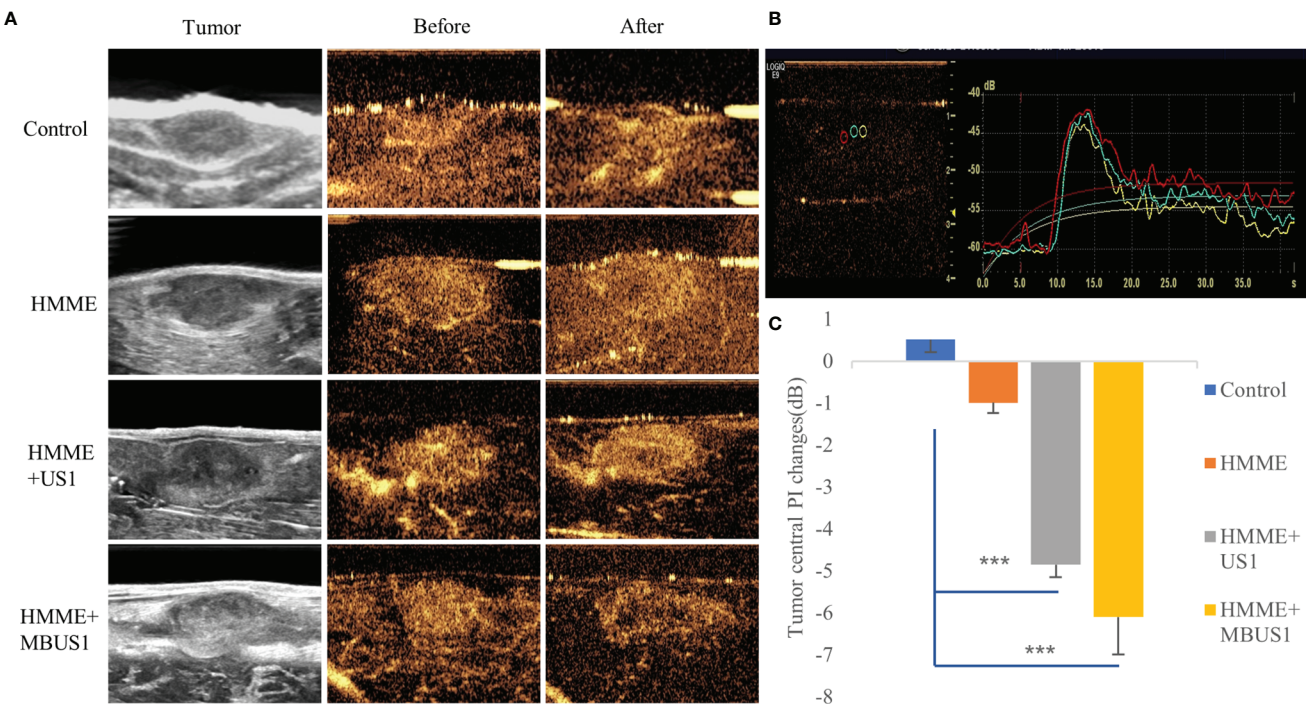

FIGURE 2 | **(A)** Peak intensity contrast images of each group before and after ultrasound irradiation. **(B)** The ultrasound diagnostic instrument quantitatively analyzed the contrast intensity at the center (yellow), edge 1/4 (green), and edge 1/8 (red). **(C)** After ultrasound irradiation, the PI changes in the tumor's central part in each group (***$p < 0.001$).

blank control group, the tumor-bearing rabbits were injected with the same volume of normal saline for 1 h, then the ultrasound was sham irradiated for 5 min. The tumor IFP was measured by the WIN method before and after ultrasonic treatments.

Tumor IFP Measurement

The WIN method (17) was used to measure the tumor's IFP (**Figure 3A**). The central and peripheral regions of the tumor were distinguished by taking 1/4 of the tumor diameter at the boundary point. At different time nodes, immediately before and after each treatment, the WIN method was used to measure the three tumor regions (the central 1/2, the marginal 1/4, and the peripheral 1/8) **(Figure 3B)**. All measurements were repeated three times and averaged as the results. First, the instrument connected the puncture needle with a side hole to the biological signal acquisition and analysis system, filled the hydraulic measurement system with heparin sodium saline sealing solution, was calibrated and blanked before measurements, and was horizontally placed on the horizontal plane at the same height as the tumor. Then, the puncture needle entered the center of the tumor under ultrasound guidance and marked the curve after the pressure curve was stably displayed for 1 min. At the beginning of the measurement, the pressure was recorded for 10 s, and the curve marked the end. The average reading of the pressure curve within 10 s was used as the initial IFP value of the tumor. After treatments, the puncture needle was slowly withdrawn and the IFP was measured in the peripheral area of the tumor and the normal tissue around it by the same method. Measurement results were determined by the bl-420s biological function experimental system (developed by Chengdu taimeng Software Co, Ltd.; model BL-420s. Pressure sensor model FT-100s).

HMME Content and Distribution in Tumors

After the above measurements, all tumor-bearing rabbits were euthanized and the tumor was removed. The tumor tissues were divided into four parts and fixed with paraformaldehyde then stored away from light. The tumors 1/4~1/8 near the edge were accurately weighed (1 g), 1 mL of normal saline homogenate was added and grinded, shaken for 15 min, and centrifuged (3000 rpm for 10 min). The supernatant was recovered and the fluorescence intensity was measured with an ultra microspectrophotometer (American DeNovix model DS ll +). The standard concentration curve consisted of different HMME concentrations.

A portion of tumor tissues shielded from light were sliced, then DAPI (excitation wavelength 340 nm, emission wavelength 488 nm) was used to stain the tumor nucleus, and the HMME distribution (excitation wavelength 395nm, emission wavelength 611nm) in the tumor tissue was observed by confocal laser microscopy (Japan Nikon Ti-E-A1).

Pathological Analyses

Half of each tumor was sliced for staining analysis, HE staining was used to observe tumor vascular permeability and surrounding changes. The Masson and Gordon sweets reticular fiber stainings were used to observe the changes of collagen fibers

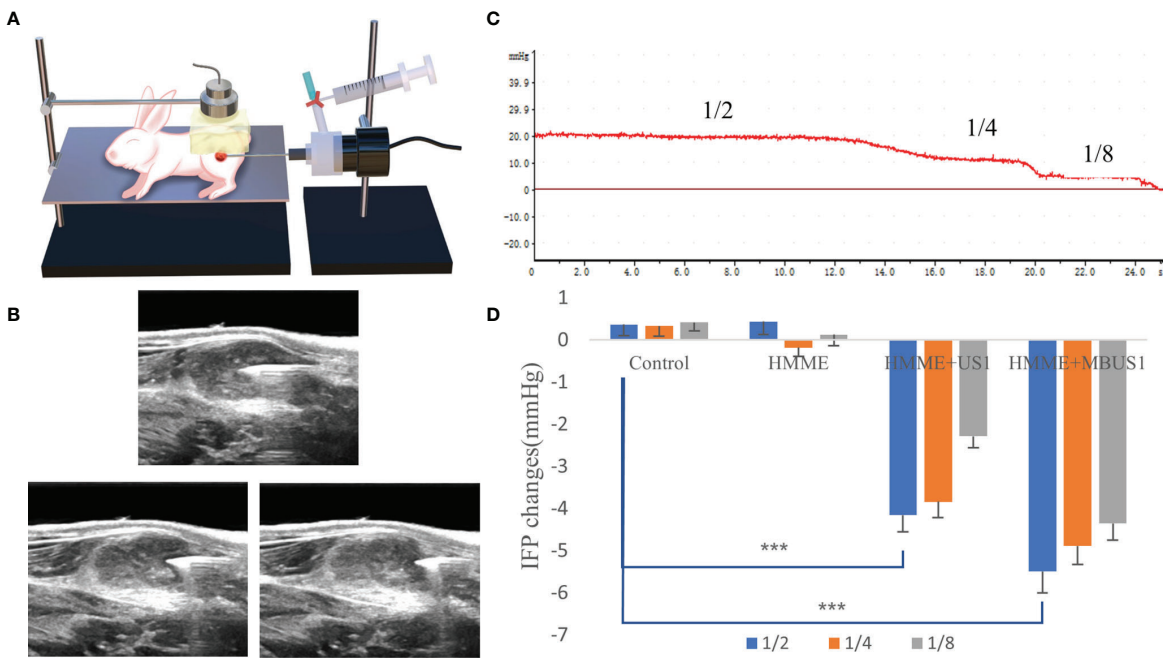

FIGURE 3 | **(A)** The VX2 tumor pattern was measured by ultrasound irradiation and the WIN method. **(B)** Schematic diagram of needle core position. IFP of 1/2, 1/4, and 1/8 tumors were respectively measured. **(C)** Schematic diagram of IFP measurements of a single tumor. The values corresponding to different steps are the IFP values at that point. **(D)** Changes of IFP values at different tumor locations after ultrasound irradiation (***$p < 0.001$).

and reticular microscopic content in tumor tissues after ultrasonic treatments. Pathological sections were scanned by a pathological scanner (Chinese SDPTOP, model HS6) and observed by image scope software.

SDT

Twenty tumor-bearing rabbits were divided into four groups (five rabbits in each group): HMME + MBUS1 + SDT, HMME + SDT, HMME + MBUS1, and blank control. The rabbits in each group were treated once a week according to different treatment methods. The HMME dose, MBUS parameters, and instruments were the same as before, and the SDT instrument (Shenzhen Wilde Medical Electronics Co., Ltd., model wed-100) had an effective probe diameter of 20 mm, pulse waveform, ultrasonic frequency of 1 MHz, an ultrasonic intensity of 3 W/cm^2, a duty cycle of 60%, and the treatment time was 15 min. The length, width, and thickness of the tumor were measured by an ultrasonic diagnostic instrument once two days, according to the formula: $v = L \times W \times H \times \pi/6$, where: length (L), width (W), and height (H) were used to calculate the tumor volume (V) and draw the tumor growth curve. All measurements were repeated three times and averaged as the results. After eight weeks of treatment in February, the tumor-bearing rabbits in different groups were euthanized and weighed before the tumor removed (**Figure 6A**). The lung and liver were also removed. They were fixed with paraformaldehyde, embedded in paraffin, cut, and stained. The histopathological changes and metastasis were observed under an optical microscope.

Statistics

The SPSS 22.0 software was used for statistical analyses. The measured values are expressed as means ± standard deviations (SDs). Pairwise comparisons were determined using the t-test. The differences between groups were determined by the one-way analysis of variance (ANOVA) test, and the homogeneity of variance test was performed before analysis. $p<0.05$ was considered to be statistically significant.

RESULTS

Effect of Microbubbles Ultrasonic Cavitation on Tumor Blood Perfusion Evaluated by Contrast-Enhanced Ultrasound

Before treatments, the contrast-enhanced ultrasound showed that, in each group, the microbubbles were rapidly and evenly filled in the tumor and reached the peak value in about 12 s. No filling defect was detected. After the 2.5 MPa ultrasound irradiation, we quantitatively analyzed the peak intensity at the tumor's center 1/2 and the edge 1/4 and 1/8 (**Figure 2B**). The square difference homogeneity test was performed in each group and all presented a $p > 0.05$. Moreover, the one-way ANOVA results were significant. In the central part of the tumor, the PI values of the HMME, HMME + MBUS1, and HMME + MBUS1 groups significantly decreased in varying degrees different ($F = 18.384$, $p = 0.000$). In the HMME + MBUS1 group, a decrease of 6.01 dB was detected, with a 10.01% degree before angiography. However, we detected a little filling defect in the central part of the tumor in the HMME + MBUS1 and HMME + US1 groups under naked-eye observations (**Figure 2A**). Additionally, the HMME + MBUS1 defective area was larger compared to the HMME + US1 group. After treatments, the contrast image in the HMME group could not be distinguished by the naked eye, but the PI value in the central part decreased slightly, while the qualitative and quantitative scores in the blank control group did not significantly change (**Figure 2C**). No significant changes were detected At the tumor's edge 1/4 ($F = 2.717$, $p = 0.079$) and 1/8 ($F = 2.849$, $p = 2.070$) in tumor PI values before and after ultrasound irradiation. Finally, the contrast medium was well filled in the above parts of the image, and no significant differences before and after irradiation were detected for the tumor's center 1/2 ($p = 0.236$), and edge 1/4 ($p = 0.140$), and 1/8 ($p = 0.071$).

Tumor IFP Changes After Microbubbles Ultrasonic Cavitation

Before ultrasonic cavitation, when the puncture needle was stably placed in the center of the tumor and moved outward to 1/2 and 1/8 (**Figure 3**), the tumor IFP waveform curve in each group showed a positive and stepped form (**Figure 3C**). Before treatment, the average tumor IFP value at the center 1/2, and the edge 1/4 and 1/8 of the 20 tumor-bearing rabbits were (means ± SDs) 16.76 ± 2.77, 11.42 ± 2.25, and 4.65 ± 1.94 mmHg, respectively. Also, when the ultrasound needle moved out from the edge of the tumor to the muscle tissue, the curve decreased to zero and negative values. After cavitation irradiation treatment, the puncture needle punctured the same part of the tumor. Results showed that in the three different tumor parts, the tumor IFP decreased in different degrees in HMME + US1 and HMME + MBUS1 groups. The decrease was more clear in the HMME + MBUS1 group, followed by HMME + US1. Meanwhile, in blank control and HMME groups (sham irradiation groups), the IFP in each part of the tumor did not significantly change. Overall, there were significant differences among groups (all $p = 0.000$). After irradiation, The ΔIFP values of HMME + US1 and HMME + MBUS1 groups were the highest in the center (-4.15 ± 1.81 and -5.50 ± 2.47 mmHg, respectively), 25 and 32.8% lower than those before treatment (**Figure 3D**). The IFP values of the two edge positions also decreased, and the decline degree of the HMME + MBUS1 was 42.8 (1/4) and 93.5% (1/8). The IFP at the tumor's edge 1/4 and 1/8 of the HMME + US1 group decreased by 33.6 and 83%, respectively, compared with the values before ultrasonic irradiation. Although the IFP value at the edge was relatively small, the decline rate was related to the low IFP before ultrasonic irradiation ($p < 0.05$).

HMME Content in Tumor Tissues After Ultrasound Irradiation

We used two methods to qualitatively and quantitatively analyze the HMME content in tumor tissues. The laser confocal image under DAPI staining showed that a little red fluorescence could be seen in tumor tissues after intravenous HMME injection,

which was mainly concentrated outside tumor cells (**Figure 4A**). The intracellular and extracellular red fluorescence increased in the HMME + US1 group. Also, the red fluorescence in tumor tissues increased in the HMME + MBUS1 group due to the addition of microbubbles The HMME content in the tumor tissue of each treatment group significantly increased over time (F = 32.221, p = 0.000). The HMME concentration in tumor tissues of the HMME + MBUS1 group was the highest, reaching 31.5 μg/g, comprehending a 31% increase compared to the HMME group. In the HMME + US1 group (without microbubbles), the HMME content in the tumor tissue only increased by 4% (**Figure 4B**).

Pathological Changes of Tumor Sections

The HE staining results of tumor tissues showed that the pathological changes in the control and HMME groups were similar (**Figure 5**). The cells in the tumor tissue were disordered and distributed in a strip-like manner. In each proliferative stage, tumor cells were dense and structurally complete. Meanwhile, passing blood vessels were detected, branching or cystic, with a clear structure, complete and continuous pipe walls, without clear damage, with red blood cells in the lumen and around the blood vessels. No clear red blood cell escape was found. In the HMME + MBUS1 group, tumor cells were disorderly distributed with few nuclear pyknosis and tumor microvessels distributed. Among them, a small amount of red blood cell leakage was scattered around blood vessels. In the HMME + MBUS1 group, flake necrotic foci were also seen in the sparse tumor tissues, and clear nuclear pyknosis or fragmentation accompanied by a large number of nuclear fragments were detected. Microvessels were congested and dilated, the blood vessel wall was incomplete, and a large number of red blood cells escaped around the blood vessel. The Masson staining showed that the collagen fibers were blue, the blood cells and cytoplasm red, and the nucleus blue-purple (**Figure 5**). Moreover, no significant correlation between ΔIFP and the content of collagen fibers in tumor tissues was detected in each group. The Gordon sweets reticular fiber staining showed black hairy reticular fibers in all pathological sections. The content of reticular fibers in tumor sections was similar between groups and did not correlate with the ΔIFP.

Therapeutic Effect of SDT

The tumor growth curve results showed a significant difference in tumor volume between groups two days after the first treatment (F = 7.432, p = 0.002). The tumor volume of the blank group presented the fastest increase followed by the HMME + MBUS1 group. The slowest tumor growth was observed in the HMME + MBUS1 + SDT group (**Figure 6B**). Moreover, the weight change of rabbits in **Figure 6C** testified that the rabbits weight had no noticeable change over the course of the experiment. Pathological sections were scored In order to quantitatively evaluate lung and liver metastasis, 10 different high-power fields were randomly observed in each section, and the score was based on the positive cell rate. The scoring criteria were as follows: 0 points, no metastatic cells were observed. Score 1, 2, 3 and 4 were positive cell rates of 1%-25%, 26%-50%, 50%-75% and 76%-100% respectively (**Figure 6D**). The anatomical specimens showed that the blank group lungs were covered with miliary metastases of different sizes, Multiple white metastases were also seen in the lungs of the HMME + MBUS1 group. In

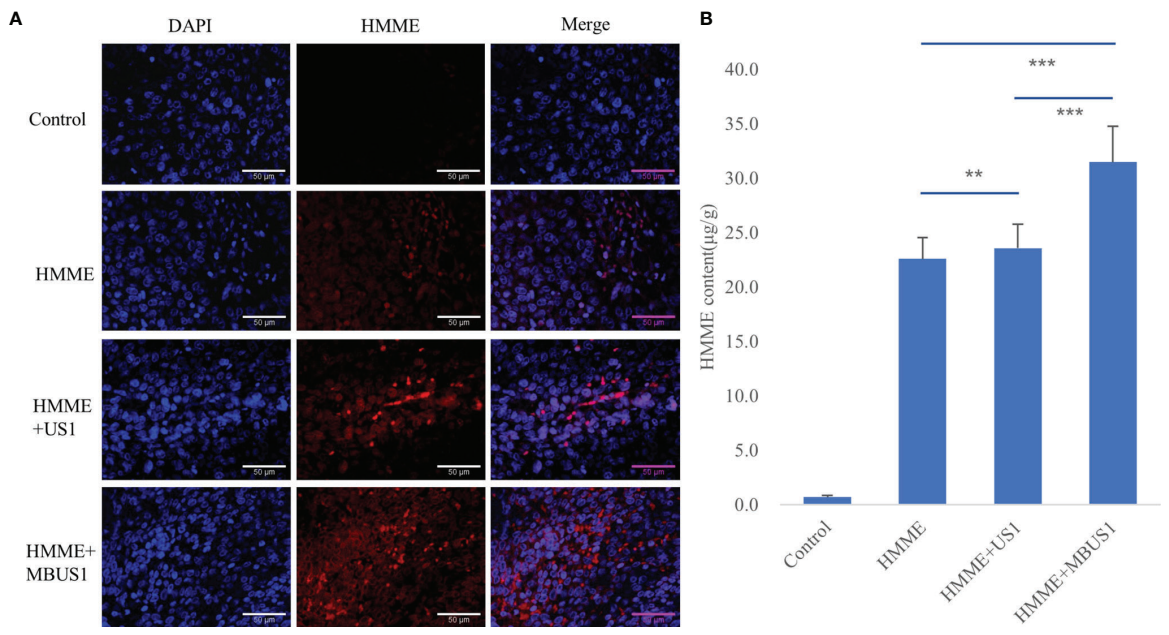

FIGURE 4 | **(A)** DAPI staining images of tumors under laser confocal microscope. Blue represents the nucleus and red the HMME. **(B)** The HMME content in tumor tissues was quantitatively analyzed by an ultramicro photometer (**p < 0.01,***p <0.001).

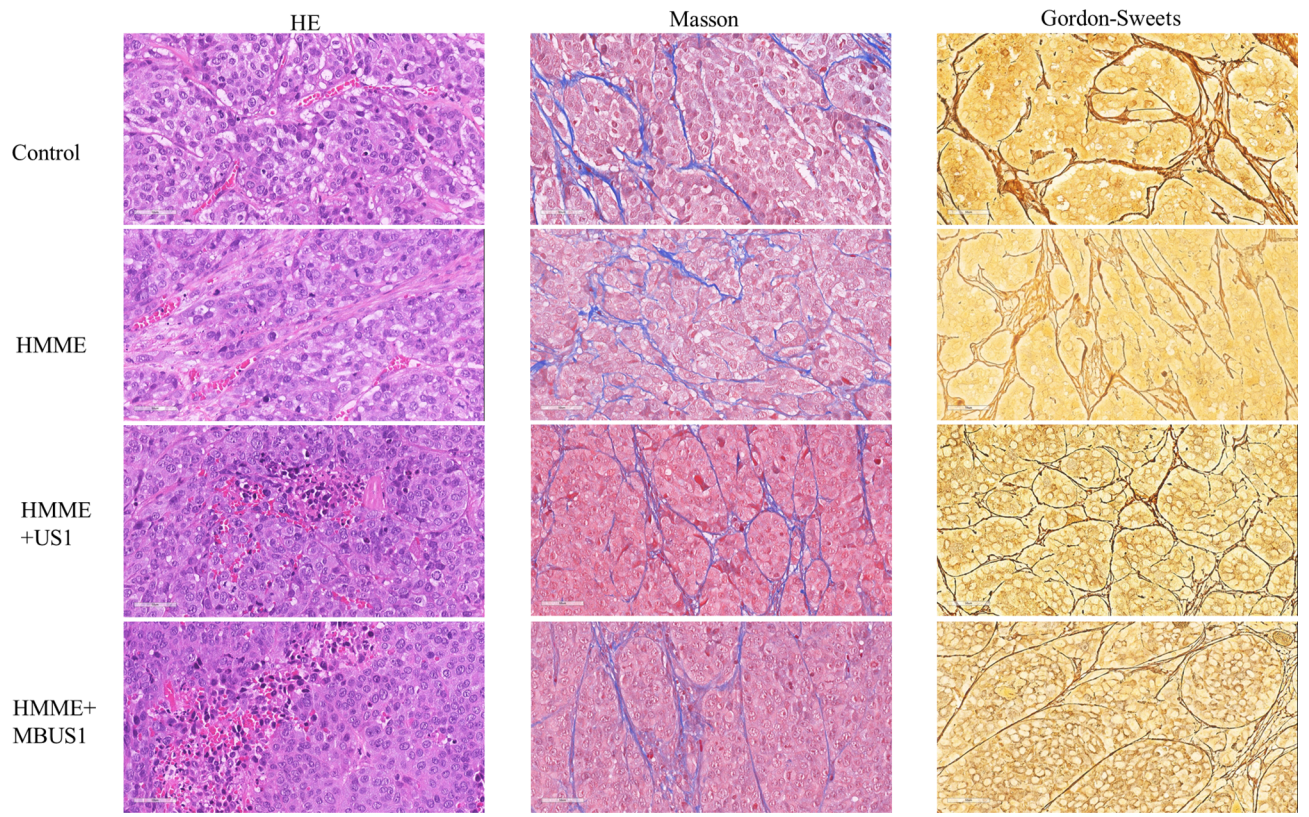

FIGURE 5 | HE, Masson, and Gordon sweets stainings in each group after ultrasonic irradiation.

these groups, large metastases were also present in lung tissues (**Figure 7A**) with the pathological scorings of 2.41 and 2.00. No clear metastasis was detected for the HMME + SDT group using the naked eye, but the staining showed occasional punctate metastases in the lung tissue, the pathological scorings of this group is 0.69. What's more, We only see one field with a pathological scoring of 1 point among 15 lung tissue sections in the group of HMME + MBUS1 + SDT group **(Figure 7B)**. Finally, the liver tissues of tumor-bearing rabbits in each group did not present metastasis with pathological scoring of 0.

4 DISCUSSION

Compared with photodynamic therapy, SDT has deeper tissue penetration, higher precision, fewer side effects, and good patient compliance. Therefore, it has a good application prospect for deep solid tumors such as liver cancer, glioma, etc. (18). Moreover, the treatment can be repeated, being especially suitable for elderly and weak cancer patients who cannot undergo surgery, radiotherapy, or chemotherapy (19). Our study was aiming to enhance SDT by using microbubbles combined with ultrasonic cavitation to increase the penetration of sonosensitizers into tumors.

The accumulated concentration of sonosensitizers in tumors limits SDT's clinical application. HMME is the most commonly used photosensitizer and sonosensitizers in photodynamic and sonodynamic therapies (20). For example, Liang et al. (21) reported the HMME-SDT synergistic effect with the anticancer agent DOX. The combined application of HMME-SDT and DOX significantly inhibited the proliferation of human cholangiocarcinoma QBC939 cells *in vitro*. Moreover, HMME has advantages such as single composition, stable performance, high tumor selectivity, and low phototoxicity to normal tissues. but a high tumor IFP hinders the accumulation of sonosensitizers in tumor sites (22). Due to tumor vascular heterogeneity, the IFP in tumor tissues can be increased by normal, dense stroma and abnormal fibrosis, abnormal function of collagen fibers and reticular fibers, and abnormal lymphatic vessels, which hinder the material from entering the tumor stroma from capillaries (**Figure 1**).Tumor IFP increases (23) can be caused by abnormal tumor blood vessels and dense interstitial matrix and abnormal fibrosis, increased hyaluronic acid in the interstitial matrix, and abnormal lymphatic vessels. In the present study, before treatments, the pressure in the central part of the tumor was the highest, showing a downward trend from the center to the periphery. However, the tumor IFP was still positive and the pressure in the surrounding muscle tissue was negative.

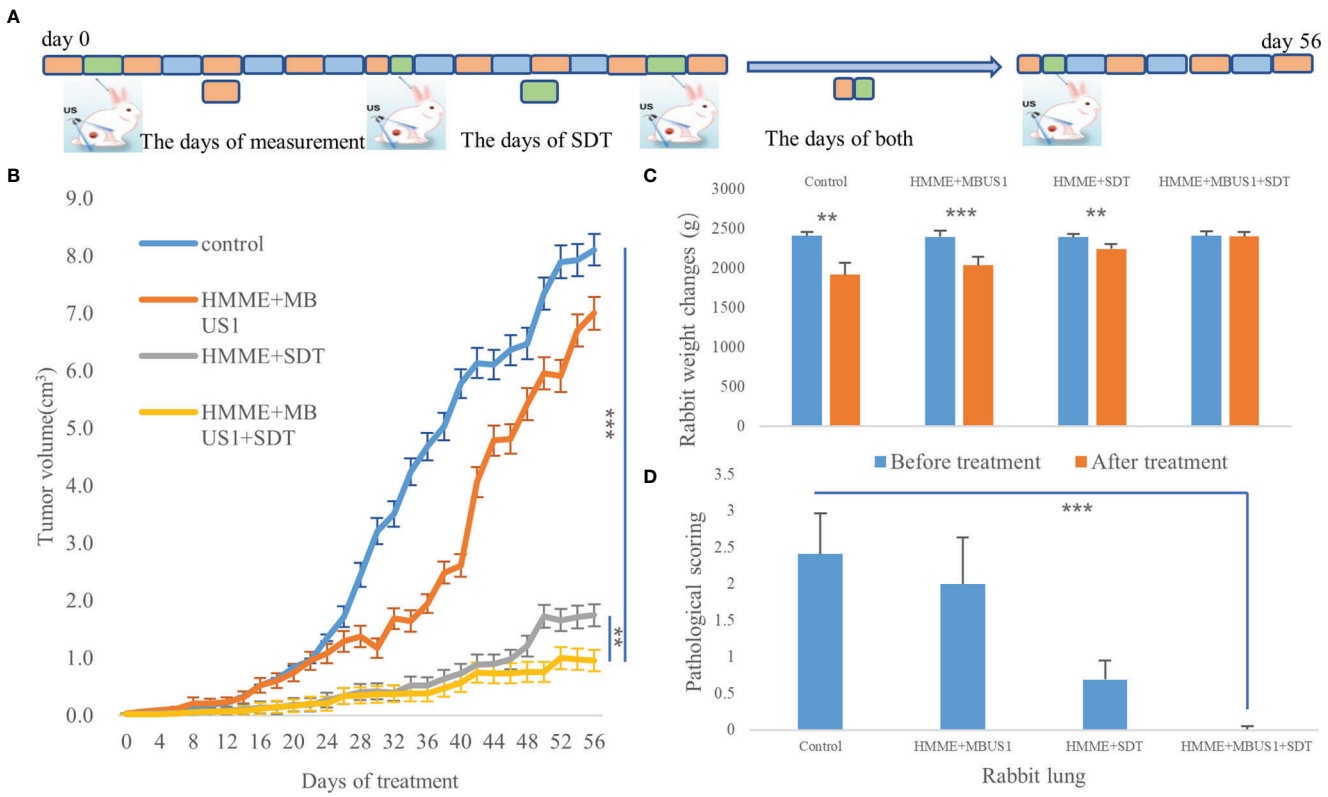

FIGURE 6 | **(A)** The days of measurement, SDT, and both of them. **(B)** Tumor volume changes with time after treatments. **(C)** Changes of rabbits body weight before and after SDT (**p < 0.01,***p < 0.001). **(D)** Pathological scorings of rabbits lung metastasis (***p < 0.001).

The main methods to reduce tumor IFP are to "normalize" blood vessels. Besides, reducing the content of hyaluronic acid in the interstitial matrix and improving lymphatic function can increase the efficacy of antitumor drugs. In the current experiment, the combination of microbubbles with low-frequency unfocused ultrasound irradiation could reduce the tumor's IFP. We believe that this was possible due to: first, the cavitation effect (**Figure 1**). Microbubbles generate cavitation under ultrasound irradiation, resulting in a shock wave and microjets, resulting in tumor vascular damage, rupture, and micro thrombosis, thereby destroying the blood perfusion of the tumors and causing necrosis and apoptosis of tumor cells. At the same time, the vibration and explosion of microbubbles in blood vessels can destroy the tumor microvascular structure, damage endothelial cells, and even lyse cells. Second, As confirmed by our pathological images, the destruction of tumor blood vessels reduces the microvascular area in the tumor, consistent with our ultrasound imaging results before and after cavitation. After cavitation, the PI value of all tumors' central parts decreased in the experimental group (**Figure 3**), as the tumor blood flow and macromolecular substances escaped from blood vessels, finally reducing the tumor IFP. Third, cavitation caused the destruction of tumor vascular structure and induced apoptosis and necrosis by disrupting the integrity of the endothelial cytoskeleton. Besides, endothelial cell necrosis can indirectly reduce tumor IFP. Previous studies indicated that the tumor IFP is positively correlated with the content of collagen and reticular fibers in tumor tissues. Here, the tumor IFP changed after the combination of low-frequency ultrasound with microbubbles irradiation, but the structure and content of collagen and reticular fibers in each group did not significantly change.

Tumor cells produce mechanical forces in the process of excessive growth and reproduction, which compress tumor blood vessels and lymphatic vessels, reduce microcirculation blood perfusion, and increase tumor IFP. In this project, it was found that ultrasonic cavitation of microbubbles could increase the permeability of tumor microvessels to sonosensitizers, thus increasing the accumulation of sonosensitizers at the tumor site **(Figure 4).** HE staining showed obvious direct damage to vascular endothelium at 2.5MPa sound pressure, incomplete structure of vascular wall, and overflow of red blood cells from the rupture into the surrounding blood vessels (**Figure 5**). Partial tumor vascular structure is incomplete, and the tumor cells around the blood vessels appear scattered focal necrosis. Confocal laser microscopy **(Figure 4).** showed that the content of HMME in the cavitation group increased in the edges of the tumor with relatively abundant blood vessels, which may be because HMME entered the extravascular space through the enlarged vascular space, and it

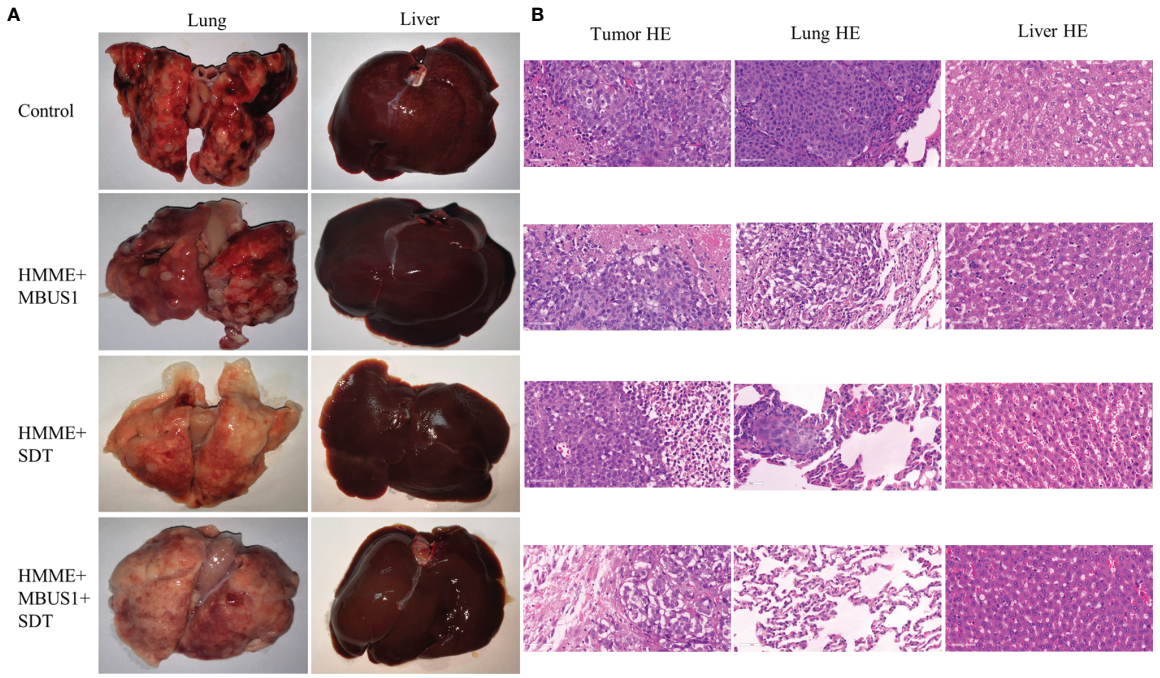

FIGURE 7 | **(A)** Liver and lung metastasis of tumor-bearing rabbits in each group after treatment was observed by the naked eye. **(B)** Tumor tissue, lung, and liver of each group were observed by HE staining.

was difficult for HMME to flow in the dense extravascular matrix and thus accumulated here. Collagen fiber and reticular fiber is an important component of the extracellular matrix of tumor, how much of its content is also an important factor affecting the tumor IFP, pathological section shows each tumor in the structure and content of collagen fiber and reticular fibers and no obvious change (**Figure 5**), possible reason is that blood vessels has played a more important role in regulating tumor IFP, This also indicates that microbubbles combined with ultrasonic cavitation can effectively change tumor IFP without causing changes in skeletal structure such as collagen fibers and reticular fibers in tumor extracellular matrix.

One hour after HMME intravenous injection at the rabbit ear edge, the HMME content in tumor tissues was at a high level. Then, SonoVue microbubbles were intravenously injected and reached tumor tissues. Under ultrasound stimulation, the microbubbles produce a cavitation effect, which can temporarily form acoustic holes in the blood vessel wall or cell membrane. The diameter of these holes ranges from a few nanometers to 150 nm. They can enhance the permeability of blood vessels and cell membranes, then promote drug penetration and cellular uptake in the treatment area. Combining ultrasound with microbubbles to enhance chemotherapeutic drugs is also known as sonochemotherapy (24). Ultrasound-enhanced chemotherapy drug release only occurs in the ultrasound irradiation area, and the therapeutic drug concentration increases specifically in the focus area, resulting in significant therapeutic response, which can also reduce the side effects of drugs in other parts. Sonochemotherapy has been used in the clinical treatment of various solid tumors, such as prostate cancer (25), melanoma (26), and pancreatic cancer (27). In this study, there was no obvious change in tumor blood perfusion at the 1/4-1/8 tumor edge, while IFP decreased significantly. Qualitative and quantitative analysis showed that the accumulation of HMME in this region increased. Then, we performed the second step ultrasound SDT treatment at this time and achieved a good therapeutic effect. The exact and definitive mechanism of SDT remains unresolved. Possible theories include generation of ROS, ultrasonic cavitation effect and thermal destruction (28).

At present, 0.15-2.0 MHz ultrasound is generally used during SDT. The normal irradiation amount is 2-3 W/cm^2 for 60 s-30 min (29). High-frequency ultrasound with high ultrasound intensity can produce a thermal effect and directly kill cells. At the same time, this might lead to increased reactive oxygen species (ROS) in the normal tissue around the tumor and cause irreversible damages (30). Low-frequency ultrasound has deeper penetration, which can temporarily enhance the cell membrane permeability, protect the surrounding normal tissues. Also, tumor cells in the cell proliferation stage are more sensitive to reactive oxygen species. Additionally, compared with high-frequency ultrasound, low-frequency ultrasound produces a larger cavitation bubble radius and greater spatial-temporal intensity of bubble rupture. In the current study, the SDT was conducted with 3 W/cm^2, single treatment for 15 min, for 8 times. Results showed a clear tumor inhibition effect in the treatment group (**Figure 6**). Ninomiya et al. found that under

the same conditions when TiO_2 was irradiated with two ultrasonic waves with different energies and frequencies (0.5 MHz and 800 MW/cm^2, and 1 MHz and 0.4 W/cm^2), more active hydroxide was produced, better than one ultrasonic wave (31). Therefore, the combination of ultrasounds with different energies and frequencies can lead to better therapeutic effects than single ultrasound. Two ultrasound frequencies were also used in the present experiment after the injection of an acoustic sensitizer. On the other hand, it is not clear whether ROS will be produced in the first ultrasound step. However, based on the tumor growth curve **(Figure 6)**, the growth rate of the HMME + MBUS1 group was only the second, after the blank control group, which was significantly faster than the HMME + MBUS1 + SDT group. Therefore, we speculated that the main reason for the tumor tissue growth inhibition was the second SDT step. The first step of the HMME + MBUS1 mainly reduced tumor IFP and increased the accumulation of the acoustic sensitizer at the tumor site. SDT utilizes the interaction between ultrasound and non-toxic acoustic sensitizers, which selectively accumulate in the target tissue, eradicating solid tumors in a non-invasive and highly selective way.

However, SDT still has some problems requiring further studies:(I) The specific mechanisms of SDT for cancer treatment are not completely clear; (II) New sonosensitizers with less phototoxicity and higher therapeutic effects need to be explored;(III) The ultrasound frequency, intensity, and irradiation time corresponding to specific tumors still need to be studied in more detail;(IV) Long-term toxicity studies of existing sonosensitizers need to be performed in the future. Finally, due to its good biomedical performance, SDT has attracted increasing attention from many cutting-edge interdisciplinary areas related to cancer. We believe that SDT will shortly have a great impact on the treatment of cancer patients.

DATA AVAILABILITY STATEMENT

The original contributions presented in the study are included in the article/supplementary material. Further inquiries can be directed to the corresponding author.

ETHICS STATEMENT

The animal study was reviewed and approved by South China University of Technology.

AUTHOR CONTRIBUTIONS

FX and JL conceived and designed the experiments and wrote the paper; FX and YF performed the experiments and analyzed the data; LC and QC contributed reagents/materials/analysis tools. All authors provided their approval for publication.

FUNDING

This work was supported by the National Natural Science Foundation of China (Grant No.: 82071935).

ACKNOWLEDGMENTS

We thank all the members of the Second Affiliated Hospital, School of Medicine, South China University of Technology for their support.

REFERENCES

1. Xu M, Zhou L, Zheng L, Zhou Q, Liu K, Mao Y, et al. Sonodynamic Therapy-Derived Multimodal Synergistic Cancer Therapy. *Cancer Lett* (2021) 497:229–42. doi: 10.1016/j.canlet.2020.10.037
2. Lee S, Han H, Koo H, Na JH, Yoon HY, Lee KE, et al. Extracellular Matrix Remodeling *In Vivo* for Enhancing Tumor-Targeting Efficiency of Nanoparticle Drug Carriers Using the Pulsed High Intensity Focused Ultrasound. *J Control Release* (2017) 263:68–78. doi: 10.1016/j.jconrel.2017.02.035
3. Yan S, Lu M, Ding X, Chen F, He X, Xu C, et al. HematoPorphyrin Monomethyl Ether Polymer Contrast Agent for Ultrasound/Photoacoustic Dual-Modality Imaging-Guided Synergistic High Intensity Focused Ultrasound (HIFU) Therapy. *Sci Rep* (2016) 6:31833. doi: 10.1038/srep31833
4. Hao D, Song Y, Che Z, Liu Q. Calcium Overload and *In Vitro* Apoptosis of the C6 Glioma Cells Mediated by Sonodynamic Therapy (Hematoporphyrin Monomethyl Ether and Ultrasound). *Cell Biochem Biophys* (2014) 70 (2):1445–52. doi: 10.1007/s12013-014-0081-7
5. Dai S, Hu S, Wu C. Apoptotic Effect of Sonodynamic Therapy Mediated by Hematoporphyrin Monomethyl Ether on C6 Glioma Cells *In Vitro*. *Acta Neurochir (Wien)* (2009) 151(12):1655–61. doi: 10.1007/s00701-009-0456-5
6. Böckelmann LC, Schumacher U. Targeting Tumor Interstitial Fluid Pressure: Will it Yield Novel Successful Therapies for Solid Tumors? *Expert Opin Ther Targets* (2019) 23(12):1005–14. doi: 10.1080/14728222.2019.1702974
7. Heldin CH, Rubin K, Pietras K, Ostman A. High Interstitial Fluid Pressure - An Obstacle in Cancer Therapy. *Nat Rev Cancer* (2004) 4(10):806–13. doi: 10.1038/nrc1456
8. Cavin S, Wang X, Zellweger M, Gonzalez M, Bensimon M, Wagnières G, et al. Interstitial Fluid Pressure: A Novel Biomarker to Monitor Photo-Induced Drug Uptake in Tumor and Normal Tissues. *Lasers Surg Med* (2017) 49 (8):773–80. doi: 10.1002/lsm.22687
9. Boucher Y, Baxter LT, Jain RK. Interstitial Pressure Gradients in Tissue-Isolated and Subcutaneous Tumors: Implications for Therapy. *Cancer Res* (1990) 50(15):4478–84.
10. Gao X, Zhang J, Huang Z, Zuo T, Lu Q, Wu G, et al. Reducing Interstitial Fluid Pressure and Inhibiting Pulmonary Metastasis of Breast Cancer by Gelatin Modified Cationic Lipid Nanoparticles. *ACS Appl Mater Interf* (2017) 9 (35):29457–68. doi: 10.1021/acsami.7b05119
11. Lunt SJ, Kalliomaki TM, Brown A, Yang VX, Milosevic M, Hill RP. Interstitial Fluid Pressure, Vascularity and Metastasis in Ectopic, Orthotopic and Spontaneous Tumours. *BMC Cancer* (2008) 8:2. doi: 10.1186/1471-2407-8-2
12. Curti BD, Urba WJ, Alvord WG, Janik JE, Smith JW2nd, Madara K, et al. Interstitial Pressure of Subcutaneous Nodules in Melanoma and Lymphoma Patients: Changes During Treatment. *Cancer Res* (1993) 53(10 Suppl):2204–7.
13. Pi Z, Huang Y, Shen Y, Zeng X, Hu Y, Chen T, et al. Sonodynamic Therapy on Intracranial Glioblastoma Xenografts Using Sinoporphyrin Sodium Delivered by Ultrasound With Microbubbles. *Ann BioMed Eng* (2019) 47(2):549–62. doi: 10.1007/s10439-018-02141-9

14. Choi W, Kim C. Synergistic Agents for Tumor-Specific Therapy Mediated by Foc Used Ultrasound Treatment. *Biomater Sci* (2021) 9(2):422–36. doi: 10.1039/d0bm01364a
15. Zhang Q, Jin H, Chen L, Chen Q, He Y, Yang Y, et al. Effect of Ultrasound Combined With Microbubble Therapy on Interstitial Fluid Pressure and VX2 Tumor Structure in Rabbit. *Front Pharmacol* (2019) 10:716. doi: 10.3389/fphar.2019.00716
16. Wei Y, Shang N, Jin H, He Y, Pan Y, Xiao N, et al. Penetration of Different Molecule Sizes Upon Ultrasound Combined With Microbubbles in a Superficial Tumour Model. *J Drug Target* (2019) 27(10):1068–75. doi: 10.1080/1061186X.2019.1588279
17. Ley CD, Horsman MR, Kristjansen PE. Early Effects of Combretastatin-A4 Disodium Phosphate on Tumor Perfusion and Interstitial Fluid Pressure. *Neoplasia* (2007) 9(2):108–12. doi: 10.1593/neo.06733
18. Chen B, Zheng R, Liu D, Li B, Lin J, Zhang W. The Tumor Affinity of Chlorin E6 and its Sonodynamic Effects on Non-Small Cell Lung Cancer. *Ultrason Sonochem* (2013) 20(2):667–73. doi: 10.1016/j.ultsonch.2012.09.008
19. Lafond M, Yoshizawa S, Umemura SI. Sonodynamic Therapy: Advances and Challenges in Clinical Translation. *J Ultrasound Med* (2019) 38(3):567–80. doi: 10.1002/jum.14733
20. Sun H, Ge W, Gao X, Wang S, Jiang S, Hu Y, et al. Apoptosis-Promoting Effects of Hematoporphyrin Monomethyl Ether-Sonodynamic Therapy (HMME-SDT) on Endometrial Cancer. *PloS One* (2015) 10(9):e0137980. doi: 10.1371/journal.pone.0137980
21. Liang L, Xie S, Jiang L, Jin H, Li S, Liu J. The Combined Effects of Hematoporphyrin Monomethyl Ether-SDT and Doxorubicin on the Proliferation of QBC939 Cell Lines. *Ultrasound Med Biol* (2013) 39(1):146–60. doi: 10.1016/j.ultrasmedbio.2012.08.017
22. Lunt SJ, Fyles A, Hill RP, Milosevic M. Interstitial Fluid Pressure in Tumors: Therapeutic Barrier and Biomarker of Angiogenesis. *Future Oncol* (2008) 4 (6):793–802. doi: 10.2217/14796694.4.6.793
23. Ariffin AB, Forde PF, Jahangeer S, Soden DM, Hinchion J. Releasing Pressure in Tumors: What do We Know So Far and Where do We Go From Here? A Review. *Cancer Res* (2014) 74(10):2655–62. doi: 10.1158/0008-5472
24. Zeng H, Sun M, Zhou C, Yin F, Wang Z, Hua Y, et al. Hematoporphyrin Monomethyl Ether-Mediated Photodynamic Therapy Selectively Kills Sarcomas by Inducing Apoptosis. *PloS One* (2013) 8(10):e77727. doi: 10.1371/journal.pone.0077727
25. Yang C, Zhang Y, Luo Y, Qiao B, Wang X, Zhang L, et al. Dual Ultrasound-Activatable Nanodroplets for Highly-Penetrative and Efficient Ovarian Cancer Theranostics. *J Mater Chem B* (2020) 8(3):380–90. doi: 10.1039/c9tb02198a
26. Lentacker I, Geers B, Demeester J, De Smedt SC, Sanders NN. Design and Evaluation of Doxorubicin-Containing Microbubbles for Ultrasound-Triggered Doxorubicin Delivery: Cytotoxicity and Mechanisms Involved. *Mol Ther* (2010) 18(1):101–8. doi: 10.1038/mt.2009.160
27. Kotopoulis S, Delalande A, Popa M, Mamaeva V, Dimcevski G, Gilja OH, et al. Sonoporation-Enhanced Chemotherapy Significantly Reduces Primary Tumour Burden in an Orthotopic Pancreatic Cancer Xenograft. *Mol Imaging Biol* (2014) 16(1):53–62. doi: 10.1007/s11307-013-0672-5
28. Rengeng L, Qianyu Z, Yuehong L, Zhongzhong P, Libo L. Sonodynamic Therapy, a Treatment Developing From Photodynamic Therapy. *Photodiagn Photodyn Ther* (2017), 19:159–166. doi: 10.1016/j.pdpdt.2017.06.003
29. Araújo Martins Y, Zeferino Pavan T, Fonseca Vianna Lopez R. Sonodynamic Therapy: Ultrasound Parameters and *In Vitro* Experimental Configurations. *Int J Pharm* (2021) 610:121243. doi: 10.1016/j.ijpharm.2021.121243
30. McHale AP, Callan JF, Nomikou N, Fowley C, Callan B. Sonodynamic Therapy: Concept, Mechanism and Application to Cancer Treatment. *Adv Exp Med Biol* (2016) 880:429–50. doi: 10.1007/978-3-319-22536-422
31. Ninomiya K, Noda K, Ogino C, Kuroda S, Shimizu N. Enhanced OH Radical Generation by Dual-Frequency Ultrasound With TiO2 Nanoparticles: Its Application to Targeted Sonodynamic Therapy. *Ultrason Sonochem* (2014) 21 (1):289–94. doi: 10.1016/j.ultsonch.2013.05.005

Conflict of Interest: The authors declare that the research was conducted in the absence of any commercial or financial relationships that could be construed as a potential conflict of interest.

frontiers | Frontiers in Oncology

ORIGINAL RESEARCH
published: 28 April 2022
doi: 10.3389/fonc.2022.901182

Screening Protein Prognostic Biomarkers for Stomach Adenocarcinoma Based on The Cancer Proteome Atlas

Guo-Liang Zheng[1], *Guo-Jun Zhang*[2], *Yan Zhao*[1] *and Zhi-chao Zheng*[1*]

[1] Department of Gastric Surgery, Cancer Hospital of China Medical University (Liaoning Cancer Hospital and Institute), Shenyang, China, [2] Department of Pathophysiology, College of Basic Medicine Science, China Medical University, Shenyang, China

OPEN ACCESS

Edited by:
Zheng Huachuan,
Chengde Medical University, China

Reviewed by:
Enhong Zhao,
Affiliated Hospital of Chengde Medical College, China
Danyi Zhao,
Dalian Medical University, China
Wei Li,
The First Hospital of Jilin University, China

***Correspondence:**
Zhi-chao Zheng
drzhengzhichao@sina.com
orcid.org/0000-0001-6841-1672

Specialty section:
This article was submitted to Molecular and Cellular Oncology, a section of the journal Frontiers in Oncology

Received: 21 March 2022
Accepted: 06 April 2022
Published: 28 April 2022

Citation:
Zheng G-L, Zhang G-J, Zhao Y and Zheng Z-c (2022) Screening Protein Prognostic Biomarkers for Stomach Adenocarcinoma Based on The Cancer Proteome Atlas. Front. Oncol. 12:901182. doi: 10.3389/fonc.2022.901182

The objective was to construct a prognostic risk model of stomach adenocarcinoma (STAD) based on The Cancer Proteome Atlas (TCPA) to search for prognostic biomarkers. Protein data and clinical data on STAD were downloaded from the TCGA database, and differential expressions of proteins between carcinoma and para-carcinoma tissues were screened using the R package. The STAD data were randomly divided into a training set and a testing set in a 1:1 ratio. Subsequently, a linear prognostic risk model of proteins was constructed using Cox regression analysis based on training set data. Based on the scores of the prognostic model, sampled patients were categorized into two groups: a high-risk group and a low-risk group. Using the testing set and the full sample, ROC curves and K-M survival analysis were conducted to measure the predictive power of the prognostic model. The target genes of proteins in the prognostic model were predicted and their biological functions were analyzed. A total of 34 differentially expressed proteins were screened (19 up-regulated, 15 down-regulated). Based on 176 cases in the training set, a prognostic model consisting of three proteins (COLLAGEN VI, CD20, TIGAR) was constructed, with moderate prediction accuracy (AUC=0.719). As shown by the Kaplan-Meier and survival status charts, the overall survival rate of the low-risk group was better than that of the high-risk group. Moreover, a total of 48 target proteins were identified to have predictive power, and the level of proteins in hsa05200 (Pathways in cancer) was the highest. According to the results of the Univariate and multivariate COX analysis, tri-protein was identified as an independent prognostic factor. Therefore, the tri-protein prognostic risk model can be used to predict the likelihood of STAD and guide clinical treatment.

Keywords: stomach adenocarcinoma, TCGA database, TCPA database, protein, prognosis

INTRODUCTION

Stomach cancer, a malignancy commonly seen among patients, had over 1 million new cases reported and caused 783,000 deaths in the year of 2018 (1). Domestic and foreign studies on the pathogenesis and risk factors of gastric cancer identify known risk factors to include helicobacter pylori infection, family history of upper cancer, history of gastric resection, smoking and consumption of pickled and fumigated food (2), but pathogenesis has not been fully clarified. In recent years, despite some advances in the diagnosis and treatment of STAD, the timeliness and accuracy of prognosis of patients has improved only slightly (3).

At present, the effective treatment for gastric cancer is still surgery, supplemented by radiotherapy and chemotherapy afterwards. In recent years, molecular targeted drugs have been gradually recognized as potentially effective, especially for patients with advanced STAD. Molecular targeted drugs have been rapidly promoted due to their highly targeted toxicity and low side effects (4–6). However, due to the high heterogeneity of STAD and differences in the mechanism of action of various anti-gastric cancer drugs, efficacy is uneven and the overall therapeutic effect is hardly satisfactory. Therefore, if a more efficient and simpler method of early cancer screening can be explored and developed as soon as possible, and targeted gastric cancer drugs with satisfactory efficacy and small side effects can be developed, the survival time of gastric cancer patients can be prolonged as far as possible while also improving patients' quality of life. It is also important to study the pathogenesis and progression of STAD to guide treatment and improve prognosis.

Today, reverse phase protein array (RPPA) data on 32 cancer types could be obtained from The Cancer Genome Atlas (TCGA) which is funded by the National Institute of Health (NIH) and available on the Cancer Proteome Atlas (TCPA). In addition, from TCGA, numerous "omics" data of different cancer types and clinical data from tumor samples are now available. With the combined use of RPPA data from TCPA and clinical data from TCGA, tumor patients with poor prognosis have been identified in studies. However, as far as we know, there is no such study on STAD. Therefore, we aimed to construct a protein signature model and evaluate its prognostic power for STAD. This article proposes a new method to identify STAD-related proteins, which is beneficial for the identification of new molecular targets and the choice of effective therapies for patients.

METHODS

Data Collection

The Cancer Proteome Atlas (TCPA) was used to mine data from patient cases with stomach adenocarcinoma (STAD). Reverse phase protein array (RPPA) data (level 4 data) for STAD was downloaded from TCPA (https://www.tcpaportal.org/tcpa/download.html). This dataset consists of 392 patient cases and measures the response to 218 antibodies. We also downloaded the clinicopathological data on 443 cases of STAD from the TCGA (https://portal.gdc.cancer.gov/). Both RPPA data and clinical data were downloaded on January 21, 2020. Since the data is from TCPA and TCGA, no further approval from the ethics committee was required, but we complied with the relevant regulations on TCPA and TCGA data access and patient privacy protection.

Establishment and Evaluation of Prognostic Risk Model

In this research, the random method was used to allocate patients with STAD into a training set and a testing set, in a 1:1 ratio. Using the former set, overall survival related proteins were identified using a risk ratio (HR) and univariate Cox regression analysis, with proteins having $P<0.05$ selected as candidate proteins for biomarkers. The candidate proteins were incorporated into further multivariate Cox regression analysis. The coefficient of each model protein was calculated *via* supervised principal component analysis and important proteins were selected using 10-fold cross-validation to eventually construct a prognostic risk model based on proteins' expression levels. The prognostic model score was equal to the sum of protein expression values multiplied by the corresponding coefficient. Prognostic score= ($\beta1\times$expression level of protein 1) + ($\beta2\times$expression level of protein 2) + … ($\beta n\times$expression level of protein n).

The protein prognostic model obtained from the training set was also used to predict the prognostic scores of the testing set and the set of patients with gastric cancer. The training set, testing set and the all set were divided into a high-risk group and a low-risk group using the median prognosis score in the training set as the critical value. The existence of survival differences between the high and low risk groups was verified using the Kaplan-Meier survival curve. The predictive power of the prognostic risk model was assessed using a Time-dependent ROC curve. The prognostic value of the independent prognostic model was evaluated based on the combination of prognostic risk model and clinical parameters as well as the univariate and multivariate Cox survival analysis. Forest maps were used to show Univariate and multivariate Cox survival analysis results.

Predicting the Co-Expression of The Three Proteins in the Model and Performing Biological Function Analysis

With a correlation>0.4 and P value<0.001 as screening conditions, 48 proteins related to proteins in the model were found. The Sankey diagram was drawn by the ggalluvial package of R software. In addition, for visual functional analysis, GO and KEGG analyses were performed using Metascape (http://metascape.org/). And $P < 0.05$ was considered statistically significant.

Data Processing and Statistical Analysis

The ActivePerl (version 5.26, 64-bit) scripting language was used for the integration and extraction of clinical data. R software

Abbreviations: AUC, Area Under The Curve; Coef, Regression coefficient; FDR, False Discovery Rate; GO, Gene Ontology; HR, Hazard Ratio; KEGG, Kyoto Encyclopedia Of Genes And Genomes; LogFC, Log2 Fold Change; OS, Overall Survival; STAD, Stomach Adenocarcinoma; QPCR, Quantitative Polymerase Chain Reaction; RPPA, Reverse phase protein array; ROC, Receiver Operating Characteristic Curve; TCGA, The Cancer Genome Atlas; TCPA, The Cancer Proteome Atlas.

(version 3.6.1) and the corresponding R packages were used for data processing and analysis. The extracted clinical data included the sample number, survival time, survival status, age, gender, grade, TNM stage, T status, N status, and M status. The clinical data were merged with the RPPA data. Statistical analyses and data processing were performed using SPSS Statistics 19.0 and R software (version 3.4.4). Volcano map of differentially expressed proteins was generated using the dplyr, ggplot2, and ggrepel software packages. Risk plot, survival plot and heatmap were generated by the pheatmap software package. While the survival curve, univariate and multivariate Cox survival analysis and the ROC curve were generated by survival, survminer, and survival ROC software packages. The mean ± SD was used for the description of continuous variables. The frequency (n) and proportion (%) were used for summarizing categorized variables. The Chi-square test was used for the comparison of proportion. Also, the T test was applied to compare continuous variables, P values are two-sided, and $P < 0.05$ is considered as statistical significance.

RESULTS

In **Figure 1**, we draw a flow diagram to present the workflow more clearly.

Data of TCGA Protein and Clinicopathological Information of Patients

A total of 352 patients with gastric cancer were finally enrolled into the study, including 222 males and 130 females. The patients were randomly divided into two groups: a training set (n = 176, mean age 65.78 ± 11.03 years) and a testing set (n = 176, mean age 64.72 ± 10.72 years). No significant difference was observed among clinical covariates ($P > 0.05$) between the two groups, as shown in **Table 1**.

Screening for Differentially Expressed Proteins

The screening criterion was log2 (HR) >1 and P value < 0.05. As shown in **Figure 2**, we analyzed the RPPA data of gastric cancer (n = 392) from TCGA, and screened a total of 34 differentially expressed proteins. Of these, 19 proteins (55.9%) were up-regulated and 15 proteins (44.1%) were down-regulated in gastric cancer.

Establishment and Evaluation of Prognostic Risk Models

We further conducted univariate and multivariate Cox regression analysis of the training set to establish a prognostic risk model composed of three proteins.

Prognostic risk score = (0.562 × COLLAGEN VI expression level) + (0.499 × CD20 expression level) + (-0.321 × TIGAR expression level).

As shown in **Table 2**, two proteins (COLLAGEN VI, CD20, HR value > 1) were associated with high risk (high expression increased risk of death of the patient), and one protein (TIGAR, HR value <1) was protective (high expression decreased risk of death of the patient). We categorized the cases of the training set into low-risk and high-risk groups based on the median of risk score (score=0.937).

We first performed K-M survival analysis on these three proteins, and found that all three proteins were related to survival (**Figures 3A–C**). Further, we analyzed the risk model of the three proteins. From **Figure 4**, for the training set, the kaplan-meier curve and log-rank test showed a high risk score was associated with poor prognosis ($P=2.079\times10^{-3}$) (**Figure 4A**). Cases with high risk score tended to express high-risk proteins, while cases with low risk score tended to express protective proteins. Compared with cases in the low-risk group, those in the high-risk group were observed to have higher mortality. The conclusion was based on the analyses that the lifetime mortality was 29.89% (26/87) in the low-risk group and 55.06% (49/89) in the high-risk group ($\chi2=11.4$, $P=0.0007$) (**Figure 4B**). The analysis on the testing set and all patients showed similar results (**Figures 4C–F**).

We also obtained the area under the curve (AUC) of the risk prognostic model for the 3-year survival rate of gastric cancer patients in the training set (AUC=0.719), testing set (AUC=0.706) and all set (AUC=0.714). The AUC values were higher than 0.7, indicating that the model had good prognostic performance, as shown in **Figure 5**, and suggesting that this tri-protein model can be used to predict survival in patients.

As shown in **Figure 6**, in the training set, there was a significant correlation between age, TNM stage, N status, M status and the (tri-protein) model risk score with prognosis ($P<0.05$) (**Figures 6A, B**), based on univariate Cox regression analysis. Furthermore, the (tri-protein) model risk score was found to be an independent prognostic factor for STAD (HR = 1.593, $P <0.001$) by using multivariate Cox regression analysis. The analysis on the testing set and all patients showed similar results (**Figures 6C–F**).

Analysis of Co-Expressed Proteins and Functions

The Sankey diagram of 48 proteins with strong correlation with the three proteins in the risk model was constructed (**Figure 7A**). As shown in **Figure 7B**, the most important enrichment pathways are shown on the Metascape site (GO and KEGG analyses). We found target genes were enriched, mainly in hsa05200: Pathways in cancer, regulation of DNA metabolic process, and regulation of growth.

DISCUSSION

In this study, proteins differentially expressed in TCPA were screened by bioinformatics technology. Then, the differentially expressed proteins were integrated with clinical parameters to establish a prognostic risk model composed of three proteins.

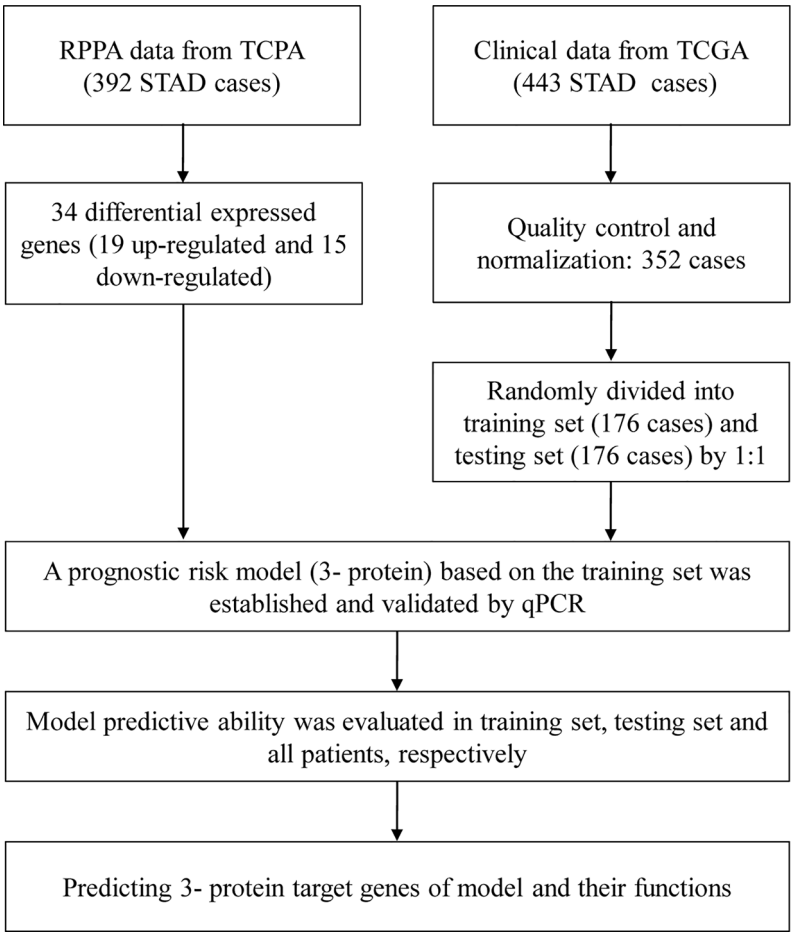

FIGURE 1 | Flow diagram.

The model showed good prognostic performance in the training set, testing set and all patients (the AUC of the ROC curve predicting 3-year survival was greater than 0.7). More importantly, the multivariate Cox regression analysis further demonstrated that it is an independent factor affecting the prognosis of STAD, so this Tri- protein can be used as a biomarker for the prediction of OS in STAD patients. The target genes and target gene enrichment pathways were predicted to be mostly related to cancer, among which hsa05200: Pathways in cancer has been reported to be involved in the development and progression of gastric cancer. This further indicates that the tri-protein model has a potential role in the molecular pathogenesis, clinical progress and gastric cancer prognosis, and that it is likely to provide help for the preventive diagnosis and individualized treatment of gastric cancer.

Two of the three proteins were high risk factors (expression level was negatively correlated with OS), including COLLAGEN VI and CD20. Originally, COLLAGEN VI was proposed as an extracellular matrix protein, forming a microfilament network and binding to extracellular matrix proteins through the functional subdomains. This is of great importance for organizing fibrillar collagens and being adhesive to the basement membrane (7). In COLLAGEN VI, there are three distinct α-chains (α-1, -2 and -3) and collagen VI α-3 (COL6A3) encodes the α-3 chain, which is longer compared with the other two chains (8). At present, it is widely believed that Collagen VI plays a role in breast and ovarian cancers, arousing the interest of researchers (9–11). There are few reports on gastric cancer at present, and only one literature suggests that COL6A3 may be an oncogene of human gastric cancer, and the antagonism of COL6A3 may be an effective method to treat gastric cancer (12).

As a transmembrane highly hydrophobic glycosylated phosphor protein of 35 kDa, the CD20 protein is encoded in humans by the MS4A1 gene (13). The CD20 protein features in the regulation and differentiation and growth of B cells based on cell activation from the resting state (G0) to the activated state (G1), and regulating cell cycle step-by-step progress from the S phase to mitosis (13). Actually, it is a portion of a cell-surface complex which regulates calcium transport and initiates an intracellular signaling pathway by

TABLE 1 | Clinicopathological data for the training and testing set.

Clinical characteristics	Total (n=352)	Training set (n=176)	Testing set (n=176)	χ2 value	P value
Age (years)	65.25 ± 10.89	65.78 ± 11.03	64.72 ± 10.72	1.059	0.707
Gender				2.391	0.122
male	222	118	104		
female	130	58	72		
Histologic Grade				1.107	0.575
well	7	3	4		
moderate	119	64	55		
poor	226	109	117		
Stage				4.339	0.231
I	39	20	19		
II	106	58	48		
III	167	83	84		
IV	40	15	25		
T				3.764	0.288
T1	12	9	3		
T2	69	36	33		
T3	169	84	85		
T4	102	47	55		
N				1.365	0.243
N0	104	47	57		
N+	248	129	119		
M				3.249	0.071
M0	325	167	158		
M1	27	9	18		

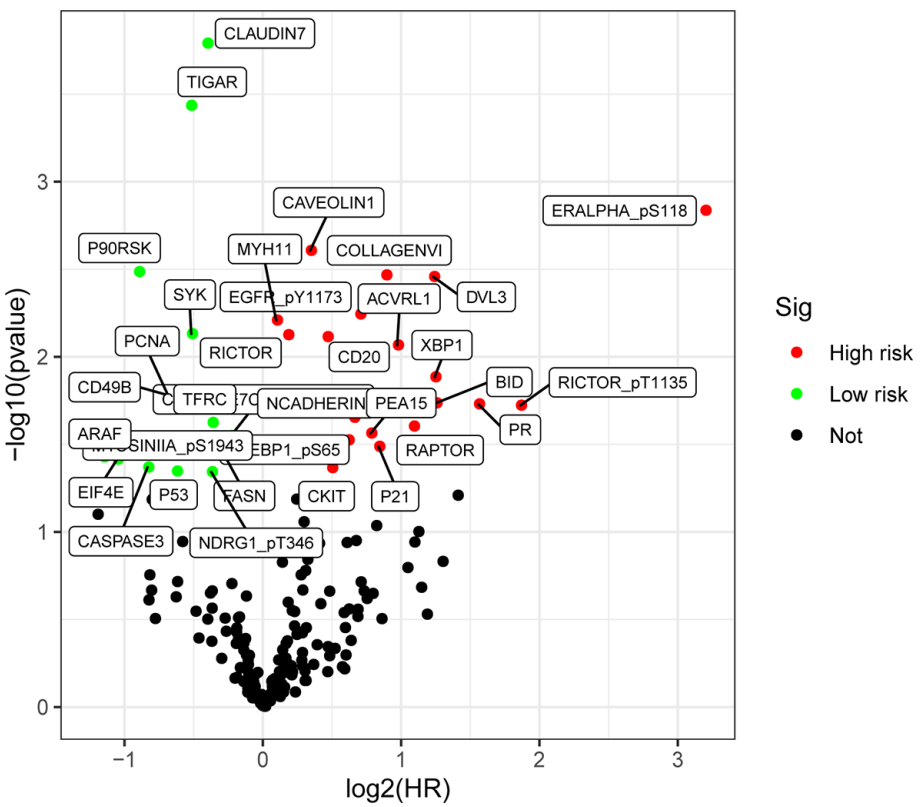

FIGURE 2 | Differential expression of proteins volcano map in gastric cancer. There is a difference in the expressions of up-regulated proteins (HR >1, P< 0.05) (highlighted in red), and down-regulated proteins (HR <1, P < 0.05) (highlighted in green).

TABLE 2 | Prognostic risk model constructed by R language.

Name	Coef	HR	HR.95L	HR.95H	P value
COLLAGEN VI	0.562	1.755	0.951	3.237	0.071
CD20	0.499	1.648	1.128	2.407	0.009
TIGAR	-0.321	0.725	0.525	1.002	0.051

Coef, regression coefficient; HR, risk ratio.

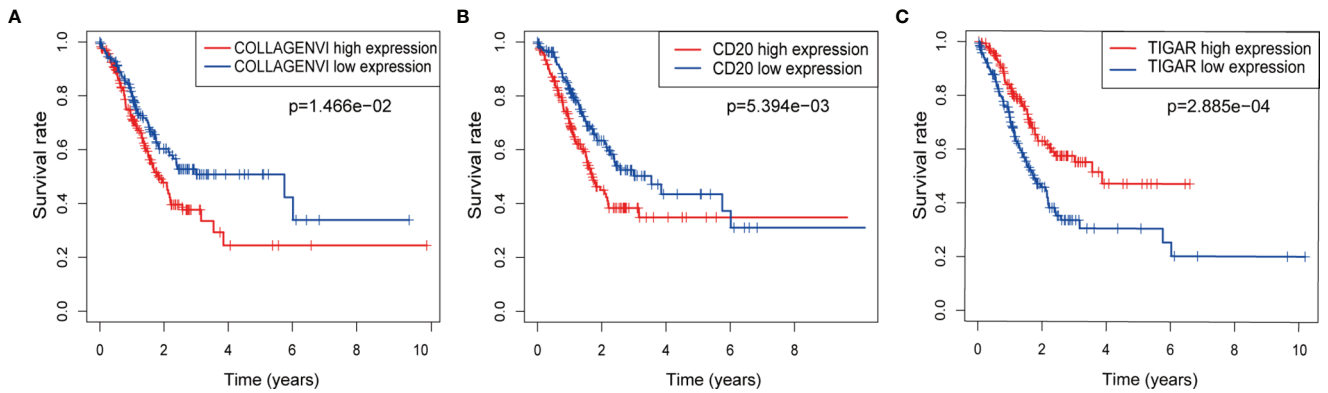

FIGURE 3 | The respective K-M survival prediction curves of the three proteins. **(A)** COLLAGEN VI; **(B)** CD20; **(C)** TIGAR.

calcium influx (14, 15). However, critical effects either on B-cell development or immune response implementation (15) have not been shown by disrupting calcium channel gene encoding. In the initial pro-B phase, CD20 has been observed within healthy mature B cells, chronic lymphocytic leukemia, LPHL and classical HL of some patients (14, 16). Moreover, it has also been found that expression of CD20 is also very important in HL disease pathophysiology and is likely to influence the patients,treatment prognosis, relapse and refractory response (16).

One of the three proteins in the developed mode, TIGAR, was low-risk (expression level is positively correlated with OS). TIGAR is a downstream regulator of p53, playing an essential function in metabolism through inhibition of glycolysis and promotion of the pentose phosphate pathway to function oxidative resistance and antiapoptosis (17). Therefore, researchers are more interested in the role of TIGAR in cancer due to its function in glycolysis and redox balance. More and more investigations have been conducted in this field, and they indicate high levels of TIGAR in hematopathy and solid tumors, including acute myeloid leukemia (18), lung cancer (19), colon cancer (20), pancreatic cancer (21) and breast cancer (22). Moreover, high TIGAR expression was an independent predictor of poor survival. Currently, the specific mechanism of the TIGAR is poorly studied, and its relationship with gastric cancer also needs further study. It is hoped that with in-depth study, its biological role and potential mechanism will become clearer.

According to ROC curve analysis, the AUC of the tri-protein model risk score prognosis was greater than 0.7 (between 0.7 and 0.9) in both the training group and the testing group, indicating that the prognostic model had certain accuracy in the diagnosis of STAD. Univariate and multivariate Cox regression analysis further revealed that the risk score model (3- protein) was an independent prognostic factor associated with OS (HR = 1.971, P <0.001). However, there are some shortcomings in this study. Firstly, the data randomly assigned to the training set and the testing set came from a single database. In future studies, setting up a separate set of external tests would make the model's results more convincing. Secondly, the follow-up time for the TCGA STAD study cohort is relatively short (the average follow-up time was only 20.78 months) and the deletion rate relatively high, which may affect the reliability of the kaplan-meier method. In the future, it is necessary to recruit more STAD patients and conduct longer follow-up studies to verify the findings of this experiment. In addition, the complex effects and specific mechanisms of these miRNAs need to be further studied.

CONCLUSION

In summary, our results suggest that our tri-protein model's risk score significantly differentiates the prognosis of patients

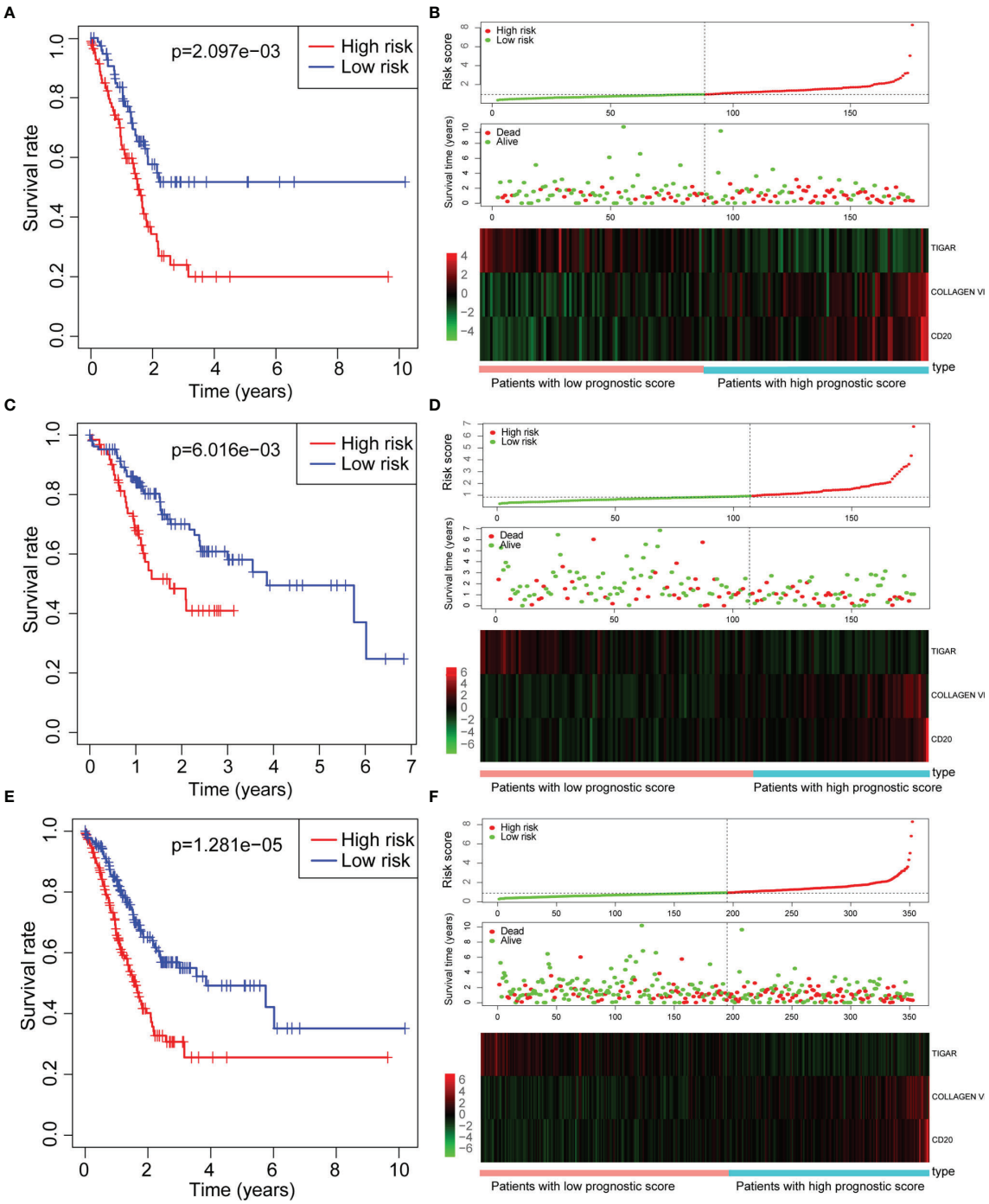

FIGURE 4 | Assessment of prognostic risk models. **(A, B)** Training set; **(C, D)** Testing set; **(E, F)** All set. **(A, C, E)** Kaplan-meier survival curve; **(B, D, F)** Risk score, scattered plots of survival time, and heat map of related proteins expression Note: Abscissa indicates cumulative frequency, and ordinate represents survival time (month). The green circle represents those alive, and the blue diamond represents deaths. The single inflection point of the risk score curve is marked by the dotted line. The gastric cancer patients were categorized into two groups: low risk group and high risk group.

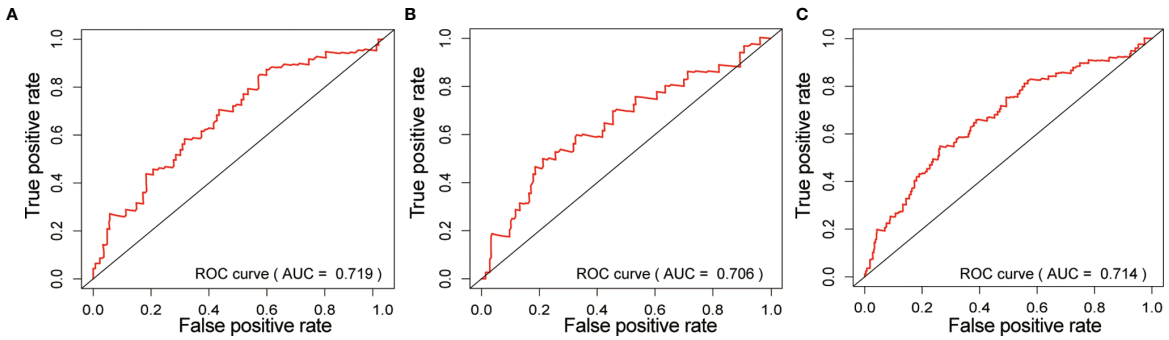

FIGURE 5 | Risk prognostic model in ROC curve of three groups. **(A)** Training set; **(B)** Testing set; **(C)** All set. the abscissa represents the true positive rate (sensitivity), and the ordinate represents the false positive rate (1-specificity).

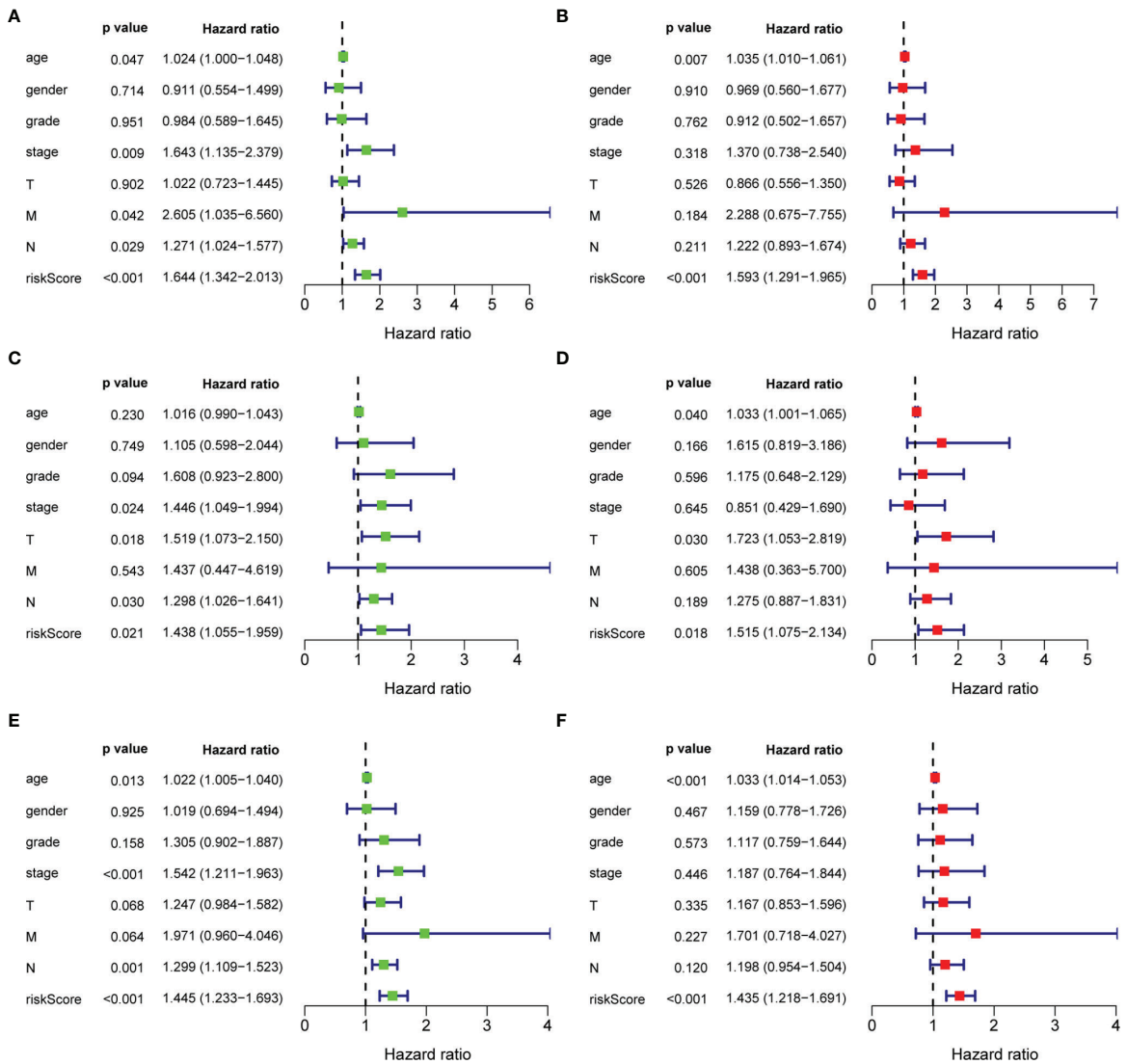

FIGURE 6 | Univariate and multivariate analysis of overall survival of patients. **(A, C, E)** Univariate analysis; **(B, D, F)** Multivariate analysis.

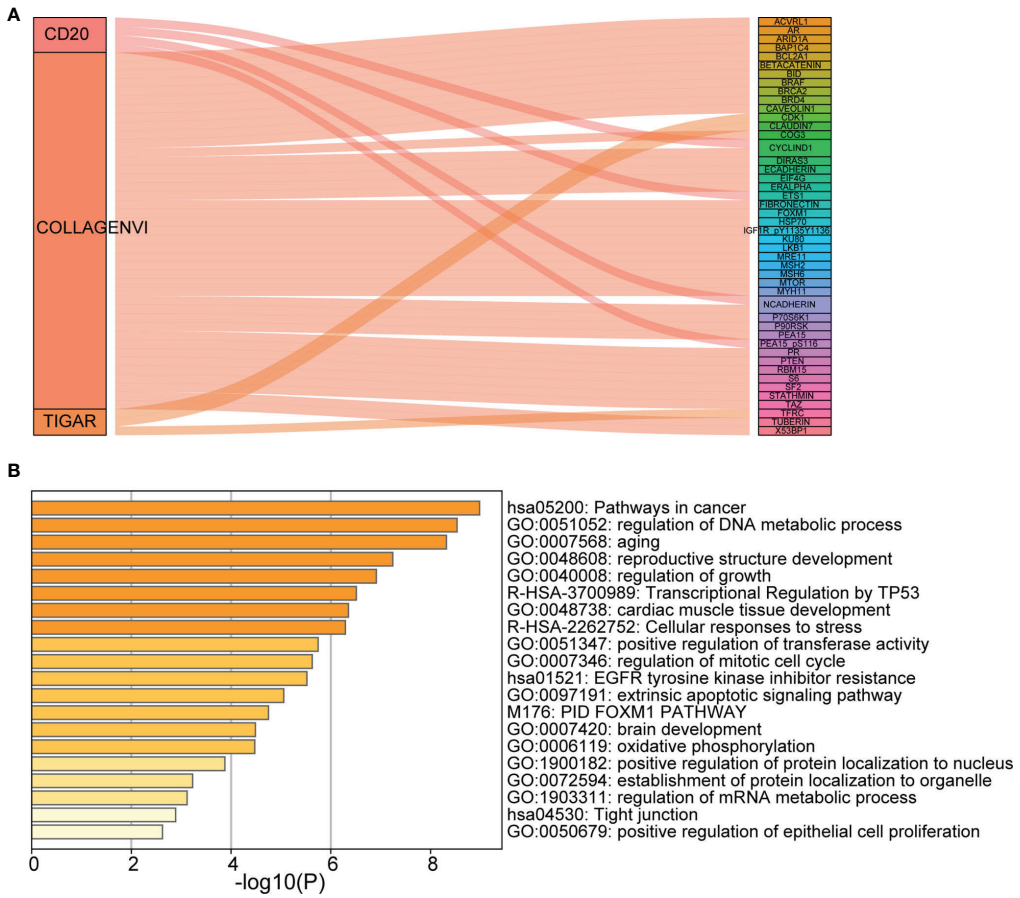

FIGURE 7 | Analysis of co-expressed proteins and functions. **(A)** Sankey diagram; **(B)** The main enrichment pathways (GO and KEGG analyses). Each rectangle denotes a gene, with the connection degree visualized by the rectangle area. The circle area reflects the number of genes on the pathway, while the color depth shows the -log10 (FDR) value. GO, Gene Ontology; KEGG, Kyoto Encyclopedia of Genes and Genomes.

with STAD during training and testing, and predicts 3-year overall survival. Therefore, this model may be a novel biomarker based on protein expression level, which is worthy of further study to determine the relevance of its clinical application.

DATA AVAILABILITY STATEMENT

The original contributions presented in the study are included in the article/supplementary material. Further inquiries can be directed to the corresponding author.

AUTHOR CONTRIBUTIONS

In this research, G-LZ made significant contributions to research conception, design of study. G-LZ and G-JZ collected, analyzed, and interpreted the data. G-LZ wrote the first draft of the manuscript. YZ and Z-cZ wrote sections of the manuscript and provided critical revisions. All authors agree to be accountable for all aspects of the work, and questions relevant to accuracy or integrity are dealt with and surveyed in an appropriate way. The final manuscript has been read and approved by all authors.

FUNDING

This study was supported in part by grants from Cultivation fund project of National Natural Science Foundation of China (No. 2021-ZLLH-06) and Medical engineering cross research fund project of Liaoning Province (No. LD202014).

REFERENCES

1. Bray F, Ferlay J, Soerjomataram I, Siegel RL, Torre LA, Jemal A. Global Cancer Statistics 2018: GLOBOCAN Estimates of Incidence and Mortality Worldwide for 36 Cancers in 185 Countries. *CA Cancer J Clin* (2018) 68 (6):394–424. doi: 10.3322/caac.21492
2. den Hoed CM, Kuipers EJ. Gastric Cancer: How Can We Reduce the Incidence of This Disease. *Curr Gastroenterol Rep* (2016) 18(7):34. doi: 10.1007/s11894-016-0506-0
3. Lazăr DC, Tăban S, Cornianu M, Faur A, Goldiş A. New Advances in Targeted Gastric Cancer Treatment. *World J Gastroenterol* (2016) 22 (30):6776–99. doi: 10.3748/wjg.v22.i30.6776
4. Bang YJ, Van Cutsem E, Feyereislova A, Chung HC, Shen L, Sawaki A, et al. Trastuzumab in Combination With Chemotherapy Versus Chemotherapy Alone for Treatment of HER2-Positive Advanced Gastric or Gastro-Oesophageal Junction Cancer (ToGA): A Phase 3, Open-Label, Randomised Controlled Trial. *Lancet* (2010) 376:687–97. doi: 10.1016/S0140-6736(10)61121-X
5. Li J, Qin S, Xu J, Xiong J, Wu C, Bai Y, et al. Randomized, Double-Blind, Placebo-Controlled Phase III Trial of Apatinib in Patients With Chemotherapy-Refractory Advanced or Metastatic Adenocarcinoma of the Stomach or Gastroesophageal Junction. *J Clin Oncol* (2016) 34:1448–54. doi: 10.1200/JCO.2015.63.5995
6. Kang YK, Boku N, Satoh T, Ryu MH, Chao Y, Kato K, et al. Nivolumab in Patients With Advanced Gastric or Gastro-Oesophageal Junction Cancer Refractory to, or Intolerant of, at Least Two Previous Chemotherapy Regimens (ONO-4538-12, ATTRACTION-2): A Randomised, Double-Blind, Placebo-Controlled, Phase 3 Trial. *Lancet* (2017) 390:2461–71. doi: 10.1016/S0140-6736(17)31827-5
7. Bönnemann CG. The Collagen VI-Related Myopathies: Muscle Meets its Matrix. *Nat Rev Neurol* (2011) 7:379–90. doi: 10.1038/nrneurol.2011.81
8. Aumailley M, Mann K, der Mark HV, Timpl R. Cell Attachment Properties of Collagen Type VI and Arg-Gly-Asp Dependent Binding to its Alpha 2(VI) and Alpha 3(VI) Chains. *Exp Cell Res* (1989) 181:463–74. doi: 10.1016/0014-4827(89)90103-1
9. Iyengar P, Espina V, Williams TW, Lin Y, Berry D, Jelicks LA, et al. Adipocyte-Derived Collagen VI Affects Early Mammary Tumor Progression *In Vivo*, Demonstrating a Critical Interaction in the Tumor/Stroma Microenvironment. *J Clin Invest* (2005) 115:1163–76. doi: 10.1172/JCI23424
10. Schäffler A, Schölmerich J, Buechler C. Mechanisms of Disease: Adipokines and Breast Cancer - Endocrine and Paracrine Mechanisms That Connect Adiposity and Breast Cancer. *Nat Clin Pract Endocrinol Metab* (2007) 3:345–54. doi: 10.1038/ncpendmet0456
11. Sherman-Baust CA, Weeraratna AT, Rangel LB, Pizer ES, Cho KR, Schwartz DR, et al. Remodeling of the Extracellular Matrix Through Overexpression of Collagen VI Contributes to Cisplatin Resistance in Ovarian Cancer Cells. *Cancer Cell* (2003) 3:377–86. doi: 10.1016/S1535-6108(03)00058-8
12. Xie X, Liu X, Zhang Q, Yu J. Overexpression of Collagen VI α3 in Gastric Cancer. *Oncol Lett* (2014) 7:1537–43. doi: 10.3892/ol.2014.1910
13. Tedder TF, Streuli M, Schlossman SF, Saito H. Isolation and Structure of a cDNA Encoding the B1 (CD20) Cell-Surface Antigen of Human B Lymphocytes. *Proc Natl Acad Sci USA* (1988) 85:208–12. doi: 10.1073/pnas.85.1.208
14. Einfeld DA, Brown JP, Valentine MA, Clark EA, Ledbetter JA. Molecular Cloning of the Human B Cell CD20 Receptor Predicts a Hydrophobic Protein With Multiple Transmembrane Domains. *EMBO J* (1988) 7:711–7. doi: 10.1002/j.1460-2075.1988.tb02867.x
15. Maloney DG. Anti-CD20 Antibody Therapy for B-Cell Lymphomas. *N Engl J Med* (2012) 366:2008–16. doi: 10.1056/NEJMct1114348
16. Küppers R, Engert A, Hansmann ML. Hodgkin Lymphoma. *J Clin Invest* (2012) 122:3439–47. doi: 10.1172/JCI61245
17. Rodríguez-Gil JE, Gómez-Foix AM, Fillat C, Bosch F, Guinovart JJ. Activation by Vanadate of Glycolysis in Hepatocytes From Diabetic Rats. *Diabetes* (1991) 40:1355–9. doi: 10.2337/diabetes.40.10.1355
18. Qian S, Li J, Hong M, Zhu Y, Zhao H, Xie Y, et al. TIGAR Cooperated With Glycolysis to Inhibit the Apoptosis of Leukemia Cells and Associated With Poor Prognosis in Patients With Cytogenetically Normal Acute Myeloid Leukemia. *J Hematol Oncol* (2016) 9:128. doi: 10.1186/s13045-016-0360-4
19. Zhou X, Xie W, Li Q, Zhang Y, Zhang J, Zhao X, et al. TIGAR is Correlated With Maximal Standardized Uptake Value on FDG-PET and Survival in non-Small Cell Lung Cancer. *PloS One* (2013) 8:e80576. doi: 10.1371/journal.pone.0080576
20. Al-Khayal K, Abdulla M, Al-Obeed O, Al KW, Zubaidi A, Vaali-Mohammed MA, et al. Identification of the TP53-Induced Glycolysis and Apoptosis Regulator in Various Stages of Colorectal Cancer Patients. *Oncol Rep* (2016) 35:1281–6. doi: 10.3892/or.2015.4494
21. Rajeshkumar NV, Dutta P, Yabuuchi S, de Wilde RF, Martinez GV, Le A, et al. Therapeutic Targeting of the Warburg Effect in Pancreatic Cancer Relies on an Absence of P53 Function. *Cancer Res* (2015) 75:3355–64. doi: 10.1158/0008-5472.CAN-15-0108
22. Won KY, Lim SJ, Kim GY, Kim YW, Han SA, Song JY, et al. Regulatory Role of P53 in Cancer Metabolism *via* SCO2 and TIGAR in Human Breast Cancer. *Hum Pathol* (2012) 43:221–8. doi: 10.1016/j.humpath.2011.04.021

Conflict of Interest: The authors declare that the research was conducted in the absence of any commercial or financial relationships that could be construed as a potential conflict of interest.

frontiers | Frontiers in Pharmacology

ORIGINAL RESEARCH
published: 02 May 2022
doi: 10.3389/fphar.2022.890891

Profilin 1 Induces Tumor Metastasis by Promoting Microvesicle Secretion Through the ROCK 1/p-MLC Pathway in Non-Small Cell Lung Cancer

*Ya Wang[1], Yichen Lu[2], Rongjun Wan[1], Yang Wang[1], Chunfang Zhang[3], Min Li[1], Pengbo Deng[1], Liming Cao[1] and Chengping Hu[1]**

[1]Department of Respiratory Medicine, Xiangya Hospital, Central South University, Changsha, China, [2]Department of Oncology, Hunan Provincial People's Hospital/The First Affiliated Hospital of Hunan Normal University, Changsha, China, [3]Department of Thoracic Surgery, Xiangya Hospital, Central South University, Changsha, China

Profilin 1 (PFN1), an actin-binding protein, plays contrasting roles in the metastasis of several cancers; however, its role in non-small cell lung cancer (NSCLC) metastasis remains unclear. Here, PFN1 expression was upregulated in metastatic NSCLC tissues. PFN1 overexpression significantly promotes NSCLC metastasis *in vitro* and *in vivo*. Proteomics analysis revealed PFN1 involvment in microvesicles (MVs) secretion. *In vitro* experiments confirmed that PFN1 overexpression increased secretion of MVs. MVs are important mediators of metastasis. Here, we show an increased abundance of MVs in the sera of patients with metastatic NSCLC compared to that in the sera of patients with non-metastatic NSCLC. Both *in vitro* and *in vivo* experiments revealed that PFN1 could increase MV secretion, and MVs derived from PFN1-overexpressing cells markedly promoted NSCLC metastasis. We then elucidated the mechanisms underlying PFN1-mediated regulation of MVs and found that PFN1 could interact with ROCK1 and enhance its kinase activity to promote myosin light chain (MLC) phosphorylation for MV secretion. Inhibition of ROCK1 decreased MV secretion and partially reversed the PFN1-induced promotion of NSCLC metastasis. Collectively, these findings show that PFN1 regulates MV secretion to promote NSCLC metastasis. PFN1 and MVs represent potential predictors or therapeutic targets for NSCLC metastasis.

Keywords: non-small cell lung cancer, Profilin 1, microvesicles, ROCK/p-MLC pathway, metastasis

OPEN ACCESS

Edited by:
Kun Zhang,
Tongji University, China

Reviewed by:
Jianwen Qin,
Tianjin Chest Hospital, China
Yi Liao,
Affiliated Hospital of Southwest Medical University, China

****Correspondence:***
Chengping Hu
huchengp28@csu.edu.cn

Specialty section:
This article was submitted to Pharmacology of Anti-Cancer Drugs, a section of the journal Frontiers in Pharmacology

Received: *07 March 2022*
Accepted: *12 April 2022*
Published: *02 May 2022*

Citation:
Wang Y, Lu Y, Wan R, Wang Y, Zhang C, Li M, Deng P, Cao L and Hu C (2022) Profilin 1 Induces Tumor Metastasis by Promoting Microvesicle Secretion Through the ROCK 1/p-MLC Pathway in Non-Small Cell Lung Cancer. Front. Pharmacol. 13:890891. doi: 10.3389/fphar.2022.890891

INTRODUCTION

Non-small cell lung cancer (NSCLC) accounts for ~85% of all lung cancer cases and has a poor 5-year survival rate of ~15% (Chen et al., 2014; Siegel et al., 2018). Despite major advances in treatment, the prognosis of lung cancer remains poor owing to extensive metastasis at diagnosis (Herbst et al., 2018). Lung cancer cells metastasize to distant organs through a complex process called the invasion–metastasis cascade (Fidler, 2003; Gupta and Massagué, 2006; Talmadge and Fidler, 2010), during which molecular signal exchange between tumor cells and between tumor cells and the stroma is crucial (Dudas, 2015).

Profilin 1 (PFN1) is a 135-amino acid, 15 kDa conservative actin-binding protein. PFN1 is expressed at every stage of embryonic development and is ubiquitously expressed by all cell types and

nearly all tissues (Alkam et al., 2017). Numerous studies have confirmed that PFN1 involved in tumor proliferation, apoptosis, stemness, immune response and metastasis (Liao et al., 2021; Wang et al., 2021). Specifically, large amount of studies focused on its roles in cancer metatasis. Accumulating evidence suggests that PFN1 participates in the metastasis of breast cancer (Ding et al., 2014), hepatocellular carcinoma (Wang et al., 2019), and renal cell cancer (Karamchandani et al., 2015). However, the role of PFN1 differs from cancer to cancer, and the mechanisms underlying PFN1 function in cancer metastasis are not fully understood. Numerous studies revealed that PFN1 plays a vital role in membrane trafficking (Dong et al., 2000; Valenzuela-Iglesias et al., 2015; Lu et al., 2018), thus providing insights into the mechanism underlying its function in cancer metastasis.

Extracellular vesicles are a heterogeneous group of nano-scale lipid-bilayered structures secreted by all cell types, including cancer cells. They are classified by size as exosomes (40–120 nm), microvesicles (MVs; 50–1,000 nm), or apoptotic bodies (500–2,000 nm) (EL Andaloussi et al., 2013; Liang et al., 2021) and play a critical role in cell-to-cell communication (Balaj et al., 2011; Chiodoni et al., 2019; Lv et al., 2019). Tumor cells can release large quantities of MVs, the abundance of which correlates with tumor invasiveness and development (Muralidharan-Chari et al., 2010; Menck et al., 2020). Proteins, lipids, and nucleic acids, including various microRNAs (miRNAs) and long non-coding RNAs (lncRNAs), are selectively trafficked into MVs, where they ultimately affect gene expression regulation and cell functions (Raposo and Stoorvogel, 2013; Tricarico et al., 2017; Fabbiano et al., 2020). Unlike exosomes, MVs bud directly from the cell membrane (Tricarico et al., 2017), a process that relies on actin-myosin interactions and ATP-dependent contraction. Phosphorylation of myosin light chain (MLC) at the neck of the budding vesicle is mediated by either the rho-associated coiled-coil containing kinase (ROCK) signaling pathway (Li et al., 2012) or the ADP-ribosylation factor 6 (ARF6) (Muralidharan-Chari et al., 2009), which activate MLC and promote MV release. As an important actin-binding protein, PFN1 is closely related to cytoskeletal regulation and membrane trafficking. However, its role in MV secretion is elusive, and whether PFN1 affects NSCLC metastasis by regulating MV secretion is unclear.

In this study, we systematically explored the roles of PFN1 in tumor metastasis and MV secretion in NSCLC, and confirmed that PFN1 promoted NSCLC metastasis by promoting the secretion of MVs *in vitro* and *in vivo*. Mechanistically, we demonstrated that PFN1 interacted with ROCK1, followed by its activation, and thus promoted phosphorylation of MLC, which in turn increased the secretion of MVs.

MATERIALS AND METHODS

Patients and Ethics Statement

Forty-five patients with lung adenocarcinoma admitted to our hospital were divided into metastatic and non-metastatic groups, according to the 2019 Chinese Society of Clinical Oncology guidelines (**Supplementary Table S1**). Patients with definite pathological diagnosis of lung adenocarcinoma and available clinical information were included. Patients with complications of other malignant diseases, inflammatory diseases, or chronic diseases, such as diabetes, hypertension, or coronary heart diseases, were excluded before recruiment. The study design and protocol were approved by the Ethics Committee of Hunan Provincial People's Hospital/The First Affiliated Hospital of Hunan Normal University (Changsha, Hunan, China, 2020-Provincial 02) and adhered to the ethical guidelines of the Declaration of Helsinki. Informed consent was obtained from all participants.

Tissue Chip and Immunohistochemistry

Tissue chips were purchased from Shanghai Outdo Biotech (Shanghai, China) (**Supplementary Table S2**). For animal experiments, lung tissues were harvested and fixed in 4% paraformaldehyde. The fixed samples were embedded in paraffin; 4-μm-thick sections were cut onto glass slides, and immunohistochemistry analysis was conducted as described previously (Feng et al., 2020). Before staining, the slides were heated at 60°C and then treated with an alcohol gradient. After removing endogenous catalase with 3% hydrogen peroxide, the slides were blocked with 3% normal sheep serum (ZSbio, Beijing, China) at room temperature for 1 h. The samples were then incubated overnight with primary antibodies at 4°C. Primary antibody concentrations were as follows: anti-PFN1, 1:500 (Abcam, Cambridge, MA, United States) and anti-phosphorylated (p)-MLC, 1:100 (Abclonal, Wuhan, China, phosphorylation site is at S18) (catalog numbers listed in **Supplementary Table S3**). Protein expression was determined using the VECTASTAIN Elite ABC HRP Kit (Vector Laboratories, Burlingame, CA, United States) and VECTOR DAB Kit (Vector Laboratories) following the manufacturer's instructions. Images were acquired using a PANNORAMIC whole slide scanner (3DHISTECH, Budapest, Hungary). The staining intensity was the product of staining characteristics of the target cell (no staining was scored as 0, light yellow as 1, yellow/brown as 2, and brown as 3) and the positive rate of cells (0–5% was scored as 0, 6–25% as 1, 26–50% was 2, 51–75% as 3, and >75% as 4).

Immunofluorescence

Tissues were fixed with 4% paraformaldehyde and permeabilized with 0.2% Triton X-100. After blocking with 3% bovine serum albumin (BSA; Servicebio, Wuhan, China), the slides were incubated with primary antibodies overnight at 4°C. Primary antibody concentrations were as follows: anti-PFN1, 1:100 (Abcam), anti-Napsin A, 1:100 (Abcam), anti-ROCK1, 1:100, (ImmunoWay, Plano, TX, United States), anti-ROCK2, 1:100 (ImmunoWay) and anti-annexin A1, 1:100 (Servicebio). Next, the slides were incubated with fluorophore-conjugated secondary antibodies (1:5,000, Proteintech, Wuhan, China) at room temperature. DAPI (Servicebio) was used to stain the nuclei. The samples were then visualized using a fluorescence microscope (Nikon, Tokyo, Japan).

Cell Culture and Treatment

H1299 and A549 cell lines were kindly provided by Stem Cell Bank, Chinese Academy of Sciences (Beijing, China). HEK-293T cells were kindly provided by Professor Chun Fang Zhang (Department of Thoracic Surgery, Xiangya Hospital, Central South University). Cells were cultured in RPMI 1640 medium (Gibco, Waltham, MA, United States) or Dulbecco's modified Eagle medium (Gibco) (HEK-293T cells only) supplemented with 10% fetal bovine serum (Gibco), 100 U/mL penicillin, and 100 μg/ml streptomycin (Gibco) and incubated at 37°C and 5% CO_2.

Plasmid Construction and Transfection

The human PFN1-coding sequence was amplified from human cDNA using 2× Phanta Master Mix (Vazyme, NanJing, China) and cloned into a pLVX-IRES-ZsGreen1 and pEGFP-C3 vector using the ClonExpress II One Step Cloning Kit (Vazyme). The primers were synthesized by TsingKe Biology Company (Beijing, China) and are listed in **Supplementary Table S4**. After gene recombination and transformation into *Escherichia coli*, plasmids were extracted using the FastPure Plasmid Mini Kit (Vazyme). The plasmids were then selected according to sequence screening. All genes were transfected into cells using lentivirus infection. pLVX-EF1α-IRES-puro, pLVX-EF1α-IRES-puro-PFN1-Flag, pLVX-EF1α-IRES-puro-PFN1-R88L-Flag, pLVX-EF1α-IRES-puro-PFN1-H119E-Flag, pLVX-EF1α-IRES-puro-PFN1-H133S-Flag, and pLVX-EF1α-IRES-puro-ROCK2-myc were purchased from General Biology Company (Chuzhou, China). ROCK1 pcDNA3.1-HA-C was purchased from You Bao Biology (Changsha, China). PFN1 siRNA and control scramble siRNA were synthesized by Guangzhou RiboBio Co. (Guangzhou, China), and the sequences are listed in **Supplementary Table S4**. Plasmids and siRNAs were transfected into cells using Lipofectamine™ 3000 Transfection Reagent (Invitrogen, Waltham, MA, United States) according to the manufacturer's instructions.

Wound Healing Assay

Cells in the logarithmic growth phase were seeded onto six-well plates (3×10^5 cells/well). The supernatants were collected from cultured cells transfected with the empty vector (EV) and those overexpressing PFN1. Pipette tips were used to make a straight scratch in each well; we ensured that the width of each scratch was similar. Images were captured under microscopy (Nikon) every 12 h until the wound was healed. Data were obtained from at least three independent experiments.

Transwell Migration Assay

Cell migration was assessed using 24-well Transwell culture chambers (Corning, Corning, NY, United States). Cells (2×10^4) suspended in 200 μl serum-free medium were seeded in the upper chamber. The lower chamber was filled with 800 μl complete medium. After incubation at 37°C for 24 h, the cells were fixed in 4% paraformaldehyde for 20 min. After being washed thrice with PBS, the cells were stained using 1% crystal violet (Solarbio, Beijing, China) for 10 min. Cells that transmigrated to the lower chamber were counted. Data were obtained from at least three independent experiments.

Isolation of Microvesicles

Microvesicles (MVs) were isolated using continuous differential centrifugation as described previously (Jeppesen et al., 2019). Briefly, H1299 and A549 cells were divided into two groups: EV and PFN1 overexpression. Approximately 2.5×10^6 cells at log phase were seeded into T75 cell culture flasks with serum-free medium. After being incubated at 37°C for 48 h, cell supernatants were collected. The supernatants were centrifuged at $750 \times g$ for 5 min followed by centrifugation at $1{,}500 \times g$ for 10 min to remove cell debris. The subsequent supernatants were centrifuged at $16{,}000 \times g$ for 45 min. The obtained pellets were resuspended in 1 ml PBS and centrifuged at $16{,}000 \times g$ for 45 min. A total of 40 μl PBS was used to resuspend the pellets for subsequent studies. MVs in the serum were also extracted using continuous differential centrifugation and stored at −80°C for use in subsequent analyses.

Electron Microscopy

MVs were fixed in 2.5% glutaraldehyde. Electron microscopy was conducted at the Department of Pathology of Xiangya Hospital, Central South University (Changsha, China).

Flow Cytometry for Quantitative Analysis of Microvesicles

The amount of MVs was analyzed using a three-laser Cytek Northern Lights SpectralFlow Cytometry instrument (Cytek, Fremont, CA, United States), according to the manufacturer's instructions. Standard microbeads (ranging from 100 nm to 1 μm) were used for size calibration. Microparticles ranging from 100 nm to 1 μm were counted. The counting endpoint was set at 25 s for all eligible granules.

Detection of Microvesicle Uptake

MVs stained with PKH67 (Sigma, Darmstadt, Germany) were added to H1299 cells. After incubation for 24 h, cells were fixed and stained with DAPI. Then, fluorescence microscopy (Nikon) was used to detect MS uptake.

RNA Extraction and Reverse Transcription-Quantitative PCR

Total RNA was extracted from cells at the logarithmic phase using TRIzol reagent (Takara, Kyoto, Japan). Reverse transcription was conducted using the PrimeScript RT Reagent Kit (Takara). RT-qPCR was conducted on a 96-well Automation Compatible Polypropylene PCR Microplate (Axygen, Darmstadt, Germany) using the TB Green Premix qPCR Mix (Takara) per manufacturer's instructions. Primer sequences are listed in **Supplementary Table S4**. Data were obtained from at least three independent experiments.

Protein Extraction, Western Blotting, and Co-Immunoprecipitation

Whole-cell lysates were prepared using RIPA Lysis Buffer (Beyotime, Shanghai, China) containing a protease inhibitor

cocktail (Bimake, Houston, TX, United States) and phosphatase inhibitor (Roche, Basel, Switzerland). The protein concentration was quantified using a BCA Kit (Beyotime). An equal amount of protein (25 μg) was used for electrophoresis. Proteins were separated using 10/12% SDS PAGE and then transferred onto polyvinylidene difluoride membranes (Millipore, Billerica, MA, United States). The membranes were then blocked with a solution of 3% BSA (Solarbio) in TBS with Tween 20 (Solarbio) at room temperature for 1 h. The membranes were next incubated with primary antibodies (dilution ratio listed in **Supplementary Table S3**) overnight at 4°C, followed by incubation with horseradish peroxidase-conjugated anti-rabbit or anti-mouse secondary antibodies (1:5,000, Proteintech) at room temperature for 2 h. After washing, the protein bands were detected using Luminata Western HRP Substrate (Millipore) and a Gene Genius Bioimaging System (Bio-Rad, Hercules, CA, United States). Co-IP was conducted using Pierce™ Protein A/G Magnetic Beads (Thermo Fisher Scientific) per manufacturer's instructions. Data were obtained from at least three independent experiments.

ROCK Kinase Assay

Purified ROCK1/2, PFN1, and PFN1 mutants were isolated from HEK-293T cells transfected with *ROCK1/2* or *PFN1* overexpression/mutant plasmids using Pierce™ Protein A/G Magnetic Beads (Thermo Fischer Scientific) per manufacturer's instruction. The ROCK Kinase assay (Abcam) was used to evaluate the effect of PFN1 or its mutants on ROCK1/2 activity per the manufacturer's instructions. Data were obtained from at least three independent experiments.

In Vivo Metastasis Assay

Nude mice (4 weeks old, female, 18–20 g) were purchased from Hunan SJA Laboratory Animal Co., Ltd. (Changsha, China). The mice were nurtured in individual ventilated caging systems under a specific pathogen-free environment. A metastasis model was constructed via intracardiac injection of H1299 cells. Briefly, after being anesthetized by injecting 2% sodium pentobarbital (40 mg/kg) intraperitoneally, the mice's skin was cut along the left parasternal line to locate the second intercostal space. Needles were inserted into the second intercostal space along the left margin of the sternum. Pulsating arterial blood indicated the correct location in the left ventricle. A total of 8×10^5 H1299 cells/mouse, suspended in PBS, were injected immediately. MVs (tatol MVs collected from 3×10^6 H1299 EV cells or PFN1 OE cells for each mouse) were injected together with cells. When significant weight loss was observed, the mice were sacrificed for subsequent analyses. All animal experimental procedures were performed in accordance with the Guide for the Care and Use of Laboratory Animals of Hunan Provincial People's Hospital/The First Affiliated Hospital of Hunan Normal University and approved by the Institutional Animal Ethics Committee. All animal experiments complied with the ARRIVE guidelines.

Sample Preparation for Proteomics

H1299 EV and PFN1 OE cells were harvested at logarithmic growth period and each cell type was collected in biological triplicate. Total cellular protein extracted by RIPA lysis buffer and concentration of proteins were determined by bicinchoninic acid (BCA) protein assay kit (Beyotime) according to manufacturer instructions. A total of 100ug proteins of each sample were then precipitated by acetone at −20°C overnight. Dissolve protein precipitation by water bath ultrasound for 3 min after adding 100 μl protein resolve buffer. Dithiothreitol (DTT) (Sigma-Aldrich) was used to reduced disulfide bond. Then reduced disulfide bonds were Alkylated by iodoacetamide (IAA) (Sigma-Aldrich). Thoroughly mixed trypsin with the samples in the ratio of trypsin: protein = 1:50 and incubate overnight at 37°C 1,000 rpm to digest proteins. Peptides were labeled by TMT Isobaric Label Reagent Set (Thermo Fisher Scientific, Waltham, MA, United States) according to manufacturer instructions. After SDS cleanup, peptide desalting and gigh-pH pre-fractionation, peptides were freeze at 80°C after vacuum drying and ready for later nanoLC-MS/MS analysis.

NanoLC-MS/MS Analysis

For each sample, 2 ug of total peptides were separated and analyzed with a nano-UPLC (EASY-nLC1200) coupled to a Q Exactive HFX Orbitrap instrument (Thermo Fisher Scientific) with a nano-electrospray ion source. Separation was performed by using a reversed-phase column (100 μ ID ×15 cm, Reprosil-Pur 120 C18-AQ, 1.9 μ, Dr. Maisch). Mobile phases were H_2O with 0.1% FA, 2% ACN (phase A) and 80% ACN, 0.1% FA (phase B). Separation of sample was executed with a 90 min gradient at 300 nl/min flow rate. Gradient B: 2–5% for 2 min, 5–22% for 68 min, 22–45% for 16 min, 45–95% for 2 min, 95% for 2 min.

Data dependent acquisition (DDA) was performed in profile and positive mode with Orbitrap analyzer at a resolution of 120,000 (@200 m/z) and m/z range of 350–1,600 for MS1. For MS2, the resolution was set to 15k with a fixed first mass of 110 m/z. The automatic gain control (AGC) target for MS1 was set to 3E6 with max IT 30 ms, and 1E5 for MS2 with max IT 96 ms. The top 20 most intense ions were fragmented by HCD with normalized collision energy (NCE) of 32%, and isolation window of 0.7 m/z. The dynamic exclusion time window was 45 s, single charged peaks and peaks with charge exceeding 6 were excluded from the DDA procedure.

MS Data Analysis

Raw MS files were processed using Proteome Discoverer (PD) software (Version 2.4.0.305, Thermo Fisher Scientific) and the built-in Sequest HT search engine . MS spectra lists were searched against their species-level UniProt FASTA databases (uniprot-Homo sapiens-2021-8.fasta), with Carbamidomethyl [C], TMT 6 plex(K) and TMT 6 plex (N-term) as a fixed modification and Oxi- dation (M) and Acetyl (Protein N-term) as variable modifications. The protease was trypsin. A maximum of two missed cleavage(s) was allowed. The false discovery rate (FDR) was set at 0.01 for both PSM and peptide levels. Peptide identification was performed with an initial precursor mass deviation of up to 10 ppm and a fragment mass deviation of 0.02 Da. Unique peptide and Razor peptide were used for protein quantification and total peptide amount for normalization. All

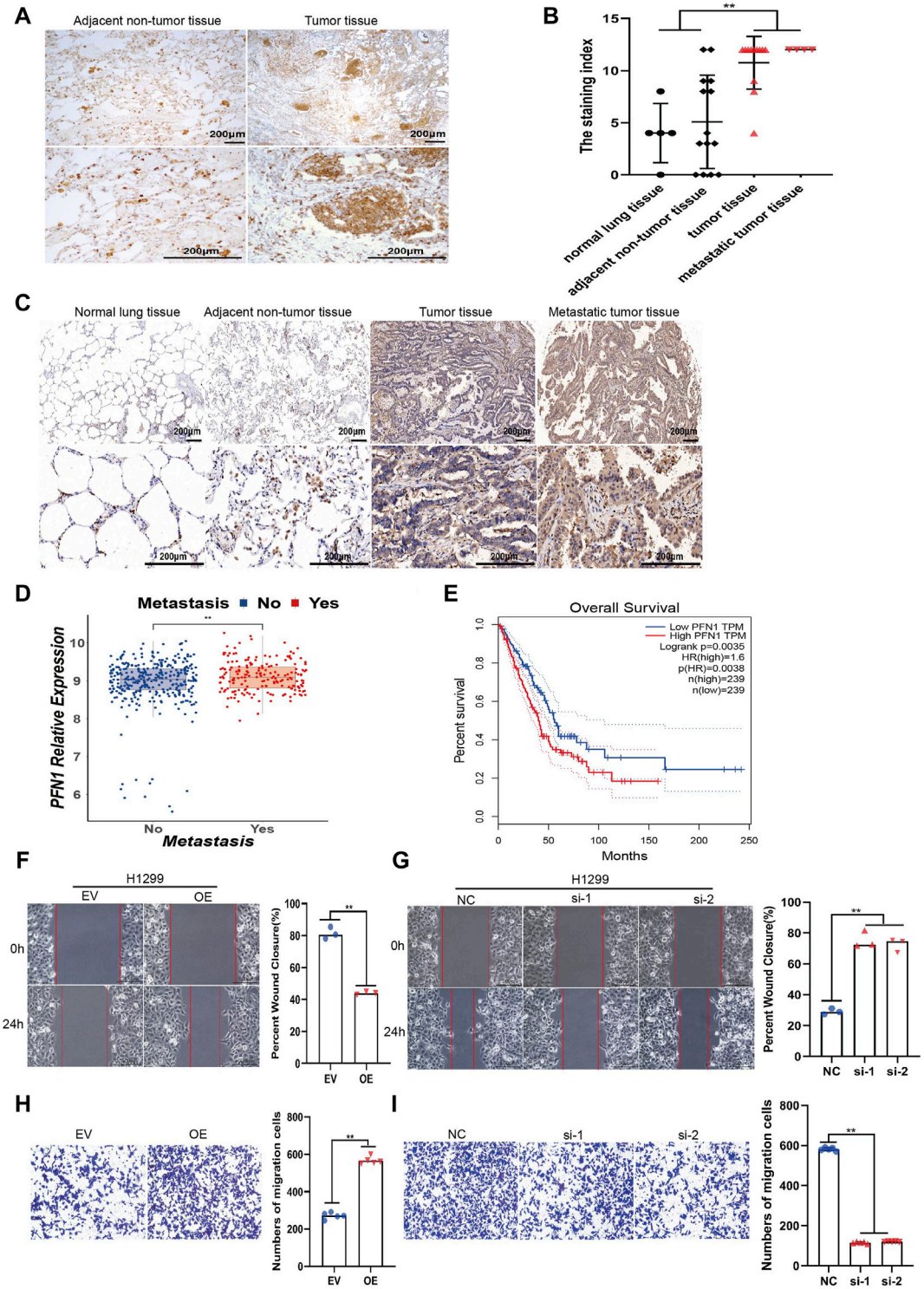

FIGURE 1 | PFN1 is correlated with NSCLC metastasis and could promote NSCLC cell migration *in vitro*. **(A)** Representative IHC images of PFN1 expression on the NSCLC tissues. **(B)** The staining index of PFN1 on the tissue chip. $^{**}p < 0.01$. **(C)** Representative IHC images of PFN1 expression on the tissue chip. **(D)** The expression of PFN1 in TCGA LUAD data. $^{**}p < 0.01$. **(E)** The Kaplan–Meier survival analysis of PFN1 in NSCLC patients. (Data source: TCGA LUAD dataset) **(F,G)** Wound healing assays conducted to evaluate the migration ability of *PFN1*-overexpressing **(F)** and *PFN1* knockdown (KD) **(G)** H1299 cells. $^{**}p < 0.01$; scale bar, 500 μm. **(H,I)** Transwell migration assays conducted to evaluate the migration of *PFN1*-overexpressing **(H)** and *PFN1* KD **(I)** H1299 cells. $^{**}p < 0.01$; scale bar, 500 μm. EV, empty vector; OE, *PFN1* overexpression; NC, negative control; si-1/ 2, PFN1 siRNA1 1/2.

the other parameters were reserved as default. The mass spectrometry proteomics data have been deposited to the ProteomeXchange Consortium via the PRIDE (Perez-Riverol et al., 2022) partner repository with the dataset identifier PXD033148.

Bioinformatics Analysis

After pretreatment, 5,438 detected proteins were retained. Data were processed with Proteome Discoverer software (Thermo Fisher Scientific, version 2.4.0.305). Principal component analysis (PCA) was performed using the R package. (version3.6.3, https://www.r-project.org/) or SIMCA (V16.0.2, Sartorius Stedim Data Analytics AB, Umea, Sweden). Differential expressed proteins (DEPs) were defined as student's *t*-test *p*-value < 0.05 and fold change ≤ 0.83 or fold change ≥ 1.2. DEPs were visualized in the form of volcano plot. Hierarchical clustering for representing the DEPs was conducted by R Package pheatmap. The eukaryotic clusters of orthologous groups (KOG) database (http://www.ncbi.nlm.nih.gov/COG/) of protein database was carried out for functional classification of DEPs. Gene ontology (GO) database (http://geneontology.org/) was used to classify and annotate the functions of differentially expressed proteins. All enrichment analyses were based on the Fisher's exact test with Benjamini–Hochberg correction ($p < 0.05$).

RNA-Seq Data Analysis

Publicly available RNA sequencing (RNA-seq) data were obtained from TCGA LUAD dataset. The clinical information and expression matrix were obtained from http://xena.ucsc.edu/ (Goldman et al., 2020). The medians of mRNA expression of PFN1 were considered as cutoffs. Survival analysis was performed by Kaplan-Meier with log-rank test. PFN1 mRNA expression in metastatic and non-metastatic LUAD patients were compared with Student *t* test.

Statistical Analysis

All data are presented as mean ± standard deviation. Student's *t*-test was used to compare differences between two experimental groups. For comparison of overall differences between three or more groups, one-way analysis of variance was used. Spearman correlation analysis was performed to reveal relationships between PFN1 and p-MLC. All analyses were carried out using SPSS 21.0 (IBM Corporation, Armonk, NY, United States); $p < 0.05$ was considered statistically significant.

RESULTS

PFN1 Is Correlated With NSCLC Metastasis and Could Promote NSCLC Cell Migration *In Vitro*

To investigate the roles of PFN1 in NSCLC, we first conducted IHC to detect the expression of PFN1 in NSCLC tissues. Results showed that PFN1 was highly expressed in NSCLC tissues compared with adjacent non-tumor tissues (**Figure 1A**). We then quantified PFN1 protein levels using tissue chip analysis. PFN1 expression was upregulated in tumor and metastatic tissues compared with that in normal lung and adjacent non-tumor tissues (**Figures 1B,C**; **Supplementary Figure S1A**), suggested that PFN1 may associated with NSCLC metastasis. Analysis of TCGA LUAD data demonstrated that PFN1 was highly expressed in patients with metastatic NSCLC (**Figure 1D**). The Kaplan–Meier survival analysis showed that prognosis of patients with higher expression of PFN1 was poorer than that of patients with lower expression of PFN1 (**Figure 1E**). These results manifested that PFN1 involves in NSCLC metastasis.

To further investigate the impact of PFN1 on NSCLC cell lines, we constructed stable PFN1-OE and PFN1-KD H1299 and A549 cell lines. The effect of overexpression and knockdown was determined using RT-qPCR (**Supplementary Figures S1B,C**) and western blotting (**Supplementary Figure S1D**). Wound healing and Transwell migration assays were conducted to determine the effect of PFN1 on migration. PFN1 overexpression promoted H1299 and A549 cell migration, whereas its downregulation inhibited cell migration (**Figures 1F–I**; **Supplementary Figures S1E–H**).

PFN1 Could Promote MVs Secretion in NSCLC

To further investigate the molecular differences between EV and PFN1 OE cells and possible signaling pathways that affect NSCLC metastasis, we utilized a proteomics-based approach to characterize protein levels between them using liquid chromatography-mass spectrometry (LC-MS). Differently expressed proteins (DEPs) were defined as *p*-value < 0.05 and fold change ≤ 0.83 or fold change ≥ 1.2. We identified 581 proteins with significant differences in abundance, as shown in the volcanic plot (**Supplementary Figure S2A**). Compared with EV cells, 327 upregulated proteins and 254 downregulated proteins in PFN1 OE cells. The expression of DEPs was visualized with heatmap (**Figure 2A**). We next utilized enrichment analysis to determine if these DEPs could point to any specific biological functions that may provide insight into their differences in biological functions (**Figure 2B**). Among the most enriched gene ontology (GO) categories in PFN1 OE cells, DEPs involve in protein binding, cellular component organization or biogenesis and organelle organization. Most differently expressed proteins were associated with organelles, which conformed with PFN1's roles in membrane trafficking. Cluster of orthologous groups of proteins (COG/KOG) analysis revealed that DEPs were involved in posttranslational modification, protein turnover, chaperons, intracellular trafficking, secretion, vesicular transport and signal transduction mechanisms (**Figure 2C**). Via proteomics analysis, we inferred that through protein interaction and signal transduction, PFN1 may participate in extracellular vesicles secretion, which in turn promote NSCLC metastasis.

As PFN1 is important in membrane trafficking and MVs are key mediators of cancer metastasis, we extracted extracellular vesicles (MVs and exosomes) from sera of clinical samples. PFN1 existed in MVs but not in exosomes or free in sera, which indicate

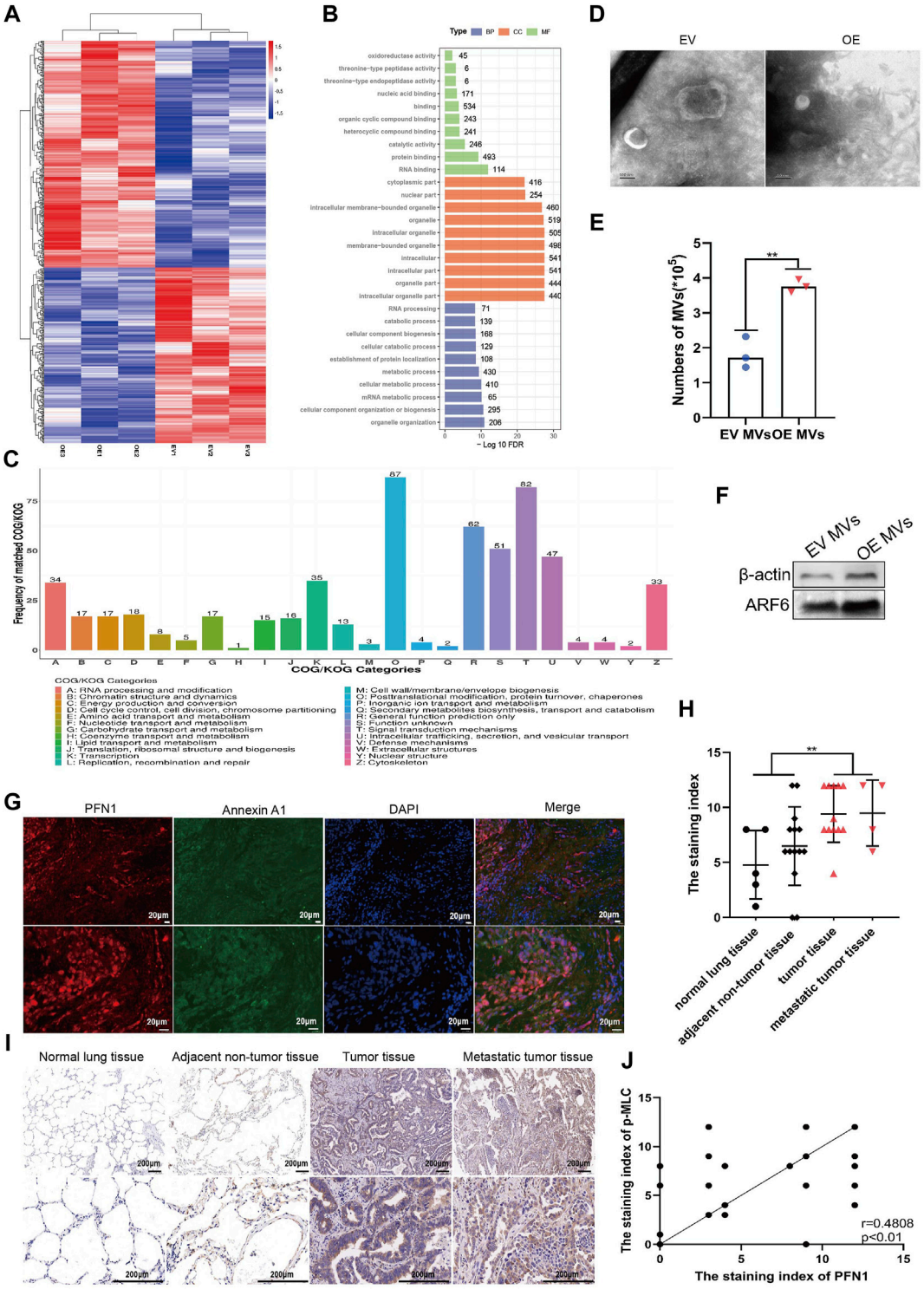

FIGURE 2 | PFN1 could promote MVs secretion in NSCLC. **(A)** Heatmap of differentially expressed proteins between EV and PFN1 OE cells. **(B)** GO enrichment analysis of differentially expressed proteins. **(C)** COG/KOG analysis of differentially expressed proteins. **(D)** MVs extracted from EV-expressing and *PFN1*-overexpressing cells, using continuous differential centrifugation, identified using transmission electron microscopy. Scale bar, 100 nm. **(E,F)** Flow cytometry **(E)** and western blotting **(F)** were used to quantify MVs in *PFN1*-overexpressing and EV-expressing cells. ARF6 and actin were used as MV markers. **(G)** Expression of PFN1 and annexin A1 in lung tumor tissues detected using immunofluorescence. **(H)**The staining index of p-MLC on the tissue chip. $^{**}p < 0.01$. **(I)** Representative IHC images of p-MLC expression. **(J)** Spearman rank correlation analysis was used to assess the relationship between PFN1 and p-MLC expression on the tissue chip; *p* and *r* values are shown in the plot.

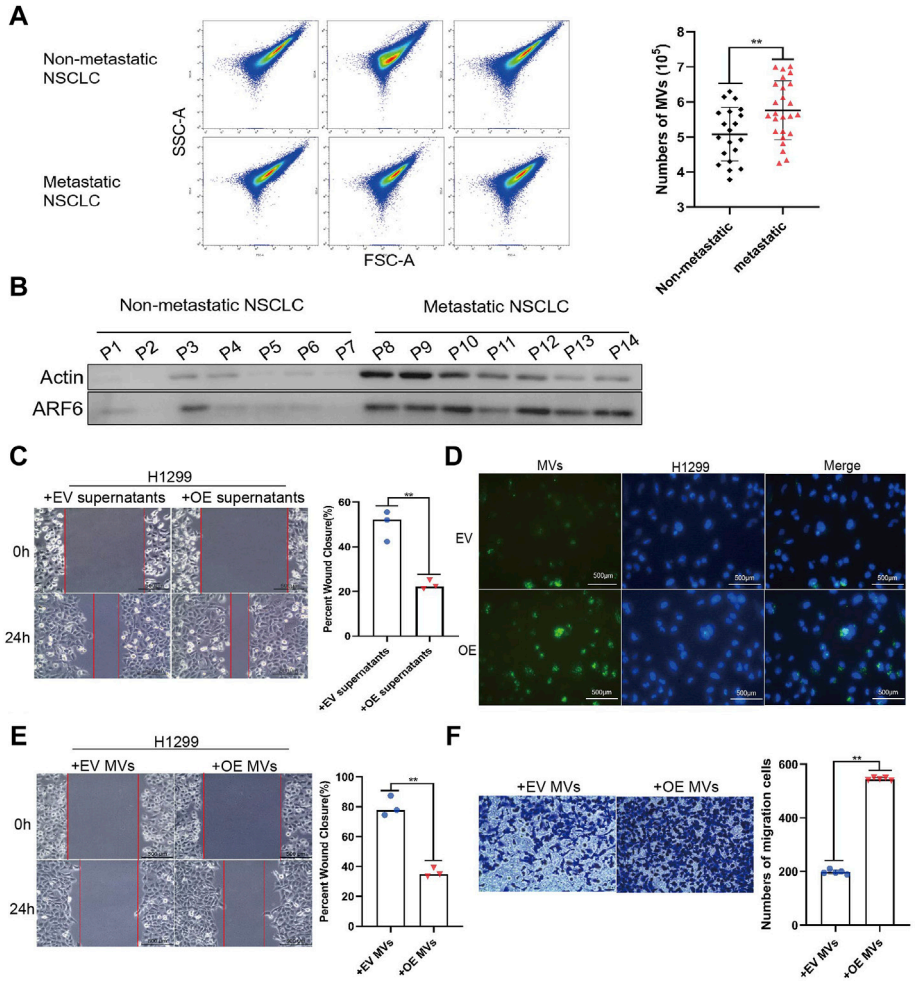

FIGURE 3 | MVs derived from PFN1 OE cells promote migration in NSCLC cells. **(A)** MVs collected from sera of patients with NSCLC quantified using flow cytometry. $^{**}p < 0.01$. **(B)** Protein expression of ARF6 and β-actin in MVs collected from sera of patients with NSCLC detected using western blotting. **(C)** Effect of *PFN1*-overexpressing cell supernatants on cell migration evaluated through wound healing assays. $^{**}p < 0.01$; scale bar, 500 μm. **(D)** PKH67-labeled MVs taken up by H1299 cells. DAPI was used to stain the nuclei of H1299 cells. Scale bar, 500 μm. **(E,F)** Wound healing **(E)** and Transwell migration **(F)** assays conducted to evaluate the migration of H1299 cells after treatment with MVs derived from EV-expressing and *PFN1*-overexpressing cells; $^{**}p < 0.01$; scale bar, 500 μm.

PFN1 was correlated with MVs (**Supplementary Figures S2B,C**). Then we extracted MVs from EV and *PFN1*-overexpressing cell supernatants. Transmission electron microscopy, western blotting, and flow cytometry were used for qualitative and quantitative analysis of the MVs (**Figures 2D–F**; **Supplementary Figure S2D**). Results confirmed that the amount of MVs derived from PFN1 OE cells were significantly larger than that from EV cells, manifested that PFN1 could promote MVs secretion.

To further investigate the relationship between PFN1 and MVs secretion, we analyzed the expression of PFN1 and the MV marker annexin A1 (Jeppesen et al., 2019) in NSCLC tissues using immunofluorescence. PFN1 was almost co-localized with annexin A1, suggesting an association between PFN1 and annexin A1 expression and that PFN1 may participate in MV biosynthesis (**Figure 2G**). Phosphorylated MLC is a key molecule in the regulation of MV secretion (Muralidharan-Chari et al., 2009; Li et al., 2012; Tricarico et al., 2017). Using IHC, we determined that p-MLC levels were significantly elevated in lung cancer and metastatic tissues compared with that in adjacent tumor and normal lung tissues (**Figures 2H,I**; **Supplementary Figure S2E**). Spearman correlation analysis of PFN1 and p-MLC revealed that the expression of p-MLC was positively correlated with that of PFN1 (**Figure 2J**), indicating that PFN1 may regulate MLC phosphorylation, which could modulate MV secretion.

MVs Derived From PFN1 OE Cells Promote Migration in NSCLC Cells

MVs are key mediators of cancer metastasis. We collected serum samples from patients with metastatic (n = 25) and non-metastatic (n = 20) lung cancer and extracted MVs. Flow cytometry (100–1,000 nm microparticles analyzed) and western blotting

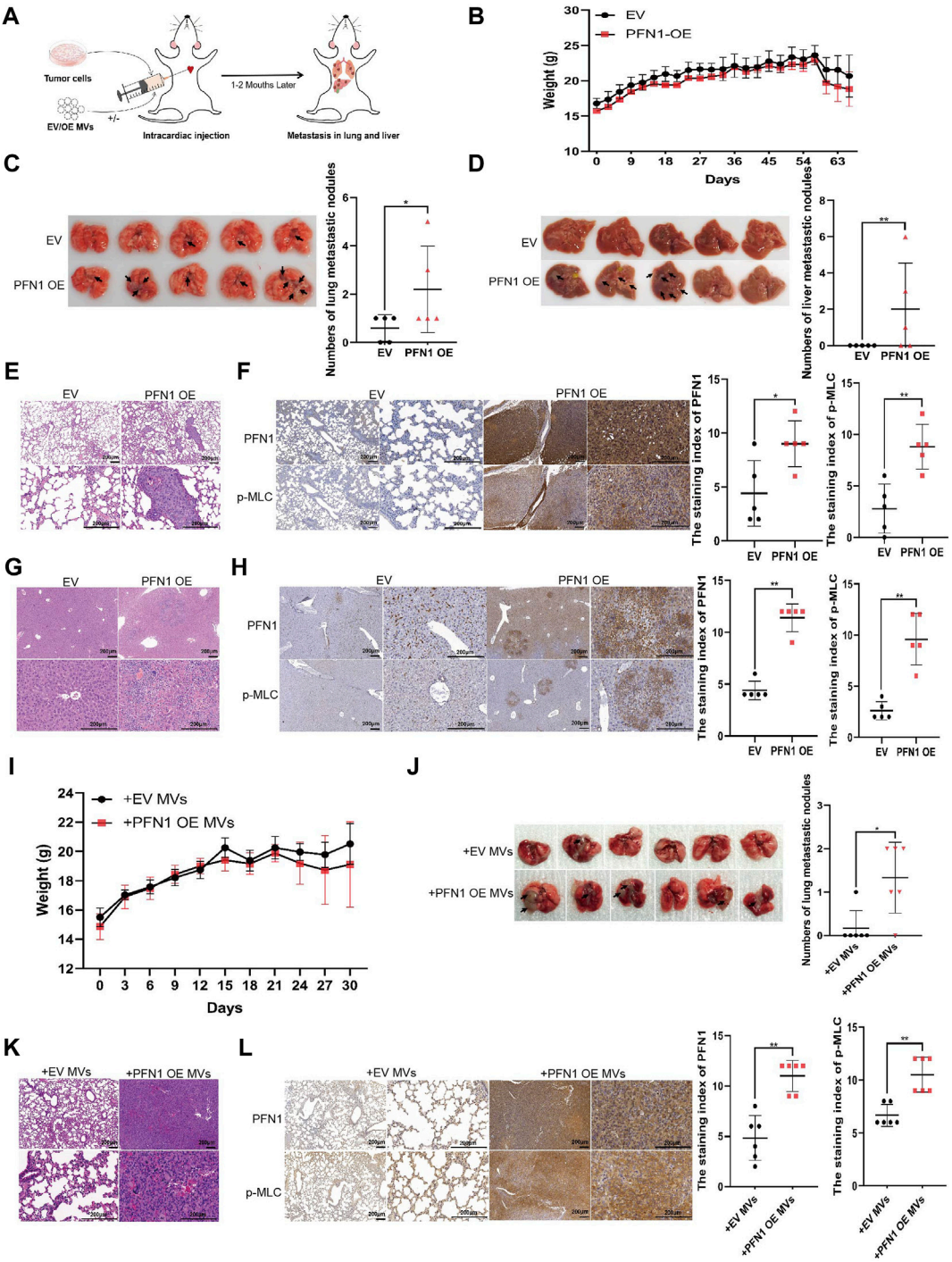

FIGURE 4 | PFN1 promotes *in vivo* NSCLC metastasis by elevating MV secretion. **(A)** Schematic illustration of the mouse model of metastatic tumor established to determine the role of PFN1 in tumor metastasis. **(B)** Body weight changes in mice after intracardiac injection of *PFN1*-overexpressing and EV-expressing cell lines. **(C,D)** Representative images of lung **(C)** and liver **(D)** metastases of the mouse model. The number of metastases is displayed in the right-hand side graph. $^{*}p < 0.05$, $^{**}p < 0.01$. **(E)** Representative images of HE-stained lung tissues of the mouse model. **(F)** Representative IHC images of PFN1 and p-MLC expression in lung tissues. The staining index is shown in the right-hand side graph. $^{**}p < 0.01$. **(G)** Representative images of HE-stained liver tissues of the mouse model. **(H)** Representative IHC images of PFN1 and p-MLC expression in liver tissues. The staining index is shown in the right-hand side graph. $^{**}p < 0.01$. **(I)** Body weight changes in mice after intracardiac injection of H1299 cells and MVs. **(J)** Representative images of lung metastases of the mouse model. The number of metastases is shown in the bottom graph. $^{*}p < 0.05$. **(K)** Representative images of HE-stained lung tissues of the mouse model. **(L)** Representative IHC images of PFN1 and p-MLC expression in lung tissues. The staining index is shown in the right-hand side graph; $^{*}p < 0.05$.

(ARF6 used as MV biomarker) (Jeppesen et al., 2019) results indicated that the number of MVs in patients with metastatic NSCLC was higher than that in patients with non-metastatic NSCLC (**Figures 3A,B**). To determine whether PFN1 promotes NSCLC migration by inducing the secretion of mediators into the environment, we treated H1299 and A549 cells with supernatants of cultured EV-expressing or *PFN1*-overexpressing H1299 and A549 cells and performed a wound healing assay. The *PFN1*-overexpressing cell supernatants significantly promoted cell migration, which was unaffected by EV-expressing cell supernatants (**Figure 3C** and **Supplementary Figure S3A**). To visualize the uptake of MVs by cells, we used PKH67 to label MVs derived from EV-expressing and *PFN1*-overexpressing cells. Immunofluorescence showed that MVs derived from *PFN1*-overexpressing cells were more abundant than those derived from EV-expressing cells. In addition, MVs were taken up by H1299 cells (**Figure 3D**). We then treated H1299 and A549 cells with EV-expressing and *PFN1*-overexpressing cell-derived MVs and found that the latter significantly promoted H1299 and A549 cell metastasis, according to wound healing and Transwell migration assays (**Figures 3E,F**; **Supplementary Figures S3B,C**). Hence, PFN1 may promote NSCLC metastasis through the induction of MV secretion.

PFN1 Promotes *In Vivo* NSCLC Metastasis by Elevating MV Secretion

To further investigate the role of PFN1 in NSCLC metastasis, we established a mouse model of tumor metastasis via intracardiac injection of H1299 NSCLC cells (**Figure 4A**). The body weights of mice are shown in **Figure 4B**. PFN1 overexpression promoted lung (**Figure 4C**) and liver (**Figure 4D**) metastasis in mice. Representative images of hematoxylin and eosin (HE)-stained lung tissues are shown in **Figure 4E**. IHC showed that PFN1 and p-MLC expression in the lung tissue of *PFN1*-overexpressing cell-treated group was higher than in the EV-expressing cell-treated group (**Figure 4F**). Representative images of hematoxylin and eosin (HE)-stained liver tissues are shown in **Figure 4G**. IHC also showed that PFN1 and p-MLC expression in the liver tissues of *PFN1*-overexpressing cell-treated group was higher than in the EV-expressing cell-treated group (**Figure 4H**).

The effects of *PFN1*-overexpressing cell-derived MVs on NSCLC metastasis were also similar to those observed in the *in vitro* assays. The body weight of mice is shown in **Figure 4I**. Compared with EV-expressing cell-derived MVs, *PFN1*-overexpressing cell-derived MVs promoted H1299 cell metastasis to the lungs (**Figure 4J**). HE results of lung tissues support these findings (**Figure 4K**). IHC analysis revealed that PFN1 and p-MLC expression in the lung tissues of the group treated with *PFN1*-overexpressing cell-derived MVs was higher than that in the group treated with EV-expressing cell-derived MVs (**Figure 4L**). These results further confirmed the role of PFN1 in NSCLC metastasis.

Mechanisms Underlying the Promotion of MLC Phosphorylation by PFN1

Previous studies have shown that the ARF6/ERK/p-MLC and ROCK/p-MLC pathways are involved in MV secretion (Li et al., 2012; Muralidharan-Chari et al., 2009). ARF6 and ERK (extracellular signal-regulated kinase 1/2) expression were not affected by PFN1 expression (**Supplementary Figure S4A**). As ROCK1/2 play important roles in actin cytoskeleton organization (Goldman et al., 2020), we speculated that PFN1 interacts with ROCK1/2 to indirectly regulate MV secretion. We, therefore, analyzed ROCK1/2, MLC, and p-MLC expression in *PFN1*-overexpressing and knockdown cells. PFN1 overexpression promoted MLC phosphorylation, whereas PFN1 knockdown inhibited it (**Figures 5A,B** and **Supplementary Figures S4B,C**). The protein expression of ROCK1/2 remained unchanged when PFN1 overexpression or downregulation. When we assessed MLC phosphorylation in cell lines expressing the PFN1 mutants R88L, H119E, or H133S (mutated PIP2/PIP3-binding site, actin-binding site, and PLP-binding site, respectively) (Sohn et al., 1995; Suetsugu et al., 1998; Julian and Olson, 2014), and observed a decrease in MLC phosphorylation with all three mutants (**Figure 5C** and **Supplementary Figure S4D**).

We next conducted a co-IP assay to characterize the interactions among ROCK1/2, PFN1, and its mutants. ROCK1 interacted with wildtype, not mutant PFN1, while ROCK2 did not interact with PFN1 (**Figure 5D**). Y27632 is an inhibitor of ROCK activity and MV secretion (Björkegren-Sjögren et al., 1997; Catalano et al., 2020). Western blotting results showed that treatment with Y27632 reduced MLC phosphorylation in *PFN1*-overexpressing cells but did not affect ROCK1/2 expression (**Figure 5E** and **Supplementary Figure S4E**).

We also overexpressed ROCK1 and ROCK2 in HEK-293T cells and purified ROCK1/2, PFN1, and its mutant proteins to conduct a ROCK kinase assay *in vitro* (**Supplementary Figures S4F,G**). Wildtype PFN1 enhanced ROCK1 activity, whereas PFN1 mutants reduced it (**Figure 5F**). PFN1 exerted no effect on ROCK2 activity (**Figure 5G**). Immunofluorescence confirmed the co-location of PFN1 and ROCK1 in H1299 cells. (**Supplementary Figures S4H,I**) Flow cytometry showed that after treatment with Y27632 (10 μM), the amount of MVs decreased in PFN1-overexpressing cells (**Figure 5H**). Hence, PFN1 can interact with ROCK1, enhance its kinase activity, and indirectly promote MLC phosphorylation to ultimately induce MV secretion. Y27632 partly reversed the effect of PFN1 in promoting MLC phosphorylation and MV secretion.

ROCK1 Inhibitor Y27632 Partially Reverses the Effect of PFN1 on NSCLC Metastasis *In Vitro* and *In Vivo*

The wound healing assay showed that migration of Y27632-treated, *PFN1*-overexpressing cells diminished to nearly that of the EV-expressing cells (**Figure 6A** and **Supplementary Figure S5A**). Next, we added *PFN1*-overexpressing cell-derived MVs to Y27632-treated cells and found that Y27632 did not reverse the migration induced by *PFN1*-overexpressing cell-derived MVs (**Figure 6B** and **Supplementary Figure S5B**). Similar results were obtained from the Transwell migration assay (**Figure 6C** and **Supplementary Figure S5C**).

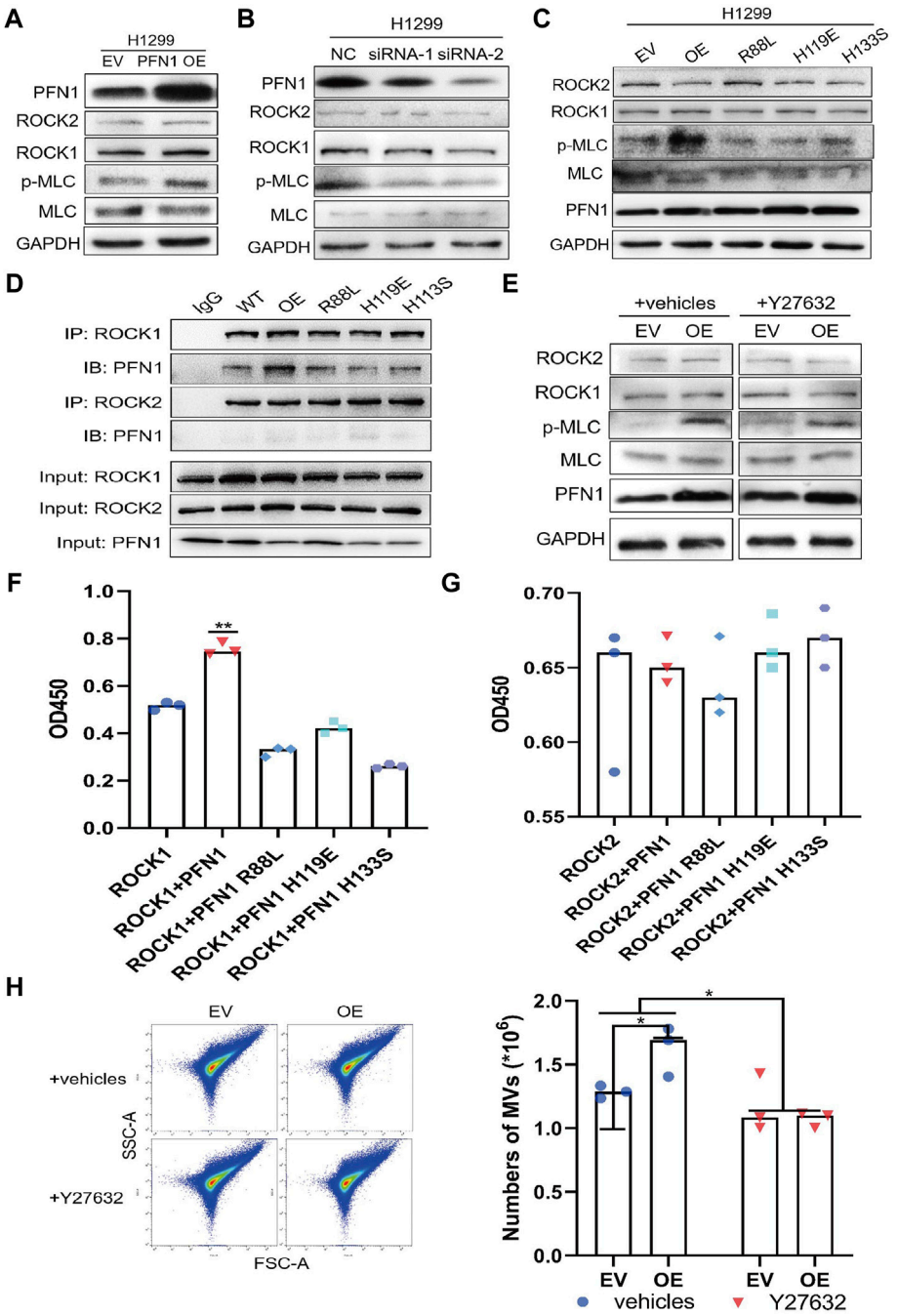

FIGURE 5 | Mechanisms underlying the promotion of MLC phosphorylation by PFN1. **(A,B)** Protein expression after *PFN1* overexpression **(A)** and knockdown **(B)** measured using western blotting. **(C)** Protein expression in PFN1 mutants measured using western blotting. **(D)** PFN1 interactions with ROCK1/2 confirmed using co-IP. **(E)** Protein expression after treatment with Y27632 (10 μM) measured using western blotting. **(F)** Effect of PFN1 on ROCK1 activity. $^{**}p < 0.01$. **(G)** Effect of PFN1 on ROCK2 activity. **(H)** Flow cytometry measuring changes in the amount of MVs after treatment with Y27632; $^{*}p < 0.05$.

We also validated these results using our mouse model (**Figure 6D**; body weight: **Figure 6E**). After treatment with Y27632 (10 mg/kg every 3 days, intraperitoneal injection), the number of metastatic nodules in the lungs and livers of mice significantly decreased compared with mice injected with *PFN1*-overexpressing cells alone. However, when mice were simultaneously injected with *PFN1*-overexpressing cell-derived MVs, the number of metastatic nodules in the lung and liver markedly increased compared with the group treated with Y27632 (**Figure 6F**). HE-staining displaying the micromorphology of tumor nodules are presented in **Figures 6G,H**. IHC analysis revealed higher PFN1 and

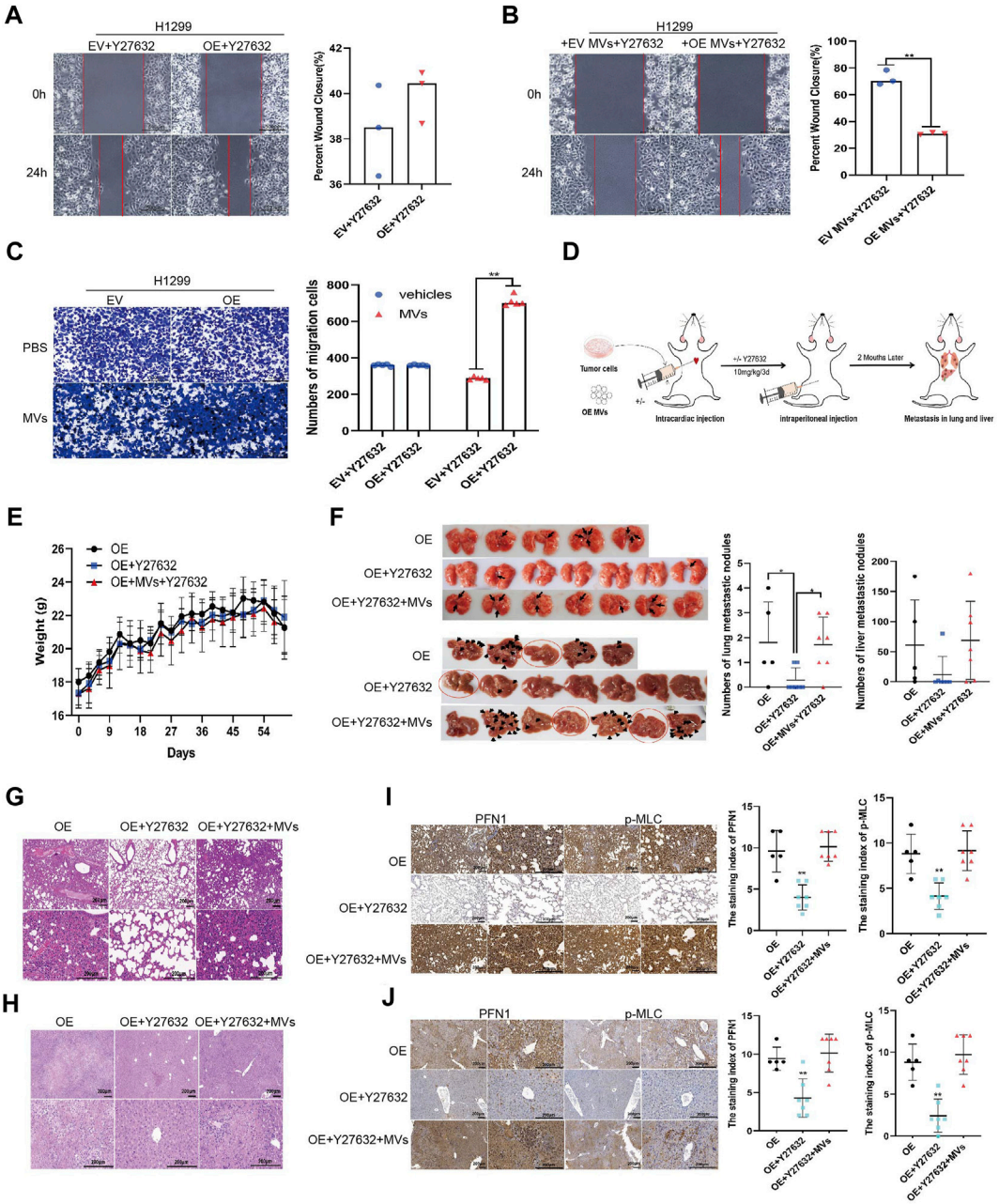

FIGURE 6 | ROCK1 inhibitor Y27632 partially reversed the promotion of lung cancer metastasis by PFN1 *in vitro* and *in vivo*. **(A,B)** Wound healing assays conducted to evaluate the effect of Y27632 **(A)** and Y27632 combined with MVs **(B)** on cell migration. $^{**}p < 0.01$; scale bar, 500 μm. **(C)** Transwell migration assays conducted to evaluate the effect of Y27632 and Y27632 combined with MVs on cell migration. $^{**}p < 0.01$; scale bar, 500 μm. **(D)** Schematic diagram of the mouse model of metastatic tumor established to determine the effect of Y27632 on PFN1-induced lung cancer metastasis. **(E)** Body weight changes in mice after intracardiac injection of *PFN1*-overexpressing H1299 cells and intraperitoneal injection of Y27632 (10 mg/kg). **(F)** Representative images of lung and liver metastatic tissue in mice. The number of metastatic nodules is shown in the right-hand side graph. $^{*}p < 0.05$. **(G,H)** Representative images of HE-stained lung **(G)** and liver **(H)** metastases. **(I)** Representative IHC images of PFN1 and p-MLC expression in lung tissues. The staining index is shown in the right-hand side graph. $^{**}p < 0.01$. **(J)** Representative IHC images of PFN1 and p-MLC expression in liver tissues. The staining index is shown in the right-hand side graph; $^{**}p < 0.01$.

p-MLC expression in both lung and liver tissues of the group treated with *PFN1*-overexpressing cells and *PFN1*-overexpressing cells + MVs + Y27632 compared to those treated with Y27632 alone (**Figures 6I,J**).

A schematic illustration of the role played by PFN1 in NSCLC metastasis is shown in **Figure 7**. During metastasis initiation, *PFN1*-overexpressing NSCLC cells secrete more MVs through PFN1 interactions with the ROCK/p-MLC pathway. These MVs

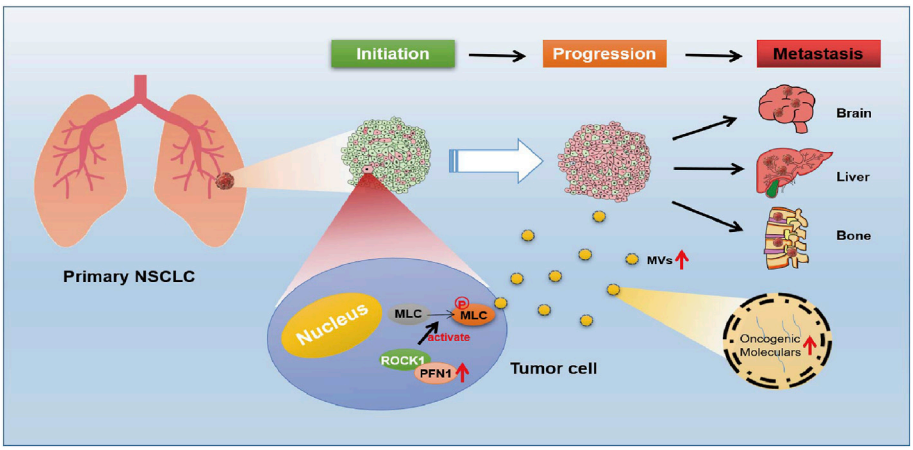

FIGURE 7 | Schematic diagram of the role of PFN1 in NSCLC metastasis. In the initiation stage of NSCLC, cells with upregulated PFN1 secret more MVs through PFN1 interactions with the ROCK/p-MLC pathway. These MVs contain numerous oncogenenic moleculars, which could enhance migration abilities of PFN1 normal expressed NSCLC cells, and untimately promote progression and metastasis of NSCLC.

deliver tumorigenic bioactive substances to recipient cells and enhance their migratory ability, thus promoting NSCLC progression.

DISCUSSION

Intratumor heterogeneity is a key contributor for therapeutic failure and drug resistance of cancer patients. (Greaves, 2015).Early detection of abnormal expression of genes and proteins thus critical for precision medicine. (Smida and Nijman, 2012; McGranahan and Swanton, 2017).In this study, we explored the role of PFN1 in NSCLC metastasis and found that PFN1 is highly expressed in advanced NSCLC tissues. Upregulation of PFN1 was correlated with worse prognosis of patients with NSCLC. PFN1 expression of patients with metatatic NSCLC was significantly higher than that of patients with non-metastatic NSCLC. These results suggested that detection of PFN1 expression in NSCLC tissues may help predict prognosis and guide early intervention of NSCLC. *In vitro* experiments confirmed that PFN1 overexpression promoted NSCLC cell migration, while its downregulation inhibited NSCLC cell migration. Previous studies pertaining to the role of PFN1 in cancer metastasis have yielded contrasting results, PFN1 exhibits variable effects on the metastasis of different tumors. For example, PFN1 promotes the metastasis of breast cancer (Ding et al., 2014) and hepatocellular carcinoma (Wang et al., 2019), while PFN1 inhibits the metastasis of bladder cancer (Frantzi et al., 2016). The mechanisms underlying the roles of PFN1 in metastasis were different from cancer to cancer and those in lung cancer are still unclear. In this study, we found that PFN1 could significantly promote MV secretion in NSCLC cells, which instigated us to study its roles in NSCLC metastasis.

Tumor-cell derived MVs play important roles in tumor development and progression (Muralidharan-Chari et al., 2010). Proteomics analysis reveals PFN1 was closely associated with membrane trafficking. Further COG/KOG analysis inferred that PFN1 involved in intracellular trafficking and vesicles secretion. *In vitro* experiments showed that PFN1 was positively correlated with MLC phosphorylation, a key process in the shedding of MVs (Tricarico et al., 2017). PFN1 overexpression significantly promoted MLC phosphorylation and increased MV secretion from NSCLC cells. MVs derived from PFN1 OE cells significantly promote NSCLC metastasis *in vitro* and *in vivo*. Dysregulation of PFN1 in cells affect surrounding cells, even distant cells, via cell communication mediated by MVs. Through regulation of MVs secretion, PFN1 exerts its positive roles in NSCLC metastasis.

In this study, PFN1 could interact with ROCK1 followed by its activation, thus promoting MLC phosphorylation. Interestingly, only wild type PFN1 could interact with ROCK1. All three mutants of PFN1 displayed no interaction with ROCK1 and even exerted inhibitory effect on ROCK1 activities. ROCK1 activity can be regulated through interaction with common activators (such as the small Rho GTPases) (Wei et al., 2016) and plasma membrane via its C-terminal PH domain (Fu et al., 1998; Feng et al., 1999). Changes in the plasma membrane structures induced by PFN1 explain ROCK1 activation by PFN1 (Davey and Moens, 2020). Mutations in PFN1 binding domains lead to radical 3D structure changes of PFN1, which could ultimately affect the interaction of PFN1 with other proteins (Boopathy et al., 2015). This may explain why the interactions between PFN1 and ROCK1 require an intact PFN1. Besides, abnormal activation of ROCK1 can enhance tumor cell migration (Wei et al., 2016). Moreover, PFN1 is a direct target of ROCK1 (Shao et al., 2008). Epigenetic regulation of PFN1 could also affect functions of PFN1, thus regulated interation between PFN1 and ROCK1 (Brahma et al., 2010). The interactions between PFN1 and ROCK1 may be much more complex *in vivo* and play important roles in cancer progression, which needs further investigation in the future.

Signaling pathways regulated by the small Ras-related GTPases (ARF6 and Rho family) are thought to govern the formation and release of tumor-derived MVs. All these

molecules ultimately regulate the shedding of MVs through the phosphorylation and activation of MLC (Muralidharan-Chari et al., 2009; Li et al., 2012). The elongation and organization of actin filament along the plasma membrane are essential for MV formation, in which several cytoskeletal proteins, such as cofilin (Li et al., 2012) and formin (Di Vizio et al., 2009), are involved. In this study, we highlight the role of PFN1 in the RhoA/ROCK signaling pathway for the formation of MVs. PFN1 may participate in the formation of MVs by regulating the polymerization and depolymerization of actin filament. In addition to the regulation of actin cytoskeleton, PFN1 may be involved in MV biogenesis and secretion, which warrants further investigations.

In conclusion, our findings suggest that PFN1, a critical actin-regulating protein, promotes MV release through the ROCK/p-MLC pathway, thereby promoting NSCLC metastasis. Thus, PFN1 may represent a potential therapeutic target for NSCLC metastasis. By reducing the release of MVs, it may be possible to partially reverse PFN1 overexpression-induced NSCLC cell migration. This study provides a potential new approach for the treatment of NSCLC by targeting metastasis that warrants further investigation.

DATA AVAILABILITY STATEMENT

The datasets presented in this study can be found in online repositories. The name of the repository and accession number can be found below: ProteomeXchange; PXD033148.

ETHICS STATEMENT

The studies involving human participants were reviewed and approved by The Ethics Committee of Hunan Provincial People's Hospital/The First Affiliated Hospital of Hunan Normal University. The patients/participants provided their written informed consent to participate in this study. The animal study was reviewed and approved by The Institutional Animal Ethics Committee of Hunan Provincial People's Hospital/The First Affiliated Hospital of Hunan Normal University. Written informed consent was obtained from the individual(s) for the publication of any potentially identifiable images or data included in this article.

AUTHOR CONTRIBUTIONS

Study concept and design: CH. Acquisition of data: YaW, YL, RW, YangW, CZ, ML, PD, and LC. Statistical analysis: YaW and RW. Analysis and interpretation of data: CH, YaW, and YL. Drafting of the manuscript: YaW. Critical revision of the manuscript: CH and YL. All authors contributed to the article and approved the submitted version.

FUNDING

This work was supported by the National Multidisciplinary Cooperative Diagnosis and Treatment Capacity Building Project for Major Diseases (Lung Cancer) (grant number z027002); the National Natural Science Foundation of China (grant number 82100223).

ACKNOWLEDGMENTS

The authors would like to thank Xiangya Hospital of Central South University for providing experimental platform. They acknowledge all colleagues of the Department of Respiratory Medicine for their assistance in experiments. They thank Biotree Biomedical Technology Company for supports of proteomics analysis.

SUPPLEMENTARY MATERIAL

The Supplementary Material for this article can be found online at: https://www.frontiersin.org/articles/10.3389/fphar.2022.890891/full#supplementary-material

REFERENCES

Alkam, D., Feldman, E. Z., Singh, A., and Kiaei, M. (2017). Profilin1 Biology and its Mutation, Actin(g) in Disease. *Cell. Mol. Life Sci.* 74, 967–981. doi:10.1007/s00018-016-2372-1

Balaj, L., Lessard, R., Dai, L., Cho, Y. J., Pomeroy, S. L., Breakefield, X. O., et al. (2011). Tumour Microvesicles Contain Retrotransposon Elements and Amplified Oncogene Sequences. *Nat. Commun.* 2, 180. doi:10.1038/ncomms1180

Björkegren-Sjögren, C., Korenbaum, E., Nordberg, P., Lindberg, U., and Karlsson, R. (1997). Isolation and Characterization of Two Mutants of Human Profilin I that Do Not Bind poly(L-Proline). *FEBS Lett.* 418, 258–264. doi:10.1016/S0014-5793(97)01376-8

Boopathy, S., Silvas, T. V., Tischbein, M., Jansen, S., Shandilya, S. M., Zitzewitz, J. A., et al. (2015). Structural Basis for Mutation-Induced Destabilization of Profilin 1 in ALS. *Proc. Natl. Acad. Sci. U. S. A.* 112, 7984–7989. doi:10.1073/pnas.1424108112

Catalano, M., and O'Driscoll, L. (2020). Inhibiting Extracellular Vesicles Formation and Release: a Review of EV Inhibitors. *J. Extracell. Vesicles.* 9, 1703244. doi:10.1080/20013078.2019.1703244

Chen, Z., Fillmore, C. M., Hammerman, P. S., Kim, C. F., and Wong, K. K. (2014). Non-small-cell Lung Cancers: a Heterogeneous Set of Diseases. *Nat. Rev. Cancer* 14, 535–546. doi:10.1038/nrc3775

Chiodoni, C., Di Martino, M. T., Zazzeroni, F., Caraglia, M., Donadelli, M., Meschini, S., et al. (2019). Cell Communication and Signaling: How to Turn Bad Language into Positive One. *J. Exp. Clin. Cancer Res.* 38, 128. doi:10.1186/s13046-019-1122-2

Davey, R. J., and Moens, P. D. (2020). Profilin: many Facets of a Small Protein. *Biophys. Rev.* 12, 827–849. doi:10.1007/s12551-020-00723-3

Di Vizio, D., Kim, J., Hager, M. H., Morello, M., Yang, W., Lafargue, C. J., et al. (2009). Oncosome Formation in Prostate Cancer: Association with a Region of Frequent Chromosomal Deletion in Metastatic Disease. *Cancer Res.* 69, 5601–5609. doi:10.1158/0008-5472.CAN-08-3860

Ding, Z., Joy, M., Bhargava, R., Gunsaulus, M., Lakshman, N., Miron-Mendoza, M., et al. (2014). Profilin-1 Downregulation Has Contrasting Effects on Early vs

Late Steps of Breast Cancer Metastasis. *Oncogene* 33, 2065–2074. doi:10.1038/onc.2013.166

Dong, J., Radau, B., Otto, A., Müller, E., Lindschau, C., and Westermann, P. (2000). Profilin I Attached to the Golgi Is Required for the Formation of Constitutive Transport Vesicles at the Trans-golgi Network. *Biochim. Biophys. Acta* 1497, 253–260. doi:10.1016/S0167-4889(00)00056-2

Dudas, J. (2015). Supportive and Rejective Functions of Tumor Stroma on Tumor Cell Growth, Survival, and Invasivity: the Cancer Evolution. *Front. Oncol.* 5, 44. doi:10.3389/fonc.2015.00044

El Andaloussi, S., Mäger, I., Breakefield, X. O., and Wood, M. J. (2013). Extracellular Vesicles: Biology and Emerging Therapeutic Opportunities. *Nat. Rev. Drug Discov.* 12, 347–357. doi:10.1038/nrd3978

Fabbiano, F., Corsi, J., Gurrieri, E., Trevisan, C., Notarangelo, M., and D'Agostino, V. G. (2020). RNA Packaging into Extracellular Vesicles: an Orchestra of RNA-Binding Proteins? *J. Extracell. Vesicles.* 10, e12043. doi:10.1002/jev2.12043

Feng, J., Ito, M., Kureishi, Y., Ichikawa, K., Amano, M., Isaka, N., et al. (1999). Rho-associated Kinase of Chicken Gizzard Smooth Muscle. *J. Biol. Chem.* 274, 3744–3752. doi:10.1074/jbc.274.6.3744

Feng, J., Lu, S. S., Xiao, T., Huang, W., Yi, H., Zhu, W., et al. (2020). ANXA1 Binds and Stabilizes EphA2 to Promote Nasopharyngeal Carcinoma Growth and Metastasis. *Cancer Res.* 80, 4386–4398. doi:10.1158/0008-5472.CAN-20-0560

Fidler, I. J. (2003). The Pathogenesis of Cancer Metastasis: the 'seed and Soil' Hypothesis Revisited. *Nat. Rev. Cancer* 3, 453–458. doi:10.1038/nrc1098

Frantzi, M., Klimou, Z., Makridakis, M., Zoidakis, J., Latosinska, A., Borràs, D. M., et al. (2016). Silencing of Profilin-1 Suppresses Cell Adhesion and Tumor Growth via Predicted Alterations in Integrin and Ca2+ Signaling in T24M-Based Bladder Cancer Models. *Oncotarget* 7, 70750–70768. doi:10.18632/oncotarget.12218

Fu, X., Gong, M. C., Jia, T., Somlyo, A. V., and Somlyo, A. P. (1998). The Effects of the Rho-Kinase Inhibitor Y-27632 on Arachidonic Acid-, GTPgammaS-, and Phorbol Ester-Induced Ca2+-Sensitization of Smooth Muscle. *FEBS Lett.* 440, 183–187. doi:10.1016/s0014-5793(98)01455-0

Goldman, M. J., Craft, B., Hastie, M., Repečka, K., McDade, F., Kamath, A., et al. (2020). Visualizing and Interpreting Cancer Genomics Data via the Xena Platform. *Nat. Biotechnol.* 38, 675–678. doi:10.1038/s41587-020-0546-8

Greaves, M. (2015). Evolutionary Determinants of Cancer. *Cancer Discov.* 5, 806–820. doi:10.1158/2159-8290.CD-15-0439

Gupta, G. P., and Massagué, J. (2006). Cancer Metastasis: Building a Framework. *Cell* 127, 679–695. doi:10.1016/j.cell.2006.11.001

Herbst, R. S., Morgensztern, D., and Boshoff, C. (2018). The Biology and Management of Non-small Cell Lung Cancer. *Nature* 553, 446–454. doi:10.1038/nature25183

Jeppesen, D. K., Fenix, A. M., Franklin, J. L., Higginbotham, J. N., Zhang, Q., Zimmerman, L. J., et al. (2019). Reassessment of Exosome Composition. *Cell* 177, 428. doi:10.1016/j.cell.2019.02.029

Julian, L., and Olson, M. F. (2014). Rho-associated Coiled-Coil Containing Kinases (ROCK): Structure, Regulation, and Functions. *Small GTPases* 5, e29846. doi:10.4161/sgtp.29846

Karamchandani, J. R., Gabril, M. Y., Ibrahim, R., Scorilas, A., Filter, E., Finelli, A., et al. (2015). Profilin-1 Expression Is Associated with High Grade and Stage and Decreased Disease-free Survival in Renal Cell Carcinoma. *Hum. Pathol.* 46, 673–680. doi:10.1016/j.humpath.2014.11.007

Li, B., Antonyak, M. A., Zhang, J., and Cerione, R. A. (2012). RhoA Triggers a Specific Signaling Pathway that Generates Transforming Microvesicles in Cancer Cells. *Oncogene* 31, 4740–4749. doi:10.1038/onc.2011.636

Liang, Y., Lehrich, B. M., Zheng, S., and Lu, M. (2021). Emerging Methods in Biomarker Identification for Extracellular Vesicle-Based Liquid Biopsy. *J. Extracell. Vesicles.* 10, e12090. doi:10.1002/jev2.12090

Liao, Y., He, D., and Wen, F. (2021). Analyzing the Characteristics of Immune Cell Infiltration in Lung Adenocarcinoma via Bioinformatics to Predict the Effect of Immunotherapy. *Immunogenetics* 73, 369–380. doi:10.1007/s00251-021-01223-8

Lu, Y., Wang, Y., Xu, H., Shi, C., Jin, F., and Li, W. (2018). Profilin 1 Induces Drug Resistance through Beclin1 Complex-Mediated Autophagy in Multiple Myeloma. *Cancer Sci.* 109, 2706–2716. doi:10.1111/cas.13711

Lv, Y., Tan, J., Miao, Y., and Zhang, Q. (2019). The Role of Microvesicles and its Active Molecules in Regulating Cellular Biology. *J. Cel. Mol. Med.* 23, 7894–7904. doi:10.1111/jcmm.14667

McGranahan, N., and Swanton, C. (2017). Clonal Heterogeneity and Tumor Evolution: Past, Present, and the Future. *Cell* 168 (4), 613–628. doi:10.1016/j.cell.2017.01.018

Menck, K., Sivaloganathan, S., Bleckmann, A., and Binder, C. (2020). Microvesicles in Cancer: Small Size, Large Potential. *Int. J. Mol. Sci.* 21, 5373. doi:10.3390/ijms21155373

Muralidharan-Chari, V., Clancy, J., Plou, C., Romao, M., Chavrier, P., Raposo, G., et al. (2009). ARF6-regulated Shedding of Tumor Cell-Derived Plasma Membrane Microvesicles. *Curr. Biol.* 19, 1875–1885. doi:10.1016/j.cub.2009.09.059

Muralidharan-Chari, V., Clancy, J. W., Sedgwick, A., and D'Souza-Schorey, C. (2010). Microvesicles: Mediators of Extracellular Communication during Cancer Progression. *J. Cel Sci.* 123, 1603–1611. doi:10.1242/jcs.064386

Perez-Riverol, Y., Bai, J., Bandla, C., García-Seisdedos, D., Hewapathirana, S., Kamatchinathan, S., et al. (2022). The PRIDE Database Resources in 2022: A Hub for Mass Spectrometry-Based Proteomics Evidences. *Nucleic Acids Res.* 50 (D1), D543–D552. doi:10.1093/nar/gkab1038

Raposo, G., and Stoorvogel, W. (2013). Extracellular Vesicles: Exosomes, Microvesicles, and Friends. *J. Cel Biol.* 200, 373–383. doi:10.1083/jcb.201211138

Shao, J., Welch, W. J., Diprospero, N. A., and Diamond, M. I. (2008). Phosphorylation of Profilin by ROCK1 Regulates Polyglutamine Aggregation. *Mol. Cel. Biol.* 28, 5196–5208. doi:10.1128/MCB.00079-08

Siegel, R. L., Miller, K. D., and Jemal, A. (2018). Cancer Statistics, 2018. *CA Cancer J. Clin.* 68, 7–30. doi:10.3322/caac.21442

Singh, B. N., Zhang, G., Hwa, Y. L., Li, J., Dowdy, S. C., and Jiang, S.-W. (2010). Nonhistone Protein Acetylation as Cancer Therapy Targets. *Expert Rev. Anticancer Ther.* 10 (6), 935–954. doi:10.1586/era.10.62

Smida, M., and Nijman, S. M. (2012). Functional Drug-Gene Interactions in Lung Cancer. *Expert Rev. Mol. Diagn.* 12 (3), 291–302. doi:10.1586/erm.12.16

Sohn, R. H., Chen, J., Koblan, K. S., Bray, P. F., and Goldschmidt-Clermont, P. J. (1995). Localization of a Binding Site for Phosphatidylinositol 4,5-bisphosphate on Human Profilin. *J. Biol. Chem.* 270, 21114–21120. doi:10.1074/jbc.270.36.21114

Suetsugu, S., Miki, H., and Takenawa, T. (1998). The Essential Role of Profilin in the Assembly of Actin for Microspike Formation. *EMBO J.* 17, 6516–6526. doi:10.1093/emboj/17.22.6516

Talmadge, J. E., and Fidler, I. J. (2010). AACR Centennial Series: the Biology of Cancer Metastasis: Historical Perspective. *Cancer Res.* 70, 5649–5669. doi:10.1158/0008-5472.CAN-10-1040

Tricarico, C., Clancy, J., and D'Souza-Schorey, C. (2017). Biology and Biogenesis of Shed Microvesicles. *Small GTPases* 8, 220–232. doi:10.1080/21541248.2016.1215283

Valenzuela-Iglesias, A., Sharma, V. P., Beaty, B. T., Ding, Z., Gutierrez-Millan, L. E., Roy, P., et al. (2015). Profilin1 Regulates Invadopodium Maturation in Human Breast Cancer Cells. *Eur. J. Cel Biol.* 94, 78–89. doi:10.1016/j.ejcb.2014.12.002

Wang, Y., Wang, Y., Wan, R., Hu, C., and Lu, Y. (2021). Profilin 1 Protein and its Implications for Cancers. *Oncology (Williston Park)* 35 (7), 402–409. doi:10.46883/ONC.2021.3507.0402

Wang, Z., Shi, Z., Zhang, L., Zhang, H., and Zhang, Y. (2019). Profilin 1, Negatively Regulated by microRNA-19a-3p, Serves as a Tumor Suppressor in Human Hepatocellular Carcinoma. *Pathol. Res. Pract.* 215, 499–505. doi:10.1016/j.prp.2018.12.012

Wei, L., Surma, M., Shi, S., Lambert-Cheatham, N., and Shi, J. (2016). Novel Insights into the Roles of Rho Kinase in Cancer. *Arch. Immunol. Ther. Exp. (Warsz)* 64, 259–278. doi:10.1007/s00005-015-0382-6

Conflict of Interest: The authors declare that the research was conducted in the absence of any commercial or financial relationships that could be construed as a potential conflict of interest.

Publisher's Note: All claims expressed in this article are solely those of the authors and do not necessarily represent those of their affiliated organizations, or those of the publisher, the editors and the reviewers. Any product that may be evaluated in this article, or claim that may be made by its manufacturer, is not guaranteed or endorsed by the publisher.

frontiers | Frontiers in Oncology

ORIGINAL RESEARCH
published: 16 May 2022
doi: 10.3389/fonc.2022.873918

Patterns and Trends of the Mortality From Bone Cancer in Pudong, Shanghai: A Population-Based Study

Gui-Fen Ma[1,2†], Qi-Yuan Bao[3,4†], Hong-Yue Zhang[5†], Yi-Chen Chen[6,7], Yue Zhang[8], Zhao-Yong Jiang[9], Xiao-Pan Li[10*] and Ju-Hua Zhang[11,12,13*]*

[1] Department of Radiation Oncology, Zhongshan Hospital, Fudan University, Shanghai, China, [2] Center for Cancer Prevention and Treatment, Zhongshan Hospital, Fudan University, Shanghai, China, [3] Department of Orthopaedics, Ruijin Hospital Jiaotong University School of Medicine, Shanghai, China, [4] Shanghai Institute of Traumatology and Orthopedics, Shanghai Key Laboratory for Bone and Joint Diseases, Shanghai, China, [5] Department of Orthopedics, First Affiliated Hospital of Naval Medical University, Shanghai, China, [6] Office of Scientific Research and Information Management, Center for Disease Control and Prevention, Pudong New Area, Shanghai, China, [7] Office of Scientific Research and Information Management, Pudong Institute of Preventive Medicine, Pudong New Area, Shanghai, China, [8] Department of Epidemiology, Shanxi Medical University School of Public Health, Taiyuan, China, [9] Department of Spinal Surgery, Yongzhou Central Hospital, Hunan, China, [10] Department of Health Management Center, Zhongshan Hospital, Shanghai Medical College of Fudan University, Shanghai, China, [11] Department of Orthopedics in Traditional Chinese Medicine, Shanghai University of Medicine & Health Sciences, Affiliated Zhoupu Hospital, Shanghai, China, [12] Department of Social Medicine and Health Career Management, School of Public Administration, Fudan University, Shanghai, China, [13] Department of Social Medicine and Health Career Management, Shanghai Pudong Health Development Research Institute, Shanghai, China

OPEN ACCESS

Edited by:
Zheng Huachuan, Chengde Medical University, China

Reviewed by:
Xiao Chen, Affiliated Hospital of Nanjing University of Chinese Medicine, China
Francesca Maffei, University of Bologna, Italy

***Correspondence:**
Xiao-Pan Li
xiaopanli0224@126.com
Zhao-Yong Jiang
jcy23_bjl@163.com
Ju-Hua Zhang
huihuis20@163.com

[†]These authors have contributed equally to this work

Specialty section:
This article was submitted to Cancer Epidemiology and Prevention, a section of the journal Frontiers in Oncology

Received: *11 February 2022*
Accepted: *11 April 2022*
Published: *16 May 2022*

Citation:
Ma G-F, Bao Q-Y, Zhang H-Y, Chen Y-C, Zhang Y, Jiang Z-Y, Li X-P and Zhang J-H (2022) Patterns and Trends of the Mortality From Bone Cancer in Pudong, Shanghai: A Population-Based Study. Front. Oncol. 12:873918. doi: 10.3389/fonc.2022.873918

Introduction: The burden of cancer-related mortality of common malignancies has been reported worldwide. However, whether bone cancer (BC), as a highly aggressive and heterogeneous group of rare cancers, followed a similar or distinct epidemiological pattern during such process remains largely unknown. We aimed to analyze the mortality and the temporal trends of BC in relation to gender, age, and premature death in Shanghai, China.

Methods: We conducted a population-based analysis of the mortality data of BC in Shanghai Pudong New Area (PNA) from 2005 to 2020. The epidemiological characteristics and long-term trends in crude mortality rates (CMRs), age-standardized mortality rates worldwide (ASMRWs), and rate of years of life lost (YLL) was analyzed using the Joinpoint regression program. The demographic and non-demographic factors affecting the mortality rate were evaluated by the decomposition method.

Results: There are 519 BC-specific deaths accounting for 0.15% of all 336,823 deaths and 0.49% of cancer-specific death in PNA. The CMR and ASMRW of BC were $1.15/10^5$ person-year and $0.61/10^5$ person-year, respectively. The YLL due to premature death from BC was 6,539.39 years, with the age group of 60–69 years having the highest YLL of 1,440.79 years. The long-term trend of CMR, ASMRW, and YLL rate significantly decreased by –5.14%, –7.64%, and –7.27%, respectively, per year (all $p < 0.05$) in the past 16 years. However, the proportion of BC-specific death within the total cancer-specific death dropped to a plateau without further improvement since 2016, and a remarkable gender and age disparity was noticed in the observed reduction in mortality.

Specifically, the elderly benefited less but accounted for a larger percentage of BC population in the last decades. Although the overall mortality of BC decreased, there was still a significant upward trend toward an increased mortality rate caused by the aging of the BC patients.

Conclusion: Our study provides novel insights on the epidemiological characteristics and longitudinal dynamics of BC in a fast urbanization and transitioning city. As a rare disease affecting all ages, the burden of BC among the elderly emerged to form an understudied and unmet medical need in an aging society.

Keywords: disease burden, bone cancer, trend analysis, aging, years of life lost, mortality, transitioning countries

INTRODUCTION

Bone cancer (BC) is a highly heterogeneous group of rare cancers, comprising over 50 different histologies (1). As a debilitating and metastasizing malignancy involving the musculoskeletal system, BC causes a significant disability and mortality and affects all age ranges compared to common cancer types. For example, as the three most common histologies, chondrosarcoma is usually diagnosed for people over 40 years of age, in contrast with Ewing sarcoma, which tends to impact children and teenagers (2). Osteosarcoma shows a bimodal distribution of the incidence, with a first peak occurring in the second decade and a second peak occurring in patients older than 60 years (3). Although the etiology and biology of bone cancer in the majority of the cases still remains unclear, the growth and development, germline genetics, somatic alterations, environmental exposure, and socioeconomic status (2) have all been proposed to be related to the predisposition and development of BC. Due to the fast transition of lifestyle behaviors, socioeconomic status, and healthcare system of modern society, the change in the spectrum of cancer mortality for several common cancer types has been widely reported. However, whether rare cancer types, such as BC, followed a similar or distinct epidemiological pattern during such process remains largely unknown. Therefore, a large-scale, population-based longitudinal study regarding the epidemiological change of BC is needed for better understanding and policy-making against such disease.

In the past several decades, China has experienced an outburst of economic growth, with Shanghai being a forerunner of such modernization process (4). Shanghai Pudong New Area (PNA) was established as and geared toward a national economic and technological development zone since the early 1990s. During the following decades, PNA became the largest and most populous region among the 16 districts, which represents one-fifth of the total population in Shanghai (4), with a geographic area of 1,210.41 km^2 (467.34 $mile^2$), and a registered permanent residency of more than 3.22 million (3). PNA is also the earliest area that began to establish modern healthcare infrastructure and to construct a sophisticated and reliable mortality registration system covering the total permanent resident population. PNA has witnessed the aging process in China's economically developed areas, and with the migration of migrants, the population structure has undergone tremendous changes. Furthermore, PNA has established a death information registration system covering the whole population, which provides a reliable guarantee for analyzing death data (5, 6). Therefore, PNA might be an ideal representative to investigate the epidemiological profile and temporal changes in BC in the context of Shanghai as a fast modernization and transitioning society.

In this report, we aimed to comprehensively analyze the mortality data of BC collected from the Vital Statistics System of the entire population of PNA, Shanghai, China, from 2005 to 2020. We estimated the disease burden and mortality trend in the past decades to explore the epidemiological characteristics and the potential preventive strategies for BC in the future.

METHODS

Data Source

According to the International Classification of Diseases 10th version (ICD-10), C40-41 refers to the primary malignant neoplasm that originated from bone and articular cartilage, also known as bone sarcoma. It accounts for 0.2% of all cancers and is one of the rare cancers. The most common subtypes of bone cancer are chondrosarcoma, osteosarcoma, chordoma, and Ewing sarcoma. In this report, data of BC (C40-C41)-related death of registered permanent residents from 2005 to 2020 were obtained from the Mortality Registration System of PNA, Shanghai. The complete population data were derived from the Public Security Bureau and the Statistics Bureau of PNA. Periodic evaluation and data cleaning are performed to maintain the integrity of the registration system according to standard guidelines. BC-specific deaths were classified according to the BC being an underlying cause of death according to the ICD-10. The causes of death were coded by clinicians according to the actual situation of patients and further checked by the local Centre for Disease Control and Prevention (CDC) (5). According to the 2000 Declaration of Helsinki, the study was performed and approved by the ethics committee of the Shanghai Pudong New Area Center for Disease Control and Prevention (IRB#2016-04-0586).

Statistical Analyses

The crude mortality rates (CMRs) and age-standardized mortality rates by Segi's world standard population (ASMRW) were shown as per 100,000 persons (/10^5). The CMR and

ASMRW were compared in gender by the Poisson approximation method and the Mantel–Haenszel test, respectively. Year of life lost (YLL) was calculated according to the original method described by Murray and Lopez. The formula of YLL adopted by the World Health Organization (WHO) (6–9).

Ages were calculated in the groups of 0–14 years, 15–29 years, 30–44 years, 45–59 years, 60–69 years, 70–79 years, and ≥80 years. The temporal trends of CMR, ASMRW, and YLL rate were calculated using the Joinpoint Regression Program 4.3.1.0 (National Cancer Institute, Bethesda, MD, USA) and expressed as average annual percent change (AAPC) with a corresponding 95% confidence interval (95% CI). The Z-test was used to assess whether the AAPC was statistically different from zero. The terms "increase" or "decrease" were used to describe a statistically significant (p <0.05) AAPC, while "stable" was used for non-significant trends (10).

The mortality rates of each year from 2006 to 2020, compared with the 2005 data, caused by demographic and non-demographic factors were estimated by the decomposition method, in which mortality rates were calculated and compared for each 5-year age group, from 0 to 4 to ≥85 years (8). All statistical analyses were conducted using SPSS (version 21.0; SPSS, Inc., Chicago, IL, USA) and R (version 3.4.3). Statistical significance was set at p <0.05.

RESULTS

Baseline

A total of 519 BC-specific deaths from 586 BC-related deaths (**Supplementary Tables S1**–**S3**) were identified, accounting for 0.15% of all 336,823 deaths from 2005 to 2020 in Shanghai PNA, which included 508 underlying cause of death (C40–C41) and 11 death (C97, C40–C41) (**Figure 1**). There were 281 male (54.14%) and 238 female (45.86%) patients who died of BC. The median age and average age at death from BC were 71.82 years and 67.26 ± 18.62 years. The CMR and ASMRW of BC were $1.15/10^5$ person-year and $0.61/10^5$ person-year, respectively. The CMR and ASMRW were $1.25/10^5$ and $1.05/10^5$ person-years and $0.71/10^5$ and $0.52/10^5$ person-years in male and female patients, respectively. The CMR and ASMRW in male patients were higher than those in female patients (all p < 0.05) (**Table 1**).

Main Comorbidities of BC

The top 3 comorbidities in 281 male patients with BC as underlying cause of death were other diseases of the respiratory system (J95–J99) (10.20%), secondary malignant neoplasm of respiratory and digestive organs (C78) (5.97%), and secondary malignant neoplasm of other sites (C79) (5.97%). The top 3 comorbidities of 238 female patients whose underlying cause of death was BC were heart disease (I05–I09, I20–I25, I26–I27, and I30–I52) (9.74%), other diseases of the respiratory system (J95–J99) (7.35%) and secondary malignant neoplasm of other sites (C79) (6.25%). The top 10 comorbidities in male and female patients with BC as underlying cause of death are presented in **Figure 2** and **Supplementary Table S1**.

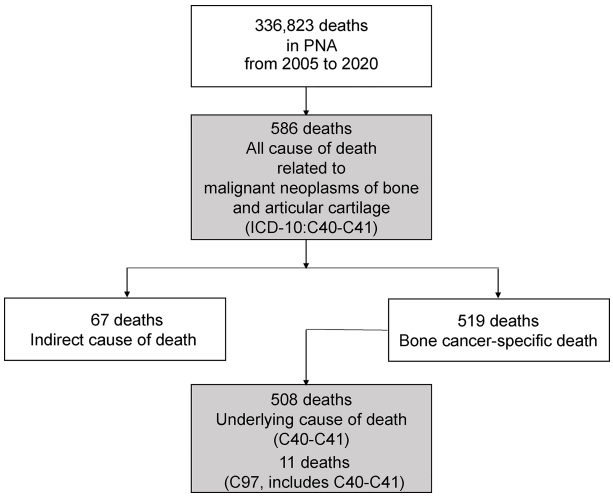

FIGURE 1 | The flow chart of deaths from bone cancer in Shanghai Pudong New Area being include in this study.

The top 3 comorbidities in 325 male patients with BC as all causes of death were lung cancer (C33–C34) (3.38%), secondary malignant neoplasm of independent (primary) multiple sites (C97) (1.85%) and heart diseases (I05–I09, I20–I25, I26–I27, I30–I52) (1.85%). The top 3 comorbidities of 261 female patients whose all cause of death including BC were secondary malignant neoplasm of independent (primary) multiple sites (C97) (1.92%), heart disease (I05–I09, I20–I25, I26–I27, I30–I52) (1.53%) and cerebrovascular disease (I60–I69) (1.15%). The top 10 comorbidities in male and female patients with BC as all cause of death are presented in **Supplementary Figure S1** and **Supplementary Table S3**.

BC-Specific Premature Death

From 2005 to 2020, the YLL due to premature death from BC was 6,539.39 years, and the rate of YLL was $14.50/10^5$. YLL and the rate of YLL in men (3,604.24 years, $16.01/10^5$) were higher than those in women (2,935.15 years, $12.99/10^5$). In 519 BC-specific deaths, the main comorbidities were the diseases of the respiratory system (J00–J99) and the circulatory system (I00–I99), accounting for 14.84% and 4.82%, respectively. Moreover, 129 (24.86%) patients died due to BC-related metastases. The main metastatic sites of BC were the lung (10.21%) and liver (2.12%). The CMR, ASMRW, YLL, and YLL rates in different gender, periods, metastatic cancer, and comorbidity are detailed in **Table 1**.

Age-Specific Burden of BC

A total of 386 (74.37%) elderly people aged over 60 years died from BC. The top 3 age groups with the highest CMR were ≥80 years, 70–79 years, and 60–69 years, which were $7.18/10^5$ person-years, $4.55/10^5$ person-years, $1.64/10^5$ person-years, respectively.

TABLE 1 | Baseline characteristics of deaths and burden in different genders and types of bone cancer during 2005–2020.

Characteristic	Deaths (n,%)	Age at years (mean ± SD)	Age at years (Median)	Age at years (Range)	CMR (/10^5)	ASMRW (/10^5)	YLL (years)	YLL rate (/10^5)
Gender								
Male	281 (54.14)	65.46 ± 18.39	68.47	5.73-93.81	1.25	0.71	3604.24	16.01
Female	238 (45.86)	69.39 ± 18.71	75.16	12.62-94.19	1.05	0.52	2935.15	12.99
Periods								
2005–2008	169 (32.56)	61.11 ± 17.98	70.96	5.73-93.77	1.62	0.99	2216.12	21.27
2009–2012	137 (26.40)	66.70 ± 19.19	73.92	13.87-92.49	1.24	0.68	1757.79	15.96
2013–2016	106 (20.42)	66.57 ± 19.50	69.94	13.74-94.19	0.92	0.52	1346.94	11.69
2017–2020	107 (20.62)	70.49 ± 17.90	73.31	13.74-93.42	0.88	0.38	1218.55	10.03
Metastatic cancer								
All metastatic bone cancer	129 (24.86)	62.54 ± 20.78	67.35	12.62-94.19	0.29	0.19	1855.60	4.11
Metastatic bone cancer to the lung (C78.0)	53 (10.21)	57.38 ± 22.12	62.87	13.45-93.32	0.12	0.09	856.61	1.90
Metastatic bone cancer to the liver (C78.7)	11 (2.12)	64.36 ± 16.46	69.66	32.31-85.92	0.02	0.01	154.97	0.34
Metastatic bone cancer to the unknown sites (C79)	47 (9.06)	66.13 ± 19.06	68.63	13.12-93.59	0.10	0.06	622.60	1.38
The main comorbidity in all causes of death								
Diseases of the respiratory system (J00–J99)	77 (14.84)	69.92 ± 17.92	72.61	13.45-93.54	0.17	0.08	880.54	1.95
Diseases of the circulatory system (I00–I99)	25 (4.82)	62.79 ± 23.42	73.66	13.12-90.99	0.06	0.04	350.40	0.78
Total bone cancer-specific death	519 (100.00)	67.26 ± 18.62	71.82	5.73-94.19	1.15	0.61	6539.39	14.50
Total all cause of death of the population	336,823 (/)	76.99 ± 14.44	80.45	0.00-116.39	746.71	279.39	3040514.99	6740.55

ASMRW, age-standardized mortality rate by Segi's world standard population; CMR, crude mortality rate; YLL, years of life lost.

Among them, the age group of 60–69 years had the highest YLL, with a loss of 1,440.79 years. The top 3 age groups with the highest rates of YLL were 70–79 years, ≥80 years, and 60–69 years, with rates of $42.77/10^5$, $37.68/10^5$, and $23.19/10^5$, respectively. The burden of BC in other age groups are shown in **Table 2**.

Trends of Burden From BC

The long-term trends in CMR (AAPC = −5.14%), ASMRW (AAPC = −7.64%), and YLL rate (AAPC = −7.27%) were significantly decreasing in the total population from 2005 to 2020 (all $p < 0.05$). Details are shown in **Figure 3** and **Supplementary Tables S4**, **S5**.

The CMR, ASMRW, and YLL rate in female patients significantly decreased by −6.67%, −8.61%, and −9.78% per year, while those of male patients significantly decreased by −4.07%, −6.86%, and −4.86% per year (all $p < 0.05$). Details are shown in **Figure 3** and **Supplementary Tables S4–S6**. The age-specific mortality rates and YLL rates of aged 0–29 years and ≥50 years showed an obvious downward trend (all $p < 0.05$), except the age group of 30–44 years and 45–59 years. Details were shown in **Figure 3** and **Supplementary Tables S5**, **S6**.

The trends of age-specific proportion of death has shown that there was a significant decrease in the proportion of death aged 0–29 years (AAPC = −29.18%). Meanwhile, there was a significantly increase in the proportion of death aged ≥80 years (AAPC= 5.51%)

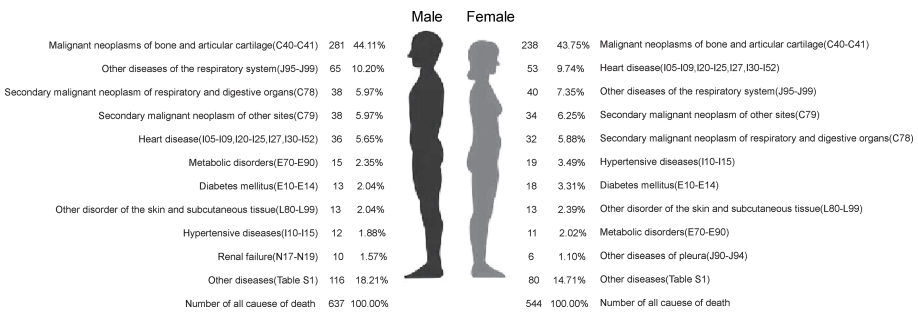

FIGURE 2 | The top 10 of all causes of death of people who died from bone cancer in genders in Pudong New Area, Shanghai, China, 2005–2020.

TABLE 2 | Age-specific mortality and burden of bone cancer during 2005–2020.

Age (years group)	Deaths (N)	Proportion (%)	CMR (/10^5)	YLL (years)	YLL rate (/10^5)
0–4	0	0.00	0.00	0.00	0.00
5–14	11	2.12	0.37	321.16	10.89
15–29	24	4.62	0.33	662.84	9.20
30–44	23	4.43	0.23	569.66	5.60
45–59	75	14.45	0.64	1436.76	12.26
60–69	102	19.65	1.64	1440.79	23.19
70–79	149	28.71	4.55	1399.62	42.77
≥80	135	26.01	7.18	708.57	37.68
Total	519	100.00	1.15	6539.39	14.50

ASMRW, age-standardized mortality rate by Segi's world standard population; CMR, crude mortality rate; YLL, years of life lost.

(all $p < 0.05$). Details are shown in **Figure 3** and **Supplementary Table S7**. Interestingly, although the mortality of BC has decreased in the past decades, the proportion of BC-specific death within the total cancer-specific death in PNA dropped to a plateau without improvement since 2016 (**Supplementary Figure S2** and **Supplementary Table S8**).

Quantitative Impacts of Demographic and Non-Demographic Factors on Mortality Rate

With the increase in the proportion of people aged ≥65 years in the local population per year (**Supplementary Figure S3**), increasing trends of CMR caused by demographic factors from 2006 to 2019 were observed, compared with the CMR in 2005 (**Figure 4** and **Supplementary Table S9**). A significant upward trend in the increase rate caused by demographic factors was noticed in the total population, with an annual percent change (APC) of 25.07% [(95% CI: 17.49%–33.14%), $p < 0.001$], whereas a significant downward trend was observed in the rate affected by non-demographic factors, with an APC of −21.06% [(95% CI: −27.23% to −14.38%, $p < 0.001$]. In male patients, the mortality rate affected by non-demographic factors decreased by −14.05% [(95% CI: −19.30% to −8.46%), $p < 0.001$], and the rate due to demographic factors increased by 27.72% [(95% CI: 19.96%–35.99), $p < 0.001$]. In female patients, the increased mortality rate due to non-demographic factors showed a downward trend [APC (95% CI) = −13.70% (−23.45% to −2.70%), $p = 0.020$], contrary to the rate due to demographic factors [APC (95% CI) = 21.30% (13.18%–30.01%), $p < 0.001$]. The concern is that, over time, the impact of demographic

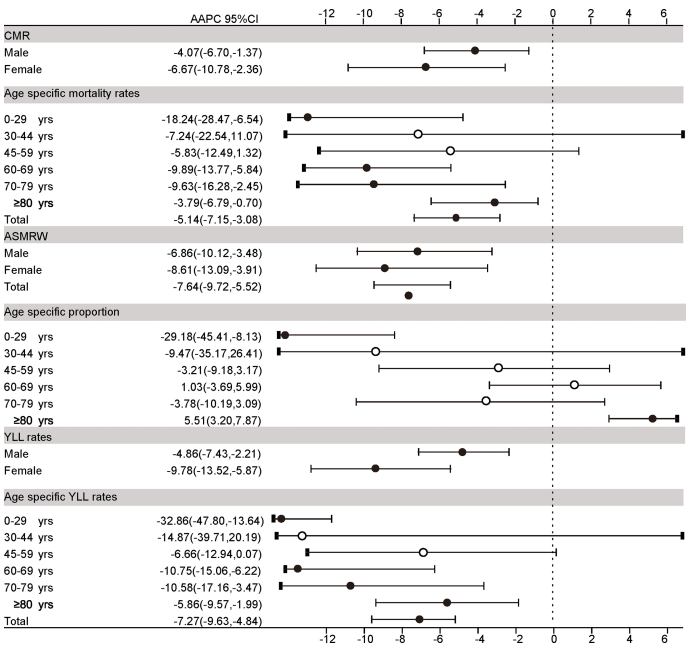

FIGURE 3 | The trends in CMR, ASMRW, age-specific proportions, and YLL rate of persons with underlying cause of death from bone cancer in genders and age groups in Pudong New Area, Shanghai, China, 2005–2019. CMR, crude mortality rate (per 100,000); ASMRW, age-standardized mortality rate by Segi's world standard population (per 100,000); YLL, year of lost, AAPC, average annual percent change; CI, confidence interval.

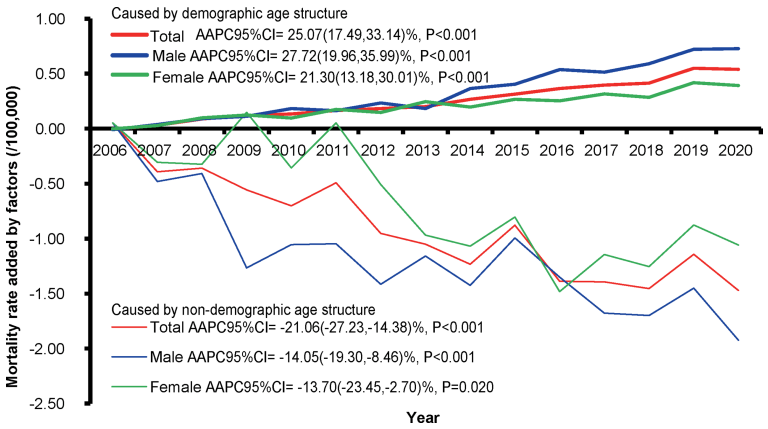

FIGURE 4 | The increased rates caused by demographic and non-demographic factors and their proportion during the period from 2006 to 2020 compared with the crude mortality rate of bone cancer during 2005 in Pudong New Area, Shanghai, China. AAPC, average annual percent change; CI, confidence interval.

factors on the CMR in male patients was more obvious than that in female patients ($p < 0.05$).

DISCUSSION

As one of the fastest modernization districts of Shanghai, PNA has a gross domestic product (GDP) increasing from 10.1 billion RMB in 1992 to 789.8 billion RMB in 2015, with an average annual growth rate of 15.6%. The permanent residence of PNA has increased from 2.40 million in 2000 (14.92% of Shanghai) to 5.55 million in 2018 (22.9% of Shanghai) (4). Consistent with the reported data from the United States (3) and Europe (11), we found an obvious decrease in the mortality trend of BC during the urbanization process in PNA. Since the protocols and regimens for BC had minimal improvement in the past three decades (12), such reduction in mortality is likely due to the advance in the healthcare system, the medical infrastructure, and better adherence to the protocols. Furthermore, public education and awareness might also contribute to the prevention and early screening of BC. For instance, Holly et al. (13) observed that regular intake of mixed vitamin supplements during childhood decreases the risk of bone tumors (RR = 0.4; 95%CI: 0.1–1.4), and exposure to herbicides, pesticides, or fertilizers might increase the risk (RR = 6.1, 95% CI: 1.7–21.9). The reduction in other environmental hazards such as smoking during pregnancy (14) and ionizing radiation (15) in the lifestyle may also contribute to the observed trend of BC mortality. However, it should be noted that the proportion of BC-specific death within the total cancer mortality reached a plateau since 2016 (**Supplementary Figure S2**), indicating that the progress of BC has lagged behind that of the common cancer types in the past years.

It is noteworthy that there is a gender and age disparity in the observed decrease in mortality in the past 16 years. The female and younger age groups were the most significant contributors to the trend of mortality reduction, while the middle-aged and older populations benefitted less in the last decades. The potential causes might be twofold. On the one hand, it is reported that bone sarcoma patients aged 0–29 years (16, 17) and being female (18, 19) may have a greater response to current treatment protocols. By contrast, the optimal regimen for the elderly, especially those older than 65 years old, remains yet to be established (20). On the other hand, the age disparity in the improvement of mortality is also likely to reflect the refinement of current treatment strategies, which considerably reduce the short-term mortality of BC in the younger age group yet increase the chance of late recurrence, including the development of secondary malignancy, of BC. In line with this hypothesis, we found a relatively high percentage of secondary malignant neoplasm (12%) among the total mortality of BC in our cohort. These results reinforce the importance of long-term surveillance to reduce late mortality for those BC patients with short-term survivorship.

BC is well-known for its impact on the young- and middle-aged population. However, our results suggest that the proportion of BC patients younger than 30 years old was decreased, while that of the patients older than 80 years old increased in the total disease mortality during the past decades. The underlying reason for this trend might relate to Shanghai as one of the most and earliest aging societies in China. In 2008, PNA became an aging society, with 14.2% of residents aged over 65 years. In 2018, PNA was defined as a super-aging society, with more than 20% of residents aged over 65 years, and such proportion is still currently increasing (**Supplementary Figure S3**). Therefore, the elderly forms a distinct, understudied, and underserved group of BC burden in cancer care following the urbanization and socioeconomic development in Shanghai as an aging society (21). Importantly, although the overall mortality of BC demonstrated a downward trend, there was still a significant upward trend toward an increased mortality rate caused by the demographic factor (age), with an APC of 25.07% [(95% CI: 17.49%–33.14%), $p < 0.001$]. Given that older age (≥65 years) was known as a predictor of poor cancer survival in patients with overall bone sarcoma, osteosarcoma, chondrosarcoma (17), it is,

therefore, an unmet medical need to take into account the age differences when designing future preventive and intervention strategies in Shanghai and other aging cities around the world.

There are several limitations to our study. First, due to the low number of BC as a rare cancer, the sample size of the present study is relatively low compared to common cancer types. Furthermore, one needs to interpret with caution when generalizing our findings to the total population of Shanghai, which is highly heterogeneous in terms of urbanization level, socio-economic status, healthcare infrastructure, etc. However, given that PNA area represents the most rapidly developing and transitioning part of Shanghai over the last decades, we proposed that our conclusions might be generalizable to those areas currently going or will go through the modernizing process in the suburban/rural part of Shanghai.

In conclusion, our study provides novel insights on the epidemiological characteristics and longitudinal dynamics of BC in a fast urbanization and transitioning society. We observed a significant reduction in BC mortality in past decades, yet with a clear gender and age disparity. As a disease affecting all ages, the burden of BC among the elderly might emerged as an understudied and unmet medical need in Shanghai, and other fast-transitioning cities worldwide.

DATA AVAILABILITY STATEMENT

The data presented in the study are available from the corresponding authors upon reasonable request and with permission of Center for Disease Control and Prevention of the Pudong New Area, Shanghai, China.

AUTHOR CONTRIBUTIONS

G-FM, Q-YB, and X-PL drafted and revised the manuscript. X-PL, G-FM, H-YZ, and Y-CC participated in the collection, analysis, and interpretation of data. Y-CC, YZ, H-YZ, and Q-YB contributed to data collection and suggestion for analysis. G-FM, X-PL, and J-HZ conceived the study and participated in its design and coordination and critically revised the manuscript. All authors read and approved the final version of the manuscript.

FUNDING

This study was funded by a grant from special program for clinical research in the health industry of Shanghai Health Commission (20204Y0166 to J-HZ), a grant from the Key Specialty of Shanghai Pudong New Area Health Committee (PWZzk2017-08 to J-HZ), a grant from Shanghai Public Health System Construction Three-Year Action Plan Outstanding Youth Talent Training Program (GWV-10.2-YQ43 to Y-CC) and the Reserve Academic Leaders Training Program of the Pudong New Area Centre for Disease Control and Prevention (PDCDC-HBXD2020-05 to X-PL), and a grant from the Shanghai Municipal Health Commission (202140124 to Q-YB).

ACKNOWLEDGMENTS

We thank all the participants in the vital statistics system of Pudong New Area from 2005 to 2020 for their great work in data collection and assuring data of high quality.

SUPPLEMENTARY MATERIAL

The Supplementary Material for this article can be found online at: https://www.frontiersin.org/articles/10.3389/fonc.2022.873918/full#supplementary-material

Supplementary Figure 1 | The top ten of underlying causes of death of people died related to bone cancer in genders in Pudong New Area, Shanghai, China, 2005-2020.

Supplementary Figure 2 | The proportion of people aged ≥65 years in genders in Pudong New Area, Shanghai, China, 2005-2020.

Supplementary Table 1 | The sequence of underlying causes of death in 586 bone cancer related deaths.

Supplementary Table 2 | The underlying causes of death in 67 deaths with bone cancer death from other diseases.

Supplementary Table 3 | The sequence of all causes of death in 519 bone cancer specific deaths.

Supplementary Table 4 | The distribution of definite pathological types in 519 bone cancer specific deaths.

Supplementary Table 5 | The case number of death, CMR and ASMRW in gender during the period from 2005 to 2020 in Pudong New Area, Shanghai, China. ASMRW, age-standardized mortality rate by Segi's world standard population; CMR, crude mortality rate.

Supplementary Table 6 | The CMR and modeled CMR by Joinpont regression in age groups during the period from 2005 to 2020 in Pudong New Area, Shanghai, Chin. CMR, crude mortality rate.

Supplementary Table 7 | The YLLr and modeled YLLr by Joinpont regression in gender and age groups during the period from 2005 to 2020 in Pudong New Area, Shanghai, China. YLL, the rate of years of life lost.

Supplementary Table 8 | The proportion and modeled proportion by Joinpont regression in age groups during the period from 2005 to 2020 in Pudong New Area, Shanghai, China.

Supplementary Table 9 | The increase value of CMR caused by demographic and non-demographic factors during the period from 2005 to 2020 in Pudong New Area, Shanghai, China. CMR, crude mortality rate.

REFERENCES

1. Choi JH, Ro JY. The 2020 WHO Classification of Tumors of Bone: An Updated Review. *Adv Anat Pathol* (2021) 28:119–38. doi: 10.1097/PAP.0000000000000293
2. Savage SA, Mirabello L. Using Epidemiology and Genomics to Understand Osteosarcoma Etiology. *Sarcoma* (2011) 2011:548151. doi: 10.1155/2011/548151
3. Mirabello L, Troisi RJ, Savage SA. Osteosarcoma Incidence and Survival Rates From 1973 to 2004: Data From the Surveillance, Epidemiology, and End Results Program. *Cancer* (2009) 115:1531–43. doi: 10.1002/cncr.24121
4. Shanghai Municipal Statistics Bureau Survey Office of The Nation. In: *Shanghai Statistical Yearbook*. Shanghai: China Statistics Press.
5. Li X, Deng Y, Tang W, Sun Q, Chen Y, Yang C, et al. Urban-Rural Disparity in Cancer Incidence, Mortality, and Survivals in Shanghai, China, During 2002 and 2015. *Front Oncol* (2018) 8:579. doi: 10.3389/fonc.2018.00579
6. Global Age-Sex-Specific Fertility, Mortality, Healthy Life Expectancy (HALE), and Population Estimates in 204 Countries and Territories, 1950-2019: A Comprehensive Demographic Analysis for the Global Burden of Disease Study 2019. *Lancet* (2020) 396:1160–203. doi: 10.1016/S0140-6736(20)30977-6
7. Global, Regional, and National Age-Sex-Specific Mortality for 282 Causes of Death in 195 Countries and Territories, 1980-2017: A Systematic Analysis for the Global Burden of Disease Study 2017. *Lancet* (2018) 392:1736–88. doi: 10.1016/S0140-6736(18)32203-7
8. Luo Z, Lv H, Chen Y, et al. Years of Life Lost Due to Premature Death and Their Trends in People With Selected Neurological Disorders in Shanghai, China, 1995-2018: A Population-Based Study. *Front Neurol* (2021) 12:625042. doi: 10.3389/fneur.2021.625042
9. Kocarnik JM, Compton K, Dean FE, Fu W, Gaw BL, Harvey JD, et al. Cancer Incidence, Mortality, Years of Life Lost, Years Lived With Disability, and Disability-Adjusted Life Years for 29 Cancer Groups From 2010 to 2019: A Systematic Analysis for the Global Burden of Disease Study 2019. *JAMA Oncol* (2021) 8(3):420–44. doi: 10.1001/jamaoncol.2021.6987
10. Luo Z, He Y, Ma G, Deng Y, Chen Y, Zhou Y, et al. Years of Life Lost Due to Premature Death and Their Trends in People With Malignant Neoplasm of Female Genital Organs in Shanghai, China During 1995-2018: A Population Based Study. *BMC Public Health* (2020) 20:1489. doi: 10.1186/s12889-020-09593-6
11. van der Meer DJ, Karim-Kos HE, van der Mark M, Aben KKH, Bijlsma RM, Rijneveld AW, et al. Incidence, Survival, and Mortality Trends of Cancers Diagnosed in Adolescents and Young Adults (15-39 Years): A Population-Based Study in The Netherlands 1990-2016. *Cancers (Basel)* (2020) 12. doi: 10.3390/cancers12113421
12. Heymann MF, Schiavone K, Heymann D. Bone Sarcomas in the Immunotherapy Era. *Br J Pharmacol* (2021) 178:1955–72. doi: 10.1111/bph.14999
13. Holly EA, Aston DA, Ahn DK, Kristiansen JJ. Ewing's Bone Sarcoma, Paternal Occupational Exposure, and Other Factors. *Am J Epidemiol* (1992) 135:122–9. doi: 10.1093/oxfordjournals.aje.a116265
14. Winn DM, Li FP, Robison LL, Mulvihill JJ, Daigle AE, Fraumeni JF Jr. A Case-Control Study of the Etiology of Ewing's Sarcoma. *Cancer Epidemiol Biomarkers Prev* (1992) 1:525–32.
15. Chmelevsky D, Kellerer AM, Land CE, Mays CW, Spiess H. Time and Dose Dependency of Bone-Sarcomas in Patients Injected With Radium-224. *Radiat Environ Biophysics* (1988) 27:103–14. doi: 10.1007/BF01214600
16. Wu J, Sun H, Li J, Guo Y, Zhang K, Lang C, et al. Increased Survival of Patients Aged 0-29 Years With Osteosarcoma: A Period Analysis, 1984-2013. *Cancer Med* (2018) 7:3652–61. doi: 10.1002/cam4.1659
17. Fukushima T, Ogura K, Akiyama T, Takeshita K, Kawai A. Descriptive Epidemiology and Outcomes of Bone Sarcomas in Adolescent and Young Adult Patients in Japan. *BMC Musculoskelet Disord* (2018) 19:297. doi: 10.1186/s12891-018-2217-1
18. Wang Z, Li S, Li Y, Lin N, Huang X, Liu M, et al. Prognostic Factors for Survival Among Patients With Primary Bone Sarcomas of Small Bones. *Cancer Manag Res* (2018) 10:1191–9. doi: 10.2147/CMAR.S163229
19. Livingston JA, Hess KR, Naing A, Hong DS, Patel S, Benjamin RS, et al. Validation of Prognostic Scoring and Assessment of Clinical Benefit for Patients With Bone Sarcomas Enrolled in Phase I Clinical Trials. *Oncotarget* (2016) 7:64421–30. doi: 10.18632/oncotarget.10910
20. Tsuda Y, Ogura K, Shinoda Y, Kobayashi H, Tanaka S, Kawai A. The Outcomes and Prognostic Factors in Patients With Osteosarcoma According to Age: A Japanese Nationwide Study With Focusing on the Age Differences. *BMC Cancer* (2018) 18:614. doi: 10.1186/s12885-018-4487-2
21. Xu P, Wang J, Sun B, Xiao Z. Integrated Analysis of miRNA and mRNA Expression Data Identifies Multiple miRNAs Regulatory Networks for the Tumorigenesis of Colorectal Cancer. *Gene* (2018) 659:44–51. doi: 10.1016/j.gene.2018.03.050

Conflict of Interest: The authors declare that the research was conducted in the absence of any commercial or financial relationships that could be construed as a potential conflict of interest.

frontiers | Frontiers in Oncology

REVIEW
published: 02 June 2022
doi: 10.3389/fonc.2022.921667

Contrast Agents for Hepatocellular Carcinoma Imaging: Value and Progression

Ying Zhang[1,2,3], *Kazushi Numata*[2*], *Yuewu Du*[1] *and Shin Maeda*[3]

[1] Department of Medical Ultrasound, Ningbo Medical Centre Li Huili Hospital, Ningbo, China, [2] Gastroenterological Center, Yokohama City University Medical Center, Yokohama, Japan, [3] Department of Gastroenterology, Graduate School of Medicine, Yokohama City University, Yokohama, Japan

Hepatocellular carcinoma (HCC) has the third-highest incidence in cancers and has become one of the leading threats to cancer death. With the research on the etiological reasons for cirrhosis and HCC, early diagnosis has been placed great hope to form a favorable prognosis. Non-invasive medical imaging, including the associated contrast media (CM)-based enhancement scan, is taking charge of early diagnosis as mainstream. Meanwhile, it is notable that various CM with different advantages are playing an important role in the different imaging modalities, or even combined modalities. For both physicians and radiologists, it is necessary to know more about the proper imaging approach, along with the characteristic CM, for HCC diagnosis and treatment. Therefore, a summarized navigating map of CM commonly used in the clinic, along with ongoing work of agent research and potential seeded agents in the future, could be a needed practicable aid for HCC diagnosis and prognosis.

Keywords: ultrasound, MRI, CECT, hepatocellular carcinoma (HCC), contrast media (CM)

OPEN ACCESS

Edited by:
Kun Zhang,
Tongji University, China

Reviewed by:
Dan Zhao,
Hangzhou Red Cross Hospital, China
Chengcheng Niu,
Central South University, China

****Correspondence:***
Kazushi Numata
kz_numa@yokohama-cu.ac.jp

Specialty section:
This article was submitted to Radiation Oncology, a section of the journal Frontiers in Oncology

Received: *16 April 2022*
Accepted: *02 May 2022*
Published: *02 June 2022*

Citation:
Zhang Y, Numata K, Du Y and Maeda S (2022) Contrast Agents for Hepatocellular Carcinoma Imaging: Value and Progression. Front. Oncol. 12:921667. doi: 10.3389/fonc.2022.921667

INTRODUCTION

Hepatocellular carcinoma (HCC) has the third-highest incidence in cancers, along with the fourth leading cause of cancer death in 2020 globally. Moreover, cirrhosis, a major source of HCC, composed 2.4% of death with all causes in 2019 according to the WHO. Meanwhile, hepatitis B virus (HBV) and hepatitis C virus (HCV) infection, alcohol abuse, and non-alcoholic steatohepatitis (NASH) are dominating etiological reasons for cirrhosis and HCC. Modern medicine believes the small HCC is preventable and curable through early diagnosis and timely etiological treatment if screening and surveillance could be well conducted for cirrhosis (1). Therefore, non-invasive medical imaging techniques, such as MRI, ultrasound (US), and CT, have contributed to HCC patients' management (2–6).

For early diagnosis, treatment assessment, and follow-up, multiple medical imaging modalities were improved and adapted in every corner of HCC prevention and supervision. In the past decades, the diagnostic efficacy of medical imaging has been elevated through the improvement of imaging resolution and associated intravenous contrast agents. US elastography and MR elastography are recommended to supervise and assess hepatic fibrosis, which may gradually progress to cirrhosis without medical intervention (7). On the other hand, taking characteristic advantage of the dual blood supply of the liver, transvenous contrast agents depict the liver lesion by illustrating the tumorous

blood supply with characteristics of arterial enhancement (wash-in) and portal hypodensity or hyposignal (wash-out). The classical imaging findings of wash-in and wash-out were believed to have a sensitivity of approximately 60% and a specificity of 96%–100% for small HCCs with a size of 10–20 mm. Still, a biopsy is needed in 40% of these lesions. Along with a deeper investigation of clinical research, an experienced radiologist can achieve a much more satisfying diagnostic efficacy through guidelines like the American College of Radiology Liver Imaging Reporting and Data System (ACR LIRADS) (8, 9). As a result, contrast enhancement imaging, like dynamic MRI and contrast-enhanced CT (CECT), is recommended in mainstream guidelines for preoperative HCC diagnosis with certainty. Screening using the non-enhanced US is also recommended for patients at a higher risk of HCC every 6 months. When it comes to contrast-enhanced US (CEUS), though it is not recommended by the World Federation for Ultrasound in Medicine and Biology (WFUMB) guidelines for liver lesion detection due to the narrow window for arterial phase observation (10), some meta-analyses indicated it to be a promising diagnostic approach for HCC with a sensitivity of 93% (95% CI: 91%–95%) and a specificity of 90% (95% CI: 88%–92%) (11), as well as the diagnostic efficacy of 93% in small HCCs (≦2 cm) (12).

Contrast-enhanced imaging for the tumor is a tracer technique of contrast media (CM) in essence. The distribution and dynamic phases of the agent are analyzed for lesion detection and characterization for early diagnosis and possible prognosis prediction. Therefore, a summarized navigating map of CM commonly used in the clinic, along with ongoing work of agent research and potential seeded agents in the future, could be a needed reference work for both physicians and radiologists.

BLOOD POOL CONTRAST AGENTS

Ultrasound Contrast Agents

As early as the late 1960s, people found that the microbubbles (MBs) that provide many reflecting interfaces for echo are a good intravascular flow tracer for US imaging (13), and the hydrogen peroxide solution was launched for echocardiography thereafter. According to the inner gas of the MB, US contrast agent (UCA) could be classified into two generations. Air core with the polymeric coat is the so-called first-generation UCA, such as Levovist (Schering, Berlin-Wedding, Germany). The first-generation UCA is a milestone in the history of medical US imaging development, though it comes with defects like unstableness and unsafety (13). Thereafter, inert gas that is enveloped with a lipid shell at a diameter of approximately several micrometers is developed as the second-generation UCA, which is slightly smaller than that of the red blood cell. Taking advantage of materials science and technology development, the second-generation UCA with greater stability and biosafety can achieve a promising diagnostic efficacy for HCC (11, 12), along with the negligible report of anaphylaxis compared with CT and MRI, which means that UCA can be employed for the patients having iodine allergy, chronic kidney disease, hepatic function failure, asthma, and so on. Moreover, the bedside operation with a portable US machine could be performed in the emergency department (ED) and intensive care unit (ICU) as needed. However, concerning clinical practice, CEUS is not good at imaging the hepatic lesion located near the lung and behind the costal bone, due to the so-called shadow zone caused by the costal bone and lung. The other weakness is US attenuation in far-field of a fatty liver can lead to the indefinable hepatic situation.

Currently, sulfur hexafluoride (i.e., SonoVue, Bracco Imaging, Milan, Italy) is the most consumed in the global UCA market, followed by perfluorinated butane (i.e., Sonazoid, GE Healthcare, Oslo, Norway). The former is a pure blood pool agent, while the latter behaves similarly at the beginning but permeates into extravascular space soon after administration, which will be discussed in Section 3.

Iodinated Agents for Contrast-Enhanced CT

Many iodinated agents are pure blood pool agents, which are the widest and longest used CM for X-ray-based enhancement scans (i.e., CECT) (**Figure 1**). To date, the effort of optimizing small-molecule iodinated agents for contrast enhancement could be mainly classified into three eras, including four categories of compounds, from ionic to non-ionic, from monomers to dimers, from high-osmolality to iso-/low-osmolality, associating with decreasing toxicity and increasing bio-tolerability. Commercially available agents are abundant in the clinic, such as iohexol (Omnipaque, GE Healthcare), iopromide (Ultravist, Bayer Healthcare, Leverkusen, Germany), iodixanol (Visipaque, GE Healthcare), iopamidol (Isovue, Bracco Imaging, Milan, Italy), and iothalamate (Cysto-Conray II, Mallinckrodt Imaging, St. Louis, MO, USA). Moreover, novel agents, like iosimenol and GE-145, are on the way to commercialization with the improvements made on an existing basis. The diagnostic efficacy of CECT for HCC in terms of area under the receiver operating characteristic (ROC) curve (AUC), sensitivity, and specificity were reported to be 0.93, 93%, and 82%, respectively (14). For HCC patients, the most distinctive role that CT perfusion imaging has played is the transarterial chemoembolization (TACE) assessment (15). However, despite great improvements that have been made in the bone and cartilage tissue, iodinated contrast agents employed in parenchymal organs, like the liver, have not yet been largely renovated (16, 17).

The blood pool agent applied to MRI is mainly established for MR angiography rather than the liver tumor, which is beyond the scope of the present review article and will not be discussed herein.

EXTRACELLULAR CONTRAST AGENTS

Non-Specific Agents

For MRI, gadolinium-based micromolecule agents that have five or seven unpaired electrons could be stimulated to be paramagnetic under an external magnetic field. Those so-called paramagnetic contrast agents for dynamic MRI are developed

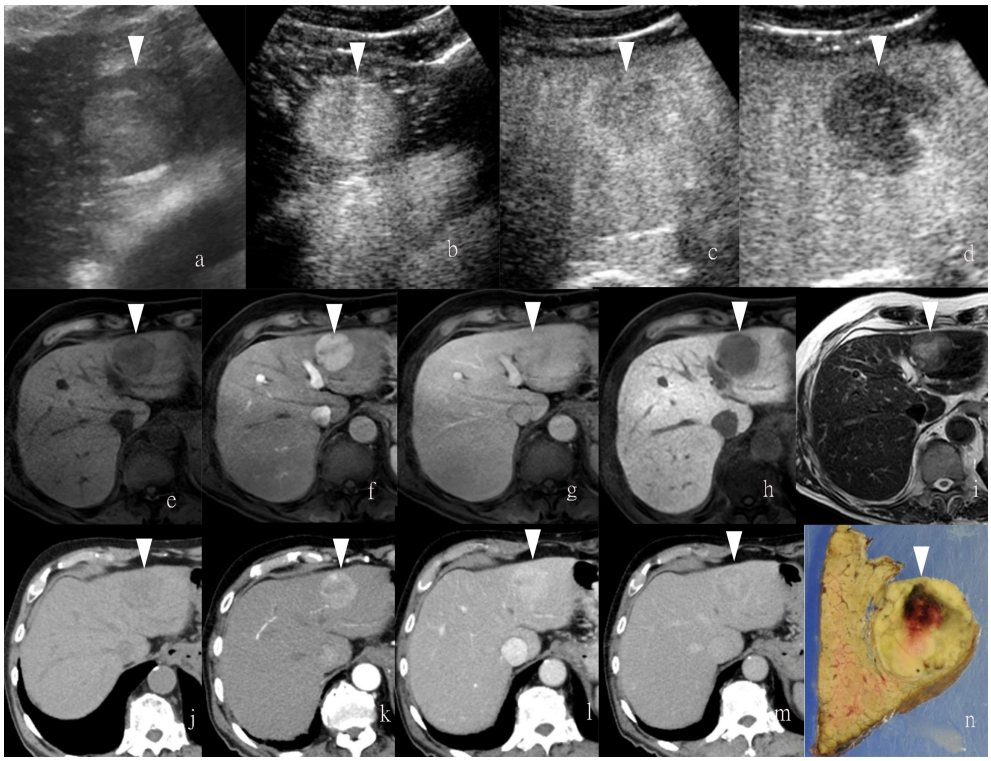

FIGURE 1 | Images of a man in his eighties with a pathological diagnosis of moderately differentiated hepatocellular carcinoma (HCC) and had a history of hepatitis **(C)** At the Sonazoid-enhanced ultrasound (US), the liver lesion at a size of 43 mm with a thin halo located at segment III was observed on B-mode US **(A)**. It was rapidly enhanced in the arterial phase (wash-in) **(B)**, started to fade (wash-out) in portal phase **(C)**, and was totally exhausted in the post-vascular phase **(D)**. At Gd-EOB-DTPA-enhanced MRI, the lesion was hypointense on T1-weighted image **(E)**, with the typical characteristics of wash-in and wash-out from arterial phase, portal phase, to delayed phase **(F–H)**. It showed hyperintensity on T2-weighted image **(I)**. At iodine agent-enhanced CT, it has low-density before enhancement **(J)**. It also showed wash-in and wash-out from arterial phase, portal phase, to delayed phase **(K–M)**. Finally, the gross specimen vividly reflected the morphological information of tumor **(N)**. Arrowheads indicate the margin of the HCC lesion.

and enriched (18). Gadolinium chelates (Gd-chelates) are clinically available mainstream for dynamic MRI on T1-weighted images, including Gd-DTPA (gadopentetic acid, Magnevist, Berlex, Berlin, Germany), Gd-DTPA-BMA (gadodiamide, Omniscan, Nycomed Amersham, Amersham, UK), Gd-HP-DO3A (gadoteridol, ProHance, Bracco Diagnostics, Milan, Italy), Gd-DTPA-BMEA (gadoversetamide, Optimark, Mallinckrodt, Staines-upon-Thames, UK), Gd-DOTA (gadoterate, meglumine, Dotarem Guerbet, Princeton, NJ, USA), and Gd-BT-DO3A (gadobutrol Gadovist, Schering Diagnostics, Berlin, Germany). These extracellular agents for non-specific liver MRI are commonly used worldwide because of the good patient tolerance and satisfying diagnostic efficacy (19). Thus, clinical recommendations from guidelines are almost based on the Gd-chelates (8, 9). Moreover, the informative images provided by contrast-enhanced MRI (CEMRI) also contribute to the therapy assessment (**Table 1**).

Reticuloendothelial System Endocytosis

Ferumoxytol, a kind of iron oxide nanoparticles (IONPs) approved by the Food and Drug Administration (FDA) as medicine for iron deficiency in adults, was recently reported to be feasible for MR angiography thanks to the characteristic of longer half-life in circulation and the advantage of superparamagnetism (20–23). The so-called negative contrast agents, containing iron oxide particles, darken the normal liver background on T2-weighted images to negatively enhance the target issue, in contrast with the so-called positive agents that brighten the target tissue on T1-weighted images, like Gd-chelates. The first commercially available reticuloendothelial system (RES)-specific contrast agent is ferumoxides (Feridex) (24), which makes lesions that contain negligible RES cells conspicuous on T2-weighted images since the normal liver background containing many RES cells can selectively take up iron oxide particulates to lower the T2 signal intensity (25). Iron oxide crystals coated with dextran or carboxydextran are named superparamagnetic iron oxide (SPIO), which is normally employed as T2 MR CM. With a sufficient infusion of SPIO, normal hepatocytes containing many Kupffer cells are supposed to catch most SPIO particles, leading to a dark area on T2-weighted images. By contrast, tumors, whether benign or malignant, primary or metastatic, that are deficient in Kupffer cells cannot exhibit SPIO uptake, shaping a relatively hyperintense area. However, focal nodular hyperplasia (FNH)

TABLE 1 | The categories of extracellular contrast agents in clinical practice.

Category	Specificity	Class	Classical agents	Featured purposes	Modality
Extracellular agent	Non-specific	Gadolinium chelates	Gadopentetic acid (Gd-DTPA)	Tumor imaging; blood pool imaging	T1 agent for MRI
Reticuloendothelial system (RES) agent (Kupffer cells included)	RES specific	Iron oxide	Ferucarbotran (Feridex)	Liver tumor imaging	T2 agent for MRI
		Microbubbles	Perfluorinated butane (Sonazoid)	Liver tumor imaging; blood pool imaging	Ultrasound contrast agent
Hepatobiliary agent	Hepatobiliary specific	Manganese-based compound	Mangafodipir (Mn-DPDP)	MR cholangiography; liver function indicator	T1 agent for MRI
			Gadobenate dimeglumine (Gd-BOPTA); gadoxetic acid (Gd-EOB-DTPA)	Liver tumor imaging	T1 agent for MRI

seems to be an exception, since SPIO particles may accumulate there and lead to a resultant isointense or even hypointense appearance (26, 27). Following SPIO, the derivative in terms of ultrasmall particulate iron oxides (USPIO) with advantages of convenient administration and striking prolonged plasma half-life that enables it also as a blood pool agent was developed thereafter (28, 29) (**Table 1**).

Regarding UCA, Sonazoid is an MB of perfluorobutane core wrapped by the shell of hydrogenated egg phosphatidylserine. At first, Sonazoid MBs were used as the blood pool contrast agent. As early as 1 min after the intravenous administration, the MBs start to diffuse into extravascular and intercellular space where they will be phagocytosed by the Kupffer cells in the normal liver sinusoids. Approximately 10 min later, once intravascular MBs are mostly eliminated, the remaining stable MBs endocytosed by resident macrophages in liver parenchyma will shape the so-called additional Kupffer phase or post-vascular phase, which can last to 2 h after injection (30–32) (**Table 1**). Moreover, in the classical enhancement features of wash-in and wash-out, HCC theoretically appears to be perfusion defects in the Kupffer phase or post-vascular phase because of Kupffer cell shortage (**Figures 1**, **2**). The characteristics of the additional post-vascular phase aid much in HCC detection and diagnosis. Recently, Sonazoid has been proven to be non-inferior to SonoVue in a retrospective clinical study for focal liver lesion (FLL) (33). However, if the lesion is isoechoic in the post-vascular phase, misdiagnosis can happen at a rate of approximately 17% (34). Worse still, owing to histological reasons of some well-differentiated HCC, the sign of perfusion defect in the Kupffer phase could be observed at a rate of only 69% among HCC patients (35). Also, some benign lesions that lack Kupffer cells have a chance to be misdiagnosed as a false-positive sign in the Kupffer phase (36). Therefore, the expected additional clinical benefit on diagnosis gained from the Kupffer phase has not yet been confirmed (37). As for HCC intervention, after US brings real-time monitoring for minimally invasive operations like lesion biopsy and regional ablation, CEUS is employed for more accurate guidance and unique immediate evaluation during therapy (38–43). Vascular-sensitive assessment makes CEUS an indispensable aid for effective

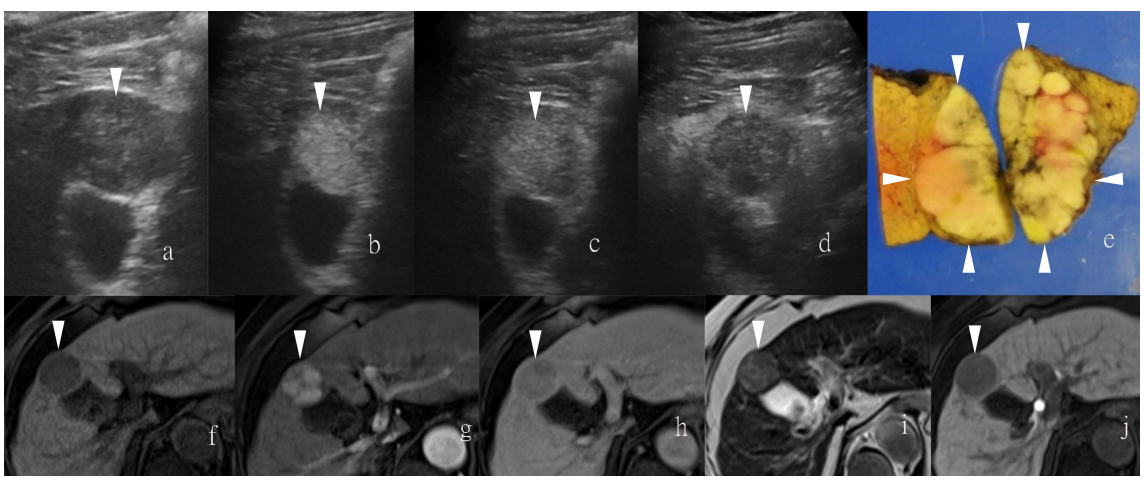

FIGURE 2 | Images of a man in his sixties with a pathological diagnosis of poorly to moderately differentiated hepatocellular carcinoma (HCC) and had a history of cirrhosis. At the Sonazoid-enhanced ultrasound (US), the liver lesion was heterogeneous hyperechoic with the indistinct margin on B-mode US **(A)**. It was rapidly enhanced in the arterial phase (wash-in) **(B)**, still iso-echoic in portal phase **(C)**, and was totally exhausted in the post-vascular phase **(D)**. At Gd-EOB-DTPA-enhanced MRI, the lesion was hypointense on T1-weighted image **(F)**, with uncharacteristic wash-in and delayed wash-out from arterial phase to delayed phase **(G, H)**. It showed hyperintensity on T2-weighted image **(I)**. The contrast media (CM) were totally exhausted till the hepatobiliary phase **(J)**. The gross specimen indicated the heterogeneous pathological differentiation of HCC **(E)**. Arrowheads indicate the margin of the HCC lesion.

radiofrequency (RF)/microwave (MV) ablation (44, 45). On the other hand, three-dimensional (3D) US can provide additional lateral and other viewing angles, and morphological information offers UCA another usable imaging modality (i.e., contrast-enhanced 3D US, CE 3D US) (46, 47) (**Figure 3**). Moreover, contrast enhancement is also employed in fusion imaging to reveal extra small liver lesions and biopsy navigation (48) (**Figure 4**).

Hepatocyte-Specific Uptake

Mangafodipir trisodium (Mn-DPDP) used to be a classical hepatocyte-selective contrast agent that was developed in the last century and has favorable contrast-to-noise measurements and lesion detection rate as compared to non-enhanced MRI (49, 50). It was high-profile at the beginning for the prolonged enhancement relative to the traditional T1 contrast agents (51). The uptake of Mn-DPDP occurs in hepatocytes, and its elimination is in the biliary tree. Thus, the metabolism process of Mn-DPDP can indicate hepatobiliary function (52, 53). Moreover, it is reported that the hepatocyte-selective contrast agent is correlative with the pathological differentiation degree of HCC (54). Since the uptake of Mn-DPDP strictly occurs in hepatocytes, the extrahepatic originated metastases can be negatively illustrated (55). However, in contrast to the question of how many normal hepatocytes are contained in a lesion, the question of whether a liver lesion is malignant or not will be the highest concern for patients.

By integrating the mechanisms of both hepatocyte-selective contrast agents and non-specific extracellular Gd-chelates, gadolinium-based hepatobiliary-specific agents were thereby developed, such as gadobenate dimeglumine (Gd-BOPTA) and gadoxetic acid (Gd-EOB-DTPA), which are worldwide commercially available and have become a promising MRI contrast agent for FLL (56–58). For HCC diagnostic imaging, the so-called hepatobiliary contrast agents achieve further detection in the early stage for primary, recurrent, and metastatic HCCs through usual dynamic imaging and additional hepatobiliary delayed phase (59–62) (**Figures 1**, **2**). Beyond diagnosis, uptake of Gd-EOB-DTPA of HCC lesions is reported to be a biomarker for prognosis (63), as well as the estimation of liver function (64). Concerning patients' tolerance, Gd-EOB-DTPA only requires a minimum injection dose to present a satisfying enhancement in the liver and smaller branch of the biliary tree relative to Gd-BOPTA (55) (**Table 1**).

MOLECULAR IMAGING AGENTS

For the diagnostic and therapeutic purpose of molecular imaging, by means of conjugating some antibody, peptide, or ligand, molecular imaging agents are artificially designed to anchor the targeted cellular and molecular hallmarks pathologically (65).

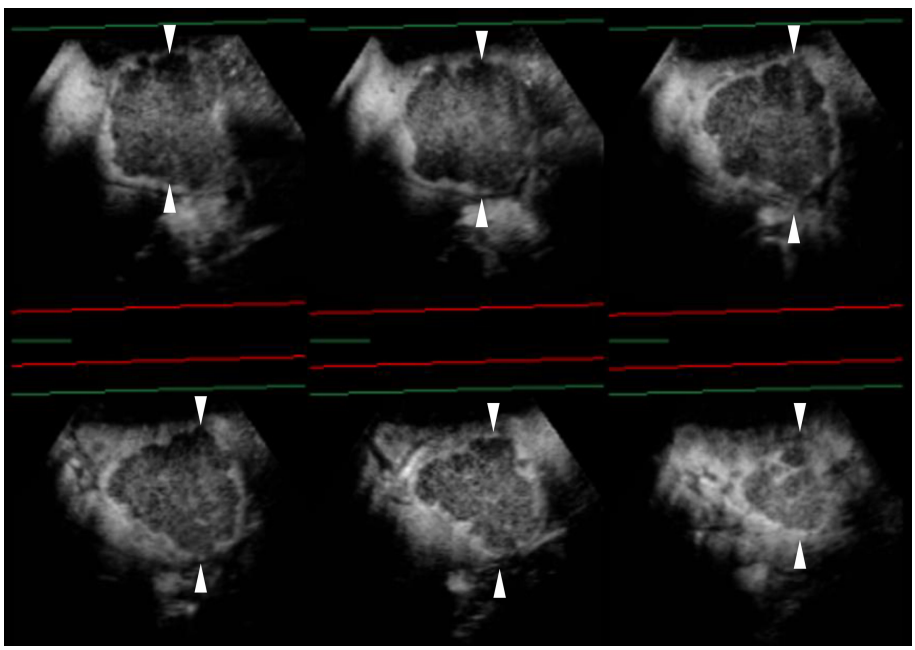

FIGURE 3 | Sonazoid-enhanced ultrasound (US) images of a man in his seventies with a pathological diagnosis of moderately differentiated hepatocellular carcinoma (HCC), who had a history of hepatitis C. The tumor was 70mm. Consecutive lateral images of the tumor remarkably illumed the irregular margin on the three-dimensional (3D) US, which was obtained by auto-sweep 3D scanning in the post-vascular phase. Tomographic ultrasound images in plane A, which can be translated from front to rear, with a slice distance of 4.8 mm. Arrowheads indicate the margin of the HCC lesion.

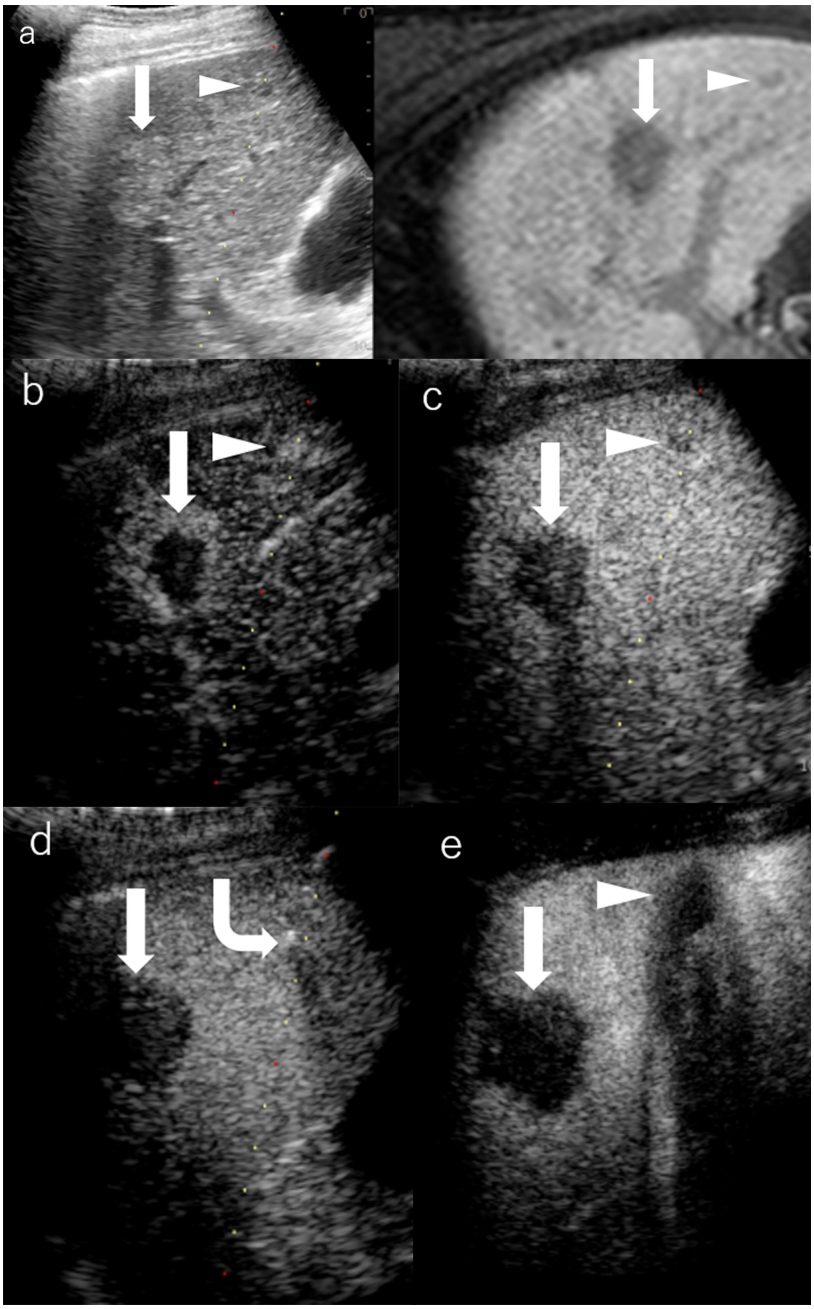

FIGURE 4 | Images of a man in his seventies with a pathological diagnosis of moderately differentiated hepatocellular carcinoma (HCC) and had a history of cirrhosis and HCC. The hepatobiliary phase of EOBMRI (right side), as the reference, was combined with conventional grayscale US (left side), displayed an 8-mm indistinctive hypointense area (the triangular arrow) in segment V on the same screen for the fusion imaging **(A)**. The extrasmall lesion was hypervascular in the arterial phase of Sonazoid-enhanced ultrasound (US) **(B)**, while the post-vascular phase indicated it to be a slightly hypoechoic area **(C)**. Pathway guidance was ready for radiofrequency ablation (RFA) needle manipulation on real-time US **(B–D)**, along with tracking for the metallic needle tip (the curved arrow) **(D)**. The contrast-enhanced US (CEUS) evaluated the target ablation area to be non-enhanced after RFA **(E)**. Arrows indicate the margin of the bigger HCC lesion, which was previously treated by RFA. And Arrowheads indicate the margin of the extrasmall HCC lesion.

Immune Molecular Anchoring

By means of immunoreaction, gadolinium-labeled reagents for liver tumor marking and monitoring of the MR modality are commonly employed in a tumor-bearing animal model for cancer research (66, 67). The molecular weight of reagents mainly ranges from dozens to hundreds of kDa. Likewise, the MBs or nanobubbles binding compounds marked with the tumor-specific immune molecule are also available for cancer research in the CEUS modality (66).

Stimulus-Responsive/Microenvironment-Dependent Contrast Agents

A T1/T2 switchable MR contrast agent was recently validated on a mouse model for HCC early diagnosis (68, 69). Previously, the diagnostic efficacy of IONP-based MRI was not as high as expected when it was simply employed as a liver-specific T2 agent (70). However, researchers recently found that IONP clusters could be accordingly disaggregated thanks to the acidic tumor microenvironment, which can generate a downstream tumor-specific T1 contrast agent. As a result, the IONP agents can additionally be employed to delineate HCC on T1-weighted images after switching to a downstream tumor-specific contrast agent. Based on IONP, agents decorated with functional small-molecular ligands through surface engineering are thereafter designed to be stimulus-responsive agents, pH-sensitive, and nanoscale distance-dependent (68, 71–75). Furthermore, concerning the aggregation phenomenon that commonly happened in nanoparticles with a large surface area/volume ratio, ultrafine nanoparticles could facilitate intratumoral homogeneous distribution of contrast agents (76). IONP at a diameter of 3.6 nm is supposed to be an optimal T1 agent *in vivo* (77). Moreover, core engineering of various designs of size, shape, composition, surface coating, molecular weight, and drug delivery has indicated IONP to be a hopeful T1 contrast agent (78–85). Beyond imaging, Yang et al. developed a novel nanoparticle that releases Fe^{2+} for the treatment of folic acid (FA) receptor-positive solid tumors through the ferroptosis pathway while being supervised through the Mn agent-enhanced imaging (86, 87). Also, Song et al. developed an assay of therapeutic natural killer cells (NK cells) conjugated with Sonazoid MB to make the antitumor process visible in real-time CEUS (88).

Scale-Dependent Particles

As nanomedicine was developed recently, emerging nanomaterials have been studied for contrast enhancement imaging. Some nanoscaled CM can permeate into tumor stroma through weak tumor vessels to depict the tumor with or without the assistance from functional parts equipped in advance (89). Moreover, sonoporation induced by external stimulation of focused US can reversibly increase the permeabilization of the cell membrane, leading to the potential visualization of HCC intracellular therapy in the future (90).

CLINICAL CHALLENGES AND PROSPECTS

As for the clinically commonly used contrast agents, Guang et al. performed a meta-analysis to compare the diagnostic value of CEUS, CT, and MRI in FLL. To rule out HCC from FLL, CECT has the highest sensitivity of 90% (95% CI: 88%–92%), followed by CEUS (88%) and CEMRI (86%). Both CEUS and CEMRI have a higher sensitivity of 81% than CECT (77%). However, all results have no statistical significance (16, 91). Moreover, Westwood et al. found that CEUS could be a cost-effective alternative for HCC diagnosis relative to CECT or CEMRI with similar diagnostic performance (92). Research about combined multimodal medical imaging (including Sonazoid-enhanced US, Gd-EOB-DTPA-enhanced MRI, and CECT) conducted by Masatoshi Kudo figured out that the sensitivity for HCC diagnosis is 72%, 74%, and 86% for CEUS, CECT, and Gd-EOB-DTPA-enhanced MRI, respectively, with no significance among the three imaging modalities. When combining US with MRI, the sensitivity soared as high as 90% (93).

Meanwhile, controversies still remain regarding the diagnostic efficacy of HCC. Despite that the hepatobiliary agent-enhanced MRI is believed to reach an early diagnosis for HCC that is still in the hypovascular stage (94), researchers analyzed the clinical trials that use different contrast agents for HCC diagnosis and found no significant difference in the diagnostic efficacy in terms of sensitivity and specificity between the MRI using extracellular agents and hepatobiliary agents (95, 96). Imbriaco et al. claimed that Gd-EOB-DTPA-enhanced MRI has a better diagnostic performance than CECT only for lesions that are smaller than 20 mm and patients with Child-Pugh class A (97). Moreover, for patients with cirrhosis, Kim et al. demonstrated better performance of hepatobiliary agent-enhanced MRI relative to routine US screening for surveillance of people at a higher risk of HCC (2). In addition, molecular imaging agents, like IONP-based MR agents, are still on the way to fulfilling the various clinical needs (98). On the other hand, although current CM has been deeply improved through materials science, biosafety is still the most crucial factor for patients having various allergies and metabolism troubles. Necessary reinjection of contrast agents for CT and MRI may come with a potential risk of side effects. Minimized dose of contrast agent that meets all clinical needs will be a future trend for CM research.

To sum up, the CM brings out the best diagnostic performance for suitable patients under appropriate conditions. Although Gd-DTPA-enhanced MRI and non-ionic iodinated agents-enhanced CT are usually recommended for HCC diagnosis by mainstream guidelines, liver-specific CM, like Gd-EOB-DTPA and Sonazoid, have already played an anticipated role in HCC diagnosis and prognosis prediction. Furthermore, the amelioration of molecular imaging agents has drawn a blueprint for future medical imaging.

AUTHOR CONTRIBUTIONS

Concept and design: KN and YZ. Manuscript writing: YZ. Figure presentation: KN. Reviewed the manuscript: all authors. All authors contributed to the article and approved the submitted version.

FUNDING

This work was partially supported by grants from the Natural Science Foundation of Ningbo (No. 2019A610313), Medical

Science and Technology Project of Zhejiang Province (No. 2021KY312), Ningbo Medical Science and Technology Project (No. 2019Y05), Ningbo Clinical Medicine Research Center Project (No. 2019A21003), Japan-China Sasakawa Medical Scholarship, and Young Talents Training Program of Ningbo Municipal Health Commission.

REFERENCES

1. Ferlay J, Colombet M, Soerjomataram I, Parkin DM, Piñeros M, Znaor A, et al. Cancer Statistics for the Year 2020: An Overview. *Int J Cancer* (2021).
2. Kim SY, An J, Lim YS, Han S, Lee JY, Byun JH, et al. MRI With Liver-Specific Contrast for Surveillance of Patients With Cirrhosis at High Risk of Hepatocellular Carcinoma. *JAMA Oncol* (2017) 3(4):456–63. doi: 10.1001/jamaoncol.2016.3147
3. Elsayes KM, Hooker JC, Agrons MM, Kielar AZ, Tang A, Fowler KJ, et al. Version of LI-RADS for CT and MR Imaging: An Update. *Radiographics* (2017) 37(7):1994–2017. doi: 10.1148/rg.2017170098
4. Marrero JA, Ahn J, Rajender Reddy K. ACG Clinical Guideline: The Diagnosis and Management of Focal Liver Lesions. *Am J Gastroenterol* (2014) 109(9):1328–47. doi: 10.1038/ajg.2014.213
5. Kudo M, Matsui O, Izumi N, Iijima H, Kadoya M, Imai Y, et al. JSH Consensus-Based Clinical Practice Guidelines for the Management of Hepatocellular Carcinoma: 2014 Update by the Liver Cancer Study Group of Japan. *Liver Cancer* (2014) 3(3-4):458–68. doi: 10.1159/000343875
6. Park J-W, Hyeok LJ, Lee JS, Tak TY, Bae SH, Yeon JE, et al. 2014 Korean Liver Cancer Study Group-National Cancer Center Korea Practice Guideline for the Management of Hepatocellular Carcinoma. *Korean J Radiol* (2015) 16 (3):465–522. doi: 10.3348/kjr.2015.16.3.465
7. Horowitz JM, Kamel IR, Arif-Tiwari H, Asrani SK, Hindman NM, Kaur H, et al. ACR Appropriateness Criteria(®) Chronic Liver Disease. *J Am Coll Radiol* (2017) 14(11s):S391–s405. doi: 10.1016/j.jacr.2017.08.045
8. American College of Radiology. *Liver Reporting and Data Systems (LI-RADS)* Available at: https://www.acr.org/Clinical-Resources/Reporting-and-Data-Systems/LI-RADS (Accessed June 4, 2019).
9. Marks RM, Masch WR, Chernyak V. LI-RADS: Past, Present, and Future, From the AJR Special Series on Radiology Reporting and Data Systems. *AJR Am J Roentgenol* (2021) 216(2):295–304. doi: 10.2214/AJR.20.24272
10. Dietrich CF, Nolsøe CP, Barr RG, Berzigotti A, Burns PN, Cantisani V, et al. Guidelines and Good Clinical Practice Recommendations for Contrast-Enhanced Ultrasound (CEUS) in the Liver-Update 2020 WFUMB in Cooperation With EFSUMB, AFSUMB, AIUM, and FLAUS. *Ultrasound Med Biol* (2020) 46(10):2579–604. doi: 10.1016/j.ultrasmedbio.2020.04.030
11. Friedrich-Rust M, Klopffleisch T, Nierhoff J, Herrmann E, Vermehren J, Schneider MD, et al. Contrast-Enhanced Ultrasound for the Differentiation of Benign and Malignant Focal Liver Lesions: A Meta-Analysis. *Liver Int* (2013) 33(5):739–55. doi: 10.1111/liv.12115
12. Niu Y, Huang T, Lian F, Li F. Contrast-Enhanced Ultrasonography for the Diagnosis of Small Hepatocellular Carcinoma: A Meta-Analysis and Meta-Regression Analysis. *Tumour Biol* (2013) 34(6):3667–74. doi: 10.1007/s13277-013-0948-z
13. Gramiak R, Shah PM. Echocardiography of the Aortic Root. *Invest Radiol* (1968) 3(5):356–66. doi: 10.1097/00004424-196809000-00011
14. Jia GS, Feng GL, Li JP, Xu HL, Wang H, Cheng YP, et al. Using Receiver Operating Characteristic Curves to Evaluate the Diagnostic Value of the Combination of Multislice Spiral CT and Alpha-Fetoprotein Levels for Small Hepatocellular Carcinoma in Cirrhotic Patients. *Hepatobiliary Pancreat Dis Int* (2017) 16(3):303–9. doi: 10.1016/S1499-3872(17)60018-3
15. Saake M, Lell MM, Eller A, Wuest W, Heinz M, Uder M, et al. Imaging Hepatocellular Carcinoma With Dynamic CT Before and After Transarterial Chemoembolization: Optimal Scan Timing of Arterial Phase. *Acad Radiol* (2015) 22(12):1516–21. doi: 10.1016/j.acra.2015.08.021
16. Kim KA, Kim MJ, Choi JY, Park MS, Lim JS, Chung YE, et al. Detection of Recurrent Hepatocellular Carcinoma on Post-Operative Surveillance: Comparison of MDCT and Gadoxetic Acid-Enhanced MRI. *Abdom Imaging* (2014) 39(2):291–9. doi: 10.1007/s00261-013-0064-y
17. Matoba M, Kitadate M, Kondou T, Yokota H, Tonami H. Depiction of Hypervascular Hepatocellular Carcinoma With 64-MDCT: Comparison of Moderate- and High-Concentration Contrast Material With and Without Saline Flush. *AJR Am J Roentgenol* (2009) 193(3):738–44. doi: 10.2214/AJR.08.2028
18. Gandhi SN, Brown MA, Wong JG, Aguirre DA, Sirlin CB. MR Contrast Agents for Liver Imaging: What, When, How. *Radiographics* (2006) 26 (6):1621–36. doi: 10.1148/rg.266065014
19. Bellin MF, Vasile M, Morel-Precetti S. Currently Used non-Specific Extracellular MR Contrast Media. *Eur Radiol* (2003) 13(12):2688–98. doi: 10.1007/s00330-003-1912-x
20. Bashir MR, Bhatti L, Marin D, Nelson RC. Emerging Applications for Ferumoxytol as a Contrast Agent in MRI. *J Magn Reson Imaging* (2015) 41 (4):884–98. doi: 10.1002/jmri.24691
21. Ersoy H, Jacobs P, Kent CK, Prince MR. Blood Pool MR Angiography of Aortic Stent-Graft Endoleak. *AJR Am J Roentgenol* (2004) 182(5):1181–6. doi: 10.2214/ajr.182.5.1821181
22. Hope MD, Hope TA, Zhu C, Faraji F, Haraldsson H, Ordovas KG, et al. Vascular Imaging With Ferumoxytol as a Contrast Agent. *AJR Am J Roentgenol* (2015) 205(3):W366–73. doi: 10.2214/AJR.15.14534
23. Huang Y, Hsu JC, Koo H, Cormode DP. Repurposing Ferumoxytol: Diagnostic and Therapeutic Applications of an FDA-Approved Nanoparticle. *Theranostics* (2022) 12(2):796–816. doi: 10.7150/thno.67375
24. Ros PR, Freeny PC, Harms SE, Seltzer SE, Davis PL, Chan TW, et al. Hepatic MR Imaging With Ferumoxides: A Multicenter Clinical Trial of the Safety and Efficacy in the Detection of Focal Hepatic Lesions. *Radiol* (1995) 196(2):481–8. doi: 10.1148/radiology.196.2.7617864
25. Tanimoto A, Kuribayashi S. Application of Superparamagnetic Iron Oxide to Imaging of Hepatocellular Carcinoma. *Eur J Radiol* (2006) 58(2):200–16. doi: 10.1016/j.ejrad.2005.11.040
26. Grazioli L, Morana G, Kirchin MA, Caccia P, Romanini L, Bondioni MP, et al. MRI of Focal Nodular Hyperplasia (FNH) With Gadobenate Dimeglumine (Gd-BOPTA) and SPIO (Ferumoxides): An Intra-Individual Comparison. *J Magn Reson Imaging* (2003) 17(5):593–602. doi: 10.1002/jmri.10289
27. Terkivatan T, van den Bos IC, Hussain SM, Wielopolski PA, de Man RA, IJzermans JNM. Focal Nodular Hyperplasia: Lesion Characteristics on State-of-the-Art MRI Including Dynamic Gadolinium-Enhanced and Superparamagnetic Iron-Oxide-Uptake Sequences in a Prospective Study. *J Magn Reson Imaging* (2006) 24(4):864–72. doi: 10.1002/jmri.20705
28. Zhao M, Liu Z, Dong L, Zhou H, Yang S, Wu W, et al. A GPC3-Specific Aptamer-Mediated Magnetic Resonance Probe for Hepatocellular Carcinoma. *Int J Nanomed* (2018) 13:4433–43. doi: 10.2147/IJN.S168268
29. Shan L. Superparamagnetic Iron Oxide Nanoparticles (SPION) Stabilized by Alginate. In: *Molecular Imaging and Contrast Agent Database (MICAD)*. Bethesda (MD: National Center for Biotechnology Information (US (2004).
30. Li P, Hoppmann S, Du P, Li H, Evans PM, Moestue SA, et al. Pharmacokinetics of Perfluorobutane After Intra-Venous Bolus Injection of Sonazoid in Healthy Chinese Volunteers. *Ultrasound Med Biol* (2017) 43 (5):1031–9. doi: 10.1016/j.ultrasmedbio.2017.01.003
31. Yanagisawa K, Moriyasu F, Miyahara T, Yuki M, Iijima H. Phagocytosis of Ultrasound Contrast Agent Microbubbles by Kupffer Cells. *Ultrasound Med Biol* (2007) 33(2):318–25. doi: 10.1016/j.ultrasmedbio.2006.08.008
32. Shunichi S, Hiroko I, Fuminori M, Waki H. Definition of Contrast Enhancement Phases of the Liver Using a Perfluoro-Based Microbubble Agent, Perflubutane Microbubbles. *Ultrasound Med Biol* (2009) 35 (11):1819–27. doi: 10.1016/j.ultrasmedbio.2009.05.013
33. Zhai HY, Liang P, Yu J, Cao F, Kuang M, Liu FY, et al. Comparison of Sonazoid and SonoVue in the Diagnosis of Focal Liver Lesions: A Preliminary Study. *J Ultrasound Med* (2019) 38(9):2417–25. doi: 10.1002/jum.14940
34. Kunishi Y, Numata K, Morimoto M, Okada M, Kaneko T, Maeda S, et al. Efficacy of Fusion Imaging Combining Sonography and Hepatobiliary Phase MRI With Gd-EOB-DTPA to Detect Small Hepatocellular Carcinoma. *AJR Am J Roentgenol* (2012) 198(1):106–14. doi: 10.2214/AJR.10.6039

35. Duisyenbi Z, Numata K, Nihonmatsu H, Fukuda H, Chuma M, Kondo M, et al. Comparison Between Low Mechanical Index and High Mechanical Index Contrast Modes of Contrast-Enhanced Ultrasonography: Evaluation of Perfusion Defects of Hypervascular Hepatocellular Carcinomas During the Post-Vascular Phase. *J Ultrasound Med* (2019) 38(9):2329–38. doi: 10.1002/jum.14926
36. Ishibashi H, Maruyama H, Takahashi M, Shimada T, Kamesaki H, Fujiwara K, et al. Demonstration of Intrahepatic Accumulated Microbubble on Ultrasound Represents the Grade of Hepatic Fibrosis. *Eur Radiol* (2012) 22 (5):1083–90. doi: 10.1007/s00330-011-2346-5
37. Barr RG, Huang P, Luo Y, Xie X, Zheng R, Yan K, et al. Contrast-Enhanced Ultrasound Imaging of the Liver: A Review of the Clinical Evidence for SonoVue and Sonazoid. *Abdom Radiol (NY)* (2020) 45(11):3779–88. doi: 10.1007/s00261-020-02573-9
38. Spârchez Z, Radu P, Kacso G, Spârchez M, Zaharia T, Al Hajjar N. Prospective Comparison Between Real Time Contrast Enhanced and Conventional Ultrasound Guidance in Percutaneous Biopsies of Liver Tumors. *Med Ultrason* (2015) 17(4):456–63. doi: 10.11152/mu.2013.2066.174.deu
39. Park HS, Kim YJ, Yu MH, Jung SI, Jeon HJ. Real-Time Contrast-Enhanced Sonographically Guided Biopsy or Radiofrequency Ablation of Focal Liver Lesions Using Perflurobutane Microbubbles (Sonazoid): Value of Kupffer-Phase Imaging. *J Ultrasound Med* (2015) 34(3):411–21. doi: 10.7863/ultra.34.3.411
40. Liu F, Yu X, Liang P, Cheng Z, Han Z, Dong B. Contrast-Enhanced Ultrasound-Guided Microwave Ablation for Hepatocellular Carcinoma Inconspicuous on Conventional Ultrasound. *Int J Hyperthermia* (2011) 27 (6):555–62. doi: 10.3109/02656736.2011.564262
41. Yan SY, Zhang Y, Sun C, Cao HX, Li GM, Wang YQ, et al. Comparison of Real-Time Contrast-Enhanced Ultrasonography and Standard Ultrasonography in Liver Cancer Microwave Ablation. *Exp Ther Med* (2016) 12(3):1345–8. doi: 10.3892/etm.2016.3448
42. Miyamoto N, Hiramatsu K, Tsuchiya K, Sato Y, Terae S, Shirato H. Sonazoid-Enhanced Sonography for Guiding Radiofrequency Ablation for Hepatocellular Carcinoma: Better Tumor Visualization by Kupffer-Phase Imaging and Vascular-Phase Imaging After Reinjection. *Jpn J Radiol* (2009) 27(4):185–93. doi: 10.1007/s11604-009-0317-4
43. Numata K, Morimoto M, Ogura T, Sugimori K, Takebayashi S, Okada M, et al. Ablation Therapy Guided by Contrast-Enhanced Sonography With Sonazoid for Hepatocellular Carcinoma Lesions Not Detected by Conventional Sonography. *J Ultrasound Med* (2008) 27(3):395–406. doi: 10.7863/jum.2008.27.3.395
44. Wiggermann P, Zuber-Jerger I, Zausig Y, Loss M, Scherer MN, Schreyer AG, et al. Contrast-Enhanced Ultrasound Improves Real-Time Imaging of Ablation Region During Radiofrequency Ablation: Preliminary Results. *Clin Hemorheol Microcirc* (2011) 49(1-4):43–54. doi: 10.3233/CH-2011-1456
45. Mauri G, Porazzi E, Cova L, Restelli U, Tondolo T, Bonfanti M, et al. Intraprocedural Contrast-Enhanced Ultrasound (CEUS) in Liver Percutaneous Radiofrequency Ablation: Clinical Impact and Health Technology Assessment. *Insights Imaging* (2014) 5(2):209–16. doi: 10.1007/s13244-014-0315-7
46. Luo W, Numata K, Morimoto M, Oshima T, Ueda M, Okada M, et al. Role of Sonazoid-Enhanced Three-Dimensional Ultrasonography in the Evaluation of Percutaneous Radiofrequency Ablation of Hepatocellular Carcinoma. *Eur J Radiol* (2010) 75(1):91–7. doi: 10.1016/j.ejrad.2009.03.021
47. Numata K, Luo W, Morimoto M, Kondo M, Kunishi Y, Sasaki T, et al. Contrast Enhanced Ultrasound of Hepatocellular Carcinoma. *World J Radiol* (2010) 2(2):68–82. doi: 10.4329/wjr.v2.i2.68
48. Kang TW, Lee MW, Song KD, Kim M, Kim SS, Kim SH, et al. Added Value of Contrast-Enhanced Ultrasound on Biopsies of Focal Hepatic Lesions Invisible on Fusion Imaging Guidance. *Korean J Radiol* (2017) 18(1):152–61. doi: 10.3348/kjr.2017.18.1.152
49. Bernardino ME, Young SW, Lee JK, Weinreb JC. Hepatic MR Imaging With Mn-DPDP: Safety, Image Quality, and Sensitivity. *Radiol* (1992) 183(1):53–8. doi: 10.1148/radiology.183.1.1549694
50. Young SW, Bradley B, Muller HH, Rubin DL. Detection of Hepatic Malignancies Using Mn-DPDP (Manganese Dipyridoxal Diphosphate) Hepatobiliary MRI Contrast Agent. *Magn Reson Imaging* (1990) 8(3):267–76. doi: 10.1016/0730-725X(90)90099-N
51. Rofsky NM, Earls JP. Mangafodipir Trisodium Injection (Mn-DPDP). A Contrast Agent for Abdominal MR Imaging. *Magn Reson Imaging Clin N Am* (1996) 4(1):73–85. doi: 10.1016/S1064-9689(21)00555-9
52. Mitchell DG, Alam F. Mangafodipir Trisodium: Effects on T2- and T1-Weighted MR Cholangiography. *J Magn Reson Imaging* (1999) 9(2):366–8. doi: 10.1002/(SICI)1522-2586(199902)9:2<366::AID-JMRI33>3.0.CO;2-E
53. Seale MK, Catalano OA, Saini S, Hahn PF, Sahani DV. Hepatobiliary-Specific MR Contrast Agents: Role in Imaging the Liver and Biliary Tree. *Radiographics* (2009) 29(6):1725–48. doi: 10.1148/rg.296095515
54. Murakami T, Baron RL, Peterson MS, Oliver JH3rd, Davis PL, Confer SR, et al. Hepatocellular Carcinoma: MR Imaging With Mangafodipir Trisodium (Mn-DPDP). *Radiol* (1996) 200(1):69–77. doi: 10.1148/radiology.200.1.8657947
55. Reimer P, Schneider G, Schima W. Hepatobiliary Contrast Agents for Contrast-Enhanced MRI of the Liver: Properties, Clinical Development and Applications. *Eur Radiol* (2004) 14(4):559–78. doi: 10.1007/s00330-004-2236-1
56. Vogl TJ, Kümmel S, Hammerstingl R, Schellenbeck M, Schumacher G, Balzer T, et al. Liver Tumors: Comparison of MR Imaging With Gd-EOB-DTPA and Gd-DTPA. *Radiol* (1996) 200(1):59–67. doi: 10.1148/radiology.200.1.8657946
57. Huppertz A, Balzer T, Blakeborough A, Breuer J, Giovagnoni A, Heinz-Peer G, et al. Improved Detection of Focal Liver Lesions at MR Imaging: Multicenter Comparison of Gadoxetic Acid-Enhanced MR Images With Intraoperative Findings. *Radiol* (2004) 230(1):266–75. doi: 10.1148/radiol.2301020269
58. Neri E, Bali MA, Ba-Ssalamah A, Boraschi P, Brancatelli G, Alves FC, et al. ESGAR Consensus Statement on Liver MR Imaging and Clinical Use of Liver-Specific Contrast Agents. *Eur Radiol* (2016) 26(4):921–31. doi: 10.1007/s00330-015-3900-3
59. Li XQ, Wang X, Zhao DW, Sun J, Liu JJ, Lin DD, et al. Application of Gd-EOB-DTPA-Enhanced Magnetic Resonance Imaging (MRI) in Hepatocellular Carcinoma. *World J Surg Oncol* (2020) 18(1):219. doi: 10.1186/s12957-020-01996-4
60. Yoo SH, Choi JY, Jang JW, Bae SH, Yoon SK, Kim DG, et al. Gd-EOB-DTPA-Enhanced MRI is Better Than MDCT in Decision Making of Curative Treatment for Hepatocellular Carcinoma. *Ann Surg Oncol* (2013) 20 (9):2893–900. doi: 10.1245/s10434-013-3001-y
61. Rimola J, Forner A, Sapena V, Llarch N, Darnell A, Díaz A, et al. Performance of Gadoxetic Acid MRI and Diffusion-Weighted Imaging for the Diagnosis of Early Recurrence of Hepatocellular Carcinoma. *Eur Radiol* (2020) 30(1):186–94. doi: 10.1007/s00330-019-06351-0
62. Kuwatsuru R, Kadoya M, Ohtomo K, Tanimoto A, Hirohashi S, Murakami T, et al. Comparison of Gadobenate Dimeglumine With Gadopentetate Dimeglumine for Magnetic Resonance Imaging of Liver Tumors. *Invest Radiol* (2001) 36(11):632–41. doi: 10.1097/00004424-200111000-00002
63. Yamashita T, Kitao A, Matsui O, Hayashi T, Nio K, Kondo M, et al. Gd-EOB-DTPA-Enhanced Magnetic Resonance Imaging and Alpha-Fetoprotein Predict Prognosis of Early-Stage Hepatocellular Carcinoma. *Hepatol* (2014) 60(5):1674–85. doi: 10.1002/hep.27093
64. Katsube T, Okada M, Kumano S, Hori M, Imaoka I, Ishii K, et al. Estimation of Liver Function Using T1 Mapping on Gd-EOB-DTPA-Enhanced Magnetic Resonance Imaging. *Invest Radiol* (2011) 46(4):277–83. doi: 10.1097/RLI.0b013e318200f67d
65. Burtea C, Laurent S, Vander Elst L, Muller RN. Contrast Agents: Magnetic Resonance. *Handb Exp Pharmacol* (2008) (185 Pt 1):135–65. doi: 10.1007/978-3-540-72718-7_7
66. Serkova NJ, Glunde K, Haney CR, Farhoud M, De Lille A, Redente EF, et al. Preclinical Applications of Multi-Platform Imaging in Animal Models of Cancer. *Cancer Res* (2021) 81(5):1189–200. doi: 10.1158/0008-5472.CAN-20-0373
67. Anani T, Rahmati S, Sultana N, David AE. MRI-Traceable Theranostic Nanoparticles for Targeted Cancer Treatment. *Theranostics* (2021) 11 (2):579–601. doi: 10.7150/thno.48811
68. Lu J, Sun J, Li F, Wang J, Liu J, Kim D, et al. Highly Sensitive Diagnosis of Small Hepatocellular Carcinoma Using pH-Responsive Iron Oxide Nanocluster Assemblies. *J Am Chem Soc* (2018) 140(32):10071–4. doi: 10.1021/jacs.8b04169
69. Lin J, Xin P, An L, Xu Y, Tao C, Tian Q, et al. Fe(3)O(4)-ZIF-8 Assemblies as pH and Glutathione Responsive T(2)-T(1) Switching Magnetic Resonance Imaging Contrast Agent for Sensitive Tumor Imaging *In Vivo*. *Chem Commun (Camb)* (2019) 55(4):478–81. doi: 10.1039/C8CC08943D

70. Yu MH, Kim JH, Yoon JH, Kim HC, Chung JW, Han JK, et al. Small (≤1-Cm) Hepatocellular Carcinoma: Diagnostic Performance and Imaging Features at Gadoxetic Acid-Enhanced MR Imaging. *Radiol* (2014) 271(3):748–60. doi: 10.1148/radiol.14131996
71. Choi JS, Kim S, Yoo D, Shin TH, Kim H, Gomes MD, et al. Distance-Dependent Magnetic Resonance Tuning as a Versatile MRI Sensing Platform for Biological Targets. *Nat Mater* (2017) 16(5):537–42. doi: 10.1038/nmat4846
72. Ling D, Park W, Park SJ, Lu Y, Kim KS, Hackett MJ, et al. Multifunctional Tumor pH-Sensitive Self-Assembled Nanoparticles for Bimodal Imaging and Treatment of Resistant Heterogeneous Tumors. *J Am Chem Soc* (2014) 136 (15):5647–55. doi: 10.1021/ja4108287
73. Kievit FM, Zhang M. Surface Engineering of Iron Oxide Nanoparticles for Targeted Cancer Therapy. *Acc Chem Res* (2011) 44(10):853–62. doi: 10.1021/ar2000277
74. Li F, Liang Z, Liu J, Sun J, Hu X, Zhao M, et al. Dynamically Reversible Iron Oxide Nanoparticle Assemblies for Targeted Amplification of T1-Weighted Magnetic Resonance Imaging of Tumors. *Nano Lett* (2019) 19(7):4213–20. doi: 10.1021/acs.nanolett.8b04411
75. Xiao S, Yu X, Zhang L, Zhang Y, Fan W, Sun T, et al. Synthesis Of PEG-Coated, Ultrasmall, Manganese-Doped Iron Oxide Nanoparticles With High Relaxivity For T(1)/T(2) Dual-Contrast Magnetic Resonance Imaging. *Int J Nanomed* (2019) 14:8499–507. doi: 10.2147/IJN.S219749
76. Wang L, Huang J, Chen H, Wu H, Xu Y, Li Y, et al. Exerting Enhanced Permeability and Retention Effect Driven Delivery by Ultrafine Iron Oxide Nanoparticles With T(1)-T(2) Switchable Magnetic Resonance Imaging Contrast. *ACS Nano* (2017) 11(5):4582–92. doi: 10.1021/acsnano.7b00038
77. Shen Z, Chen T, Ma X, Ren W, Zhou Z, Zhu G, et al. Multifunctional Theranostic Nanoparticles Based on Exceedingly Small Magnetic Iron Oxide Nanoparticles for T(1)-Weighted Magnetic Resonance Imaging and Chemotherapy. *ACS Nano* (2017) 11(11):10992–1004. doi: 10.1021/acsnano.7b04924
78. Khandhar AP, Wilson GJ, Kaul MG, Salamon J, Jung C, Krishnan KM. Evaluating Size-Dependent Relaxivity of PEGylated-USPIOs to Develop Gadolinium-Free T1 Contrast Agents for Vascular Imaging. *J BioMed Mater Res A* (2018) 106(9):2440–7. doi: 10.1002/jbm.a.36438
79. Tao C, Chen Y, Wang D, Cai Y, Zheng Q, An L, et al. Macromolecules With Different Charges, Lengths, and Coordination Groups for the Coprecipitation Synthesis of Magnetic Iron Oxide Nanoparticles as T(1) MRI Contrast Agents. *Nanomater (Basel)* (2019) 9(5). doi: 10.3390/nano9050699
80. Sherwood J, Rich M, Lovas K, Warram J, Bolding MS, Bao Y. T(1)-Enhanced MRI-Visible Nanoclusters for Imaging-Guided Drug Delivery. *Nanoscale* (2017) 9(32):11785–92. doi: 10.1039/C7NR04181K
81. Vangijzegem T, Stanicki D, Boutry S, Paternoster Q, Vander Elst L, Muller RN, et al. VSION as High Field MRI T(1) Contrast Agent: Evidence of Their Potential as Positive Contrast Agent for Magnetic Resonance Angiography. *Nanotechnology* (2018) 29(26):265103. doi: 10.1088/1361-6528/aabbd0
82. Yang L, Wang Z, Ma L, Li A, Xin J, Wei R, et al. The Roles of Morphology on the Relaxation Rates of Magnetic Nanoparticles. *ACS Nano* (2018) 12 (5):4605–14. doi: 10.1021/acsnano.8b01048
83. Tran HV, Ngo NM, Medhi R, Srinoi P, Liu T, Rittikulsittichai S, et al. Multifunctional Iron Oxide Magnetic Nanoparticles for Biomedical Applications: A Review. *Mater (Basel)* (2022) 15(2). doi: 10.3390/ma15020503
84. Reynders H, Van Zundert I, Silva R, Carlier B, Deschaume O, Bartic C, et al. Label-Free Iron Oxide Nanoparticles as Multimodal Contrast Agents in Cells Using Multi-Photon and Magnetic Resonance Imaging. *Int J Nanomed* (2021) 16:8375–89. doi: 10.2147/IJN.S334482
85. Zhang W, Liu L, Chen H, Hu K, Delahunty I, Gao S, et al. Surface Impact on Nanoparticle-Based Magnetic Resonance Imaging Contrast Agents. *Theranostics* (2018) 8(9):2521–48. doi: 10.7150/thno.23789
86. Yang B, Liu Q, Yao X, Zhang D, Dai Z, Cui P, et al. FePt@MnO-Based Nanotheranostic Platform With Acidity-Triggered Dual-Ions Release for Enhanced MR Imaging-Guided Ferroptosis Chemodynamic Therapy. *ACS Appl Mater Interfaces* (2019) 11(42):38395–404. doi: 10.1021/acsami.9b11353
87. Yang B, Dai Z, Zhang G, Hu Z, Yao X, Wang S, et al. Ultrasmall Ternary FePtMn Nanocrystals With Acidity-Triggered Dual-Ions Release and Hypoxia Relief for Multimodal Synergistic Chemodynamic/Photodynamic/Photothermal Cancer Therapy. *Adv Healthc Mater* (2020) 9(21):e1901634. doi: 10.1002/adhm.201901634
88. Song HW, Lee HS, Kim SJ, Kim HY, Choi YH, Kang B, et al. Sonazoid-Conjugated Natural Killer Cells for Tumor Therapy and Real-Time Visualization by Ultrasound Imaging. *Pharmaceutics* (2021) 13(10). doi: 10.3390/pharmaceutics13101689
89. Goertz DE, Todorova M, Mortazavi O, Agache V, Chen B, Karshafian R, et al. Antitumor Effects of Combining Docetaxel (Taxotere) With the Antivascular Action of Ultrasound Stimulated Microbubbles. *PloS One* (2012) 7(12): e52307. doi: 10.1371/journal.pone.0052307
90. Yin H, Sun L, Pu Y, Yu J, Feng W, Dong C, et al. Ultrasound-Controlled CRISPR/Cas9 System Augments Sonodynamic Therapy of Hepatocellular Carcinoma. *ACS Cent Sci* (2021) 7(12):2049–62. doi: 10.1021/acscentsci.1c01143
91. Guang Y, Xie L, Ding H, Cai A, Huang Y. Diagnosis Value of Focal Liver Lesions With SonoVue®-Enhanced Ultrasound Compared With Contrast-Enhanced Computed Tomography and Contrast-Enhanced MRI: A Meta-Analysis. *J Cancer Res Clin Oncol* (2011) 137(11):1595–605. doi: 10.1007/s00432-011-1035-8
92. Westwood M, Joore M, Grutters J, Redekop K, Armstrong N, Lee K, et al. Contrast-Enhanced Ultrasound Using SonoVue® (Sulphur Hexafluoride Microbubbles) Compared With Contrast-Enhanced Computed Tomography and Contrast-Enhanced Magnetic Resonance Imaging for the Characterisation of Focal Liver Lesions and Detection of Liver Metastases: A Systematic Review and Cost-Effectiveness Analysis. *Health Technol Assess* (2013) 17(16):1–243. doi: 10.3310/hta17160
93. Alaboudy A, Inoue T, Hatanaka K, Chung H, Hyodo T, Kumano S, et al. Usefulness of Combination of Imaging Modalities in the Diagnosis of Hepatocellular Carcinoma Using Sonazoid®-Enhanced Ultrasound, Gadolinium Diethylene-Triamine-Pentaacetic Acid-Enhanced Magnetic Resonance Imaging, and Contrast-Enhanced Computed Tomography. *Oncol* (2011) 81 Suppl 1:66–72. doi: 10.1159/000333264
94. Motosugi U, Bannas P, Sano K, Reeder SB. Hepatobiliary MR Contrast Agents in Hypovascular Hepatocellular Carcinoma. *J Magn Reson Imaging* (2015) 41 (2):251–65. doi: 10.1002/jmri.24712
95. Kim DW, Choi SH, Kim SY, Byun JH, Lee SS, Park SH, et al. Diagnostic Performance of MRI for HCC According to Contrast Agent Type: A Systematic Review and Meta-Analysis. *Hepatol Int* (2020) 14(6):1009–22. doi: 10.1007/s12072-020-10100-7
96. Zhao C, Dai H, Shao J, He Q, Su W, Wang P, et al. Accuracy of Various Forms of Contrast-Enhanced MRI for Diagnosing Hepatocellular Carcinoma: A Systematic Review and Meta-Analysis. *Front Oncol* (2021) 11. doi: 10.3389/fonc.2021.680691
97. Imbriaco M, De Luca S, Coppola M, Fusari M, Klain M, Puglia M, et al. Diagnostic Accuracy of Gd-EOB-DTPA for Detection Hepatocellular Carcinoma (HCC): A Comparative Study With Dynamic Contrast Enhanced Magnetic Resonance Imaging (MRI) and Dynamic Contrast Enhanced Computed Tomography (Ct). *Pol J Radiol* (2017) 82:50–7. doi: 10.12659/PJR.899239
98. Frtús A, Smolková B, Uzhytchak M, Lunova M, Jirsa M, Kubinová Š, et al. Analyzing the mechanisms of iron oxide nanoparticles interactions with cells: A road from failure to success in clinical applications. *J Control Release* (2020) 328:59–77. doi: 10.1016/j.jconrel.2020.08.036

Conflict of Interest: The authors declare that the research was conducted in the absence of any commercial or financial relationships that could be construed as a potential conflict of interest.

frontiers | Frontiers in Oncology

ORIGINAL RESEARCH
published: 27 June 2022
doi: 10.3389/fonc.2022.862173

Health Care Utilization and Anti-Cancer Drug Expenditure for Six Solid Cancers in Korea From 2007 to 2019

Juhee Park, Kyeongjun Moon and Dong-Sook Kim *

Health Insurance Review and Assessment Service, Wonju, South Korea

Background: The burden of care continues to rise considerably worldwide and the challenge of diversity in cancer research has become important. We aimed to examine trends of cancer care utilization and anti-cancer medication among patients with six solid cancers (gastric, colorectal, liver, lung, breast, and prostate cancer) in South Korea.

Methods: This study analyzed patients diagnosed with six types of solid cancer from 2007 to 2019 using data from the National Health Insurance claims database. We analyzed the total number of cancer cases, each patient's length of stay (LOS) in a hospital, the number of outpatient physician visits, total medical care costs, total out-of-pocket (OOP) costs, and expenditures on anti-cancer drugs.

Results: Utilization of healthcare services and spending on cancer care including anti-cancer drugs both increased in the 13-year study period. The average LOS was the highest for colorectal cancer patients at 43.5 days, and breast cancer patients had the highest average number of physician visits at 11.8. Breast cancer patients had the highest total medical costs (USD 923 million), anti-cancer drug spending (USD 156 million), and the largest increase (5 times) over the 13-year period. The anti-cancer drugs with the largest market shares were ramucirumab for gastric cancer; oxaliplatin for colorectal cancer; sorafenib for liver cancer; pembrolizumab, nivolumab, for lung cancer; trastuzumab for breast cancer; and bicalutamide for prostate cancer.

Conclusion: This study was a large-scale analysis from a nationally representative database of the total population. The study also shows the pattern of cancer care in an Asian country and can provide implications for future cancer research.

Keywords: cancer, cancer therapeutics, utilization, expenditure, six solid cancer

OPEN ACCESS

Edited by:
Guangwen Cao,
Second Military Medical University, China

Reviewed by:
Yi An,
Yale University, United States
Fu-Hui Xiao,
State Key Laboratory of Genetic Resources and Evolution (CAS), China

***Correspondence:**
Dong-Sook Kim
sttone@hanmail.net

Specialty section:
This article was submitted to Cancer Epidemiology and Prevention, a section of the journal Frontiers in Oncology

Received: *25 January 2022*
Accepted: *25 April 2022*
Published: *27 June 2022*

Citation:
Park J, Moon K and Kim D-S (2022) Health Care Utilization and Anti-Cancer Drug Expenditure for Six Solid Cancers in Korea From 2007 to 2019. Front. Oncol. 12:862173. doi: 10.3389/fonc.2022.862173

INTRODUCTION

Cancer incidence and mortality are rapidly growing worldwide, and the global cancer burden as of 2020 has risen to 19.3 million cases with 9.9 million recorded cancer deaths (1). Despite advances in cancer care, cancer was still the second leading cause of death worldwide in 2018 (2). The highest number of new cancer cases in 2020 were breast cancer, followed by lung, colon and rectum,

prostate, skin, and gastric cancer (2.26, 2.21, 1.93, 1.41, 1.20, and 1.09 million cases, respectively). The most common cause of cancer death in 2020 was lung cancer, followed by colon and rectum, liver, stomach, and breast cancer (1.80, 0.93, 0.83, 0.77, and 0.69 million deaths, respectively). To reduce cancer mortality, the World Health Assembly passed a resolution on cancer prevention and control in the context of an integrated approach (WHA70.12) in 2017 (3). In response to this action, the World Health Organization (WHO) has begun to monitor the cancer burden. However, access to cancer clinical trials of non-white racial groups remains one of the challenges of diversity to address in cancer care and biomedical research (4).

The incidence and mortality rates of cancer have increased over time in South Korea (hereafter, Korea), and cancer is regarded as one of the nation's most significant health problems (5). Cancer is the leading cause of death in Korea, with 248,837 newly diagnosed cancer cases and 79,153 cancer deaths in 2018 (6). Also, Korea spent $2.9 billion (4.9% of healthcare expenditures) on cancer patients, who accounted for 0.6% of the total Korean population in 2018 (7).

Global spending for all medicines used to treat cancer patients increased from USD 91 billion in 2012 to USD 150 billion in 2018, driven by therapeutic drugs (8). The availability of anti-cancer medication has increased greatly, and the average annual cost of new oncology medicines continues to show an upward trend. Between 2014 and 2018, 57 new oncology therapeutics cancer drugs for 89 indications launched received approval. Novel cancer medicines (particularly targeted therapies and immunotherapies) have recently revolutionized treatment for several cancers, including immuno-oncology agents, which upended the existing therapeutic paradigm (9). In particular, programmed cell death protein 1 (PD-1) and programmed cell death-ligand 1 (PD-L1) inhibitors were quickly adopted after showing remarkable success at targeting multiple cancers.

Previous studies have estimated trends associated with expenditures related to cancer care and cancer drugs (10–12); however, there have been few studies examining the magnitude of cancer care utilization and spending related to anti-cancer therapy. In Korea, several studies have analyzed cancer incidence, survival, prevalence, and mortality using the National Cancer Incidence Database (6, 13–23), but few of these studies examined trends related to anti-cancer therapy.

The purpose of this study, therefore, was to examine the utilization of cancer care [measured using a patient's length of stay (LOS) at hospitals and number of visits to an outpatient physician] and expenditures related to cancer care [total medical care costs and out-of-pocket (OOP) expenses] for six different types of cancer using the National Health Insurance (NHI) database.

METHODS

Data Source

This was a retrospective cohort study that examined data from patients with six different types of solid cancer. We used NHI claims data that covered the entire population of Korea (about 51.8 million people). The NHI claims database includes data related to all ambulatory care, inpatient services, procedures, and prescriptions administered at all medical institutions and pharmacies in Korea. It includes information on the demographic characteristics of patients, patients' disease codes, the characteristics of medical institutions, healthcare service utilization, medicine use, and medical expenditures.

Study Population

The study population consisted of cancer patients from 2007 to 2019 whose primary or secondary disease codes corresponded to one of the six types of cancer selected for this study. The diagnostic terms used in this study were from the 10th revision of the International Statistical Classification of Diseases and Related Health Problems (ICD-10). The disease codes were as follows: gastric cancer, C16; colorectal cancer, C18-C20; liver cancer, C22; lung cancer, C34; breast cancer, C50; and prostate cancer, C61.

We used a list of medicines that were eligible for reimbursement by the Health Insurance Review and Assessment Service. Therapeutic subgroups were classified according to the Anatomical Therapeutic Chemical (ATC) classification system of the WHO Collaborating Center (24). Based on the WHO ATC classification, drugs were selected if their ATC-2 classification indicated that they were antineoplastic agents (L01) or endocrine therapy (L02). We classified drugs based on the 5-level ATC system (therapeutic class).

Outcome Meausres and Variables

The outcome measures were the trends related to disease prevalence, the characteristics of medical institutions, the LOS of patients, the number of outpatient physician visits made by patients, medical expenses, OOP expenses, the main active ingredients in anti-cancer medications, and the cost of medications. The total medical cost was considered using the yearly increase of the consumer price index as of 2019.

The analytical dimensions were age, sex, and drug classification based on the ATC system. Prevalence was the number of patients per 1,000 people and was calculated as the number of cancer patients divided by the number of people in the total population of the same age and year taken from Statistics Korea. The ages of patients were divided into the following age groups: <65, ≥65 years old. Healthcare utilization was classified as inpatients and outpatients. The types of medical facilities were tertiary hospitals, secondary hospitals, primary hospitals, and clinics.

In this study, patients were the units of analysis. Portions of patients' personal identification numbers were codified and blocked out to protect their privacy, and the authors were blinded to each patient's full personal identification number. In accordance with the Declaration of Helsinki, institutional review board approval procedures were followed internally.

Statistical Analysis

We calculated the outcome measures for each person according to the year and type of cancer. SAS Enterprise version 7.1 (SAS Institute, Cary, NC, USA) was used for all analyses.

RESULTS

The Prevalence of Six Types of Cancer Among Patients

The total number of patients with one of the six different types of cancer (stomach, colorectal, lung, liver, breast, or prostate cancer) increased from 472,457 in 2007 to 880,110 in 2019. In 2019, the rate of cancer incidence per 1,000 people was the highest for breast cancer, at 4.2 (8.3 for women), followed by stomach cancer at 3.5, colorectal cancer at 3.2, prostate cancer at 2.3 (4.6 for men), lung cancer at 2.2, and liver cancer at 1.8. Stomach cancer was the most common cancer among men.

The prevalence of breast cancer increasd by 2.6 times in the 13-year study periods. Among patients who were younger than 65 years of age, the most common cancer was breast cancer, followed by stomach cancer. Among patients who were 65 years old and above, the most common cancer was prostate cancer, followed by stomach cancer, and colorectal cancer (**Table 1**).

Trends Related to Cancer Care Utilization

Table 2 shows the utilization of healthcare services and medical spending of patients. Breast cancer was the most prevalent cancer type, with 215,393 cases in 2019, and showed the largest average increase across the 13-year study period at 14.5%, followed by stomach cancer, colorectal cancer, prostate cancer, lung cancer, and liver cancer.

Healthcare utilization per patient, total medical spending, and anti-cancer drug expenditures also all increased. The average LOS per patient was the highest for colorectal cancer at 43.5 days, followed by breast cancer at 38.5 days and lung cancer at 37.8 days. The average number of physician visits was the highest for breast cancer patients at 11.8, followed by lung cancer at 11.7. Total medical costs and anti-cancer drug spending were the highest for breast cancer at USD 923 million and USD 156 million, respectively, followed by lung cancer at USD 894 million and USD 140 million. The total medical costs for prostate cancer were the lowest at USD 232 million USD, and anti-cancer drug spending was the lowest for liver cancer at USD 10 million. Total medical expenditures increased the most for prostate and breast cancer, while anti-cancer drug spending increased the most for liver and breast cancer. The cost of surgery was the highest for colorectal cancer at 48 million USD, followed by lung cancer, stomach cancer, and breast cancer at 37 million USD.

Figure 1 shows the medical costs and OOP costs per patient by type of cancer. The average inpatient cost for treatment in 2019 was the highest for colorectal cancer patients at USD 11,790

TABLE 1 | Trends in the cancer prevalence rate by cancer site, sex, and age (no. of patients per 1,000 people).

	2007	2008	2009	2010	2011	2012	2013	2014	2015	2016	2017	2018	2019
Stomach cancer													
Total	2.4	2.6	2.8	3.0	3.0	3.1	3.2	3.2	3.3	3.4	3.4	3.5	3.5
Men	3.2	3.4	3.7	4.0	4.0	4.1	4.2	4.3	4.4	4.5	4.6	4.7	4.7
Women	1.7	1.8	1.9	2.0	2.0	2.1	2.1	2.1	2.2	2.2	2.2	2.3	2.3
<65 years	0.7	0.7	0.8	0.8	0.8	0.8	0.8	0.8	0.8	0.9	0.9	0.9	0.8
≥65 years	9.6	9.9	10.4	10.9	10.6	10.6	10.6	10.5	10.3	10.3	10.1	9.9	9.7
Colorectal cancer													
Total	2.0	2.0	2.2	2.4	2.5	2.7	2.8	2.9	3.0	3.1	3.1	3.2	3.2
Men	2.3	2.3	2.6	2.8	3.0	3.2	3.4	3.5	3.5	3.7	3.7	3.8	3.8
Women	1.8	1.7	1.8	2.0	2.1	2.2	2.3	2.3	2.4	2.5	2.5	2.5	2.6
<65 years	0.6	0.5	0.6	0.6	0.6	0.7	0.7	0.7	0.7	0.7	0.7	0.7	0.7
≥65 years	8.3	8.1	8.8	9.4	9.6	10.0	10.1	10.1	10.1	10.0	9.9	9.6	9.4
Liver cancer													
Total	1.5	1.3	1.3	1.4	1.4	1.5	1.5	1.6	1.6	1.7	1.7	1.8	1.8
Men	2.1	1.9	1.9	2.0	2.1	2.1	2.2	2.3	2.4	2.5	2.5	2.6	2.6
Women	0.9	0.8	0.8	0.8	0.8	0.8	0.8	0.9	0.9	0.9	0.9	1.0	1.0
<65 years	0.5	0.4	0.4	0.5	0.5	0.5	0.5	0.5	0.5	0.5	0.5	0.5	0.5
≥65 years	4.2	3.9	3.9	4.1	4.2	4.3	4.4	4.4	4.5	4.6	4.6	4.6	4.6
Lung cancer													
Total	1.2	1.1	1.2	1.3	1.3	1.4	1.5	1.6	1.7	1.8	1.9	2.0	2.2
Men	1.6	1.6	1.6	1.7	1.8	1.9	2.0	2.1	2.2	2.3	2.4	2.6	2.7
Women	0.8	0.7	0.8	0.8	0.9	1.0	1.0	1.1	1.2	1.3	1.4	1.5	1.6
<65 years	0.3	0.2	0.2	0.3	0.3	0.3	0.3	0.3	0.3	0.3	0.3	0.4	0.4
≥65 years	6.0	5.7	5.7	5.9	6.0	6.1	6.3	6.4	6.5	6.7	6.9	7.2	7.4
Breast cancer													
Total (based on total population)	1.6	1.7	1.9	2.1	2.2	2.4	2.6	2.8	3.0	3.3	3.6	3.9	4.2
Women	3.2	3.5	3.9	4.2	4.5	4.8	5.2	5.6	6.0	6.6	7.1	7.7	8.3
<65 years	3.1	3.4	3.7	4.1	4.4	4.7	5.0	5.4	5.8	6.3	6.8	7.4	7.9
≥65 years	3.9	4.3	4.8	5.2	5.5	6.0	6.5	7.0	7.5	8.1	8.9	9.6	10.5
Prostate cancer													
Total based on total population	0.9	0.7	0.8	0.9	1.0	1.2	1.3	1.4	1.6	1.7	1.9	2.1	2.3
Men	1.8	1.4	1.7	1.8	2.0	2.3	2.6	2.8	3.1	3.5	3.8	4.2	4.6
<65 years	0.7	0.4	0.5	0.5	0.5	0.6	0.6	0.7	0.7	0.8	0.8	0.9	1.0
≥65 years	15.0	12.9	14.9	15.9	17.6	19.3	20.8	21.6	23.2	24.9	26.2	27.7	28.9

TABLE 2 | Trends in healthcare utilization and spending by cancer type and year.

	2007	2008	2009	2010	2011	2012	2013	2014	2015	2016	2017	2018	2019	Average growth rate (%)
Stomach cancer														
No. of patients	119,058	127,934	138,792	149,607	151,185	155,505	160,345	163,954	167,013	172,674	175,013	177,409	179,511	(4.2)
Length of admission per patient	28.7	29.5	29.1	29.8	29.9	30.0	30.4	30.8	32.0	31.9	33.0	33.5	33.8	
Outpatient visit days per patient	7.1	7.1	7.2	7.1	6.9	6.9	6.7	6.5	6.3	6.4	6.4	6.4	6.4	
Total medical cost (million $)	291	322	348	372	384	385	385	396	406	448	485	522	561	(7.7)
Medical cost considering inflation	372	392	413	429	425	417	412	419	426	465	494	524	561	(4.3)
Anti-cancer drug cost (million $)	35	32	32	31	32	30	31	31	30	29	27	36	44	(2.2)
Surgery	5	13	16	18	19	18	18	21	24	26	25	31	37	(59.3)
Radiation	1	2	2	2	3	3	3	3	3	4	4	4	4	(16.7)
Colorectal cancer														
No. of patients	100,383	98,787	110,082	119,745	127,549	135,828	142,231	146,438	150,917	156,336	159,110	161,881	164,683	(5.3)
Length of admission per patient	25.2	30.7	38.7	39.7	33.8	35.6	36.1	39.9	39.8	40.5	42.2	43.4	43.5	
Outpatient visit days per patient	7.0	8.1	10.0	11.0	7.9	8.0	8.5	9.6	9.0	8.2	8.3	8.4	8.5	
Total medical cost (million $)	309	349	402	443	480	485	473	530	593	690	763	818	882	(15.4)
Medical cost considering inflation	394	425	477	510	532	526	506	560	622	717	778	821	882	(10.3)
Anti-cancer drug cost (million $)	56	59	63	65	68	60	49	73	102	127	137	138	142	(12.7)
Surgery	12	13	18	21	23	25	24	28	34	36	37	43	48	(24.7)
Radiation	9	9	11	13	15	16	15	17	20	26	27	28	31	(20.4)
Liver cancer														
No. of patients	73,537	66,022	66,887	69,536	71,140	74,104	77,683	79,854	83,464	86,571	87,185	90,319	91,222	(2.0)
Length of admission per patient	28.1	30.0	29.1	29.3	30.0	29.9	30.2	30.2	29.4	30.0	30.2	30.2	30.0	
Outpatient visit days per patient	7.2	8.3	8.8	9.0	9.2	9.3	9.1	9.1	9.0	9.1	9.2	9.2	9.4	
Total medical cost (million $)	250	285	310	343	372	396	405	422	445	490	522	559	601	(11.7)
Medical cost considering inflation	318	347	367	395	412	429	433	446	467	509	532	561	601	(7.4)
Anti-cancer drug cost (million $)	3	3	3	3	4	5	9	8	8	7	7	10	10	(24.8)
Surgery	2	3	3	4	4	5	5	6	8	8	8	11	12	(33.0)
Radiation	4	6	7	7	8	9	9	10	14	17	19	21	23	(35.3)
Lung cancer														
No. of patients	58,078	56,636	58,703	63,048	66,496	71,090	75,247	79,916	84,372	90,942	97,014	104,668	112,093	(7.8)
Length of admission per patient	34.2	37.2	36.3	37.1	38.0	37.9	38.2	38.4	37.4	37.7	38.6	38.2	37.5	
Outpatient visit days per patient	10.4	11.3	11.7	11.7	11.8	11.7	11.4	11.4	11.2	11.2	11.3	11.6	11.7	
Total medical cost (million $)	276	319	342	383	408	414	428	466	493	569	656	801	894	(18.7)
Medical cost considering inflation	352	389	405	442	452	449	458	492	517	590	668	804	894	(12.8)
Anti-cancer drug cost (million $)	60	70	71	76	73	70	69	68	66	57	66	126	140	(11.2)
Surgery	4	4	7	10	11	12	13	16	20	23	26	34	38	(80.8)
Radiation	13	15	18	21	24	26	28	33	40	50	58	66	74	(38.5)
Breast cancer														
No. of patients	78,707	86,833	96,021	105,560	113,236	122,225	132,070	141,954	153,196	168,498	183,818	199,652	215,393	(14.5)
Length of admission per patient	27.8	29.6	29.6	30.6	32.7	35.1	36.7	37.6	37.5	37.6	38.3	37.8	38.5	
Outpatient visit days per patient	11.9	12.3	12.5	12.7	12.7	12.7	12.4	12.3	12.1	12.3	12.0	11.9	11.8	
Total medical cost (million $)	183	216	259	313	370	399	419	469	510	598	684	804	923	(33.7)
Medical cost considering inflation	233	263	307	361	409	432	448	495	535	621	696	807	923	(24.7)
Anti-cancer drug cost (million $)	42	47	56	81	105	113	109	118	125	88	82	119	156	(23.0)
Surgery	1	1	1	1	1	1	1	1	2	2	13	34	37	(475.4)
Radiation	19	22	27	31	37	43	48	55	69	88	99	115	127	(48.5)

(Continued)

TABLE 2 | Continued

	2007	2008	2009	2010	2011	2012	2013	2014	2015	2016	2017	2018	2019	Average growth rate (%)
Prostate cancer														
No. of patients	43,187	35,475	41,888	45,143	51,105	58,327	66,550	71,754	79,052	88,535	97,161	108,081	118,124	(14.5)
Length of admission per patient	19.1	22.4	22.0	23.2	23.8	25.6	26.9	27.0	28.2	26.1	26.3	25.9	26.3	
Outpatient visit days per patient	6.0	7.9	7.9	8.3	8.4	8.2	7.7	7.5	7.1	7.3	7.4	7.5	7.7	
Total medical cost (million $)	50	60	70	80	97	108	116	125	137	163	194	232	274	(36.9)
Medical cost considering inflation	64	73	83	92	107	117	124	132	144	169	198	233	274	(27.2)
Anti-cancer drug cost (million $)	14	16	18	20	21	21	22	22	23	25	26	29	32	(10.4)
Surgery	0	0	0	0	0	0	0	0	0	0	0	0	1	(34.4)
Radiation	4	4	4	5	10	17	18	20	23	30	35	43	52	(110.8)

(with an average annual increase of 7.9%), followed by lung cancer at USD 10,712, and it was the lowest for prostate cancer at USD 3,933. The average total cost of outpatient physician visits in 2019 was the highest for lung cancer at USD 2,671, followed by breast cancer at USD 2,431. The annual cost of cancer care per capita ranged USD 2,321 for prostate cancer to USD 7,976 for lung cancer. The average annual increase in inpatient costs and outpatient costs were the highest for colorectal cancer at 7.9%, breast cancer at 9.0%, and stomach cancer at 48.6%, followed by liver cancer at 48.3%.

Colorectal cancer had the highest average inpatient OOP cost per patient in 2019 at USD 830, followed by lung cancer at USD 789. Breast cancer had the highest average outpatient OOP cost per patient at USD 173, also followed by lung cancer at USD 153. The increases in both the inpatient and outpatient OOP costs per patient were lower than the annual growth rate of total medical expenditures per patient. The annual growth rate of outpatient OOP costs decreased for lung cancer.

Anti-Cancer Drugs With the Largest Market Shares

Figure 2 shows the anti-cancer drugs with the largest market shares for each of the six types of cancer. For stomach cancer, the drugs with the largest market share in 2019 were ramucirumab and oxaliplatin at 17 million USD and 14.2 million USD, and the market share of ramucirumab showed a sharp increase since its introduction in 2018. For colorectal cancer, cetuximab and oxaliplatin showed the highest market share at 55.1 million USD and 38.8 million USD, respectively in 2019. For lung cancer pembrolizumab at 48.1 million USD, nivolumab at 22.9 million USD, pemetrexed, gefitinib, and erlotinib had the highest market share. For breast cancer, pertuzumab, trastuzumab, and trastuzuma emtasine had the highest market share at 50.6 million USD, 49.5 million USD, and 27.1 million USD, respectively. For prostate cancer, leuprorelin and goserelin had the highest market share.

DISCUSSION

The present study is the first to analyze trends in the utilization of cancer care and expenditures for six different types of solid cancers among the entire national population of Korea over a long period of time (13 years). Our study showed that total medical costs and anti-cancer drug spending related to treatment for the six selected cancer types increased by 2-3 times, from USD 1.4 billion and USD 0.2 billion, respectively, in 2007 to USD 4.2 billion and USD 0.4 billion in 2019. Although the cost per cancer patient has increased, the proportion of anti-cancer drugs relative to the overall medical costs related to cancer care decreased from 2007 to 2019. Our finding indicate that annual cost of cancer care excluding anti-cancer therpy cost per capita ranged USD 2,321 for prostate cancer to USD 7,976 for lung cancer.

The prevalence rates of the selected cancer types showed being somewhat different from the global cancer trend (25), however, these were consistent with a previous study that stomach cancer had the highest prevalence rate for both sexes

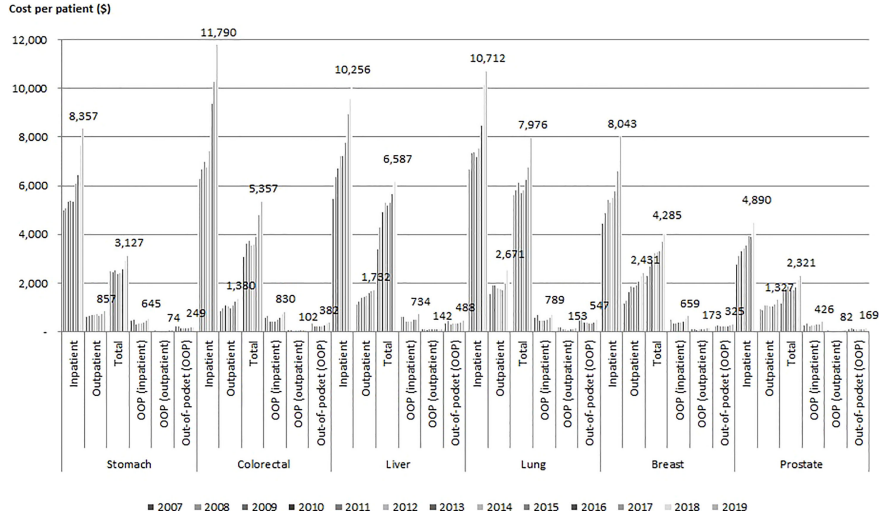

FIGURE 1 | Trends in total healthcare spending by cancer type and year (USD).

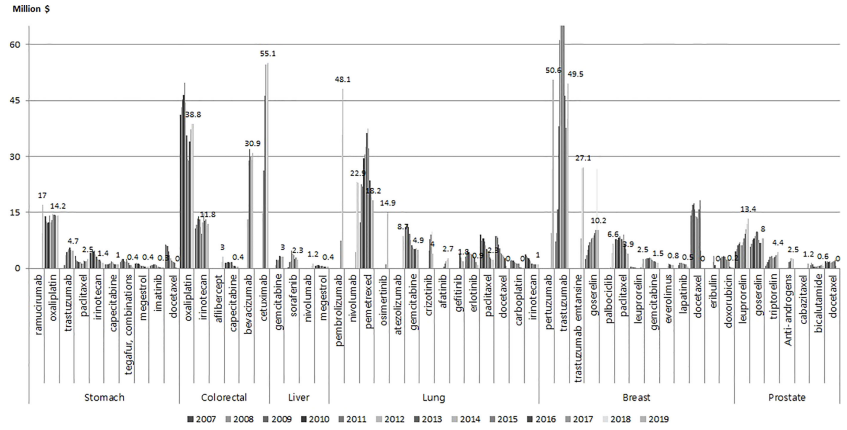

FIGURE 2 | Market share of anti-cancer drugs by cancer type and year (million USD).

in Korea (6). This pattern likely occurred due to the cancer incidence rate in Korea being somewhat different from other countries (25).

Depite limitation in direct comparison, in our study, total medical costs for the six selected cancer types increased more than doubled and this result was consistent with previous study in other countries. Several studies reported cancer-specific health expentirue in Europe. In 31 countries of Europe, the total cost of cancer care was EUR 199 billion, and expenditures almost doubled, from EUR 52 billion to EUR 103 billion, from 1995 to 2018, and the number of newly diagnosed cancer cases increased by about 50% (12). Additionally, in Europe, the proportion of cancer-specific health expenditures increased from 5.9% in 1995 to 6.2% in 2018. In 2018, the average health expenditure related to cancer care per patient was EUR 195, and the average cancer drug spending per patient was EUR 61 (12). Another study in Canada identified the growth factors related to overall cancer drug expenditures (11). In the US, cancer treatment accounts for USD 60.9 billion of direct medical costs and USD 15.5 billion of indirect morbidity costs based on data that ranged from 1998 to 2000 (10). However, a study based on literature review across 5 countries (France, Gernany, Italy, Spain, and United Kingdom) reported direct per patient expenditures was average EUR 4,966 and decreased between 2006-2015.While cancer drug spending per patient increased over the 10-year study period, and was average EUR 1,457 in 2015 (26). Even considering that the helath policy and health care environment differs from country to country, the pattern of increase in cancer care cost is common.

To the best of our knowledge, this is the first population-based study to analyze the magnitude of costs related to cancer care and expenditures related to anti-cancer drugs. To date, few large-scale analyses of the use of anti-cancer medications that cover an entire national population have been published, in either Korea or internationally. Most existing studies used the IQVIA database; thus, the estimated results used in other studies might differ from actual expenditures. This study used data from a nationally representative dataset that covered the total population of Korea, and it therefore included all recorded cancer cases in Korea.

This study examined the utilization of healthcare services by cancer patients and expenditures related to their care using an actual database that accounted for the entire national population of Korea, and the real-world findings of the present study elucidate real-life changes in cancer treatment patterns. These results could thus provide insights to aid in the development of clinical treatment guidelines in other countries. Furthermore, the LOS of patients in hospitals, number of outpatient visits, total medication expenditures (including those for outpatient visits), and drug costs by cancer type were evaluated in the present study. In addition, we analyzed patterns in anti-cancer drugs according to the market shares and we found that the use of high-cost anti-cancer drugs is rapidly increasing. These results can provide the real-world practice of anti-cancer usage, thus the need for clinical guidance to consider cost-effectiveness in order to optimize the treatment of drug therapy.

Despite increasing attention to cancer care, ethnic disparites have been coutinued to be a critical problem even in developed countires such as Europe and Untied States. Also, there is a lack of evidence in cancer care oversight among heterogenous population from Asia and Africa countires (4). This results will be important evidence of epidemiological data on cancer patients and cancer care treatement pattern.

This study also has several limitations. We included all prevalent cases in our analysis, so patients who did not utilize any healthcare services may not have been included. In addition, patients receiving treatment in the context of clinical trials were excluded. A study in the US also reported that 56% of cancer survivors were diagnosed within the past 10 years using data from the Surveillance, Epidemiology, and End Results cancer registries (27). Also, the rapid rise in total medical expenses might be caused by the increase in hospitalization costs and consultation fees, since these hospitalization fees have increased over the past decade and the coverage of health insurance has expanded. Given that cancer care is associated with high initial treatment costs, it may be more appropriate to analyze similar datasets according to the period of cancer morbidity. This study instead focused on analyzing treatment patterns on an annual basis, however, and we did not attempt to analyze the morbidity period. Further studies should therefore analyze per capita healthcare expenditures by distinguishing between initial treatment and end-of-life treatment.

In conclusion, the utilization patterns of cancer care services among cancer patients and spending related to cancer care have both increased. The market share of anti-cancer drugs for lung and breast cancer has also increased significantly due to novel drugs. Further studies are needed to provide better insight for policymakers to make efforts to improve the cost-efficiency of cancer care and the usage of new, high-cost anti-cancer drugs.

DATA AVAILABILITY STATEMENT

Data are not accessed because only those with restrictions can perform analysis at our institution. Requests to access the datasets should be directed to https://opendata.hira.or.kr/op/opc/selectOpenDataInfoView.do.

ETHICS STATEMENT

The studies involving human participants were reviewed and approved by Institutional Review Board in Health Insurance Review and Assessment Service. Written informed consent for participation was not required for this study in accordance with the national legislation and the institutional requirements.

AUTHOR CONTRIBUTIONS

D-SK: Data management, analysis, and writing the draft paper. JP: Design of study, writing, and revising the manuscript. KM: Data management. All authors contributed to the article and approved the submitted version.

REFERENCES

1. Sung H, Ferlay J, Siegel RL, Laversanne M, Soerjomataram I, Jemal A, et al. Global Cancer Statistics 2020: GLOBOCAN Estimates of Incidence and Mortality Worldwide for 36 Cancers in 185 Countries. *CA* (2021) 71 (3):209–49. doi: 10.3322/caac.21660
2. WHO. *Health Topics - Cancer Overview* (2018). Available at: https://www.who.int/health-topics/cancer#tab=tab_1.
3. WHA. Agenda Item 15.6 in WHA 70.12. In: *Cancer Prevention and Control in the Context of an Integrated Approach*. Geneva: World Health Organization (2017).
4. El-Deiry WS, Giaccone G. Challenges in Diversity, Equity, and Inclusion in Research and Clinical Oncology. *Front Oncol* (2021) 11:642112. doi: 10.3389/fonc.2021.642112
5. Korea Statistics. *Cause of Death Statistics*. Statistics Korea, Daejeon (2018).
6. Hong S, Won YJ, Lee JJ, Jung KW, Kong HJ, Im JS, et al. Cancer Statistics in Korea: Incidence, Mortality, Survival, and Prevalence in 2018. *Cancer Res Treat* (2021) 53(2):301–15. doi: 10.4143/crt.2021.291
7. HIRA. *National Health Insurance Statistical Yearbook in 2020*. Wonju: Health Insurance Review & Assessment Service (2021).
8. IQVIA. *Gobal Oncology Trends 2019 - Therapeutics*. Clinical Development and Health System Implications: Quintiles IMS Institute (2019).
9. Alsaab HO, Sau S, Alzhrani R, Tatiparti K, Bhise K, Kashaw SK, et al. PD-1 and PD-L1 Checkpoint Signaling Inhibition for Cancer Immunotherapy: Mechanism, Combinations, and Clinical Outcome. *Front Pharmacol* (2017) 8:561. doi: 10.3389/fphar.2017.00561
10. Chang S, Long SR, Kutikova L, Bowman L, Finley D, Crown WH, et al. Estimating the Cost of Cancer: Results on the Basis of Claims Data Analyses for Cancer Patients Diagnosed With Seven Types of Cancer During 1999 to 2000. *J Clin Oncol* (2004) 22(17):3524–30. doi: 10.1200/JCO.2004.10.170
11. Pataky R, Tran DA, Coronado A, Alvi R, Boehm D, Regier DA, et al. Cancer Drug Expenditure in British Columbia and Saskatchewan: A Trend Analysis. *CMAJ Open* (2018) 6(3):E292–E9. doi: 10.9778/cmajo.20170161
12. Hofmarcher T, Lindgren P, Wilking N, Jonsson B. The Cost of Cancer in Europe 2018. *Eur J cancer* (2020) 129:41–9. doi: 10.1016/j.ejca.2020.01.011
13. Hong S, Won YJ, Park YR, Jung KW, Kong HJ, Lee ES, et al. Cancer Statistics in Korea: Incidence, Mortality, Survival, and Prevalence in 2017. *Cancer Res Treat* (2020) 52(2):335–50. doi: 10.4143/crt.2020.206
14. Jung KW, Park S, Kong HJ, Won YJ, Boo YK, Shin HR, et al. Cancer Statistics in Korea: Incidence, Mortality and Survival in 2006-2007. *J Korean Med sci* (2010) 25(8):1113–21. doi: 10.3346/jkms.2010.25.8.1113
15. Jung KW, Park S, Kong HJ, Won YJ, Lee JY, Park EC, et al. Cancer Statistics in Korea: Incidence, Mortality, Survival, and Prevalence in 2008. *Cancer Res Treat* (2011) 43(1):1–11. doi: 10.4143/crt.2011.43.1.1
16. Jung KW, Park S, Kong HJ, Won YJ, Lee JY, Seo HG, et al. Cancer Statistics in Korea: Incidence, Mortality, Survival, and Prevalence in 2009. *Cancer Res Treat* (2012) 44(1):11–24. doi: 10.4143/crt.2012.44.1.11
17. Jung KW, Won YJ, Kong HJ, Lee ES. Cancer Statistics in Korea: Incidence, Mortality, Survival, and Prevalence in 2016. *Cancer Res Treat* (2019) 51 (2):417–30. doi: 10.4143/crt.2019.138
18. Jung KW, Won YJ, Kong HJ, Lee ES. Community of Population-Based Regional Cancer R. Cancer Statistics in Korea: Incidence, Mortality, Survival, and Prevalence in 2015. *Cancer Res Treat* (2018) 50(2):303–16. doi: 10.4143/crt.2018.143
19. Jung KW, Won YJ, Kong HJ, Oh CM, Cho H, Lee DH, et al. Cancer Statistics in Korea: Incidence, Mortality, Survival, and Prevalence in 2012. *Cancer Res Treat* (2015) 47(2):127–41. doi: 10.4143/crt.2015.060
20. Jung KW, Won YJ, Kong HJ, Oh CM, Lee DH, Lee JS. Cancer Statistics in Korea: Incidence, Mortality, Survival, and Prevalence in 2011. *Cancer Res Treat* (2014) 46(2):109–23. doi: 10.4143/crt.2014.46.2.109
21. Jung KW, Won YJ, Kong HJ, Oh CM, Seo HG, Lee JS. Cancer Statistics in Korea: Incidence, Mortality, Survival and Prevalence in 2010. *Cancer Res Treat* (2013) 45(1):1–14. doi: 10.4143/crt.2013.45.1.1
22. Jung KW, Won YJ, Oh CM, Kong HJ, Lee DH, Lee KH, et al. Cancer Statistics in Korea: Incidence, Mortality, Survival, and Prevalence in 2014. *Cancer Res Treat* (2017) 49(2):292–305. doi: 10.4143/crt.2017.118
23. Oh CM, Won YJ, Jung KW, Kong HJ, Cho H, Lee JK, et al. Cancer Statistics in Korea: Incidence, Mortality, Survival, and Prevalence in 2013. *Cancer Res Treat* (2016) 48(2):436–50. doi: 10.4143/crt.2016.089
24. *WHOCC. Anatomical Therapeutic Chemical (ATC)/Defined Daily Dose (DDD) Index*. (2020). Oslo, Norway. Available at: https://www.whocc.no/atc_ddd_index/.
25. Ferlay J, Colombet M, Soerjomataram I, Parkin DM, Pineros M, Znaor A, et al. Cancer Statistics for the Year 2020: An Overview. *Int J Cancer J Int du Cancer* (2021). doi: 10.1002/ijc.33588
26. Schlueter M, Chan K, Lasry R, Price M. The Cost of Cancer - A Comparative Analysis of the Direct Medical Costs of Cancer and Other Major Chronic Diseases in Europe. *PloS One* (2020) 15(11):e0241354. doi: 10.1371/journal.pone.0241354
27. Miller KD, Nogueira L, Mariotto AB, Rowland JH, Yabroff KR, Alfano CM, et al. Cancer Treatment and Survivorship Statistics, 2019. *CA* (2019) 69 (5):363–85. doi: 10.3322/caac.21565

Conflict of Interest: The authors declare that the research was conducted in the absence of any commercial or financial relationships that could be construed as a potential conflict of interest.

frontiers | Frontiers in Oncology

ORIGINAL RESEARCH
published: 01 July 2022
doi: 10.3389/fonc.2022.889433

The Risk Factors, Incidence and Prognosis of Postpartum Breast Cancer: A Nationwide Study by the SMARTSHIP Group

*Sungmin Park[1], Ji Sung Lee[2], Jae Sun Yoon[3], Nam Hyoung Kim[4], Seho Park[5], Hyun Jo Youn[6], Jong Won Lee[7], Jung Eun Lee[8], Jihyoun Lee[9], Ho Hur[10], Joon Jeong[11], Kweon-Cheon Kim[12] and Soo Youn Bae[13]**

[1] Department of Surgery, Chungbuk National University Hospital, College of Medicine, Chungbuk National University, Cheongju, South Korea, [2] Clinical Research Center, Asan Institute for Life Sciences, Asan Medical Center, University of Ulsan College of Medicine, Seoul, South Korea, [3] Department of Biostatistics, Korea University, Seoul, South Korea, [4] Advertising and Branding, Kaywon University of Art and Design, Uiwang-si, South Korea, [5] Division of Breast Surgery, Department of Surgery, Yonsei University College of Medicine, Seoul, South Korea, [6] Department of Surgery, Jeonbuk National University Medical School, Jeonju, South Korea, [7] Department of Surgery, University of Ulsan College of Medicine, Asan Medical Center, Seoul, South Korea, [8] Department of Food and Nutrition, College of Human Ecology, Seoul National University, Seoul, South Korea, [9] Department of Surgery, Soonchunhyang University Seoul Hospital, Seoul, South Korea, [10] Department of Surgery, National Health Insurance Service Ilsan Hospital, Koyang-si, South Korea, [11] Department of Surgery, Gangnam Severance Hospital, Yonsei University College of Medicine, Seoul, South Korea, [12] Department of Surgery, Chosun University Medical School, Gwangju, South Korea, [13] Department of Surgery, Seoul St. Mary's Hospital, The Catholic University of Korea, Seoul, South Korea

OPEN ACCESS

Edited by:
Kun Zhang,
Tongji University, China

Reviewed by:
Marcus Vetter,
University Hospital of Basel, Switzerland
Dexiang Gao,
University of Colorado Denver, United States

***Correspondence:**
Soo Youn Bae
baessu@gmail.com

Specialty section:
This article was submitted to Cancer Epidemiology and Prevention, a section of the journal Frontiers in Oncology

Received: *04 March 2022*
Accepted: *31 May 2022*
Published: *01 July 2022*

Citation:
Park S, Lee JS, Yoon JS, Kim NH, Park S, Youn HJ, Lee JW, Lee JE, Lee J, Hur H, Jeong J, Kim K-C and Bae SY (2022) The Risk Factors, Incidence and Prognosis of Postpartum Breast Cancer: A Nationwide Study by the SMARTSHIP Group. Front. Oncol. 12:889433. doi: 10.3389/fonc.2022.889433

The term 'pregnancy-associated breast cancer' is no longer used as it has been consistently reported that breast cancer during pregnancy and breast cancer after delivery (postpartum breast cancer) have different characteristics and prognosis. The purpose of this study is to define postpartum breast cancer by analyzing the incidence rate, related factors, and prognosis according to the timing of breast cancer. Data from the Korean National Health Insurance Service were used to analyze 1,292,727 women aged 20-49 years who birthed their first child between 2007 and 2012. The annual incidence rate of breast cancer after delivery increased every year (7.7 per 10,000 person-years after 5 years, 19.36 per 10,000 person-years after 10 years). The risk of breast cancer was significantly higher (hazard ratio 1.15, 95% CI 1.05-1.27, P=0.0037) in women diagnosed with gestational diabetes, but that was not associated with overall survival (OS). Patients diagnosed with breast cancer within 5 years of delivery had a poorer prognosis than those diagnosed later (5-year OS, <5 years: 91.1% vs. 5-10 years: 96.0%). In multivariate analysis of OS, the hazard ratio of patients diagnosed within 5 years after delivery was twice as high as of patients diagnosed between 5 and 10 years. Women diagnosed with gestational diabetes had an increased risk of breast cancer. Breast cancer patients diagnosed within 5 years of delivery had a poorer prognosis than those diagnosed later. In this regard, careful screening for early diagnosis of high-risk patients and intensive research on new treatment strategies are needed.

Keywords: breast neoplasm, postpartum, pregnancy, delivery, gestational, diabetes

INTRODUCTION

Pregnancy, childbirth and lactation produce the greatest physiologic changes in the breast. Breast cancer is related to the duration of exposure to female hormones, and it is well known that childbirth and breast feeding lower long-term risk of breast cancer. However, a temporary increase in the risk of breast cancer after pregnancy and childbirth has also been reported (1–3).

During pregnancy, the ductal system undergoes rapid proliferation and forms intra-branch alveolar structures extending from the ducts, which are used for milk production. The unique biological characteristics of the involution process, the process in which the breast returns to the mammary state before pregnancy after lactation, are related to the development of breast cancer after childbirth (3, 4). Similar to the wound healing process, immune cell influx during mammary gland involution is thought to be associated with tumor progression (5).

Studies of mouse mammary glands suggest that the involution process is also related to the induction of acute-phase response genes and increases in inflammatory cytokines and modulators of apoptosis and immune cascades (3, 6–8), and remodeling of the postpartum mammary microenvironment promotes tumor growth and tumor cell invasion and metastasis (9–11).

In the past, the term pregnancy-associated breast cancer (PABC) was used to describe breast cancer in relation to pregnancy and childbirth (12). PABC has various definitions, but is generally defined as breast cancer diagnosed during pregnancy or within 1 year after delivery. PABC has a poor prognosis due to late diagnosis or limitations in treatment.

However, more recently, the disease has been divided into breast cancer during pregnancy and breast cancer after delivery (postpartum breast cancer) (12, 13). Breast cancer during pregnancy can be treated with chemotherapy from the second trimester, and there are many reports that the prognosis is not different from that of non-PABC (12, 14–18). However, postpartum breast cancer accounts for more than 50% of breast cancers in young women and has a poorer prognosis than breast cancer in nulliparous women (19–22).

The definition of postpartum breast cancer is also diverse, with some definitions based on 1 year or 5 years postpartum, while recently an increase in risk has been reported up to 22 years (17, 18, 20, 22). In terms of risk of breast cancer, postpartum breast cancer is sometimes defined on the basis that the incidence rate temporarily increases for up to 5 years after delivery, and thereafter there is no difference from the incidence rate of the general population. In terms of prognosis, postpartum breast cancer is also defined on the basis that the prognosis of breast cancer that occurs within a certain period after delivery is different from that of breast cancer that occurs later (23).

Therefore, in this study, the following questions were explored to define and understand the characteristics of postpartum breast cancer.

1) Breast cancer incidence rate according to time after delivery - Is there a period when the incidence of breast cancer increases after delivery?
2) Breast cancer after delivery (postpartum breast cancer) risk factors and related diseases - Are there factors associated with increased incidence of breast cancer after delivery? (age, frequency, interval, comorbidities)
3) Clinical features and pathological characteristics according to the interval between delivery and breast cancer - Are there any differences in the characteristics of breast cancer according to onset timing after childbirth?
4) Prognosis according to the interval between delivery and breast cancer - Does breast cancer occurring within 5 years of delivery have a worse prognosis?

METHODS

In Korea, all medical providers and users (all citizens) are obliged to subscribe to the National Health Insurance Service (NHIS). The NHIS categorizes insurance qualifications and payment amount by insured person, and insurance policyholders (all citizens) are required to pay premiums to the NHIS. When medical services are used at a healthcare institution, the healthcare institution bills the Health Insurance Review and Assessment Service (HIRA) for the cost of medical care benefits, excluding out-of-pocket expenses. The NHIS pays insurance money, and the HIRA reviews insurance claims and evaluates the quality of medical services.

The NHIS includes data on eligibility and insurance premiums from birth to death, hospital and hospital usage history and national health checkup results, rare incurable disease and cancer registration information, medical benefit data, and long-term care data for the elderly. The National Health Insurance Sharing Service (https://nhiss.nhis.or.kr/bd/ay/bdaya001iv.do) had provided support of policy and academic research utilizing National Health information since 2002. Research data is largely provided as a customized DB and a sample cohort DB. "Customized DB" refers to data that are processed and provided as demand-tailored data so that the health information data that are collected, held, and managed by the NHIS can be used for policy and academic research purposes. Customized health information data are provided using statistical analysis tools in the "data analysis room," which is a place in the industrial complex where a PC can be used for research and analysis because the size of the data is very large. The NHIS covers all citizens who reside in Korea except Medical Aid Beneficiaries and Health Care Beneficiaries for veterans; the NHIS covers 97% of the Korean population.

Among the data from 1,620,700 female patients provided by the NHIS, this study was conducted on those under the age of 50 who experienced their first childbirth between 2007 and 2012. Eighteen patients with the same date of birth and death were excluded. Finally, 1,292,706 patients were enrolled. Of these, 235,872 (18.25%) women were defined as having their first childbirth in 2007. The last follow-up of these subjects was December 31, 2017.

Definition

Delivery was defined for inpatients using the Code of Conduct (ICD-9-CM Procedures Vol 3. version 32). First delivery was defined as a case where there was no insurance claim related to delivery between 2002 and 2006. Delivery included all kinds of delivery including vaginal delivery and Caesarean section, and the codes are listed in the **Supplement (S1)**. Breast cancer that occurred during the observation period was defined as ICD-10 codes C50 and D05, and cases with breast cancer codes before first delivery were excluded. Preeclampsia/eclampsia was defined as cases claimed under ICD-10 codes O11, O14, and O15. Gestational diabetes was defined based on code O24.

Statistical Analyses

The baseline characteristics of the women with/without breast cancer were compared using Student's t-test and the chi-square test. The annual incidence rates of breast cancer were calculated by Poisson regression. Characteristics of breast cancer occurring within 5 years/5 to 10 years/>10 years after delivery were compared and analyzed using ANOVA and chi-square test. For survival analysis, the Kaplan-Meier method and log rank test and Cox proportional hazards regression were used. The Cox proportional hazards model was used to estimate the hazard ratios (HR) and 95% confidence intervals (CIs) and to identify prognostic factors for survival. P-values < 0.05 were considered statistically significant. Statistical analyses were performed using Statistical Analysis System (SAS) version 9.4 (SAS Institute, Cary, NC, USA).

This study was approved by the Institutional Review Board of the Korea University Anam Hospital (No. 2020an0530).

RESULTS

Baseline Characteristics

The median age of the 1,292,706 women who had their first delivery between 2007 and 2012 was 30 years (range 28-33 years), among whom 44.61% were in their 20s (20-29 years), 53.23% in their 30s (30-39 years), and 2.13% in their 40s (40-49 years) (**S2**). During the follow-up period, 67.6% of women gave birth once, 30.7% of women gave birth twice, and 1.7% of women gave birth three or more times. During the observation period, 11,927 women were diagnosed with breast cancer and the median age at diagnosis was 39 years. The first childbirth age of these patients was a median of 32 years, and 70.6% of patients gave birth between the ages of 30-39 years. The period from first delivery to breast cancer diagnosis was within 5 years in 23.5%, from 5 to 10 years in 57.8%, and over 10 years in 18.6%.

The median age of the 235,872 women who had their first delivery in 2007 was 30 years (range 27-32 years) (**Table 1**). In total, 48.97% of these women were in their 20s (20-29 years) for their first delivery, 49.34% in their 30s (30-39 years), and 1.69% in their 40s (40-49 years). During the 5 years from 2007 to 2012, 44.55% of these women experienced one delivery, 50.11% two deliveries, and 5.33% three or more deliveries. Among women who delivered twice, the interval between the two deliveries was 12-24 months in 24.73%, 24-36 months in 35.33%, 36-48 months in 12.85%, and 60 months or longer in 3.82%.

Of the 235,872 women who gave birth in 2007, 2,971 patients were diagnosed with breast cancer. The median age at the time of diagnosis of breast cancer in these patients was 40 years (33-44 years), 37.80% of patients were in their 30s (30-39 years) and 58.57% of patients were in their 40s (40-49 years). The median age at first delivery of these breast cancer patients was 32 years (29-35 years), of whom 28.58% were in their 20s (20-29 years) and 68.02% were in their 30s (30-39 years). There were 1,681 cases (56.58%) of single births, 1,194 cases (40.19%) of two births, and 96 cases (3.23%) of three or more births. Among the 1,194 breast cancer patients who delivered twice, the interval between the two deliveries was 12-24 months in 295 (24.71%) and 24-36 months in 421 (35.26%). The period from first delivery to the diagnosis of breast cancer was less than 5 years in 477 patients (16.06%), between 5 and 10 years after delivery in 1,229 (41.37%), and more than 10 years in 1,265 (42.58%).

Incidence Rate of Breast Cancer

Among women who gave birth for the first time in 2007 and were observed for 12 years, the diagnosis of breast cancer showed a steady increase every year. The incidence of breast cancer 5 years after delivery was 7.7 per 10,000 person-years (95% CI 6.62-8.91), and this increased to 19.36 per 10,000 person-years after 10 years (95% CI 17.60-21.22) (**Table 1**). The incidence rate of breast cancer in women with a first delivery between 2007 and 2012 was 8.84 per 10,000 person-years (95% CI 8.33-9.37) after 5 years and 21.06 (95% CI 19.87-22.31) per 10,000 person-years after 10 years.

The risk of breast cancer increased with age at first delivery (**Figure 1**). Compared to women who gave birth for the first time in their 20s, the risk of breast cancer was HR 2.36 (95% CI 2.18-.56), for women who gave birth for the first time in their 30s and HR 3.47 (2.82-4.26) for women who gave birth for the first time in their 40s (**Table 2**).

The risk of breast cancer also increased with age at the last delivery. Compared to women in their 20s during their last delivery, the risk of breast cancer was HR 2.20 (95% CI 1.99-2.44) when their last delivery was in their 30s, and HR 3.62 (95% CI 2.99-4.39) when their last delivery was in their 40s.

The risk of breast cancer decreased as the number of deliveries increased (**Figure 2**). Compared to women who delivered only once, women who delivered twice had a risk of HR 0.63 (95% CI 0.58-0.68), and those who delivered three or more times showed a risk of HR 0.47 (95% 0.38-0.58).

In women who delivered twice, the risk of breast cancer was significantly higher when the two deliveries were less than 60 months apart compared with more than 60 months apart (HR 1.59 to 2.48). The HR increased to 2.48 (95% CI 1.18-5.22) when the delivery interval was less than 12 months, compared with more than 60 months.

Subgroup Analysis by Age at First Delivery and Number of Deliveries

Analysis of the risk of breast cancer by age at first delivery and number of deliveries revealed that risk decreased as the number

TABLE 1 | Annual incidence rate of women who had first delivery (a) between 2007 and 2012 (b) in 2007

1) women who had first delivery between 2007 and 2012

Follow-up duration (years)	No. of population	No. of event	Incidence rate per 10,000 person-years (95% CI)
0 – 1 yr	1292348	275	2.13 (1.88, 2.39)
1yr – 2yr	1291725	434	3.36 (3.05, 3.69)
2yr – 3yr	1290920	553	4.28 (3.93, 4.66)
3yr – 4yr	1289963	667	5.17 (4.79, 5.58)
4yr – 5yr	1288856	878	6.81 (6.37, 7.28)
5yr – 6yr	1287471	1138	8.84 (8.33, 9.37)
6yr – 7yr	1285796	1385	10.77 (10.21, 11.35)
7yr – 8yr	1178336	1575	13.37 (12.71, 14.04)
8yr – 9yr	967373	1437	14.85 (14.10, 15.64)
9yr – 10yr	755993	1359	17.98 (17.03, 18.96)
10yr – 11yr	553585	1166	21.06 (19.87, 22.31)
11yr – 12yr	342787	770	22.46 (20.90, 24.11)
>12yr	112901	290	25.69 (22.81, 28.82)

2) women who had first delivery in 2007

Follow-up duration (years)	No. of population	No. of event	Incidence rate per 10,000 person-years (95% CI)
0 – 1 yr	235804	59	2.50 (1.90, 3.23)
1yr – 2yr	235702	70	2.97 (2.32, 3.75)
2yr – 3yr	235563	90	3.82 (3.07, 4.70)
3yr – 4yr	235388	120	5.10 (4.23, 6.10)
4yr – 5yr	235188	138	5.87 (4.93, 6.93)
5yr – 6yr	234939	181	7.70 (6.62, 8.91)
6yr – 7yr	234656	225	9.59 (8.38, 10.93)
7yr – 8yr	234350	223	9.52 (8.31, 10.85)
8yr – 9yr	234023	239	10.21 (8.96, 11.59)
9yr – 10yr	233650	361	15.45 (13.90, 17.13)
10yr – 11yr	233134	451	19.35 (17.60, 21.22)
11yr – 12yr	232548	524	22.53 (20.64, 24.55)
>12yr	112901	290	25.69 (22.81, 28.82)

**By poisson regression.*

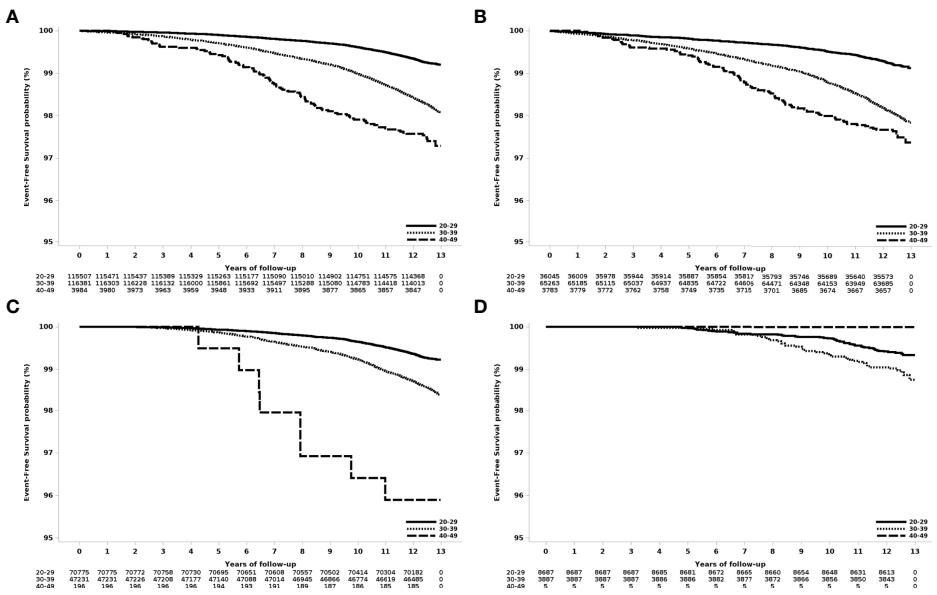

FIGURE 1 | Event-free survival according to age at first delivery in women who gave birth in 2007. **(A)** All patients, **(B)** those with one delivery, **(C)** those with two deliveries, and **(D)** those with three or more deliveries.

TABLE 2 | Incidence rate of breast cancer in women who had first delivery in 2007.

	No. of patients (N = 235,872)	No. of Events (N = 2,971)	Incidence rate per 10,000 person years (95% CI)	10-Year cumulative rate	P-value by log rank test	Crude HR (95% CI)	P-value
Age at first delivery					<.0001		
<30	115507	849	5.92 (5.53-6.33)	0.39 (0.35-0.42)		Ref	
30-39	116381	2021	14.00 (13.40-14.62)	1.01 (0.95-1.07)		2.36 (2.18, 2.56)	<.0001
40-49	3984	101	20.56 (16.92-24.99)	2.09 (1.65-2.54)		3.47 (2.82, 4.26)	<.0001
Age at last delivery					<.0001		
20-29	66222	439	5.34 (4.86-5.86)	0.38 (0.34-0.43)		Ref	
30-39	163948	2396	11.77 (11.31-12.25)	0.82 (0.78-0.87)		2.20 (1.99, 2.44)	<.0001
40-49	5702	136	19.32 (16.33-22.86)	1.85 (1.50-2.20)		3.62 (2.99, 4.39)	<.0001
Number of delivery					<.0001		
1	105091	1681	12.92 (12.32-13.56)	1.00 (0.94-1.06)		Ref	
2	118202	1194	8.12 (7.67-8.60)	0.52 (0.48-0.56)		0.63 (0.58, 0.68)	<.0001
>=3	12579	96	6.12 (5.01-7.47)	0.39 (0.28-0.50)		0.47 (0.38, 0.58)	<.0001
Interval of delivery (women with two deliveries)					0.0973		
≥ 10 months, < 12 months	570	9	12.70 (6.61-24.42)	0.70 (0.02-1.39)		2.48 (1.18, 5.22)	0.0170
≥ 12 months, < 24 months	29231	295	8.12 (7.25-9.11)	0.58 (0.49-0.67)		1.59 (1.09, 2.31)	0.0159
≥ 24 months, < 36 months	41757	421	8.12 (7.38-8.93)	0.50 (0.44-0.57)		1.59 (1.10, 2.30)	0.0144
≥ 36 months, < 48months	26936	273	8.15 (7.23-9.17)	0.50 (0.42-0.59)		1.59 (1.09, 2.32)	0.0159
≥ 48 months, < 60 months	15187	166	8.78 (7.54-10.22)	0.51 (0.40-0.63)		1.71 (1.16, 2.53)	0.0066
≥ 60 months	4521	30	5.25 (3.67-7.51)	0.38 (0.20-0.55)		Ref	

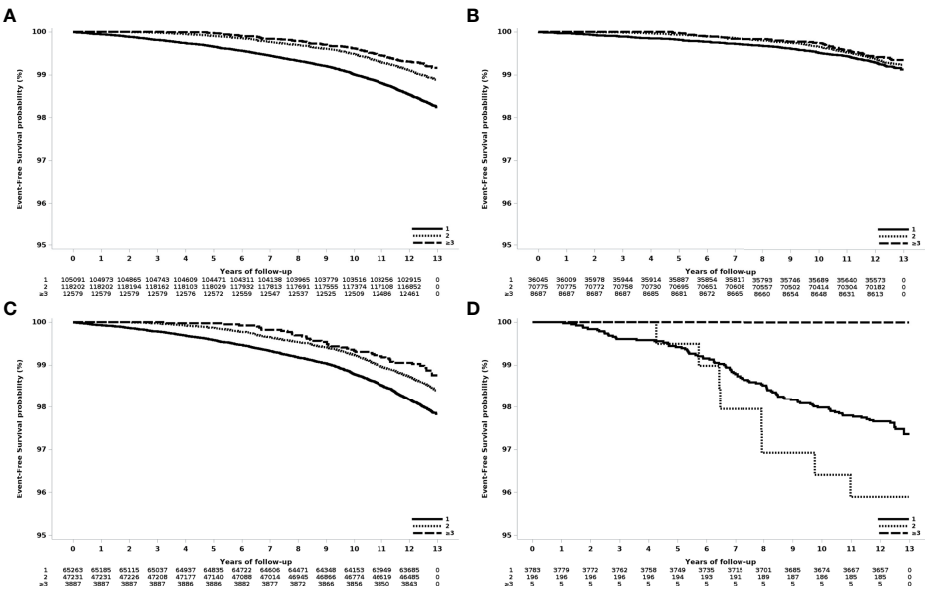

FIGURE 2 | Event-free survival according to the number of deliveries in women who had their first delivery in 2007. **(A)** All patients, **(B)** age at first delivery: 20-29 years old, **(C)** age at first delivery 30-39 years old, and **(D)** age at first delivery 40-49 years old.

TABLE 3 | Incidence rate by pregnancy associated diseases (a) preeclampsia, (b) gestational diabetes mellitus in women who had first delivery in 2007.

	No. of patients (N = 235,872)	No. of Events (N = 2,971))	Incidence rate per 10,000 person-years (95% CI)	10-Yearcumulative rate	p-value by log rank test	HR (95% CI)	p-value*
Preeclamsia					0.1950		
No	232,462	2,920	10.12 (9.76-10.49)	0.72 (0.68-0.75)		ref	
Yes	3,410	51	12.13 (9.22-15.96)	1.12 (0.77-1.48)		1.20 (0.91, 1.58)	0.1953
Gestational DM					0.0037		
No	200,242	2,467	9.92 (9.54-10.32)	0.71 (0.67-0.75)		ref	
Yes	35,630	504	11.41 (10.46-12.45)	0.80 (0.71-0.89)		1.15 (1.05, 1.27)	0.0037

P-value by Cox PH regression.

of deliveries increased in women who gave birth in their 30s. The incidence rate per 10,000 person-years was 16.09 in women who delivered once, 11.55 in women who delivered twice, and 8.66 in women who delivered three or more times (**S3**). In women who gave birth in their 30s, the HR for women who delivered twice (0.72 [95% CI 0.65-0.79]) and who delivered three or more times (0.54 [95% CI 0.39-0.73]) were significantly lower compared to women who delivered once. Among women who delivered once or twice, those who gave first birth in their 30s and 40s had a significantly higher risk of breast cancer than those who gave birth for the first time in their 20s (**S4**).

Pregnancy-Associated Diseases (Preeclampsia, Gestational Diabetes Mellitus)

During the observation period, 3,410 (1.45%) of 235,872 patients were diagnosed with preeclampsia, and 51 (1.49%) of these patients were also diagnosed with breast cancer. There was no significant difference in the risk of breast cancer with or without preeclampsia (HR 1.20, 95% CI 0.91-1.58, *P*=0.1953) (**Table 3**).

During the observation period, 35,630 (15.11%) patients were diagnosed with gestational diabetes mellitus (GDM), and 504 (1.41%) of these patients were also diagnosed with breast cancer. The annual breast cancer incidence rate in women diagnosed with GDM continued to increase, and the incidence was higher than that of women who were not diagnosed with GDM. The annual incidence rate in women with GDM was 9.58 (95% CI 6.63-13.38) after 5 years and 30.48 (95% CI 24.98-36.83) after 11 years (**S5**). The risk of breast cancer was significantly higher (HR 1.15, 95% 1.05-1.27, P=0.0037) in women diagnosed with GDM than in women without GDM.

Overall Survival

There were differences in overall survival according to age at diagnosis, age at first childbirth, treatment and timing of diagnosis of breast cancer after childbirth (**Table 4**). On univariate analysis, age at diagnosis of breast cancer, age at first and last delivery, and number of deliveries were not related to overall survival. However, there was a significant difference in overall survival according to the duration from first delivery to diagnosis of breast cancer and duration from last delivery to diagnosis of breast cancer. Compared to those diagnosed within 5 years of first delivery, HR were 0.44 (95% CI, 0.30-0.64, P <0.0001) and 0.42 (95% CI 0.24-0.71, P=0.0013) for those diagnosed 5-10 years or >10 years after first delivery, respectively (**Table 4**).

In the analysis of overall survival adjusted for age at diagnosis of breast cancer, patients diagnosed within 5 years after their first delivery had a significantly poorer prognosis than those diagnosed later (diagnosed at 5-10 years, HR 0.48, 95% 0.32-0.71, P=0.002; diagnosed at ≥10 years, HR 0.49, 95% 0.27-0.87, P=0.0152) (**Table 5**). After adjustment for age and treatment method (endocrine therapy, chemotherapy, targeted therapy) at the time of breast cancer diagnosis, patients diagnosed within 5 years of delivery had a significantly worse prognosis than patients diagnosed 5 to 10 years after delivery (HR 0.50, 95% CI 0.34-0.74, P=0.0006)

DISCUSSION

This study sought to determine whether there is transient increased risk of breast cancer after delivery. Previous studies reported an increased incidence of breast cancer 5–10 years after childbirth (13, 17, 21, 24). However, on follow-up for up to 12 years after delivery in this study, a continuous increase in the incidence of breast cancer was confirmed. The period during which an increase in the risk of breast cancer is observed after delivery may vary due to differences in study sample such as race, age range of subjects, and age at first childbirth. In this study, women under the age of 50 were defined and analyzed as women of childbearing age. Compared to other studies, this age range of subjects is relatively wide.

We also evaluated risk factors for breast cancer related to delivery. As previously established, the older women are at first delivery, the higher their risk of breast cancer is. Among women with one or two deliveries, risk increased with the age at first delivery. There was no difference according to age at first delivery when the number of deliveries was three or more. Higher risk of breast cancer was also observed with older age at last delivery. However, a higher the number of deliveries decreased risk of breast cancer. Even in the case of women whose first delivery occurred in their 30s, a decrease in risk of breast cancer was

TABLE 4 | Univariate analysis of survival (overall survival) for breast cancer patients.

	No of patient (n = 2971)	No of event (n = 145)	Incidence rate per 10,000 person-years (95% CI)	5-Year overall survival	10-Year overall survival	p-value*	Unadjusted HR (95% CI)	p-value**
Age at diagnosis of breast cancer						0.0391		
20-29	35	5	146.69 (61.06-352.44)	91.43 (82.15-100.00)	84.21 (71.34-97.08)		ref	
30-39	1123	87	129.06 (104.60-159.23)	92.64 (90.96-94.33)	88.80 (86.28-91.31)		0.73 (0.30, 1.81)	0.4988
40-49	1740	52	89.80 (68.43-117.84)	95.37 (93.97-96.77)	93.49 (90.82-96.17)		0.46 (0.18, 1.17)	0.1024
≥50	73	1	59.44 (8.37-422.00)	97.50 (92.66-100.00)	Non-estimable		0.30 (0.03, 2.55)	0.2680
Age at first delivery						0.404		
20-29	849	32	91.83 (64.94-129.85)	94.95 (92.95-96.95)	89.85 (84.92-94.78)		ref	
30-39	2021	107	119.37 (98.76-144.27)	93.36 (91.99-94.73)	90.41 (88.25-92.56)		1.31 (0.88, 1.94)	0.1850
40-49	101	6	101.27 (45.50-225.42)	96.80 (93.24-100.00)	88.75 (79.04-98.47)		1.13 (0.47, 2.69)	0.7909
Age at last delivery						0.7965		
20-29	439	19	94.77 (60.45-148.57)	95.23 (92.96-97.49)	92.30 (87.67-96.94)		ref	
30-39	2396	117	113.63 (94.80-136.20)	93.66 (92.39-94.93)	90.07 (87.83-92.30)		1.16 (0.72, 1.89)	0.5389
40-49	136	9	121.73 (63.34-233.95)	94.82 (90.75-98.90)	87.61 (78.47-96.75)		1.25 (0.57, 2.77)	0.5768
Number of delivery						0.5631		
1	1681	93	114.98 (93.83-140.89)	93.65 (92.22-95.07)	89.90 (87.54-92.27)		ref	
2	1194	47	102.35 (76.90-136.22)	94.42 (92.64-96.20)	91.01 (87.09-94.94)		0.84 (0.59, 1.19)	0.3220
>=3	96	5	138.77 (57.76-333.40)	94.05 (88.09-100.00)	86.82 (72.13-100.00)		1.13 (0.46, 2.78)	0.7894
Time-since-first-delivery						<.0001		
< 5yr	477	67	152.74 (120.21-194.06)	89.73 (87.00-92.45)	85.59 (82.37-88.80)		ref	
5yr-10yr	1229	57	89.78 (69.25-116.39)	95.26 (93.99-96.53)	Non-estimable		0.44 (0.30, 0.64)	<.0001
>=10yr	1265	21	91.09 (59.39-139.70)	Non-estimable	Non-estimable		0.42 (0.24, 0.71)	0.0013
Time-since-last delivery						<.0001		
< 5yr	759	87	143.17 (116.04-176.65)	91.10 (89.06-93.13)	87.16 (84.53-89.79)		ref	
5yr-10yr	1508	46	79.86 (59.82-106.62)	96.01 (94.80-97.23)	Non-estimable		0.44 (0.30, 0.64)	<.0001
>=10yr	704	12	99.62 (56.58-175.42)	Non-estimable	Non-estimable		0.53 (0.28, 1.01)	0.0546
Preeclampsia						0.5516		
No	2920	141	110.44 (93.64-130.26)	94.02 (92.93-95.11)	90.33 (88.31-92.36)		ref	
Yes	51	4	145.99 (54.79-388.97)	91.55 (82.11-100.00)	85.01 (69.87-100.00)		1.35 (0.50, 3.65)	0.5516
Gestational DM						0.5560		
No	2467	119	108.53 (90.68-129.89)	94.10 (92.91-95.28)	90.10 (87.87-92.33)		ref	
Yes	504	26	125.20 (85.25-183.89)	93.28 (90.55-96.02)	91.48 (88.13-94.84)		1.14 (0.74, 1.74)	0.5562

**P-value by log rank test.*

***P-value by Cox PH regression.*

observed as the number of deliveries increased. However, in the case of women who delivered less than two times, the risk of breast cancer also appears to increase with age at first delivery. The risk of breast cancer was higher in cases with a delivery interval of less than 5 years than if the delivery interval was more than 5 years. Although the number of patients was small, breast

TABLE 5 | Multivariate analysis (model I) of survival (overall survival) for breast cancer patients in women who had first delivery in 2007.

		Adjusted Hazard Ratio (95% CI)	P Value
(model I)			
Age at diagnosis of breast cancer	20-29	ref	
	30-39	0.94 (0.38, 2.33)	0.8874
	40-49	0.73 (0.28, 1.91)	0.5270
	≥50	0.51 (0.06, 4.56)	0.5506
Time-since-first-delivery	<5yr	ref	
	5yr-10yr	0.48 (0.32, 0.71)	0.0002
	>10yr	0.49 (0.27, 0.87)	0.0152
(model II)			
Age at diagnosis of breast cancer	20-29	ref	
	30-39	0.73 (0.29, 1.83)	0.5029
	40-49	0.78 (0.30, 2.04)	0.6070
	≥50	0.42 (0.05, 3.71)	0.4324
Time -since-first-delivery	<5yr	ref	
	5yr-10yr	0.50 (0.34, 0.74)	0.0006
	>10yr	0.63 (0.35, 1.14)	0.1305
Endocrine therapy	No	ref	
	Yes	0.29 (0.20, 0.42)	<.0001
Chemotherapy	No	ref	
	Yes	6.59 (4.08, 10.65)	<.0001
Target therapy	No	ref	
	Yes	0.89 (0.57, 1.38)	0.6025

cancer risk increased by HR 1.6-1.7 when the delivery interval was less than 1 year.

Preeclampsia is a multisystem syndrome that occurs in 2% to 5% of pregnancies (25). A previous systematic review and meta-analysis as well as prospective and retrospective cohort studies reported no increased risk of breast cancer (HR 1.04, 95% 0.78 to 1.39) due to preeclampsia (26). A population study also demonstrated no association between antiangiogenic factor levels during pregnancy and risk of breast cancer in the first decade after delivery (27). However, in a recently published meta-analysis that included 13 cohort studies comprising 5,254,150 participants, women with preeclampsia had a lower incidence of breast cancer than women without preeclampsia (28). One possible mechanism for this reduced risk of breast cancer is hormonal changes and responsiveness to hormones. Compared with healthy pregnant women, pregnant women with preeclampsia have low estrogen levels and high progesterone levels, and these hormonal changes may suppress estrogen-induced cancer (29, 30). Inflammatory responses and antiangiogenic factors during pregnancy may also be associated with breast cancer prevention or better prognosis (31, 32). However, there was no association between breast cancer and preeclampsia in this study. Preeclampsia/pregnancy hypertension does not increase the risk of breast cancer, although this may vary by race and age of the population.

In this study, GDM was identified as a risk factor for breast cancer. Several previous studies have also shown that diabetes mellitus (primarily type 2) is associated with increased risk of breast cancer (33–36). However, studies to date on GDM and breast cancer have shown conflicting results. There was no association with increased risk of GDM and invasive breast cancer in a large cohort of American women, the Nurses Health Study II (37), while the Sister Study (1,609 invasive breast cancers) reported a positive association between GDM and estrogen receptor (ER)-negative breast cancer (38). In a long-term cohort study of 753 women in New Zealand, gestational glucose intolerance was found to be associated with breast cancer (39). However, a US study of 1,239 women diagnosed with breast cancer and 1,166 controls did not find an association between GDM and breast cancer (40). With regard to menopause status, GDM was related to elevated risk of postmenopausal breast cancer (29) and reduced risk of premenopausal breast cancer (41). However, although GDM increased the risk of breast cancer, there was no difference in the survival rate of breast cancer patients according to GDM.

Whether postpartum breast cancer has a worse prognosis also remains unclear. PABC has a poorer prognosis than non-PABC. The definition of PABC varies, but it is generally defined as during pregnancy and within one year of delivery. A high frequency of higher grade, triple-negative breast cancers, and HER2+breast cancer was observed in PABC, and 5-year OS was worse (42–44). In a meta-analysis, PABC had a higher risk of death (OS) than non-PABC (HR 1.44, 95% CI 1.27-1.63) and postpartum breast cancer had poorer outcomes than breast cancer during pregnancy (45).

Recent studies have shown that breast cancer during pregnancy does not differ in prognosis from breast cancer in non-pregnant women. However, since postpartum breast cancer has a significantly poorer prognosis, it is more appropriate to divide breast cancer during pregnancy from postpartum breast cancer, rather than grouping them as PABC (13). In this study, patients diagnosed with breast cancer within 5 years postpartum had a poorer prognosis than those diagnosed >5 years postpartum. Since most patients diagnosed with breast cancer within 5 years of delivery are young women, the prognosis of breast cancer may be poor due to the characteristics of breast cancers that affect younger women. However, even after adjusting for age at diagnosis, prognosis was significantly poor

in patients diagnosed with breast cancer within 5 years of delivery.

Breast cancer occurring within 5-10 years of delivery is estimated to account for 35-55% of all breast cancer cases in women under the age of 45 (20)[20]. Several previous studies of young breast cancer patients have shown that breast cancer within 5-10 years of delivery has a worse prognosis than that of breast cancer in nulliparous women (46–48). Many preclinical studies have suggested that it this related to a developmental tissue remodeling process of mammary gland involution (9–11, 13, 23, 49), which may result in distinct gene expression profiles. Recent studies have shown that postpartum breast cancer is a unique entity with distinct genomic signatures. Asztalos et al. reported that distinct immune signals persist for up to 10 years after delivery (50). Genomic alterations in breast cancer were associated with age at first pregnancy; the tumors that developed in early parous patients were characterized by a higher number of indels, a lower frequency of CDH1 mutations (1.2%), a higher frequency of TP53 mutations (50%), and MYC amplification (28%) (2). PABC was associated with increased tumor infiltrating lymphocyte (TIL) infiltration (2), and programmed cell death protein 1 (PD-L1) is highly expressed in TILs in PABC (51, 52). In a recent study using RNA expression data from clinically matched estrogen receptor positive (ER+) cases (n = 16), postpartum breast cancer had pronounced T-cell presence and T-cell activation/exhaustion signatures, reduced TP53 activity, reduced ER signaling, and increased cell cycle gene signatures compared with breast cancer in nulliparous women (53).

The major limitation of this study is that stage and subtype could not be confirmed from this data. However, when the pattern of adjuvant treatment was analyzed, patients diagnosed within 5 years had a higher proportion of chemotherapy than those diagnosed within 5-10 years (**S6**). This suggests that there are differences in stage and subtype between groups, and further research is needed.

In this study, breast cancer risk continued to increase steadily until 12 years after delivery and did not show an increase in a specific time period. Those diagnosed with GDM had a higher risk of breast cancer. Older age at first delivery, fewer total births, and shorter intervals between deliveries were associated with higher risk of breast cancer. However, there was no difference in OS based on these factors. For postpartum women with these risk factors, the importance of screening should be further emphasized. The prognosis of patients who developed breast cancer within 5 years after delivery was worse than that of patients diagnosed later. Therefore, intensive screening and new treatment strategies for postpartum breast cancer patients are necessary.

DATA AVAILABILITY STATEMENT

This data is managed by the National Health Insurance Service of Korea. Only approved researchers may use the data in the designated "data analysis room". Requests to access these datasets should be directed to (https://nhiss.nhis.or.kr/bd/ay/bdaya001iv.do).

ETHICS STATEMENT

This study was approved by the Institutional Review Board of the Korea University Anam Hospital (No. 2020an0530). Written informed consent for participation was not required for this study in accordance with the national legislation and the institutional requirements.

AUTHOR CONTRIBUTIONS

All authors contributed to the study conception and design. Material preparation, data collection and analysis were performed by SP, JSL, JY, and SYB. The first draft of the manuscript was written by SB and all authors commented on previous versions of the manuscript. All authors read and approved the final manuscript.

FUNDING

This work was supported by the research grant of the Korean Breast Cancer Society.

ACKNOWLEDGMENTS

This study used the NHIS-NSC data (NHIS-2021-1-007), generated by the NHIS. We appreciate the contributions of the Multi-Disciplinary Teamwork for Breast Cancer Survivorship (SMARTSHIP) Group to this study.

SUPPLEMENTARY MATERIAL

The Supplementary Material for this article can be found online at: https://www.frontiersin.org/articles/10.3389/fonc.2022.889433/full#supplementary-material

REFERENCES

1. Borges VF. Management of the Patient With Postpartum Breast Cancer. *Oncology (Williston Park)* (2014) 28(9):768–70.
2. Nguyen B, Venet D, Lambertini M, Desmedt C, Salgado R, Horlings HM, et al. Imprint of Parity and Age at First Pregnancy on the Genomic Landscape of Subsequent Breast Cancer. *Breast Cancer Res* (2019) 21(1):25. doi: 10.1186/s13058-019-1111-6
3. Schedin P. Pregnancy-Associated Breast Cancer and Metastasis. *Nat Rev Cancer* (2006) 6(4):281–91. doi: 10.1038/nrc1839
4. Macias H, Hinck L. Mammary Gland Development. *WIREs Dev Biol* (2012) 1 (4):533–57. doi: 10.1002/wdev.35
5. Martinson HA, Jindal S, Durand-Rougely C, Borges VF, Schedin P. Wound Healing-Like Immune Program Facilitates Postpartum Mammary Gland Involution and Tumor Progression. *Int J Cancer* (2015) 136(8):1803–13. doi: 10.1002/ijc.29181

6. Oskarsson T. Extracellular Matrix Components in Breast Cancer Progression and Metastasis. *Breast* (2013) 22:S66–72. doi: 10.1016/j.breast.2013.07.012
7. Clarkson RWE, Wayland MT, Lee J, Freeman T, Watson CJ. Gene Expression Profiling of Mammary Gland Development Reveals Putative Roles for Death Receptors and Immune Mediators in Post-Lactational Regression. *Breast Cancer Res* (2003) 6(2):R92. doi: 10.1186/bcr754
8. Stein T, Morris JS, Davies CR, Weber-Hall SJ, Duffy M-A, Heath VJ, et al. Involution of the Mouse Mammary Gland is Associated With an Immune Cascade and an Acute-Phase Response, Involving LBP, CD14 and STAT3. *Breast Cancer Res* (2003) 6(2):R75. doi: 10.1186/bcr753
9. McDaniel SM, Rumer KK, Biroc SL, Metz RP, Singh M, Porter W, et al. Remodeling of the Mammary Microenvironment After Lactation Promotes Breast Tumor Cell Metastasis. *Am J Pathol* (2006) 168(2):608–20. doi: 10.2353/ajpath.2006.050677
10. Lyons TR, O'Brien J, Borges VF, Conklin MW, Keely PJ, Eliceiri KW, et al. Postpartum Mammary Gland Involution Drives Progression of Ductal Carcinoma *in Situ* Through Collagen and COX-2. *Nat Med* (2011) 17 (9):1109–15. doi: 10.1038/nm.2416
11. Schedin P, O'Brien J, Rudolph M, Stein T, Borges V. Microenvironment of the Involuting Mammary Gland Mediates Mammary Cancer Progression. *J Mammary Gland Biol Neoplasia* (2007) 12(1):71–82. doi: 10.1007/s10911-007-9039-3
12. Lyons TR, Schedin PJ, Borges VF. Pregnancy and Breast Cancer: When They Collide. *J Mammary Gland Biol Neoplasia* (2009) 14(2):87–98. doi: 10.1007/s10911-009-9119-7
13. Amant F, Lefrère H, Borges VF, Cardonick E, Lambertini M, Loibl S, et al. The Definition of Pregnancy-Associated Breast Cancer is Outdated and Should No Longer be Used. *Lancet Oncol* (2021) 22(6):753–4. doi: 10.1016/S1470-2045(21)00183-2
14. Loibl S, Han SN, von Minckwitz G, Bontenbal M, Ring A, Giermek J, et al. Treatment of Breast Cancer During Pregnancy: An Observational Study. *Lancet Oncol* (2012) 13(9):887–96. doi: 10.1016/S1470-2045(12)70261-9
15. Amant F, von Minckwitz G, Han SN, Bontenbal M, Ring AE, Giermek J, et al. Prognosis of Women With Primary Breast Cancer Diagnosed During Pregnancy: Results From an International Collaborative Study. *J Clin Oncol* (2013) 31(20):2532–9. doi: 10.1200/JCO.2012.45.6335
16. Goddard ET, Bassale S, Schedin T, Jindal S, Johnston J, Cabral E, et al. Association Between Postpartum Breast Cancer Diagnosis and Metastasis and the Clinical Features Underlying Risk. *JAMA Netw Open* (2019) 2(1):e186997–e. doi: 10.1001/jamanetworkopen.2018.6997
17. Johansson AL, Andersson TM, Hsieh CC, Cnattingius S, Lambe M. Increased Mortality in Women With Breast Cancer Detected During Pregnancy and Different Periods Postpartum. *Cancer Epidemiol Biomarkers Prev* (2011) 20 (9):1865–72. doi: 10.1158/1055-9965.EPI-11-0515
18. Stensheim H, Møller B, van Dijk T, Fosså SD. Cause-Specific Survival for Women Diagnosed With Cancer During Pregnancy or Lactation: A Registry-Based Cohort Study. *J Clin Oncol* (2009) 27(1):45–51. doi: 10.1200/JCO.2008.17.4110
19. Borges V, Elder A, Lyons T. Deciphering Pro-Lymphangiogenic Programs During Mammary Involution and Postpartum Breast Cancer. *Front Oncol* (2016) 6(227). doi: 10.3389/fonc.2016.00227
20. Callihan EB, Gao D, Jindal S, Lyons TR, Manthey E, Edgerton S, et al. Postpartum Diagnosis Demonstrates a High Risk for Metastasis and Merits an Expanded Definition of Pregnancy-Associated Breast Cancer. *Breast Cancer Res Treat* (2013) 138(2):549–59. doi: 10.1007/s10549-013-2437-x
21. Liu Q, Wuu J, Lambe M, Hsieh S-F, Ekbom A, Hsieh C-C. Transient Increase in Breast Cancer Risk After Giving Birth: Postpartum Period With the Highest Risk (Sweden). *Cancer Causes Control* (2002) 13(4):299–305. doi: 10.1023/A:1015287208222
22. Borges VF, Lyons TR, Germain D, Schedin P. Postpartum Involution and Cancer: An Opportunity for Targeted Breast Cancer Prevention and Treatments? *Cancer Res* (2020) 80(9):1790–8. doi: 10.1158/0008-5472.CAN-19-3448
23. Lefrère H, Floris G, Schmidt MK, Neven P, Warner E, Cardonick E, et al. Breast Cancer Diagnosed in the Post-Weaning Period is Indicative for a Poor Outcome. *Eur J Cancer* (2021) 155:13–24. doi: 10.1016/j.ejca.2021.06.009
24. Lambe M, C-c H, Trichopoulos D, Ekbom A, Pavia M, Adami H-O. Transient Increase in the Risk of Breast Cancer After Giving Birth. *N Engl J Med* (1994) 331(1):5–9. doi: 10.1056/NEJM199407073310102
25. Abalos E, Cuesta C, Grosso AL, Chou D, Say L. Global and Regional Estimates of Preeclampsia and Eclampsia: A Systematic Review. *Eur J Obstet Gynecol Reprod Biol* (2013) 170(1):1–7. doi: 10.1016/j.ejogrb.2013.05.005
26. Bellamy L, Casas JP, Hingorani AD, Williams DJ. Pre-Eclampsia and Risk of Cardiovascular Disease and Cancer in Later Life: Systematic Review and Meta-Analysis. *Bmj* (2007) 335(7627):974. doi: 10.1136/bmj.39335.385301.BE
27. Vatten LJ, Romundstad PR, Jenum PA, Eskild A. Angiogenic Balance in Pregnancy and Subsequent Breast Cancer Risk and Survival: A Population Study. *Cancer Epidemiol Biomarkers Prev* (2009) 18(7):2074–8. doi: 10.1158/1055-9965.EPI-09-0207
28. Wang F, Zhang W, Cheng W, Huo N, Zhang S. Preeclampsia and Cancer Risk in Women in Later Life: A Systematic Review and Meta-Analysis of Cohort Studies. *Menopause* (2021) 28(9):1070–1078. doi: 10.1097/GME.0000000000001806
29. Nechuta S, Paneth N, Velie EM. Pregnancy Characteristics and Maternal Breast Cancer Risk: A Review of the Epidemiologic Literature. *Cancer Causes Control* (2010) 21(7):967–89. doi: 10.1007/s10552-010-9524-7
30. Innes KE, Byers TE. Preeclampsia and Breast Cancer Risk. *Epidemiology* (1999) 10(6):722–32. doi: 10.1097/00001648-199911000-00013
31. Carbillon L. Hypertensive Diseases in Pregnancy and Subsequent Lower Risk of Breast Cancer: The Common Immune and Antiangiogenic Profile. *Br J Cancer* (2012) 107(11):1915–6. doi: 10.1038/bjc.2012.487
32. Gilbert JS, Bauer AJ, Gilbert S, Banek CT. The Opposing Roles of Anti-Angiogenic Factors in Cancer and Preeclampsia. *Front Biosci* (2012) 4:2752–69. doi: 10.2741/e581
33. Giovannucci E, Harlan DM, Archer MC, Bergenstal RM, Gapstur SM, Habel LA, et al. Diabetes and Cancer: A Consensus Report. *CA Cancer J Clin* (2010) 60(4):207–21. doi: 10.3322/caac.20078
34. Chodick G, Zucker I. Diabetes, Gestational Diabetes and the Risk of Cancer in Women: Epidemiologic Evidence and Possible Biologic Mechanisms. *Womens Health (Lond)* (2011) 7(2):227–37. doi: 10.2217/WHE.11.4
35. Larsson SC, Mantzoros CS, Wolk A. Diabetes Mellitus and Risk of Breast Cancer: A Meta-Analysis. *Int J Cancer* (2007) 121(4):856–62. doi: 10.1002/ijc.22717
36. Wolf I, Sadetzki S, Catane R, Karasik A, Kaufman B. Diabetes Mellitus and Breast Cancer. *Lancet Oncol* (2005) 6(2):103–11. doi: 10.1016/S1470-2045(05)01736-5
37. Powe CE, Tobias DK, Michels KB, Chen WY, Eliassen AH, Manson JE, et al. History of Gestational Diabetes Mellitus and Risk of Incident Invasive Breast Cancer Among Parous Women in the Nurses' Health Study II Prospective Cohort. *Cancer Epidemiol Prev Biomarkers* (2017) 26(3):321–7. doi: 10.1158/1055-9965.EPI-16-0601
38. Park Y-MM, O'Brien KM, Zhao S, Weinberg CR, Baird DD, Sandler DP. Gestational Diabetes Mellitus may be Associated With Increased Risk of Breast Cancer. *Br J Cancer* (2017) 116(7):960–3. doi: 10.1038/bjc.2017.34
39. Dawson SI. Long-Term Risk of Malignant Neoplasm Associated With Gestational Glucose Intolerance. *Cancer: Interdiscip Int J Am Cancer Soc* (2004) 100(1):149–55. doi: 10.1002/cncr.20013
40. Troisi R, Weiss HA, Hoover RN, Potischman N, Swanson CA, Brogan DR, et al. Pregnancy Characteristics and Maternal Risk of Breast Cancer. *Epidemiology* (1998) 9(6):641–7. doi: 10.1097/00001648-199811000-00014
41. Rollison DE, Giuliano AR, Sellers TA, Laronga C, Sweeney C, Risendal B, et al. Population-Based Case-Control Study of Diabetes and Breast Cancer Risk in Hispanic and non-Hispanic White Women Living in US Southwestern States. *Am J Epidemiol* (2008) 167(4):447–56. doi: 10.1093/aje/kwm322
42. Prior L, O'Dwyer R, Farooq AR, Greally M, Ward C, O'Leary C, et al. Pregnancy-Associated Breast Cancer: Evaluating Maternal and Foetal Outcomes. A National Study. *Breast Cancer Res Treat* (2021) 189(1):269–83. doi: 10.1007/s10549-021-06263-y
43. Simoes E, Graf J, Sokolov AN, Grischke EM, Hartkopf AD, Hahn M, et al. Pregnancy-Associated Breast Cancer: Maternal Breast Cancer Survival Over 10 Years and Obstetrical Outcome at a University Centre of Women's Health. *Arch Gynecol Obstet* (2018) 298(2):363–72. doi: 10.1007/s00404-018-4822-5
44. Suelmann BBM, van Dooijeweert C, van der Wall E, Linn S, van Diest PJ. Pregnancy-Associated Breast Cancer: Nationwide Dutch Study Confirms a

Discriminatory Aggressive Histopathologic Profile. *Breast Cancer Res Treat* (2021) 186(3):699–704. doi: 10.1007/s10549-021-06130-w
45. Azim HAJr., Santoro L, Russell-Edu W, Pentheroudakis G, Pavlidis N, Peccatori FA. Prognosis of Pregnancy-Associated Breast Cancer: A Meta-Analysis of 30 Studies. *Cancer Treat Rev* (2012) 38(7):834–42. doi: 10.1016/j.ctrv.2012.06.004
46. Lefrère H, Lenaerts L, Borges VF, Schedin P, Neven P, Amant F. Postpartum Breast Cancer: Mechanisms Underlying its Worse Prognosis, Treatment Implications, and Fertility Preservation. *Int J Gynecol Cancer* (2021) 31 (3):412–22. doi: 10.1136/ijgc-2020-002072
47. Lima SM, Kehm RD, Swett K, Gonsalves L, Terry MB. Trends in Parity and Breast Cancer Incidence in US Women Younger Than 40 Years From 1935 to 2015. *JAMA Netw Open* (2020) 3(3):e200929. doi: 10.1001/jamanetworkopen.2020.0929
48. Shao C, Yu Z, Xiao J, Liu L, Hong F, Zhang Y, et al. Prognosis of Pregnancy-Associated Breast Cancer: A Meta-Analysis. *BMC Cancer* (2020) 20(1):746. doi: 10.1186/s12885-020-07248-8
49. Lyons TR, Borges VF, Betts CB, Guo Q, Kapoor P, Martinson HA, et al. Cyclooxygenase-2–Dependent Lymphangiogenesis Promotes Nodal Metastasis of Postpartum Breast Cancer. *J Clin Invest* (2014) 124(9):3901–12. doi: 10.1172/JCI73777
50. Asztalos S, Pham TN, Gann PH, Hayes MK, Deaton R, Wiley EL, et al. High Incidence of Triple Negative Breast Cancers Following Pregnancy and an Associated Gene Expression Signature. *SpringerPlus* (2015) 4(1):710. doi: 10.1186/s40064-015-1512-7
51. Blanco L, Pincus J, Siziopikou K. Abstract PD6-07: PD-L1 is Highly Expressed in Tumor Infiltrating Lymphocytes in Pregnancy Associated Breast Cancer. *Cancer Res* (2017) 77(4 Supplement):PD6–07-PD6. doi: 10.1158/1538-7445.SABCS16-PD6-07
52. Jerzak KJ, Lipton N, Nofech-Mozes S, Boles D, Slodkowska E, Pond GR, et al. Clinical Outcomes and Prognostic Biomarkers Among Pregnant, Post-Partum and Nulliparous Women With Breast Cancer: A Prospective Cohort Study. *Breast Cancer Res Treat* (2021) 189(3):797–806. doi: 10.1007/s10549-021-06327-z
53. Jindal S, Pennock ND, Sun D, Horton W, Ozaki MK, Narasimhan J, et al. Postpartum Breast Cancer has a Distinct Molecular Profile That Predicts Poor Outcomes. *Nat Commun* (2021) 12(1):6341. doi: 10.1038/s41467-021-26505-3

Conflict of Interest: The authors declare that the research was conducted in the absence of any commercial or financial relationships that could be construed as a potential conflict of interest.

Publisher's Note: All claims expressed in this article are solely those of the authors and do not necessarily represent those of their affiliated organizations, or those of the publisher, the editors and the reviewers. Any product that may be evaluated in this article, or claim that may be made by its manufacturer, is not guaranteed or endorsed by the publisher.

frontiers | Frontiers in Oncology

ORIGINAL RESEARCH
published: 04 July 2022
doi: 10.3389/fonc.2022.920094

Using Period Analysis to Timely Assess and Predict 5-Year Relative Survival for Liver Cancer Patients From Taizhou, Eastern China

Youqing Wang[1†], Luyao Zhang[2†], Fang Han[3†], Runhua Li[1], Yongran Cheng[4], Xiyi Jiang[4], Liangyou Wang[5], Jinfei Chen[6], Jianguang Ji[7], Yuhua Zhang[3*] and Tianhui Chen[1*]*

[1] Department of Cancer Prevention/Zhejiang Cancer Institute, Cancer Hospital of the University of Chinese Academy of Sciences (Zhejiang Cancer Hospital); Institute of Basic Medicine and Cancer (IBMC), Chinese Academy of Sciences, Hangzhou, China, [2] Department of Cancer Epidemiology and Prevention, Henan Engineering Research Center of Cancer Prevention and Control, Henan International Joint Laboratory of Cancer Prevention, The Affiliated Cancer Hospital of Zhengzhou University, Henan Cancer Hospital, Zhengzhou, China, [3] Department of Hepatobiliary and Pancreatic Surgery, Cancer Hospital of the University of Chinese Academy of Sciences (Zhejiang Cancer Hospital); Institute of Basic Medicine and Cancer (IBMC), Chinese Academy of Sciences, Hangzhou, China, [4] School of Public Health, Hangzhou Medical College, Hangzhou, China, [5] Department of Non-Communicable Chronic Disease Control and Prevention, Taizhou Center for Disease Control and Prevention, Taizhou, China, [6] Department of Oncology, The First Affiliated Hospital of Wenzhou Medical University, Wenzhou, China, [7] Center for Primary Health Care Research, Department of Clinical Sciences, Lund University, Malmö, Sweden

Introduction: While timely assessment of long-term survival for patients with liver cancer is essential for the evaluation of early detection and screening programs of liver cancer, those data are extremely scarce in China. We aimed to timely and accurately assess long-term survival for liver cancer patients in eastern China.

Methods: Patients diagnosed with liver cancer during 2004–2018 from four cancer registries with high-quality data from Taizhou, eastern China, were included. The period analysis was used to calculate the 5-year relative survival (RS) for overall and the stratification by sex, age at diagnosis, and region. The projected 5-year RS of liver cancer patients during 2019–2023 was also assessed using a model-based period analysis.

Results: The overall 5-year RS for patients with liver cancer during 2014–2018 reached 32.4%, being 29.3% for men and 36.1% for women. The 5-year RS declined along with aging, decreasing from 38.2% for age <45 years to 18.8% for age >74 years, while the 5-year RS for urban area was higher compared to rural area (36.8% vs. 29.3%). The projected overall 5-year RS of liver cancer patients could reach 41.4% during the upcoming period 2019–2023.

OPEN ACCESS

Edited by:
Zheng Huachuan, Chengde Medical University, China

Reviewed by:
Fangfang Song, Tianjin Medical University Cancer Institute and Hospital, China
Qinghe Tang, Tongji University, China

***Correspondence:**
Tianhui Chen
chenth@zjcc.org.cn
Yuhua Zhang
zhangyh@zjcc.org.cn
Jianguang Ji
jianguang.ji@med.lu.se

†These authors have contributed equally to this work

Specialty section:
This article was submitted to Cancer Epidemiology and Prevention, a section of the journal Frontiers in Oncology

Received: *14 April 2022*
Accepted: *27 May 2022*
Published: *04 July 2022*

Citation:
Wang Y, Zhang L, Han F, Li R, Cheng Y, Jiang X, Wang L, Chen J, Ji J, Zhang Y and Chen T (2022) Using Period Analysis to Timely Assess and Predict 5-Year Relative Survival for Liver Cancer Patients From Taizhou, Eastern China. Front. Oncol. 12:920094. doi: 10.3389/fonc.2022.920094

Conclusions: We provided, for first time in China using the period analysis, the most up-to-date 5-year RS for patients with liver cancer from Taizhou, eastern China, and also found that the 5-year RS for liver cancer patients have improved greatly during 2004–2018, which has important implications for the timely evaluation of early detection and screening programs for patients with liver cancer in eastern China.

Keywords: 5-year relative survival, liver cancer, period analysis, cancer registry, eastern China

INTRODUCTION

Liver cancer ranks as the sixth most common cancer and the third leading cause of cancer death globally according to the latest data of GLOBOCAN 2020 (1). While, overall, 108,081 new cases and 94,213 deaths of liver cancer occurred in 2016 across China from the National Cancer Registry Annual Report 2019 (2), liver cancer ranked as the fourth most common cancer and the second leading cause of cancer death during 2010–2016 in Taizhou, eastern China, with the crude incidence rate reaching $35.16/10^5$ and the crude mortality rate reaching $33.78/10^5$ (3).

Long-term survival estimates assessed using population-based cancer registry data are essential for the evaluation of cancer burden. The 5-year relative survival (RS) is the most important index assessing cancer burden and is essential for the evaluation of early detection and screening programs for the majority of cancer types, which shall be as up-to-date as possible. The assessment of the 5-year RS has been commonly used by cohort, complete, and period approaches (4). Nevertheless, because traditional cohort and complete methods have to use 5-year follow-up data, the approaches will delay 5 years at least for survival estimates (in addition to other time requests for data collection, calculation, and publication). The period analysis, which does not require 5-year follow-up data to calculate survival estimates, is the "gold standard" for the assessment of the long-term survival of cancer patients using data from population-based cancer registries and has been widely used in Western populations (5, 6). Later in 2006, Brenner and Hakulinen (7) proposed a model-based period analysis approach using the generalized linear model, which could forecast future survival during an upcoming period (8). However, the application of the period approach in China has been scarce.

Our group found, for the first time, by systematically using the period analysis and cancer registry data from eastern China, that the period analysis is superior to traditional cohort and complete methods, which can provide more up-to-date precise estimates of the long-term survival for overall and the stratification by sex, age at diagnosis, region, and cancer sites (9). For instance, for liver cancer, during 2009–2013, the 5-year RS derived from the period analysis was found to be much closer to the observed actual survival compared to those derived from complete and cohort methods. Thus, the period analysis performed better than the traditional method for liver cancer patients.

In this study, we aimed to provide the most up-to-date (during 2014–2018) estimates of the 5-year RS for liver cancer patients from the Chinese population using the period analysis and population-based cancer registry data from Taizhou city, eastern China. We also aimed to assess the trends of the 5-year RS during 2004–2018 and to forecast the 5-year RS for the upcoming 2019–2023 period using the data during 2004–2018 and a model-based period analysis.

MATERIALS AND METHODS

Data Sources

Taizhou city with 6.6 million inhabitants is located at the eastern coast of Zhejiang province and approximately 300 km away from southern Shanghai, China. The Information and Management System for Zhejiang Provincial Chronic Disease Surveillance was established in 2001 as a platform for monitoring the incidence and mortality rates of chronic diseases (including cancer) for inhabitants living in Zhejiang province (10). This population-based cancer surveillance system was used to assess the incidence rates for cancer from nine registries in Taizhou. The proportion of death certificate only (DCO) cases as a fraction of total cases was used to judge the quality of these data, with <13% being considered acceptable (7). In light of these criteria, data from four (Luqiao, Yuhuan, Xianju, and Wenling) out of nine registries from Taizhou region were included for further analyses.

The International Classification of Diseases, 10th Revision (ICD-10), and the third edition of the International Classification of Diseases for Oncology (ICD-O-3) were used for cancer coding. Liver cancer patients (using the ICD-10 code C22) diagnosed between January 1, 2004, and December 31, 2018, were included, while follow-up information was collected through December 31, 2018, using a combination of passive and active methods. Overall, 11,519 liver cancer patients were initially identified, and among them, 664 were lost to follow-up, 136 were unknown cases, and 2,361 were missing at the last follow-up, which were eventually excluded. Thus, 8,250 patients during 2004–2018 were included for further analyses.

Statistical Analysis

The distribution differences in the basic characteristics of the patients were compared among the three periods of 2004–2008, 2009–2013, and 2014–2018. Data were analyzed using the χ^2 test for categorical variables. A P value <0.05 was considered to be statistically significant.

Throughout this article, the 5-year RS estimates for liver cancer patients were calculated as the ratio of the observed survival in the patient group with liver cancer and the expected survival from a comparable group in the general population (11). The expected survival was derived from life tables for the four cities (Luqiao, Wenling, Xianju, and Yuhuan) of the Taizhou population stratified by sex, age, region, and calendar year using the Ederer II approach.

The period approach was used to calculate the 5-year RS for patients during the 2014–2018 interval. All of the patients were separated into two subsets, i.e., those who were newly diagnosed from 2014 to 2018 and those who had been diagnosed prior to this period (2009–2013) who remained alive within this period. The period analysis was used to deal with left-censored data diagnosed prior to the period of interest and right-censored data corresponding to patients remaining alive at the end of the interest period. Using this approach, data were compiled to generate a life table, with 1-year RS (S_i) at year i of follow-up being calculated as follows:

$$S_i = 1 - \frac{\mathrm{d}_i}{n_i - c_i/2}$$

Where n_i corresponds to the population at the start of year i of follow-up, d_i corresponds to the number of deaths at the end of year i, and c_i corresponds to the number of censored data in year i.

The observed survival (S_k) values for k-years were determined by multiplying by the k-year conditional 1-year survival rate as follows:

$$\overline{S_k} = \prod_{i=1}^{k} S_i$$

RS was defined as the ratio of observed to expected survival and was calculated as follows:

$$R_i = \frac{\overline{S_k}}{S_k^*}$$

Where k was 5 when calculating 5-year RS, $\overline{S_k}$ corresponded to observed survival, and S_k^* corresponded to expected survival. RS estimates and corresponding standard error (*SE*) values were calculated as per the Greenwood method (6).

Model-based period analyses were then used to predict the 5-year RS rates for liver cancer patients over the 2019–2023 period, with additional patient stratification based on age at diagnosis, sex, and region. For these analyses, data from the 2004–2008, 2009–2013, and 2014–2018 intervals were included, with follow-up year and conditional 1-year survival rates for each year, respectively, serving as independent and dependent variables. The 5-year RS over the 2019–2023 period was then predicted by establishing a generalized linear model (GLM) *via* binomial regression.

The "periodR" package for R version 3.13 (R Foundation for Statistical Computing, Vienna, Austria) was used for all statistical analyses (7).

RESULTS

Basic Characteristics of Liver Cancer Patients

The basic characteristics of liver cancer patients are presented in **Table 1**. Overall, 8,250 liver cancer patients were included, and the number of patients increased over 2004–2018. While more men were found compared to women (6,422 men and 1,828 women), the male-to-female sex ratio reached 3.5 for overall and over 2004–2018, but no difference in sex distribution was found over 2004–2018 (P = 0.94). Rural areas had more patients compared to urban areas (89% vs. 11%), and this difference reached statistical significance over 2004–2018 (P < 0.001). Overall, the average age at diagnosis reached 61.5 years, age at diagnosis <45 years accounted for only 9%, and >50% of the patients ranged 55–74 years, while over the 2004–2008 period, this distribution was retained and reached statistical significance (P < 0.001).

Five-Year Relative Survival of Liver Cancer Patients During 2014–2018

As shown in **Table 2**, we found that the 5-year RS during 2014–2018 reached 32.4% and women had a higher 5-year RS compared to that in men (36.1% vs. 29.3%). We found a clear age gradient for the 5-year RS, declining from 38.2% for age at diagnosis <45 years to 18.8% for age >74 years. Urban areas had a higher 5-year RS compared to that in rural areas (36.8% vs. 29.3%).

Prediction During the Upcoming 2019–2023 and Trends in the 5-Year Relative Survival During 2004–2023

As shown in **Table 3**, we predicted that the overall 5-year RS during the upcoming period could reach 41.4% (38.3% for men and 47.2% for women) using three continuous 5-year (2004–2008, 2009–2013, and 2014–2018) data on survival and a model-based period analysis. We also found a clear age gradient for the 5-year RS, declining from 45.9% for age at diagnosis <45 years to 23.7% for age >74 years. Urban areas had a higher 5-year RS compared to that in rural areas (44.8% vs. 37.7%). We found a clear increasing trend in the 5-year RS during 2004–2023 for overall and the stratification by sex (**Figure 1**), age at diagnosis (**Figure 2**), and region (**Figure 3**).

DISCUSSION

We provided, for the first time in China using the period analysis, the most up-to-date 5-year RS for patients with liver cancer from Taizhou, eastern China, reaching 32.4% for overall during 2014–2018. Women had a higher 5-year RS compared to that in men (36.1% vs. 29.3%), and urban areas had a higher 5-year RS compared to that in rural areas (36.8% vs. 29.3%). We also found a clear age gradient for the 5-year RS, declining from 38.2% for age at diagnosis <45 years to 18.8% for age >74 years.

TABLE 1 | Basic characteristics of liver cancer patients diagnosed during 2004–2018 in Taizhou, eastern China.

Characteristics	Number of cases (%)	Diagnosed interval			*P*
		2004–2008	2009–2013	2014–2018	
Total	8,250 (100)	1,516 (100)	2,941 (100)	3,793 (100)	
Sex					
Male	6,422 (77.8)	1,181 (77.9)	2,283 (77.6)	2,958 (78.0)	0.9381
Female	1,828 (22.2)	335 (22.1)	658 (22.4)	835 (22.0)	
Male-to-female ratio	3.51	3.53	3.47	3.54	
Region					
Urban area	904 (11.0)	12 (0.8)	366 (12.4)	526 (13.9)	<0.001
Rural area	7,346 (89.0)	1,504 (99.2)	2,575 (87.6)	3,267 (86.1)	
Average age (years)	61.5	60.7	61.2	61.7	
Age at diagnosis (years)					
<45	748 (9.1)	202 (13.3)	278 (9.5)	268 (7.1)	<0.001
45–54	1,831 (22.2)	317 (20.9)	667 (22.7)	847 (22.3)	
55–64	2,389 (28.9)	382 (25.2)	882 (30.0)	1,125 (29.7)	
65–74	1,944 (23.6)	378 (24.9)	680 (23.1)	886 (23.3)	
>74	1,338 (16.2)	237 (15.6)	434 (14.7)	667 (17.6)	

Additionally, we predicted that the overall 5-year RS during the upcoming period could reach 41.4% (38.3% for men and 47.2% for women) using three continuous 5-year (2004–2008, 2009–2013, and 2014–2018) data on survival and a model-based period analysis. We found a clear increasing trend in the 5-year RS during 2004–2023 for overall and the stratification by sex, age at diagnosis, and region.

Liver cancer ranks as the second leading cause of cancer death in Taizhou, eastern China (3). Our finding of the 5-year RS reaching 32.4% during 2014–2018 for Taizhou is higher than the report of 19.1% during 2005–2010 for Zhejiang province (10) and is also higher than the report of 12.1% during 2012–2015 for China (11). Nevertheless, our result is plausible due to the following reasons. First, the calculation period was 8 years earlier for the report of 19.1% during 2005–2010 for Zhejiang province compared to our data (2014–2018). It is common sense that the survival of liver cancer patients shall be improved along with the progress of science and technology and the improvement of treatment over recent years (8 years later for our data) (12–16), as well as the implementation of early screening programs for liver cancer patients (17–20) and the accessibility of medical insurance systems for the local population. Second, the report of 19.1% for 2005–2010 was calculated by the cohort approach, which shall be significantly lower compared to the survival estimate calculated by the period approach, as confirmed by our group for the 5-year RS during 2009–2013 (9). Third, the report of 12.1% during 2012–2015 for China was actually projected rather than estimated. Because the data for the study were from 17 cancer registries only with cancer patients diagnosed until the end of 2013 and followed up until the end of 2015 (11), the 5-year RS for patients with any cancer type including liver cancer could be calculated at the latest for 2013, while the survival data after 2013 could only be projected, which may be biased by existing data. Taken together, our data could be significantly higher, considering that our data source was from eastern China with qualified data and an advanced health care system compared to the data on the 17 cancer registries from varied health care systems (11).

TABLE 2 | Survival of liver cancer patients during 2014–2018 in Taizhou, eastern China.

	Estimated value (%)	Standard error (SE)
Total	32.4	0.7
Sex		
Men	29.3	0.9
Women	36.1	1.3
Age at diagnosis (years)		
<45	38.2	2.4
45–54	35.4	1.6
55–64	29.2	0.7
65–74	19.3	0.5
>74	18.8	1.5
Region		
Urban area	36.8	2.3
Rural area	29.3	0.7

Our finding of women with a higher 5-year RS compared to that in men (36.1% vs. 29.3%) is plausible because men have a higher possibility of alcohol consumption, tobacco smoking, and hepatitis B virus (HBV)/hepatitis C virus (HCV) infection (21–24) compared to that in women. Prior studies have confirmed liver cancer incidence and mortality rates to be higher among men relative to those in women, with men exhibiting worse survival, which could be attributed to the protective effects of estrogens (21, 25–27). We also found that the 5-year RS rate for urban areas was higher than that in rural areas (36.8% vs. 29.3%), which may be mainly attributed to differences between rural and urban populations with respect to socioeconomic status, medical/health resource allocation, and/or health education (28–30). Additionally, the limited numbers of medical professionals and outdated equipment in rural areas can lead to the further aggravation of resource allocation in rural areas. Government officials should thus pay further attention to equity as a function of geographic area, guiding patients toward rational

TABLE 3 | Prediction of the survival of liver cancer patients during 2019–2023 in Taizhou, eastern China.

	Estimated value (%)
Total	41.4
Sex	
Men	38.3
Women	47.2
Age at diagnosis (years)	
<45	45.9
45–54	43.2
55–64	40.1
65–74	24.2
>74	23.7
Region	
Urban area	44.8
Rural area	37.7

treatment selection while optimizing resource investment in these different areas. We observed a clear age gradient for the 5-year RS, declining from 38.2% for age at diagnosis <45 years to 18.8% for age>74 years, indicating that survival rates are higher among young patients, in line with other reports (31, 32) and with the common sense that overall liver functionality shall be better in younger individuals compared to that in the elderly.

Our findings of a clear increasing trend in the 5-year RS during 2004–2023 for overall and the stratification by sex, age at diagnosis, and region are also plausible due to the following reasons. Firstly, while advances in clinical treatment approaches have been beneficial to liver cancer patient survival, surgical resection remains the most beneficial treatment associated with improvements in survival for the liver cancer patient (12–15). Second, B-ultrasound and alpha fetoprotein (AFP)-based

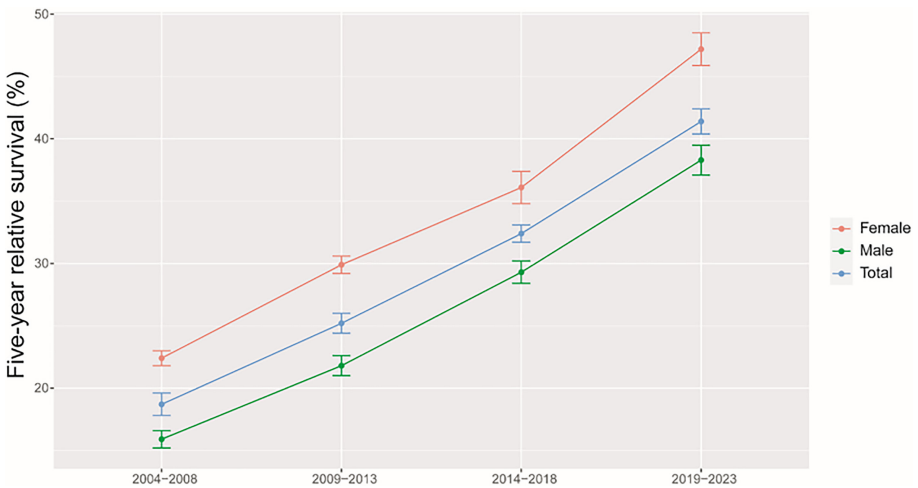

FIGURE 1 | Five-year relative survival for total, male and female liver cancers in 2004–2008, 2009–2013, 2014–2018, and 2019–2023.

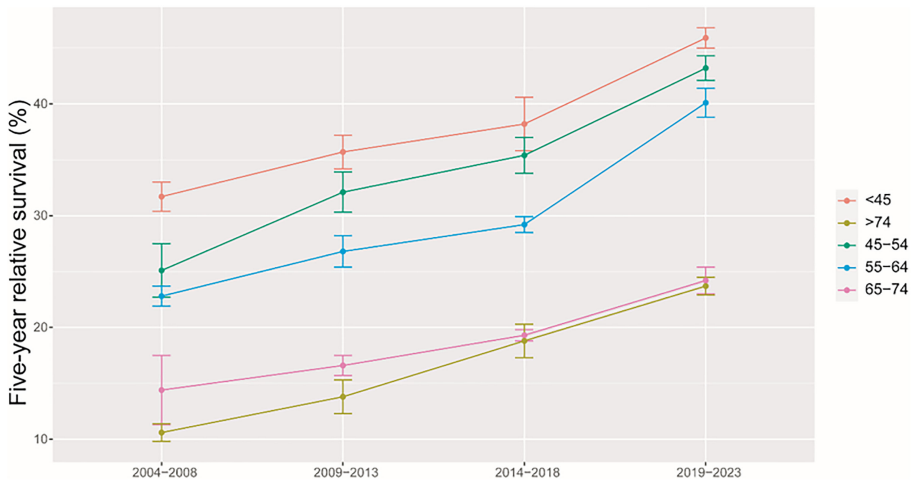

FIGURE 2 | Five-year relative survival of liver cancers for different ages at diagnosis in 2004–2008, 2009–2013, 2014–2018, and 2019–2023.

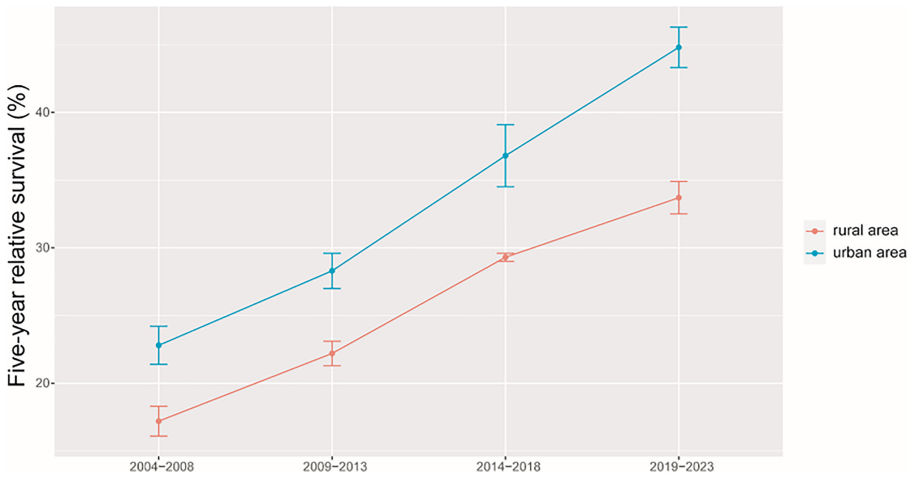

FIGURE 3 | Five-year relative survival of liver cancers for urban and rural areas in 2004–2008, 2009–2013, 2014–2018, and 2019–2023.

screening approaches have been used in routine physical examinations over recent years, enabling the potential detection of abnormalities in individuals who are otherwise largely asymptomatic (18–20). Therefore, substantial improvements in survival for the liver cancer patient over the past 10 years could be likely attributable to improvements in surveillance, screening, and early detection. Third, Taizhou, being a coastal city in Zhejiang Province, eastern China, has a rapidly growing economy and a wide coverage of medical insurance system. The improvements in survival for liver cancer patients over time may be also attributable to the highly educated nature of the Taizhou population, since the awareness rates about core knowledge of cancer prevention in Zhejiang is reaching 75% (32), given that these individuals may be more aware of the importance of physical health as compared to individuals from other regions.

Our study has a number of strengths and limitations. Three strengths are listed below. First, we provided, for the first time in China using the period analysis, the most up-to-date (during 2014–2018) 5-year RS for patients with liver cancer from Taizhou, eastern China. Second, we assessed the survival trends and found that the 5-year RS for liver cancer patients has improved greatly during 2004–2008, 2009–2013, and 2014–2018. Third, we projected the upcoming 5-year RS during 2019–2023. We also have limitations. First, we could not provide stratified survival data on stage, histology, and treatment of liver cancer patients. Nevertheless, population-based cancer registries commonly do not include clinical information on stage (such as TNM), histology, and treatment of cancer patients. Hopefully, hospital-based cancer registries including detailed information on cancer patients will be available soon in the near future. Second, we only provided the most up-to-date survival data for liver cancer patients from Taizhou, eastern China. Therefore, further investigations using provincial or national data are also highly warranted.

CONCLUSION

In this study, we provided, for the first time in China using the period analysis, the most up-to-date 5-year RS for patients with liver cancer. Overall, the results of this study show that the overall 5-year RS among liver cancer patients has gradually increased, regardless of gender, age at diagnosis, and region at diagnosis. Our timely data on 5-year RS for liver cancer patients from Taizhou, eastern China, are essential for the evaluation of early detection and screening programs for liver cancer in Taizhou, eastern China.

DATA AVAILABILITY STATEMENT

The raw data supporting the conclusions of this article will be made available upon reasonable request to the corresponding authors.

ETHICS STATEMENT

Although the data from the nine cancer registries from Taizhou City, eastern China, were completely anonymous and their use did not entail ethical problems, ethical approval by the institutional review board of Zhejiang Cancer Hospital, China, was obtained.

AUTHOR CONTRIBUTIONS

TC was responsible for the study concept and design. TC obtained funding. LW and TC acquired the data. YC analyzed and interpreted the data. YW, LZ, FH, JC, JJ, YZ, and TC drafted

the article, and all authors revised it for important intellectual content. All authors contributed to the article and approved the submitted version.

FUNDING

This work was supported by grants from the National Key Research-Development Program of China (2021YFC2500400 and 2021YFC2500401), Zhejiang Provincial Ten-Thousand Talents Plan (2021R52020), and Joint Key Program of Zhejiang Province-Ministry of Health (WKJ-ZJ-1714). The funding agencies had no role in the design and conduct of the study; collection, management, analysis, and interpretation of the data; preparation, review, or approval of the article; and decision to submit the article for publication.

ACKNOWLEDGMENTS

The authors are grateful to all of the staff at Taizhou Center for Disease Control and Prevention and the 4 county-level centers (Luqiao, Yuhuan, Xianju, and Wenling) for their support of data collection, sorting, verification, and database creation. The authors take full responsibility for data analysis and result interpretation of this article.

REFERENCES

1. Sung H, Ferlay J, Siegel RL, Laversanne M, Soerjomataram I, Jemal A, et al. Global Cancer Statistics 2020: GLOBOCAN Estimates of Incidence and Mortality Worldwide for 36 Cancers in 185 Countries. *CA Cancer J Clin* (2021) 71(3):209–49. doi: 10.3322/caac.21660
2. National Health Commission of China. *2020 Report on Health Hazards of Smoking in China*. Beijing, BJ: People's Health Publishing House (2021) p. 1–5.
3. Chai W, Wang L, Qiao D, Ye X. Analysis on the Incidence and Mortality Trend of Liver Cancer Among Residents in Taizhou From 2010 to 2016. *Prev Mde* (2019) 31(9):31–4. doi: 10.19485/j.cnki.issn2096-5087.2019.09.019
4. Woods LM, Rachet B, Cooper N, Coleman MP. Predicted Trends in Long-Term Breast Cancer Survival in England and Wales. *Br J Cancer* (2007) 96 (7):1135–8. doi: 10.1038/sj.bjc.6603668
5. Brenner H, Gefeller O. An Alternative Approach to Monitoring Cancer Patient Survival. *Cancer* (1996) 78(9):2004–10.
6. Brenner H. Long-Term Survival Rates of Cancer Patients Achieved by the End of the 20th Century: A Period Analysis. *Lancet* (2002) 360(9340):1131–5. doi: 10.1016/S0140-6736(02)11199-8
7. Brenner H, Hakulinen T. Up-To-Date and Precise Estimates of Cancer Patient Survival: Model-Based Period Analysis. *Am J Epidemiol* (2006) 164 (7):689–96. doi: 10.1093/aje/kwj243
8. Sirri E, Castro FA, Kieschke J, Jansen L, Emrich K, Gondos A, et al. Recent Trends in Survival of Patients With Pancreatic Cancer in Germany and the United States. *Pancreas* (2016) 45(6):908–14. doi: 10.1097/MPA.0000000000000588
9. Jiang X, Wang L, Cheng Y, Tang H, Chen T. Assessment of Long-Term Survival of Cancer Patients Using Cancer Registry Data From Eastern China: Period Analysis is Superior to Traditional Methods. *Int J Cancer* (2020) 147 (4):996–1005. doi: 10.1002/ijc.32866
10. Fei FR, Hu RY, Gong WW, Pan J, Wang M. Analysis of Mortality and Survival Rate of Liver Cancer in Zhejiang Province in China: A General Population-Based Study. *Can J Gastroenterol Hepatol* (2019) 2019:1074286. doi: 10.1155/2019/1074286
11. Zeng H, Chen W, Zheng R, Zhang S, Ji JS, Zou X, et al. Changing Cancer Survival in China During 2003-15: A Pooled Analysis of 17 Population-Based Cancer Registries. *Lancet Glob Health* (2018) 6(5):e555–67. doi: 10.1016/S2214-109X(18)30127-X
12. Lee S, Kang TW, Cha DI, Song KD, Lee MW, Rhim H, et al. Radiofrequency Ablation vs. Surgery for Perivascular Hepatocellular Carcinoma: Propensity Score Analyses of Long-Term Outcomes. *J Hepatol* (2018) 69(1):70–8. doi: 10.1016/j.jhep.2018.02.026
13. Kim H, Ahn SW, Hong SK, Yoon KC, Kim HS, Choi YR, et al. Survival Benefit of Liver Resection for Barcelona Clinic Liver Cancer Stage B Hepatocellular Carcinoma. *Br J Surg* (2017) 104(8):1045–52. doi: 10.1002/bjs.10541
14. Hsiao CY, Hu RH, Ho CM, Wu YM, Ho MC. Surgical Resection Versus Radiofrequency Ablation for Barcelona Clinic Liver Cancer Very Early Stage Hepatocellular Carcinoma: Long-Term Results of a Single-Center Study. *Am J Surg* (2020) 220(4):958–64. doi: 10.1016/j.amjsurg.2020.03.017
15. Dong W, Zhang T, Wang ZG, Liu H. Clinical Outcome of Small Hepatocellular Carcinoma After Different Treatments: A Meta-Analysis. *World J Gastroenterol* (2014) 20(29):10174–82. doi: 10.3748/wjg.v20.i29.10174
16. Fodor M, Zoller H, Oberhuber R, Sucher R, Seehofer D, Cillo U, et al. The Need to Update Endpoints and Outcome Analysis in the Rapidly Changing Field of Liver Transplantation. *Transplantation* (2022) 106(5):938–49. doi: 10.1097/TP.0000000000003973
17. Tanaka H, Nouso K, Kobashi H, Kobayashi Y, Nakamura S, Miyake Y, et al. Surveillance of Hepatocellular Carcinoma in Patients With Hepatitis C Virus Infection may Improve Patient Survival. *Liver Int* (2006) 26(5):543–51. doi: 10.1111/j.1478-3231.2006.01270.x
18. Hong TP, Gow PJ, Fink M, Dev A, Roberts SK, Nicoll A, et al. Surveillance Improves Survival of Patients With Hepatocellular Carcinoma: A Prospective Population-Based Study. *Med J Aust* (2018) 209(8):348–54. doi: 10.5694/mja18.00373
19. Chen JG, Zhang YH, Zhu J, et al. Early Diagnosis and Early Treatment for Liver Cancer in Qidong: Survival of Patients and Effectiveness of Screening. *Chi J Oncol* (2017) 39(12):946–51. doi: 10.3760/cma.j.issn.0253-3766.2017.12.013
20. Chen JG, Zhu J, Zhang YH, Chen YS, Ding LL, Chen HZ, et al. Liver Cancer Survival: A Real World Observation of 45 Years With 32,556 Cases. *J Hepatocell Carcinoma* (2021) 8:1023–34. doi: 10.2147/JHC.S321346
21. Ding C, Fu X, Zhou Y, Liu X, Wu J, Huang C, et al. Disease Burden of Liver Cancer in China From 1997 to 2016: An Observational Study Based on the Global Burden of Diseases. *BMJ Open* (2019) 9(4):e025613. doi: 10.1136/bmjopen-2018-025613
22. Zhou ZW, Liu YC, Xiang BD, Yu HP. Global Outlook for Primary Liver Cancer: Prevalence, Risk Factors, and Population Attributable Fraction. *Chin J Oncol Prev Treat* (2021) 13(1):14–21. doi: 10.3969/j.issn.1674-5671.2021.01.03
23. Jiang JJ, Shiels MS, O'Brien TR. Death Certificates Compared to SEER-Medicare Data for Surveillance of Liver Cancer Mortality Due to Hepatitis B or Hepatitis C Infection. *J Viral Hepat.* (2021) 28(6):934–41. doi: 10.1111/jvh.13498
24. Chen W, Xia C, Zheng R, Zhou M, Lin C, Zeng H, et al. Disparities by Province, Age, and Sex in Site-Specific Cancer Burden Attributable to 23 Potentially Modifiable Risk Factors in China: A Comparative Risk Assessment. *Lancet Glob Health* (2019) 7(2):e257–69. doi: 10.1016/S2214-109X(18)30488-1
25. Zheng R, Qu C, Zhang S, Zeng H, Sun K, Gu X, et al. Liver Cancer Incidence and Mortality in China: Temporal Trends and Projections to 2030. *Chin J Cancer Res* (2018) 30(6):571–9. doi: 10.21147/j.issn.1000-9604.2018.06.01
26. Zeng H, Zheng R, Guo Y, Zhang S, Zou X, Wang N, et al. Cancer Survival in China, 2003-2005: A Population-Based Study. *Int J Cancer* (2015) 136 (8):1921–30. doi: 10.1002/ijc.29227
27. Yang D, Hanna DL, Usher J, LoCoco J, Chaudhari P, Lenz HJ, et al. Impact of Sex on the Survival of Patients With Hepatocellular Carcinoma: A Surveillance, Epidemiology, and End Results Analysis. *Cancer* (2014) 120 (23):3707–16. doi: 10.1002/cncr.28912

28. Islami F, Miller KD, Siegel RL, Fedewa SA, Ward EM, Jemal A. Disparities in Liver Cancer Occurrence in the United States by Race/Ethnicity and State. *CA Cancer J Clin* (2017) 67(4):273–89. doi: 10.3322/caac.21402
29. Singh GK, Jemal A. Socioeconomic and Racial/Ethnic Disparities in Cancer Mortality, Incidence, and Survival in the United States, 1950-2014: Over Six Decades of Changing Patterns and Widening Inequalities. *J Environ Public Health* (2017) 2017:2819372. doi: 10.1155/2017/2819372
30. Zhang W, Sun B. Impact of Age on the Survival of Patients With Liver Cancer: An Analysis of 27,255 Patients in the SEER Database. *Oncotarget* (2015) 6 (2):633–41. doi: 10.18632/oncotarget.2719
31. Yamanaka N, Okamoto E, Oriyama T, Fujimoto J, Furukawa K, Kawamura E, et al. A Prediction Scoring System to Select the Surgical Treatment of Liver Cancer. Further Refinement Based on 10 Years of Use. *Ann Surg* (1994) 219 (4):342–6. doi: 10.1097/00000658-199404000-00003
32. Wang L, Wang YQ, Li HZ, Zhu C, Du LB. Awareness of Core Knowledge About Cancer Prevention and its Influencing Factors Among Residents in Zhejiang Province. *Prev Med* (2021) 33(8):757–61+67. doi: 10.19485/j.cnki.issn2096-5087.2021.08.001

Conflict of Interest: The authors declare that the research was conducted in the absence of any commercial or financial relationships that could be construed as a potential conflict of interest.

frontiers | Frontiers in Oncology

CASE REPORT
published: 13 July 2022
doi: 10.3389/fonc.2022.873338

Case Report: Rare Acute Abdomen: Focal Nodular Hyperplasia With Spontaneous Rupture

Ying Si[1], *Bo Sun*[2], *Ting Zhao*[1], *Ke Xiao*[1], *Dong-Xia Zhao*[1] *and Yong-Mao Huang*[1]*

[1] Department of Infectious Diseases, The Affiliated Hospital of Southwest Medical University, Luzhou, China, [2] Department of Ultrasound, The Affiliated Hospital of Southwest Medical University, Luzhou, China

Focal nodular hyperplasia (FNH) of the liver is a benign lesion characterized by hypertrophic nodules with central star-shaped fibrous scars. The etiology and pathogenesis of FNH are not completely understood. A 43-year-old man was hospitalized because of acute abdominal pain. Emergency computed tomography(CT) showed hepatic tumor rupture and bleeding. The patient's condition improved following arteriographic embolization to stop bleeding. Laparotomy confirmed spontaneous rupture and hemorrhage of focal hyperplasia and the patient remains asymptomatic after an uneventful recovery. FNH with spontaneous rupture and bleeding is extremely rare. Currently, there is no unified management standard for FNH and most previous studies recommend observation and follow-up. We recommend consideration of surgical treatment of cases with spontaneous rupture and bleeding.

Keywords: focal nodular hyperplasia (FNH), liver, rupture, acute abdomen, surgery

OPEN ACCESS

Edited by:
Kun Zhang,
Tongji University, China

Reviewed by:
Alessio Vagliasindi,
Santa Maria delle Croci Hospital, Italy
Jose M. Ramia,
Hospital General Universitario de Alicante, Spain

***Correspondence:**
Yong-Mao Huang
huang5616@sina.com

Specialty section:
This article was submitted to Surgical Oncology, a section of the journal Frontiers in Oncology

Received: *10 February 2022*
Accepted: *20 June 2022*
Published: *13 July 2022*

Citation:
Si Y, Sun B, Zhao T, Xiao K, Zhao D-X and Huang Y-M (2022) Case Report: Rare Acute Abdomen: Focal Nodular Hyperplasia With Spontaneous Rupture. Front. Oncol. 12:873338. doi: 10.3389/fonc.2022.873338

INTRODUCTION

Focal nodular hyperplasia (FNH) is the second most common benign liver tumor and accounts for approximately 8% of all primary hepatic tumors. It is thought to be a hyperplastic response to increased blood flow in an arterial malformation rather than a true neoplasm (1, 2). Spontaneous hemorrhage of an FNH is very rare, and only 10 cases have been reported (3). This patient with spontaneous rupture and bleeding of a FNH in the right liver was successfully treated by second step surgical treatment.

CASE PRESENTATION

A 43-year-old Chinese man was admitted to the hospital because of acute abdominal pain. He had no history of trauma, was in good health, and had been an intermittent alcohol user for about 20 years. Physical examination revealed no palpable mass or tenderness in the right upper abdomen. Blood routine showed that Hemoglobin was 142g/L.Alanine aminotransferase(502.6/U/L)and

Abbreviations: FNH, Focal nodular hyperplasia; CT, Computed tomography; MRI, magnetic resonance imaging; CEUS, contrast-enhanced ultrasound; GS, glutamine synthetase; RFA, radiofrequency ablation; TAE, transarterial embolization; PVA, polyvinyl alcohol.

aspartate aminotransferase(527.9/U/L)were significantly increased. Blood coagulation tests and tumor-marker levels were normal. Abdominal enhanced computed tomography (CT) showed a round, approximately8.0cm×8.0cm mass with a slightly blurred border in the right lobe of the liver, and blood around the liver. A tumor hemorrhage was suspected (**Figure 1**) and as continued bleeding could not be ruled out, the patient underwent hepatic arteriographic embolization in the emergency department. Intraoperative angiographic findings the tumor was stained in irregular mass, with irregular outer border and widened perihepatic shadow. During the operation, lipiodol and gelatin sponge particles were used to embolize the responsible blood supply artery of the tumor. Re-imaging after embolization showed that the imaging of tumor supplying arteries was significantly reduced, the tumor staining range was significantly reduced, and the embolic agent was well deposited and the patient's condition improved after 2 weeks of conservative treatment. After preoperative and intraoperative evaluation, the patient underwent right hemihepatectomy. Intraoperative exploration revealed that most of the tumor was located in segment VII and VIII, and a small part was located in segment V, adjacent to the right hepatic artery. Tumor size is about 8.0cm×8.0cm cm with an incomplete capsule, the boundary was clear, and an old blood accumulation was seen around the liver. The resected tumor was round, with clear boundaries and contained a hematoma. Pathologic examination of hematoxylin–eosin-stained tissue showed hepatocyte proliferation and vasodilation, and no atypical hyperplasia (**Figures 2**). Immunohistochemistry showed focally positive CK19 and CD34 cells consistent with capillary formation (**Figures 3**). The pathological features resulted in a final diagnosis of FNH with spontaneous rupture and bleeding. The patient recovered uneventfully and remains asymptomatic for 2 years. **Figure 4**, **5**, **6**

DISCUSSION

FNH is the second most prevalent benign liver tumor after hepatic cavernous hemangioma. The incidence is highest in those 20–50 years of age, but FNH can occur at any age (4, 5). It most often occurs in women of childbearing age with a history of oral contraceptives (6, 7). The etiology is not fully understood, but vascularization by an anomalous artery, reactive hyperplasia after hepatocellular injury induced by vasculitis, or aberrant, increased blood flow have been implicated (8–10).

Previous cases of FNH with intraperitoneal hemorrhage, including this patient, reported in English-language publications are shown in **Table 1** (3, 14–20). This review reviewed 11 patients, including 2 males and 9 females. The incidence was mainly female, with an average age of 31.7 years. As most FNH patients have no symptoms, most lesions are found by accident. Most symptomatic patients present with abdominal pain, discomfort in the right upper abdomen, and nausea. Very few have palpable masses (21–26). Liver enzyme values are abnormal in the serum of 10% to 14% of patients (27).Abdominal ultrasound, CT, and magnetic resonance imaging (MRI) with radioactive labels may reveal star scars (28).MRI has higher sensitivity and specificity for diagnosis of FNH than CT and abdominal ultrasound, especially magnetic resonance cholangiopancreatography (29, 30). Contrast-enhanced

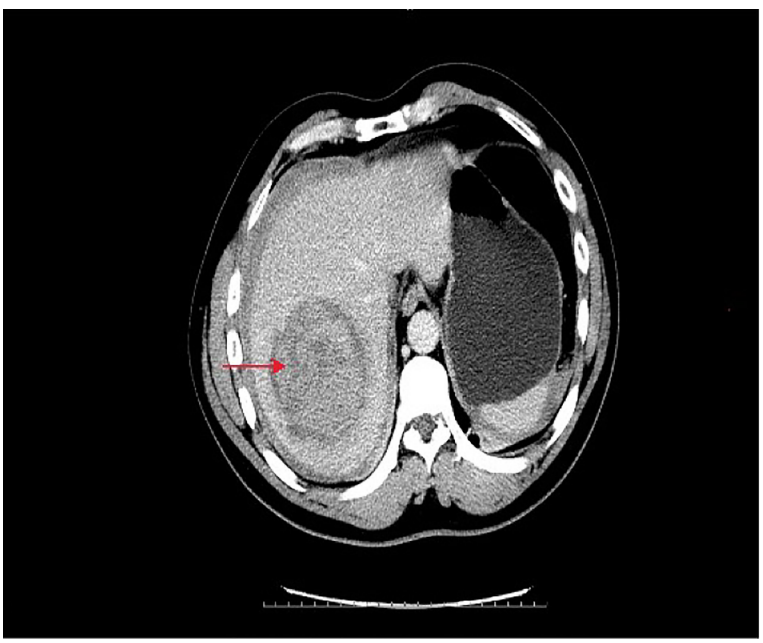

FIGURE 1 | Emergency CT of the abdomen showed a mixed density mass of about 8*8 cm in the right lobe of the liver. The lesion was near the right hepatic artery and free liquid density was visible around it.

FIGURE 2 | The tumor is nodular to the naked eye, and the cut surface is grayish yellow, and blood is visible.

ultrasound with sonazoid may provide hemodynamic information of the vascular pattern and Kupffer-phase imaging improves diagnostic confidence and is effective for follow-up in clinical practice (31).

The occurrence of spontaneous rupture and bleeding of FNH might be explained as follows: Bleeding in FNH patients may be the result of vascular malformations and intratumoral pressure associated (2, 9, 10). Increased intratumoral pressure compresses the malformed blood vessels, eventually leading to results in spontaneous bleeding. For this patient, he had a history of alcoholic hepatitis, and the liver tissue was fragile. The tumor was located around the liver and adjacent to the right hepatic

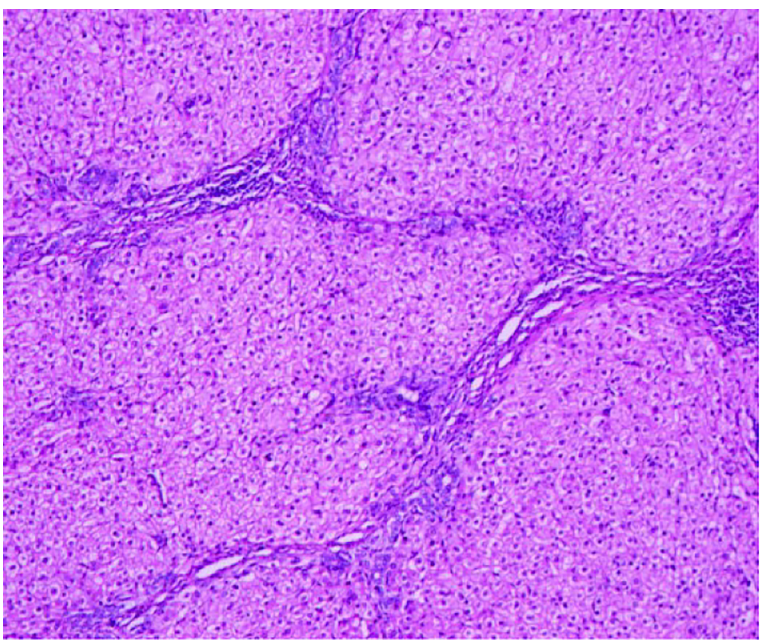

FIGURE 3 | Hematoxylin-eosin staining showed hepatocyte proliferation and vasodilation, and no atypical cells.

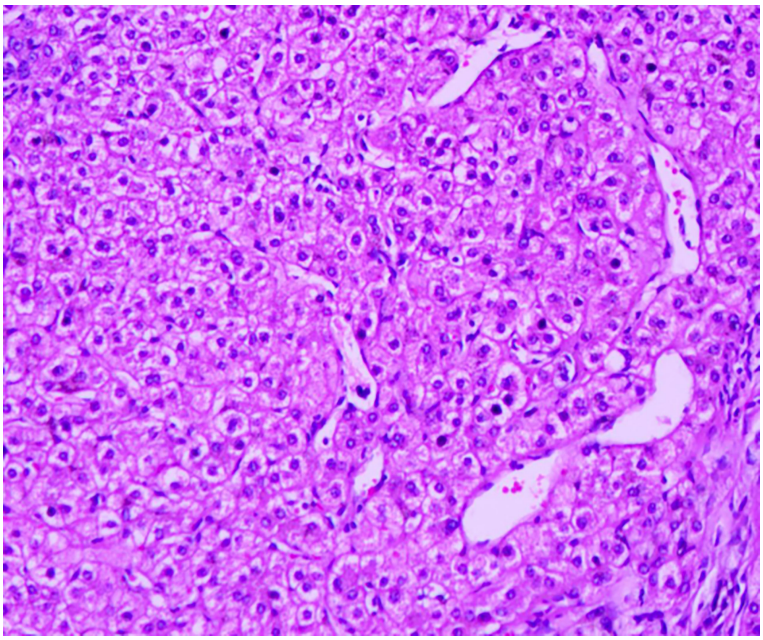

FIGURE 4 | Hematoxylin-eosin staining showed hepatocyte proliferation and vasodilation, and no atypical cells.

artery and was large and vulnerable to external force. Therefore, the combined effect of the above factors may have caused the rupture of the tumor.

Nguye et al. (32) described FNH as having two pathologies classical and non-classical. Non-classical FNH includes telangiectasia, mixed hyperplasia, and adenoma-like characteristics. Classical FNH accounts for the vast majority of diagnoses. Fabre et al. (33) proposed FNH histology scoring criteria including four main characteristics (fibrous elements, thick-walled blood vessels, hyperplastic small bile ducts, and nodules) and two minor characteristics (dilatation of liver blood sinuses and sinus fibrosis). FNH can be diagnosed if three of the

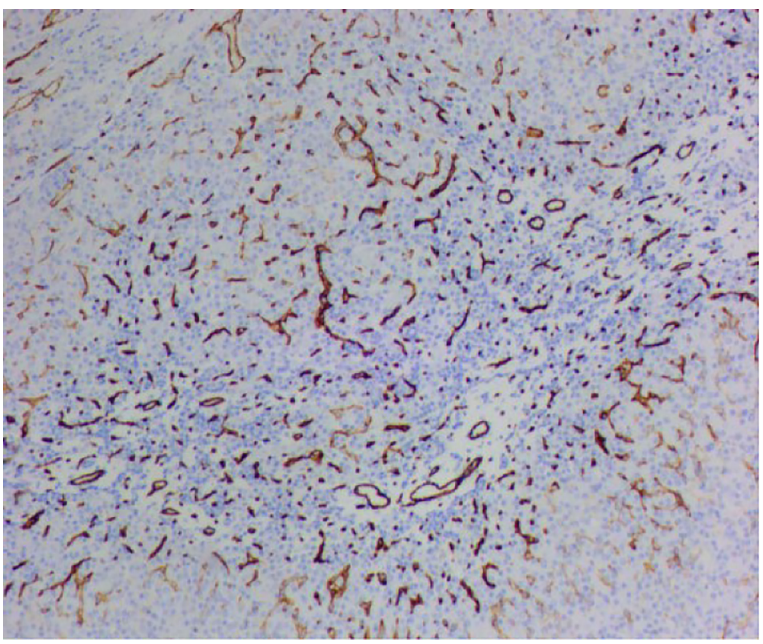

FIGURE 5 | Immunohistochemistry showed CK19 (focal +).

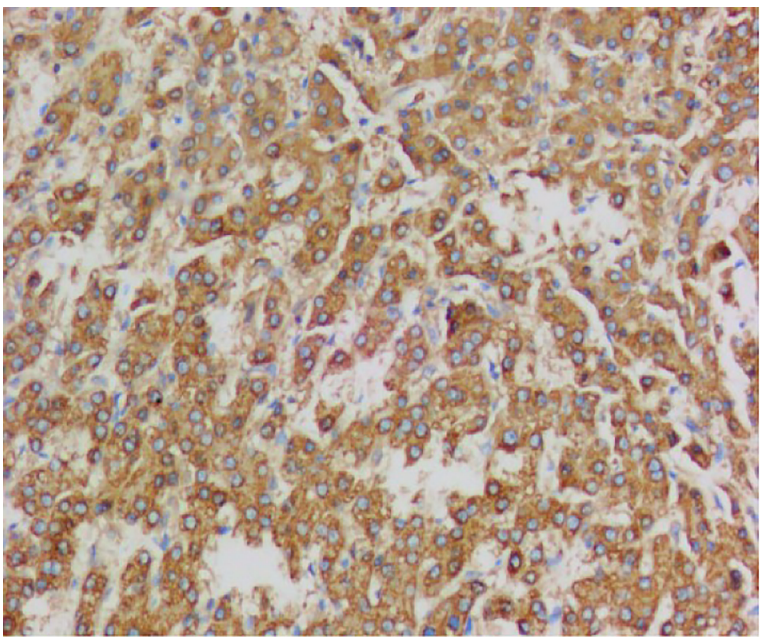

FIGURE 6 | Immunohistochemistry showed CD34(+).

four main characteristics, two main characteristics, and one or two minor characteristics are present. The presence of two or fewer major characteristics does not support a diagnosis of FNH. FNH currently has no specific immunohistochemical markers. CK19 and CK56 are markers of liver precursor cells and bile duct epithelium and CK7 is a marker of immature hepatocytes. The combined use of CK7 and CK19 is helpful for the diagnosis of FNH. CD34 is a marker of vascular endothelium, and because dilated arteries with thick walls or cavernous hemangioma occur in FNH lesions, CD34 staining is often positive. CD19 is a membrane antigen associated with cell proliferation. FNH is a local vascular malformation of the liver with increased perfusion that results in abnormal proliferation of local hepatocytes and formation of nodular lesions. Therefore, CD19 staining is often positive. There are reports in the literature that β-catenin can activate glutamine synthetase (GS), which results in typical map-like staining. Therefore, GS staining may assist in the diagnosis of FNH (34, 35).

At present, there is no consensus on the standard treatment of FNH, which is a benign lesion with no underlying malignancy. Most recommendations are for follow-up of asymptomatic patients (36). Surgery is the mainstay of treatment for patients with symptoms, enlarged lesions, and imaging indeterminate lesions during follow-up. Rupture and bleeding of liver tumors is a life-threatening condition. Emergency arteriographic embolization of unexplained hepatic mass hemorrhage can successfully control bleeding in 99% of patients (13). After the patient's condition improves, the second-stage mass can be removed and the condition diagnosed. In our experience, combined first-stage interventional embolization and second-stage mass resection can be used as the standard treatment for FNH rupture and bleeding.

TABLE 1 | Documented patients of hemorrhage caused by FNH.

First author (year)	Age (years)/sex	Diameter (mm)	Location	No	Imaging findings	Treatment	Outcome	(Refs.)
Mays ET(1974)	26/F	100	Right lobe	1	NR	Surgery	NR	(11)
Becker YT(1995)	18/F	45	Right lobe	2	NR	Surgery	NR	(12)
Hardwigsen J(2001)	37/F	50	Right lobe	1	NR	Surgery	NR	(13)
Bathe OF(2003)	27/F	60	Right lobe	1	HHAF	Surgery	Alive/18 mo	(14)
Rahili A(2005)	35/F	98	Lobus caudatus	1	HHAF	Surgery	Alive/78 mo	(15)
Chang SK(2005)	42/F	100	Right lobe	1	HHAF	Surgery	NR	(16)
Demarco MP(2006)	37/F	52	Left lobe	4	HHAF	Surgery	NR	(17)
Li T (2006)	26/F	150	Left robe	NR	HHAF	Surgery	Alive/8 mo	(18)
Yajima D(2013)	23/F	10	Right lobe	1	NR	Revealed at autopsy	Dead	(19)
Kinoshita M (2016)	35/M	80	Right lobe	1	HHAF	Surgery	Alive/48 mo	(3)
Present study (2020)	43/M	80	Right lobe	1	HHAF	Surgery	Alive/to date	(-)

M, male; F, female; mo, months; No, number; HHAF, high-density hematoma area formed; NR, not reported.

CONCLUSION

Spontaneous rupture and bleeding of FNH is very rare, but should be fully considered in patients who experience sudden abdominal pain during follow-up.

DATA AVAILABILITY STATEMENT

The original contributions presented in the study are included in the article/Supplementary Material. Further inquiries can be directed to the corresponding author.

ETHICS STATEMENT

Written informed consent was obtained from the participant for the publication of this case report.

AUTHOR CONTRIBUTIONS

YS wrote all drafts. BS discussed the meaning of the draft. TZ and KX collect all the references. D-XZ carried out the pathology and collected the clinical data. Y-MH offered conception and finalized the draft. All authors read and approved the final manuscript.

REFERENCES

1. Vilgrain V. Focal Nodular Hyperplasia. *Eur J Radiol* (2006) 58(2):236–45. doi: 10.1016/j.ejrad.2005.11.043
2. Oldhafer KJ, Habbel V, Horling K, Makridis G, Wagner KC. Benign Liver Tumors. *Visceral Med* (2020) 36(4):292–303. doi: 10.1159/000509145
3. Kinoshita M, Takemura S, Tanaka S, Hamano, Ito G, Aota T, et al. Ruptured Focal Nodular Hyperplasia Observed During Follow-Up: A Case Report. *Surg Case Rep* (2017) 3(1):44. doi: 10.1186/s40792-017-0320-4
4. Pekli D, Kokas B, Bárdos D, Fülöp A, Pajor P, Hahn O, et al. A Focalis Nodularis Hyperplasia Multimodális Kezelése. *Orvosi Hetilap* (2022) 163 (15):606–12. doi: 10.1556/650.2022.32439
5. Assy N, Nasser G, Djibre A, Beniashvili Z, Elias S, Zidan J. Characteristics of Common Solid Liver Lesions and Recommendations for Diagnostic Workup. *World J Gastroenterol* (2009) 15(26):3217–27. doi: 10.3748/wjg.15.3217
6. Herman P, Pugliese V, Machado MA, Montagnini AL, Salem MZ, Bacchella T, et al. Hepatic Adenoma and Focal Nodular Hyperplasia: Differential Diagnosis and Treatment. *World J Surg* (2000) 24(3):372–6. doi: 10.1007/s002689910059
7. Pain JA, Gimson AE, Williams R, Howard ER. Focal Nodular Hyperplasia of the Liver: Results of Treatment and Options in Management. *Gut* (1991) 32 (5):524–7. doi: 10.1136/gut.32.5.524
8. Chiorean L, Cui XW, Tannapfel A, Franke D, Stenzel M, Kosiak W, et al. Benign Liver Tumors in Pediatric Patients - Review With Emphasis on Imaging Features. *World J Gastroenterol* (2015) 21(28):8541–61. doi: 10.3748/wjg.v21.i28.8541
9. Franchi-Abella S, Branchereau S. Benign Hepatocellular Tumors in Children: Focal Nodular Hyperplasia and Hepatocellular Adenoma. *Int J Hepatol* (2013) 2013:215064. doi: 10.1155/2013/215064
10. European Association for the Study of the Liver (EASL). EASL. Clinical Practice Guidelines on the Management of Benign Liver Tumours. *J Hepatol* (2016) 65(2):386–98. doi: 10.1016/j.jhep.2016.04.001
11. Hsueh KC, Fan HL, Chen TW, Chan DC, Yu JC, Tsou SS, et al. Management of Spontaneously Ruptured Hepatocellular Carcinoma and Hemoperitoneum Manifested as Acute Abdomen in the Emergency Room. *World J Surg* (2012) 36(11):2670–6. doi: 10.1007/s00268-012-1734-6
12. Mays ET, Christopherson WM, Barrows GH. Focal Nodular Hyperplasia of the Liver. Possible Relationship to Oral Contraceptives. *Am J Clin Pathol* (1974) 61(6):735–46. doi: 10.1093/ajcp/61.6.735.
13. Becker YT, Raiford DS, Webb L, Wright JK, Chapman WC, Pinson CW. Rupture and Hemorrhage of Hepatic Focal Nodular Hyperplasia. *Am Surg* (1995) 61(3):210–4. doi: 00000478-199503000-00018.
14. Hardwigsen J, Pons J, Veit V, Garcia S, Le Treut YP. A Life-Threatening Complication of Focal Nodular Hyperplasia. *J Hepatol* (2001) 35(2):310–2. doi: 10.1016/S0168-8278(01)00096-4
15. Bathe OF, Mies C, Franceschi D, Casillas J, Livingstone AS. Massive Hemorrhage and Infarction Complicating Focal Nodular Hyperplasia of the Liver. *HPB (Oxford)* (2003) 5(2):123–6. doi: 10.1080/13651820310000
16. Rahili A, Cai J, Trastour C, Juwid A, Benchimol D, Zheng M, et al. Spontaneous Rupture and Hemorrhage of Hepatic Focal Nodular Hyperplasia in Lobus Caudatus. *J Hepatobiliary Pancreat Surg* (2005) 12(2):138–42. doi: 10.1007/s00534-004-0936-1
17. Chang SK, Chung YF, Thng CH, Loo HW. Focal Nodular Hyperplasia Presenting as Acute Abdomen. *Singapore Med J* (2005) 46(2):90–2.
18. Demarco MP, Shen P, Bradley RF, Levine EA. Intraperitoneal Hemorrhage in a Patient With Hepatic Focal Nodular Hyperplasia. *Am Surg* (2006) 72 (6):555–9. doi: 10.1177/000313480607200620
19. Li T, Qin LX, Ji Y, Sun HC, Ye QH, Wang L, et al. Atypical Hepatic Focal Nodular Hyperplasia Presenting as Acute Abdomen and Misdiagnosed as Hepatocellular Carcinoma. *Hepatol Res* (2007) 37(12):1100–5. doi: 10.1111/j.1872-034X.2007.00164.x
20. Yajima D, Kondo F, Nakatani Y, Saitoh H, Hayakawa M, Sato Y, et al. A Fatal Case of Subcapsular Liver Hemorrhage in Late Pregnancy: A Review of Hemorrhages Caused by Hepatocellular Hyperplastic Nodules. *J Forensic Sci* (2013) 58 Suppl 1:S253–7. doi: 10.1111/j.1556-4029.2012.02246.x
21. Guttmacher AE, Marchuk DA, White RIJr. Hereditary Hemorrhagic Telangiectasia. *N Engl J Med* (1995) 333(14):918–24. doi: 10.1056/NEJM199510053331407
22. Buscarini E, Danesino C, Plauchu H, de Fazio C, Olivieri C, Brambilla G, et al. High Prevalence of Hepatic Focal Nodular Hyperplasia in Subjects With Hereditary Hemorrhagic Telangiectasia. *Ultrasound Med Biol* (2004) 30 (9):1089–97. doi: 10.1016/j.ultrasmedbio.2004.08.004
23. Scardapane A, Ficco M, Sabbà C, Lorusso F, Moschetta M, Maggialetti N, et al. Hepatic Nodular Regenerative Lesions in Patients With Hereditary Haemorrhagic Telangiectasia: Computed Tomography and Magnetic Resonance Findings. *Radiol Med* (2013) 118(1):1–13. doi: 10.1007/s11547-012-0789-3
24. Bonney GK, Gomez D, Al-Mukhtar A, Toogood GJ, Lodge JP, Prasad R. Indication for Treatment and Long-Term Outcome of Focal Nodular Hyperplasia. *HPB (Oxford)* (2007) 9(5):368–72. doi: 10.1080/13651820701504173
25. Hsee LC, McCall JL, Koea JB. Focal Nodular Hyperplasia: What are the Indications for Resection? *HPB (Oxford)* (2005) 7(4):298–302. doi: 10.1080/13651820500273624
26. Shawcross DL, Naoumov N, Pachiadakis I, Mamais C, Williams R, Jalan R, et al. Should a Biopsy Precede Liver Resection or Transplantation for Presumed Hepatocellular Carcinoma When the Alfa Fetoprotein is Normal? *Transplantation* (2004) 77(4):637–8. doi: 10.1097/01.TP.0000109783.98513.E3
27. Fioole B, Kokke M, van Hillegersberg R, Rinkes IH. Adequate Symptom Relief Justifies Hepatic Resection for Benign Disease. *BMC Surg* (2005) 5:7. doi: 10.1186/1471-2482-5-7
28. Grazioli L, Morana G, Federle MP, Brancatelli G, Testoni M, Kirchin MA, et al. Focal Nodular Hyperplasia: Morphologic and Functional Information From MR Imaging With Gadobenate Dimeglumine. *Radiology* (2001) 221 (3):731–9. doi: 10.1148/radiol.2213010139
29. Bieze M, van den Esschert JW, Nio CY, Verheij J, Reitsma JB, Terpstra V, et al. Diagnostic Accuracy of MRI in Differentiating Hepatocellular Adenoma From Focal Nodular Hyperplasia: Prospective Study of the Additional Value of Gadoxetate Disodium. *AJR Am J Roentgenol* (2012) 199(1):26–34. doi: 10.2214/AJR.11.7750

30. Auer TA, Walter-Rittel T, Geisel D, Schning W, Fehrenbach U. HBP-Enhancing Hepatocellular Adenomas and How to Discriminate Them From FNH in Gd-EOB MRI. *BMC Med Imaging* (2021) 21(1):1–11. doi: 10.1186/s12880-021-00552-0
31. Lee J, Jeong WK, Lim HK, Kim AY. Focal Nodular Hyperplasia of the Liver: Contrast-Enhanced Ultrasonographic Features With Sonazoid. *J Ultrasound Med* (2018) 37(6):1473–80. doi: 10.1002/jum.14490
32. Nguyen BN, Fléjou JF, Terris B, Belghiti J, Degott C. Focal Nodular Hyperplasia of the Liver: A Comprehensive Pathologic Study of 305 Lesions and Recognition of New Histologic Forms. *Am J Surg Pathol* (1999) 23 (12):1441–54. doi: 10.1097/00000478-199912000-00001
33. Fabre A, Audet P, Vilgrain V, Nguyen BN, Valla D, Belghiti J, et al. Histologic Scoring of Liver Biopsy in Focal Nodular Hyperplasia With Atypical Presentation. *Hepatology* (2002) 35(2):414–20. doi: 10.1053/jhep.2002.31103
34. Rowan DJ, Allende DS, Bellizzi AM, Gill RM, Liu X, McKenzie CA, et al. Diagnostic Challenges of Focal Nodular Hyperplasia: Interobserver Variability, Accuracy, and the Utility of Glutamine Synthetase Immunohistochemistry. *Histopathology* (2021) 79(5):791–800. doi: 10.1111/his.14424
35. Bioulac-Sage P, Laumonier H, Rullier A, Cubel G, Laurent C, Zucman-Rossi J, et al. Over-Expression of Glutamine Synthetase in Focal Nodular Hyperplasia: A Novel Easy Diagnostic Tool in Surgical Pathology. *Liver Int* (2009) 29 (3):459–65. doi: 10.1111/j.1478-3231.2008.01849.x
36. Perrakis A, Demir R, Müller V, Mulsow J, Aydin Ü, Alibek S, et al. Management of the Focal Nodular Hyperplasia of the Liver: Evaluation of the Surgical Treatment Comparing With Observation Only. *Am J Surg* (2012) 204(5):689–96. doi: 10.1016/j.amjsurg.2012.02.006

Conflict of Interest: The authors declare that the research was conducted in the absence of any commercial or financial relationships that could be construed as a potential conflict of interest.

Publisher's Note: All claims expressed in this article are solely those of the authors and do not necessarily represent those of their affiliated organizations, or those of the publisher, the editors and the reviewers. Any product that may be evaluated in this article, or claim that may be made by its manufacturer, is not guaranteed or endorsed by the publisher.

Frontiers in Oncology

Advances knowledge of carcinogenesis and tumor progression for better treatment and management

The third most-cited oncology journal, which highlights research in carcinogenesis and tumor progression, bridging the gap between basic research and applications to imrpove diagnosis, therapeutics and management strategies.

Discover the latest Research Topics

See more →

Frontiers

Avenue du Tribunal-Fédéral 34
1005 Lausanne, Switzerland
frontiersin.org

Contact us

+41 (0)21 510 17 00
frontiersin.org/about/contact